

STUDY OF POLAR ICE USING REMOTE SENSING DATA

Thesis Submitted for the degree of

DOCTOR OF PHILOSOPHY
In
MARINE SCIENCES
To the
GOA UNIVERSITY

By

Nilay Sharma

574.92

SHA / stu

T - 360

National Centre for Antarctic and Ocean Research
Head Land Sada, Vasco da Gama
Goa India 403 804

August 2006

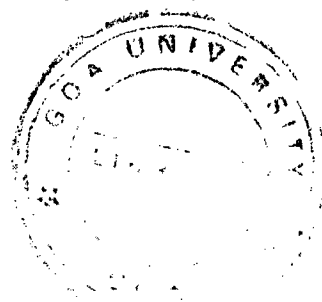


DECLARATION

I hereby declare that the thesis entitled "***STUDY OF POLAR ICE USING REMOTE SENSING DATA***" is a genuine record of research work carried out by me and no part of this thesis has been submitted by me to any University or Institution for the award of any degree or diploma.

Vasco-da-gama
August, 2006


(Nilay Sharma)

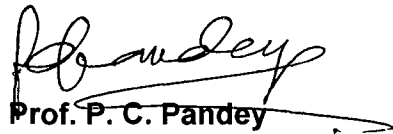


CERTIFICATE

This is certify that the thesis entitled, "**STUDY OF POLAR ICE USING REMOTE SENSING DATA**", Submitted by Mr. Nilay Sharma for the award of the degree of Doctor of Philosophy in Marine Sciences is based on his original studies carried out by him under my supervision. The thesis or any part thereof has not been previously submitted for any other degree or diploma in any universities or institutes.

Place: NCAOR, Goa

Date:



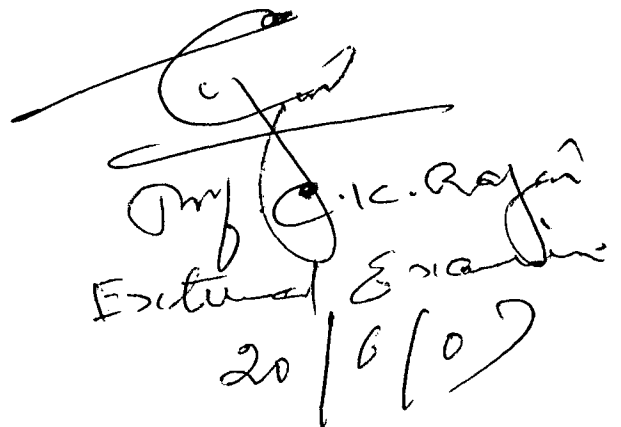
Prof. P. C. Pandey

Visiting Professor, CORAL,
Dept of Ocean science and Naval,
Architecture, Ocean Research, IIT,
Kharagpur, 721 302 -INDIA

No Correction is suggested as



HOD



Prof. P. C. Rajan
External Examiner
20/6/07

ACKNOWLEDGEMENTS

I am extremely grateful to my Research Guide, Prof. P.C. Pandey, Founder Director, National Centre for Antarctic and Ocean Research (NCAOR), for his eminent guidance, valuable suggestions, and constant encouragement in pursuing this research work. His insightful suggestions, zeal and never dying attitude gave me a direction and sense to my work. I thank him sincerely for offering an opportunity to do research work under his supervision in National Centre for Antarctic and Ocean Research (NCAOR) and Space Applications Centre (SAC), Ahmedabad. I sincerely thank him as without his valuable guidance and critical comments, it would not have been possible for me to accomplish this task

I am extremely thankful to my Co-guide, Dr. G. N. Nayak, Dean, Goa University, Goa, for his constant support and insight to pursue the knowledge and framing into form of thesis. It would have been really impossible for me to conclude the research work in valuable findings.

I accord my sincere thanks to Shri Rasik Ravindra, Director, and NCAOR for allowing me to carry out this research work and also providing all the facilities I required to complete research work.

I would like to acknowledge Dr. Nand Kishore Vyas, Scientist-SG, Oceanic Sciences Division, Space Applications Centre, Indian Space Research Organization (ISRO) for his constant guidance throughout the work. I am certain that the directions, comments, suggestions, and encouragements I got from Dr. Vyas, for throughout this study helped me to complete this work in a better way. He always came forward to provide all the support as colleague, guide and guardian, as and when I needed in due course of time.

I can't forget Dr. S.M. Bhandari, Scientist-SG, Oceanic Sciences Division, SAC for his encouraging attitude, powerful insight and scientific vision and views provided during my Ph.D. work

I am extremely grateful to all senior scientists, Shri T.V.P. Rao, Dr. M. Sudhakar, Dr. S. Rajan, Dr. N. Khare and Dr. A. Shivaji for their support during the entire research work.

I am especially thankful to Mr. H. I. Andharia and all the members of MOG, SAC Computer Facility for extending their full cooperation and support during various phases of development of this thesis work.

I am thankful to Dr. Menon, Department of Marine sciences, Goa University. He always supported to follow hard work for research. I am greatly acknowledged to him.

I wish to acknowledge the encouragement and support given by Dr. R. R. Navalgund Director, SAC, Dr. M. S. Narayanan, (Former Group Director, MOG), Dr. V.K. Agarwal, Group Director, MOG during Dr. Abhijit Sarkar, Group Head, Dr. P. S. Desai and Dr. P.C. Joshi MOG during entire thesis work.

I find no appropriate words to express my gratitude to Mrs. Savita Pandey and Mrs. Annpurna Vyas for their unending love, unrelented support like my parents.

I sincerely acknowledge to Dr. A. Luis, Dr. M.K. Dash and Mr. K.N. Babu for their encouraging ideas towards application oriented research, rather concrete research work. I am thankful for their support due to which I came up with the end of this herculean task

I am thankful to Mr. Somnath Samanta, Mr. Raju Das, Mr. P. Shetekar, Vaman, Nixon, Abhijit, Lalit and all the member of NCAOR Computer Facility for extending their full cooperation and support during various phases of development of this thesis work.

I express my due regards and affection to like my elder brother Shri Anoop Tiwari and Dr. Subodh Chaturvedi who support me during my tough time. I thank to Shri Pradeep Sharma, Shri Praveen Vohat, Dharmendra Tomar, Annant Parikh, Kamlesh Verma, Amita Prabhu and late Shri Kaushik who always had been with my family during my smooth and tough time.

I am thankful to Dr. Rahul Mohan, Dr. D. Pandey, Dr. S.M. Singh, Dr. Manish Tiwari, Dr. Thambon M, Dr. Anil, Dr. Raja kumar, Shushant, Shailesh, Witty, Shri S.K. Pandey for their support and suggestions during the work.

I really enjoyed my association with my special friends Ms. Vijaylaxmi N., Arvind Sahay, Rahman, Samir Pokhrel, Abhishek, Rambir, Shankar, Dr. Ravi Mishra, Dr. Ramesh, Ms. Meena, Vikram, Devendra, Dr. Benidhar Deshmukh, Dr. Yaswant Pradhan, Bintu, Vishal, Anurup, Sunil, Manoj, Poonam, Vidhya, Rajashree, Reena, Sarita and Ms. Nirmala. I should say that I am fortunate to have such nice friends. I really thank them for all their help during the entire thesis work. I was always greatly cheered up by their warm company.

It is difficult for me to express my gratitude to my family in few words. My parents have been a guiding force behind the entire endeavor. I would not have finished my thesis without the constant encouragement and inspiration of my father Shri C. K. Sharma and my family members specially grand father, grand mother, mother, uncle, aunty, brother: Anay, Vishwas, Abhay, Saurabh, Nitish, master Tanmay, and Sister: Ratna, Vinita, Pallavi, Rashmi, Sheetal and brother-in law Mr. Ashish Joshi. I can't forget support from my -in-law Mr. & Mrs. T. R. Rajput , Mr. Raj , Mr. Ravi and Mrs. Sweta Rajput.

My little son Aashay, at the last stage of my work, entered in this world and whose glittering eyes always filled me with new enthusiasm to complete the work and always made me feel happy, whenever I felt tired of working.

I find no appropriate words to express my feelings and appreciation to my wife Renuka Sharma (Rani) who deserves kudos for maintaining congenial atmosphere at home and for keeping me always in high spirits despite several odd situations. Her unending love, great sacrifice, advice and deep affection gave me the determination to fulfill research study.

Last but not least I thank to all those who directly or indirectly are associated with the completion of this work.

(Nilay Sharma)
August-2006

ABSTRACT

This Thesis discusses the analysis of the data obtained over the Polar Oceans region during the period June 1999 – September 2001 through the use of Multi-channel Scanning Microwave Radiometer (MSMR) onboard India's Oceansat-1 satellite. The procedures and the algorithms developed for

- (i) estimating sea ice extent and concentration over the polar oceans
- (ii) studying seasonal and long term variability of these parameters over different sectors of the polar oceans, and
- (iii) studying the secular trend in polar sea ice by combining MSMR data with SMMR and SSM/I data.

have been described in detail. As a prelude to using the MSMR data for the above mentioned studies, a detailed exercise was also undertaken to inter-compare the MSMR observed brightness temperatures and the MSMR derived sea ice characteristics with the concurrently available SSM/I values. This was done to validate and establish full confidence in the accuracy of MSMR data. As a part of the study, weekly/monthly color maps of the distribution of sea ice have been generated for the polar oceans.

Then the analysis of the extent of sea ice in different sectors of the polar oceans and their time variation have been taken up in the context of the climate change scenario. The MSMR data has been combined with the SMMR data and the SSM/I data onboard Nimbus-5, Nimbus-7 and DMSP satellites to study the secular trends in sea ice extent over the entire period 1978-2001.

The mean rates of change of the sea ice extent of over different sectors of the Antarctic Ocean and for the region as a whole have been determined. It has been found that the increasing trend in the sea ice extent over the Antarctic region may be slowly accelerating in time, particularly over the last decade. This is in contrast to the slowly and regularly decreasing sea ice extent over the Arctic region. The new hypothesis, thus generated by the authors, about the acceleration of sea ice cover over Antarctic region has found support from a variety of other studies that have come out subsequently. Continually increasing sea ice extent over the Antarctic Southern Polar Ocean, along with the observed decreasing trends in Antarctic ice surface temperatures over the last two decades, as reported by other investigators, appears to be paradoxical in the global warming scenario resulting from the increasing greenhouse gases in the atmosphere. This calls for continued monitoring towards achieving a better understanding of the role of sea ice conditions in the polar oceans in influencing the earth's climate, in the future decades to come.

CONTENT

CHAPTER 1: GENERAL INRODUCTION		
1.1	Introduction	1
1.2	Polar Ice	5
	1.2.1 Icebergs	5
	1.2.2 Ice – Sheets	5
	1.2.3 Glaciers	6
	1.2.4 Snow cover	7
	1.2.5 Frozen Ground & Permafrost	7
	1.2.6 Sea Ice	8
1.3	OBJECTIVES & ORGANIZATION OF THE THESIS	8
	1.3.1 Objectives	9
	1.3.2 Thesis outline	9
CHAPTER 2: REMOTE SENSING AND POLAR ICE		
2.1	Introduction	15
2.2	Basics of Remote Sensing	16
2.3	Sensor Technology	17
2.4	Interaction of Electromagnetic Radiation with Ocean and Ice Surfaces	21
	2.4.1 Emissivity of Different Types of Earth Surfaces	21
	2.4.1.1 Emissivity of the Ocean Surface	22
	2.4.1.2 Emissivity of the Sea Ice Surface	23
2.5	Remote Sensing of Polar Cryosphere : Historical Background	25
	2.5.1 Optical Remote Sensing of Cryosphere	26
	2.5.2 Passive Microwave Remote Sensing of Cryosphere	27
	2.5.3 Active Microwave Remote Sensing of the Cryosphere	29
	2.5.2.1 Scatterometer	30

2.5.2.2 Altimeter	30
CHAPTER 3: DATA DESCRIPTION	
3.1 Introduction	37
3.2 Introduction to Oceansat-1	37
3.3 The Orbit and Coverage of Oceansat – 1	37
3.4 Sensor Description	38
3.5 Telemetry, Tracking And Command Network	40
3.6 Data Reception	40
3.7 MSMR Instrument	41
3.7.1 MSMR Data and Data Products	42
3.7.2 Overview of MSMR Data Products	42
3.7.2.1 Raw data product	43
3.7.2.2 Antenna temperature data files (ATD product)	43
3.7.2.3 Brightness temperature data files (BTD product)	44
3.7.2.4 Geophysical Parameter data files (GPD product)	45
3.7.2.5 Monthly averaged product files (MAP product)	45
3.7.3 MSMR Data file structure	45
CHAPTER 4: PROCESSING OF MSMR DATA FOR SEA ICE STUDIES	
4.1 Introduction	51
4.2 Extraction of Data	51
4.2.1 Extraction of data for the region of interest	51
4.2.2 Development of the interpolation scheme to fill the data gaps	52
4.2.3 Geographical gridding of the data	53
4.3 Mapping Of MSMR Data	53
4.3.1 Polar Stereographic projection and its application to sea ice studies	54
4.3.2 Mapping of MSMR data into polar stereographic projection	55
4.4 Calculation of Sea Ice Extent	55

CHAPTER 5: INTER-COMPARISON OF MSMR AND SSM/I OVER SOUTHERN POLAR OCEAN (SPO)

5.1	Introduction	59
5.2	Inter -Comparison	59
	5.2.1 Comparison of the Emissivity of Sea Ice and open water	60
	5.2.2 Comparison of Brightness Temperature levels	65
5.3	Development of Sea Ice Concentration (sic) Algorithm from MSMR data	67
	5.3.1 Development of SIC algorithm based on MSMR T_B 's	68
	5.3.2 Development of SIC Algorithm from MSMR Polarization and Spectral Gradient Ratios	70

CHAPTER 6: SEA ICE COVER OVER THE SOUTHERN POLAR OCEAN (SPO)

6.1	Introduction	81
6.2	Defining the Sectors in SPO	82
6.3	Methodology	83
	6.3.1 Channel Selection	84
	6.3.2 Methodology to Process the Data	84
	6.3.3 Details of Processing	86
6.4	Seasonal variation (Intra-Annual) of Sea Ice extent	86
6.5	Secular trends of SIE (Inter-Annual Trends : combination with SMMR and SSM/ I results)	87
	6.5.1 Weddell Sea Sector	87
	6.5.2 Ross Sea Sector	93
	6.5.3 Indian Ocean	100
	6.5.4 Pacific Ocean Sectors	101
	6.5.5 Bellingshausen-Amundsen Sea	109
	6.5.4 Southern Polar Ocean Region (as a whole)	115
6.6	Time Evolution of the Melting Process of Sea Ice as Observed By MSMR	122

CHAPTER-7: SEA ICE COVER OVER THE NORTHERN POLAR REGION (NPR)

7.1	Introduction	129
7.2	Sector Definitions in NPR	130
7.3	Methodology	133
7.4	Inter-Comparison of MSMR and SSM/I Data	136
7.5	Inter-annual Variation of Sea Ice Extent	137
	7.5.1 Bering Sea	137
	7.5.2 Sea of Okhotsk and Japan	138
	7.5.3 Greenland Sea	146
	7.5.4 Kara and Barents Seas	151
	7.5.5 North American Sector	157
	7.5.6 Arctic Ocean	163
7.6	NORTH POLAR REGION (as a whole)	169
	7.6.1 Intra-annual Range of Ice Coverage	169
	7.6.2 Interannual Variability of Ice Coverage	170
CHAPTER-8: GLOBAL SEA ICE COVER		
8.1	Introduction	177
8.2	Comparison Of The Sea Ice In The Southern & The Northern Polar Regions	178
8.3	Seasonal Cycle On A Global Scale	181
8.4	Global Sea Ice Trend And Temperature	182
CHAPTER-9 DISCUSSION, CONCLUSIONS AND SCOPE FOR FUTURE WORK		
9.1	Scope for Future Work	191

LIST OF TABLES

No.	Title	Page Nos.
3.1	Orbital details of OCEANSAT – 1	38
3.2	Major specifications of OCM	39
3.3	Spectral band of OCM and their applications	39
3.4	Major specifications of MSMR	39
3.6	Receiving system specifications	41
3.7	MSMR data structure	46
5.1	Types of Sea ice and their properties	63
5.2	Signatures of sea ice and open water from P4 MSMR	64
5.3	Regions selected for the development of MSMR data for multiple regression between MSMR T_B 's and SSM/I Sea ice concentration	69
6.1	The areas of different sectors of the Southern Polar Ocean (from Gloersen et al. 1992)	83
6.2	Variation of sea ice extent and sea ice area from trend Southern Polar Ocean	121
7.1	The areas of different sectors of the Northern Polar Region (from Gloersen et al. 1992)	131
8.1	Variation of sea ice extent in Global Sea Ice Cover	184

FIGURES

1.1	Global effect of polar Ice	13
1.2	Annual average of the combined land –air and SST anomalies (blue bars): (a) Global, (b)Northern Hemisphere, and (c)Southern hemisphere	13
1.3	General Circulation pattern over the globe	14
1.4	Globally albedo distribution	14
2.1	Electro-Magnetic Spectrum and different type of Remote Sensing	31
2.2	Atmospheric radiations, transmission and absorption at different wavelength	31
2.3	Cross-track & Along-track scanning	32
2.4	Viewing geometry for the scanning radiometer	32
2.5	Contribution from different sources reaching satellite sensor in case of MWR	33

2.6	Absorption of water vapour and oxygen	33
2.7	The Emmissivity of water as a function of radio frequency	34
2.8	Reflectance & emmissivity of a plane sea-water as a function as of incident angle for two different	34
2.9	Change in sea surface brightness temperature per change in surface temperature over the range 0 – 30°C as function of radio frequency	35
2.10	NIMBUS-7 with SMMR and a number of other instrument	36
2.11	F08 SSM/I orbit and scan geometry	36
3.1	Block Diagram of OCEANSAT -1	49
3.2	Viewing Geometry (a), MSMR Viewing Geometry (b)	50
4.1	The concept of polar stereographic projection	54
4.2	Presentations of pixel area on the earth surface	57
4.3	Depth/Elevation Map of the world	57
5.1	Frequency distribution of sea ice and open water 90°W-92° W(June 10-11, 1999)	72
5.2	Spectra of polar oceanic surface over MSMR Frequency (a) and Emissivity of polar oceanic surfaces over the MSMR wavelengths (b)	73
5.3	Emissivity of polar oceanic surface over MSMR wavelengths	74
5.4	Scatter plot of MSMR (18 GHz) vs. SSM/I (19.35 GHz) TB for vertical and horizontal polarization for October 15-16, 1999 (a) and February 15-16, 2000 (b).	75
5.5	Scatter plot between SIC derived from MSMR using T_B and SSM/I SIC (a) and Scatter plot between SIC derived from MSMR using PR & GR and SSM/I SIC (b)	77
5.6	Comparison between monthly averages SIE derived from MSMR TB and SSM/I SIC for Sept. 1999 and Jan 2000.	78
5.7	Comparison between monthly averages SIE derived from MSMR SIC and SSM/I SIC for Sept. 1999 and Jan 2000.	79
5.8	Comparison between monthly averages SIE derived from MSMR PR&GR and SSM/I SIC for Sept. 1999 and Jan 2000.	80
5.9:	Sea Ice Extent MSMR vs. SSM/I data for the Southern Polar Ocean (June1999 – December 2000)81	
6.1	Indian research base at Antarctica	81
6.2	Base map of the different sectors of the study area of Southern Polar Ocean	83
6.3	MSMR T_B images of different seasons in Weddell Sea Sector	89
6.4	SIE in four different seasons in Weddell Sea Sector during SMMR and SSM/I period	90

6.5	Monthly SIE in Weddell Sea Sector during MSMR period (a) and long term monthly SIE from SMMR and SMM/I (b)	91
6.6	Yearly averaged SIE Trend in Weddell Sea Sector with SMMR and SMM/I (a) and SMMR and SMM/I with MSMR	92
6.7	MSMR T_B images of different seasons in Ross Sea Sector	96
6.8	SIE in four different seasons in Weddell Sea Sector during SMMR and SSM/I period	97
6.9	Monthly SIE in Ross Sea Sector during MSMR period (a) and long term monthly SIE SMMR and SMM/I (b)	98
6.10	Yearly averaged SIE Trend in Ross Sea Sector with SMMR and SMM/I (a) and SMMR and SMM/I with MSMR (b)	99
6.11	MSMR T_B images of different seasons in Indian Ocean and W. Pacific Ocean Sectors	103
6.12	Four different seasons in Indian Ocean Sector (a) and W. Pacific Ocean Sector (b), during SMMR & SSM/I period.	104
6.13	Monthly SIE in Indian Ocean and W. Pacific Ocean Sectors during MSMR period	105
6.14	Long term monthly SIE in Indian Ocean Sector (a) and W. Pacific Sectors (b) during SMMR & SSM/I period	106
6.15	Yearly averaged SIE trend in Indian Ocean Sector with SMMR and SMM/I (a) and SMMR and SMM/I with MSMR (b)	107
6.16	Yearly average SIE trend in W. Pacific Ocean Sector with SMMR and SMM/I (a) and SMMR and SMM/I with MSMR (b)	108
6.17	MSMR T_B images of different seasons in Belligshausen & Amundsen Seas Sector	111
6.18	SIE in four different seasons in Belligshausen & Amundsen Seas Sector during SMMR and SSM/I period	112
6.19	Monthly SIE in Belligshausen & Amundsen Seas Sector during MSMR period (a) and long term monthly SIE from SMMR and SMM/I (b)	113
6.20	Yearly averaged SIE trend in Belligshausen & Amundsen Seas Sector from SMMR and SMM/I (a) and SMMR and SMM/I with MSMR (b)	114
6.21	Seasonal and Inter-annual T_B Images of MSMR in the SPO	117
6.22	SIE in four different seasons in the total SPO during SMMR and SSM/I period	118
6.23	Monthly SIE in the total SPO during MSMR period (a) and long term monthly SIE from SMMR and SMM/I (b)	119
6.24	Yearly averaged SIE trend in the total SPO with SMMR and SMM/I (a) and from SMMR &	

	SMM/I with MSMR (b)	120
6.25	Evolution of melting process in the SPO during MSMR period (a,b,c,d)	125 - 128
7.1	Base map of the different sectors of the study area of the Northern Polar Region	132
7.2	Political Map of the Northern Polar Region	132
7.3	Brightness Temperature Maps from MSMR – Total set at a glance.	134
7.4	MSMR T_B Images Seasonal and Inter-annual variation of Sea Ice in the NPR	135
7.5	Inter-Comparison in SIE in the Arctic Ocean Sector between MSMR and SSM/I during June 1999- September 2001	136
7.6	MSMR T_B images of different seasons in Bering Sea and Japan & Okhotsk Seas Sectors	140
7.7	SIE in four different Seasons in Bering Sea (a) and Japan & Okhotsk Seas (b) Sectors during SMMR and SMM/I Period	141
7.8	Monthly SIE in Bering Sea and Japan & Okhotsk Seas Sectors during MSMR period	142
7.9	Long term monthly SIE in Bering Sea Sector (a) and Japan & Okhotsk Seas Sector (b) from SMMR and SMM/I	143
7.10	Yearly averaged SIE trend in Bering Sea Sector from SMMR and SMM/I (a) and from SMMR and SMM/I with MSMR (b)	144
7.11	Yearly averaged SIE trend in Japan & Okhotsk Seas Sector from SMMR and SMM/I and from SMMR and SMM/I with MSMR (b)	145
7.12	MSMR T_B images of different seasons in Seas Sector Greenland Sea Sector	147
7.13	SIE in four different seasons in Greenland Sea Sector from SMMR and SMM/I	148
7.14	Monthly SIE in Greenland Sea Sector during MSMR period (a) and long term monthly SIE in Greenland Sea Sector from SMMR and SMM/I (b)	149
7.15	Yearly averaged SIE trend in Greenland Sea Sector from SMMR and SMM/I and from SMMR and SMM/I with MSMR (b)	150
7.16	MSMR T_B images of different seasons in Kara & Barents Seas Sector	153
7.17	SIE in four different seasons in Kara & Barents Seas Sector	154
7.18	Monthly SIE in Kara & Barents Seas Sector during MSMR period (a) and long term monthly SIE in Kara & Barents Seas Sector from SMMR and SMM/I (b)	155
7.19	Yearly averaged SIE trend in Kara & Barents Seas Sector from SMMR and SMM/I and from SMMR and SMM/I with MSMR	156
7.20	MSMR T_B images of different seasons in North Americans Seas Sector	159
7.21	SIE in four different seasons in North Americans Seas Sector from SMMR & SMM/I	160

7.22	Monthly SIE in North Americans Seas Sector during MSMR period (a) and long term monthly SIE in North Americans Seas Sector from SMMR and SMM/I	161
7.23	Yearly averaged SIE trend in North Americans Seas Sector from SMMR and SMM/I and from SMMR and SMM/I with MSMR	162
7.24	MSMR T_B images of different seasons in Arctic Ocean Sector	165
7.25	SIE in four different seasons in Arctic Ocean Sector from SMMR and SMM/I	166
7.26	Monthly SIE in Arctic Ocean Sector during MSMR period (a) and long term monthly SIE in Arctic Ocean Sector from SMMR and SMM/I	167
7.27	Yearly averaged SIE trend in Arctic Ocean Sector from SMMR and SMM/I (a) and from SMMR and SMM/I with MSMR(b)	168
7.28	MSMR T_B images of different seasons in the total Northern Polar Region (NPR)	173
7.29	SIE in four different seasons in the total NPR during from SMMR and SMM/I	174
7.30	Monthly SIE in the total NPR during MSMR period (a) and long term monthly SIE in monthly SIE in the total NPR from SMMR and SMM/I (b)	175
7.31	Yearly averaged SIE trend in the total NPR from SMMR and SMM/I (a) and from SMMR and SMM/I with MSMR	176
8.1	Monthly SIE in Global Sea Ice cover (GSIC) during MSMR period (a) and long term monthly SIE in GSIC from SMMR and SMM/I	185
8.2	SIE in four different seasons in GSIC from SMMR and SMM/I	186
8.3	Yearly averaged SIE trend in GSIC from SMMR and SMM/I (a) and from SMMR and SMM/I with MSMR (b)	187
8.4	The temperature trend from 1978-2003	188

CHAPTER -1

GENERAL INTRODUCTION

1.1. INTRODUCTION

The polar ice plays a significant role in Global climate. It acts as an early and sensitive indicator of change in the climate system (fig. 1.1). It is also important in hydrology and in the context of sea level rise. It is estimated by the climate models that the increase in the polar temperatures caused by climate change would be substantially greater than that in the global average. For example, one estimate is that an average rise of 2°C in the global temperatures would be accompanied by a change of 10°C in the Arctic (Editorial, Science, 1989). The global average surface temperature has increased by $0.6 \pm 0.2^{\circ}\text{C}$ over the 20th century, where as in the Arctic, extensive land areas show a warming of as much 5°C in air temperature. Over sea ice, there has been slight warming in 1961 -1990 period (fig. 1.2). In Antarctic, over the past half-century there has been a marked warming trend in the Antarctic Peninsula.

The terrestrial polar ice (e.g., snow, lake ice, river ice, glaciers, frozen ground, permafrost, etc.) plays a key role in atmosphere-ice-land interaction. Cryosphere influences the climate through changes in the surface heat budget and heat budget of full atmospheric air column. The land ice acts to keep the land and the overlying atmosphere cool, creating high pressure and affecting the atmospheric circulation. Heavy snow fall in the northern hemisphere landmass at mid-latitudes makes the atmosphere of that region cooler reducing the land-ocean temperature contrast, and affects the atmospheric circulation in the northern hemisphere. For example, it was found that heavier than the normal snowfall in Eurasian region in the spring season leads to subsequent poor monsoon over the Southeast Asia (Barnett et. al., 1989).

The seasonal variation of frozen ground influences the water and energy fluxes and the exchange of carbon between the land and the atmosphere. It is already known that carbon cycle is an important part of global climate system. Carbon cycles affect the production of greenhouse gases, resulting in climate changes.

Polar Regions act as heat sink of the global heat engine. The Polar Regions are covered by the ice most of the time during the year. Ice cover in the sea (sea ice) serves as an effective insulator between ocean and atmosphere, restricting the exchange of heat, mass, momentum and chemical constituents. Major interaction between atmosphere, ice, ocean,

biota and the land surface take place in these regions. These interactions influence the total earth atmosphere system through feedback mechanisms, biogeochemical cycle, deep ocean circulation, changes in the ice mass balance and the atmospheric transport. Many unique climate processes take place in these regions. Fig 1.3 shows the general circulation pattern over the globe. Some involve the complex interactions and feed back loops that may lead to glacial/interglacial climate transition (Petit et al., 1999; White and Steig, 1998). The contrast in the heat/energy balance between the equator and the poles drives the atmospheric and oceanic circulation.

Ice has a high albedo. It reflects major part of the incoming radiation and causes cooling of the surface, which, in turn enhances the formation of ice. In contrast to this, water absorbs most of the incoming solar radiation. Fig 1.4 represents the Albedo variations over the globe. This means that the surface energy budget of an open polar ocean differs significantly from that of the ice covered one. The melting ice absorbs more and more solar insolation increasing the surface temperature, thus accelerating the melt rate. This positive feedback is a very important process in the context of global climate.

Sea ice influences the climate in several ways. The inter-annual variability of the seasonal cycle of the Polar ice cover plays an important role in the climatic processes. The ice cover greatly reduces the exchange of heat, mass, momentum and energy between the atmosphere and the ocean. Anomalies in polar cooling cause corresponding anomalies in the general circulation.

Sea ice formation/depletion also affects the ocean circulation. When sea ice is formed, it ejects the brine to the seawater underneath. The salt concentration in that region of ocean increases. The seawater becomes denser than the surrounding water masses. This cold, dense water sinks to the bottom forming the bottom water. The bottom water slowly moves equator-ward, affecting the ocean circulation over the climatic time scale. The bottom water formation is significant in the Antarctic region.

Icebergs coming from the ice shelves drift slowly into the polar oceans and continually melt, resulting in extended cold water masses. The air overlying the water mass also gets cooled. The effect of the coolness on the weather in and around the iceberg is felt almost immediately through the formation of fog in that region. The iceberg cooling effect on the climate is much more important, particularly in the southern Atlantic (Schwerdtfeger,

1979). This is more important not only for the ice budget problem, but also for the understanding and forecasting the regional temperatures.

Cryosphere attract human attention more and more due to its potential effect on the **sea level**. In the global warming scenario, sea level rise poses a diverse range of threats to human settlements, natural ecosystems and landscape in the coastal zones. Projection of future sea level scenarios based on cryospheric melting is of great interest for the study of impact assessment and adaptation feasibilities and for the future of human race living along the coastal zones. Tide gauge and wave height records of half a century or more are required along with information on severe weather and coastal processes to establish the reference levels and trend prediction.

Rising concentration of CO₂ and other greenhouse gases in the atmosphere will cause the air temperature to increase and the precipitation patterns to change. These changes have a direct impact on the great ice sheets, ice caps and glaciers of the polar region. However, the response of each individual component of the cryosphere will depend on several climatological parameters of that region. Some may grow where as others may shrink. For example, Greenland ice sheet is thinning day by day and sea ice extent in the Arctic is reducing ~3% per decade due to global warming (Maslanik et al, 1996; Parkinson et al., 1999), whereas we get mixed response from the Antarctic region. The thickness of glaciers in the eastern part of the Antarctic is increasing due to heavy precipitation in that region. However, the response of West Antarctic Ice Sheet (WAIS) is not very clear. Some part of the West Antarctic ice sheet is rising in thickness. A positive mass balance of 26.8giga-ton per year is reported in the Ross ice streams of the West Antarctic region (Joughin and Tulaczyk, 2002). On the other hand, breaking of ice shelves from the Antarctic Peninsula is being frequently reported. Thus, the contribution from the Antarctic ice sheet to sea level rise is still debatable.

Observational records show that, on an average, the earth's climate has warmed over the past century (Hansen and Lebedeff, 1987; Karl et al., 1994; Halpert and Bell, 1997). Other changes that have occurred in the climate system alongwith the warming include glacier retreats in Europe (Williams and Ferrigno, 1993), Africa (Young and Hastenrath, 1991), and elsewhere (e.g., Williams and Ferrigno, 1989; Thompson et al., 1993) and sea level rise (Gornitz et al., 1982; Warrick et al., 1996), caused both by

thermal expansion of the water and by the addition of water to the oceans through the melting of land ice.

Calculations suggest that predicted future atmospheric warming will have significant impacts on the Arctic sea ice cover, noticeably reducing the ice thickness and ice concentration, or percent aerial coverage of ice (Parkinson and Kellogg, 1979). Furthermore, ice reductions generate feedbacks that enhance the warming (Kellogg, 1975). In fact, calculations using the general circulation model (GCM) of the Goddard Institute for Space Studies suggest that as much as 37% of the simulated global temperature rise in the event of a doubling of atmospheric CO₂ results from the sea ice changes and their feedbacks to the rest of the climate system (Rind et al., 1995).

Sea ice is also very important for the environment of polar marine plant and animal life, (e.g., Horner, 1989; Spindler, 1990; Melnikov, 1997). Algae colonize the ice, These are consumed by protozoan, crustaceans, and nematodes. High phytoplankton and zooplankton concentrations are frequently found in the water of the marginal ice zones and polynyas, or open water areas within the ice cover (Smith and Sakshaug, 1990; Smith and Schnack-Schiel, 1990). The resulting availability of food, along with the platform provided by the ice surface, makes these areas popular for numerous species of birds and marine mammals. Among the larger animals taking advantage of the ice platform are seals and polar bears. However, polar bears feed predominantly from the platform of sea ice floes, and so they require the presence of ice thick enough to bear their weight. Whales, in contrast, are hindered by the ice and rely upon leads and open water as they travel in polar oceans. Any major changes in sea ice distributions would affect all of these Arctic life forms, along with numerous others (e.g., see Ainley and DeMaster, 1990; Smith and Schnack-Schiel, 1990; Grebmeier et al., 1995; Stirling, 1997).

Taking all the above considerations in mind, there is need for monitoring of ice in the two Polar Regions for studying the environmental and the ecological balance on the earth. However, records of polar sea ice are insufficient for a proper analysis of ice coverage over the past century, fortunately, that situation has changed by the end of the 20th century through repetitive satellite observations. Now we can prepare consistent, large-scale, long-term records of the polar sea ice cover. In our study, now we can use

the most complete record of large-scale polar sea ice coverage over the past two and a half decades that are derived from satellite passive-microwave observations.

In this work, we have made a modest attempt, through the use of passive microwave remote sensing data, to study the polar ice with special attention on the sea ice extent trends.

1.2. POLAR ICE

Polar ice consists of sea ice formed from the freezing of seawater, and ice sheets and glaciers formed by the accumulation and compaction of solid precipitation in the form of snow. Both types of ice extend over vast areas of the Polar Regions. Ice sheets, Glaciers, Icebergs, Snow cover, Ice shelves, Permafrost and Sea Ice are the important components of Polar Ice from the climatic point of view.

1.2.1 Icebergs

Icebergs are massive pieces of ice broken away from glaciers or ice shelves and floating in the sea. They are generally more than 5 m in height. They are found in a variety of shapes, e.g., tabular, dome-shaped, sloping, pinnacled, weathered or glacier bergs. One such iceberg, seen off the Cape of Good Hope, was two miles in circumference, and a hundred and fifty feet high. Typically, around 8/9 of the volume of an iceberg is under water, and that portion's shape can be difficult to imagine from looking at what is visible above the surface. The mass can be very durable and can easily damage metallic sheets. As a result of these factors, icebergs are considered extremely dangerous hazards to shipping.

Iceberg discharge from Greenland is estimated to be about 235×10^{12} kg yr⁻¹, whereas that from Antarctica amounts to 2072×10^{12} kg/yr (Church et al., 2001).

1.2.2 Ice Sheet

A mass of glacier ice which is greater than 50,000 km² in size is considered as an Ice sheet. The only currently existing ice sheets are in Antarctica and Greenland. Both ice sheets play significant role in the global atmospheric circulation, especially in the global energy balance and in the movement of cyclonic systems in Polar Regions.

Ice masses less than 50,000 km² in size are considered as ice caps. The surface of an ice sheet is cold, but its base is generally warmer. At some places it melts and the melt-water lubricates the ice sheet and sets it into slow motion. When the motion is relatively faster, the fast-flowing channels in an ice sheet are called ice streams. The West Antarctic Ice Sheet (WAIS) has several such ice streams.

The Antarctic ice sheet is the largest ice sheet on Earth. It covers an area of almost 14 million km² and contains 30 million km³ of ice. This ice is 90 percent of the entire world's ice and 70 percent of the entire world's fresh water. Antarctica comprises of a 3000 m – 4000 m high ice plateau. It covers around 97% of the surface area of Antarctica, and if it gets melted, it would contribute to a sea level rise of about 60 m. In East Antarctica the ice sheet is on an average 2.5 km thick and rests on a major land mass. At its thickest point the ice sheet is 4,776 meters deep. In West Antarctica it is lying over the sea bed which is at some places more than 2500 m below the sea level. If the ice sheet gets actually removed, isostatic rebound would occur and Antarctica is expected to rise to an average height of 800 m above sea level.

The Greenland ice sheet occupies about 82% of the surface of Greenland. It has relatively lower elevations that exceed 3000 m in the central part. Greenland contains about 8 percent of the Earth's grounded ice. Melting all the ice on Greenland - a very unlikely event that could take thousands of years – might raise the world's sea level by about 6.5 m. But long before that happens; a creeping rise in sea level could displace millions of people who now live along the world's coasts. "You would have major effects if the sea level goes up" only a few inches (Abdalati, 1998).

1.2.3 Glacier

Glaciers are huge masses of ice, formed on land by the compaction and recrystallization of snow that moves very slowly down slope or outward due to their own weight. They are rivers of ice flowing on land. They are formed due to multi-year surplus accumulation of snowfall in excess of snowmelt on land and slowly move out in response to gravity. They may terminate on land or in water.

1.2.4 Snow Cover

The snow cover over the earth's surface varies spatially and the temporally. Its spatial extent at any time depends on the seasonal cycle and the geographic location of that area. It is formed through the solid precipitation composed of white or translucent ice crystals, mainly in complex branched hexagonal form and generally clustered into snowflakes. Although Polar Regions receive very little snowfall each year, they remain perennially snow covered due to very cold temperatures prevailing there.

Seasonal snow cover is the largest component of the cryosphere with a mean winter maximum aerial extent of 47 million square kilometers, about 98 percent of which is located in the Northern Hemisphere. In northern hemisphere, the snow cover extent varies from 46.5×10^6 km² during January to 3.8×10^6 km² in August (Robinson et al., 1993). The global climate system is sensitive to the spatial and temporal variation in the snow covered regions. Heavier than normal Eurasian snow cover in spring leads to a poor monsoon over Southeast Asia (Barnett et al. 1989).

1.2.5 Frozen Ground & Permafrost

A permanently frozen layer of soil or subsoil, or even bedrock, which occurs at variable depths below the Earth's surface in the Arctic or Sub-Arctic regions is called frozen ground. **Permafrost** is the soil that stays in a frozen state for more than two years continuously. It occupies approximately 22.79 million square kilometers of the Northern Hemisphere. It occurs as far north as 84° N in the northernmost Greenland, and as far south as 26° N in the Himalayas (Zhang et al. 1999).

Permafrost (perennially frozen ground) may occur where the mean annual air temperature is less than -1°C and is generally continuous in the regions where mean annual air temperature is less than -7° C It is estimated that permafrost underlies 24.5% of the exposed Northern Hemisphere land area with a maximum aerial extent between about 60°N to 68°N. Thickness of the permafrost can go up to hundreds of meters. Its thickness exceeds 600 m along the Arctic coasts of northeastern Siberia and Alaska, but thins towards the margins (World climate research program, 2001).

The extent of permafrost can vary as the climate changes. Seasonal frost commonly overlies permafrost and is called the active layer, as it will thaw during the summer. The active layer can support plant life, permafrost does not.

1.2.6 Sea Ice

Sea ice is ocean water that freezes, due to the colder temperatures prevailing in the polar oceans of the earth. The North Pole lies in the Arctic Ocean and is always covered by sea ice. The South Pole lies on the land surface of the Antarctic continent, and is situated on a thick ice sheet. Sea ice is different from icebergs, which are big pieces of glaciers fallen into the ocean.

The surface waters become denser by the ejection of brine during the formation of ice and thereby drive the oceanic convection and lead to bottom water formation (Stossel et al. 2002). Over the continental shelf region, cold and salty dense water is produced, which forms the major part of the bottom water, especially Antarctic bottom water (AABW) (Orsi et al., 1999). In the southern hemisphere, seasonal sea ice extent varies by a factor of 5, from a minimum of $3 \times 10^6 \text{ km}^2$ to $4 \times 10^6 \text{ km}^2$ in February to a maximum of $17 \times 10^6 \text{ km}^2$ to $20 \times 10^6 \text{ km}^2$ in September, where as in Northern hemisphere, seasonal sea ice extent varies by a factor of 2 from a minimum of $7 \times 10^6 \text{ km}^2$ to $9 \times 10^6 \text{ km}^2$ in September to a maximum of $14 \times 10^6 \text{ km}^2$ to $16 \times 10^6 \text{ km}^2$ in March (Gloersen et al., 1992).

Monitoring and study of the Polar Regions present great logistic difficulties due to harsh, cold, windy and inhospitable environmental conditions existing there. Above all, the Polar Regions remain do not get proper solar illumination for half of the year. Thus, most of the Polar Regions remain under-explored. Remote sensing from the satellites or from the airborne sensors plays an important role in collecting information about these regions.

1.3. OBJECTIVES AND ORGANIZATION OF THE THESIS

Polar ice covers a huge part of the earth's surface. Its response to the global warming and the changing world climate resulting from the anthropogenic factors has become sources of major concern to the climatologists /scientist.

1.3.1 Objectives

Present work focuses mainly on the study of sea ice in the Polar Ocean. For this study, passive microwave radiometer data have been used. A part of the study is devoted to discriminate sea ice from open water based on the physical properties of the two surfaces using the remotely sensed data. The specific objectives of the study include:

- To explore the potential of OCEANSAT – 1 MSMR data for the study of sea ice in the Antarctic and the Arctic.
- To map and monitor the sea ice in both of the polar regions of the earth over and study its seasonal variation over the MSMR operational period.
- Retrieval of sea ice concentrations from the brightness temperature data.
- To validate and inter-calibrate the sensor performance through inter-comparison of the OCEANSAT–1 MSMR data with the data from other satellites.
- To study the feasibility of detecting the melting of land ice from the MSMR data.
- Inter-annual variations in Sea ice extent and their trend.

1.3.2 Thesis Outline

The whole thesis is divided into 9 chapters. A small description of each chapter given below:-

Chapter-1: Introduction

This chapter discusses the importance of polar ice, motivation and objectives of the research and the structure of the thesis. At first, we have discussed the importance of polar ice and its role in climate evolution. The different physical processes occurring during the formation of sea ice (for example: energy balance of the region, bottom water formation, ocean circulation, atmospheric circulation, etc), the effect of significant climatic variations, such as ENSO and the Antarctic oscillation on the southern hemisphere sea ice cover is discussed. Next is the description of different components of the polar ice. Third sections discuss the scientific problems related to polar ice processes. Towards the end of the chapter, objectives & the structure of the thesis have been discussed.

Chapter-2: Remote Sensing and Polar Ice

This chapter provides general introduction to remote sensing, the basic concepts involved and the description of different types of sensors used from satellite platforms. This is followed by the description of the energy radiated from different types of ice and snow surfaces in the microwave region at different frequencies and polarizations. Then, the interaction of the Electro-Magnetic Radiation (EMR) with earth's surface is described, giving the mathematical formulation for the relationship between the emissivity and dielectric constant. Next, the remote sensing of polar ice in different spectral regions (i.e. optical, infrared, active- and passive- microwave) is discussed (Comiso & Gordan, 1996 & 1998, and Comiso & Steffen, 2001). A brief review of the work carried out by different researchers using the above techniques is also described. Then, the advantages and the limitations of different types of remote sensing are discussed. At the end of the chapter, it is pointed out that the microwave remote sensing is possibly the most suitable technique for mapping and monitoring of the Polar ice for climate related studies.

Chapter-3: Data Description

This chapter describes India's microwave remote sensing satellite IRS – P4, later renamed as OCEANSAT –1. The orbit and the coverage of OCEANSAT-1 are described in the beginning. Then the over all description of the sensors onboard OCEANSAT –1 (i.e., the Ocean Colour Monitor (OCM) and the Multi-frequency Scanning Microwave Radiometer (MSMR) are provided in the same section in brief. The next section gives a detailed description of the MSMR instrument (such as frequency of operation, polarization, scanning geometry, etc.). The next section focuses on the different types of data and data products available from MSMR at different resolutions. The structure of the data and the details of the arrangement of information in the same are also given in this section. The last section describes the details of the ground calibration of MSMR and also discusses the validation carried out for the geophysical products (ISRO, 1999).

Chapter – 4: Processing of MSMR Data for Sea Ice Studies

This describes the methodology adopted in the present study. The first section describes different methodologies used to extract the MSMR data for the region of interest. The same section also discusses the details of the methods (such as interpolation techniques and the techniques to arrange the data in suitable geographical grid elements) to make

the data more useful for the study purpose. The next section focuses on the projection used for mapping the data. We use the polar stereographic projection, which is most suitable for the study of Polar Regions. The same section also discusses the quality of the data available at different frequencies and polarizations. The following section discusses the method developed to calculate the aerial extent of sea ice in the Antarctic and the Arctic regions. For calculation of the aerial extent of sea ice, the corresponding brightness temperature (TB) threshold is derived and used as the boundary between the ice and the open water. The integration procedure to calculate the area of each pixel and that of the whole region is also described in detail, in the same section.

Chapter-5: Inter-Comparison of MSMR and SSM/I over Southern Polar Ocean (SPO)

This chapter has been organized in the following manner. The first section gives the details of the inter-satellite comparison of MSMR and SSM/I data for near – synchronous observations. Both are compared with their brightness temperatures brought to the same grid resolution. For this purpose, the SSM/I data is brought to a lower resolution equivalent to that of MSMR. The next section is devoted to the sea ice algorithm development for the Antarctic. For the algorithm development, multiple linear regression technique is used. The ice concentration is derived in two different ways. In the first method, the brightness temperature values are directly used for the calculation of sea ice concentration. In the second method, an attempt is made to calculate the ice concentration using normalized values of brightness temperatures called the Polarization Ratio (PR) and the Spectral Gradient Ratio (GR). To the end of the section MSMR derived ice concentrations are compared with those derived from SSM /I (Bhandari et al., 2005).

Chapter– 6: Sea Ice Cover Over the Southern Polar Ocean (SPO)

This chapter is related to sea ice cover in the southern polar ocean, which is divided into five sectors for convenience. At first we discuss the methodology used by us for determining the sea ice extent from MSMR data. Then, the growth and decay of sea ice, the lead - lag relationship between the maximum / minimum ice extent and the minimum / maximum solar insolation during winter/ summer in the southern polar ocean are described here. The seasonal variation of sea ice over the different sectors of the southern polar ocean (SPO) and that of the SPO as a whole have been described in the next section. The sea ice extent trends from SMMR and SSM/I for the past two and a

half decades have been derived and discussed in addition to comparing them with the limited duration MSMR observations. This section describes the prevailing trends in different sectors of the southern polar ocean. The sea-saw effect between different sectors is also described in this section. A sub-section of the above section describes the sea ice extent trend analysis for the total SPO (Bhandari et al., 2002; Vyas et al., 2003).

Chapter-7: Sea Ice Cover Over the Northern Polar Region (NPR)

This chapter is related to sea ice cover in the Northern Polar Region (NPR), which has been divided into six sectors for convenience. At first a brief description of inter-comparison with SSM/I derived SIE over the Arctic Ocean has been given. The growth and decay of sea ice, the lead - lag relation between the maximum / minimum ice extent and the minimum / maximum solar insolation during winter/ summer in the NPR are described here. The seasonal variations of sea ice over the different sectors of the NPR and also total sea ice in NPR as a whole has been described in the next section. The sea ice extent trends from SMMR and SSM/I for the past two and a half decades have been analyzed in addition to comparing them with the limited duration MSMR observations. This section describes the prevailing trends in different sectors of the northern polar ocean. The sea-saw effect between different sectors is also described in this section. In the end, the sea ice extent trend analysis for the NPR has been described and discussed.

Chapter-8: Global Sea Ice Cover

This chapter describes the results of the present study on global sea ice cover. The trend of global sea ice cover has been described in this chapter. Some interesting results of the analysis in the context of global warming are presented in this chapter. The comparison of the ice extent trends in the two hemispheres is also described here which brings out and reconfirms the intriguing hemispheric asymmetry of sea ice cover in the two Polar Regions.

Chapter-9: Conclusion and Future Scope

This chapter presents the discussion and conclusions of the study. At first, a brief account of the entire work is presented and then the main findings of this study are summarized. At the end of the chapter, the scope for future work is discussed.

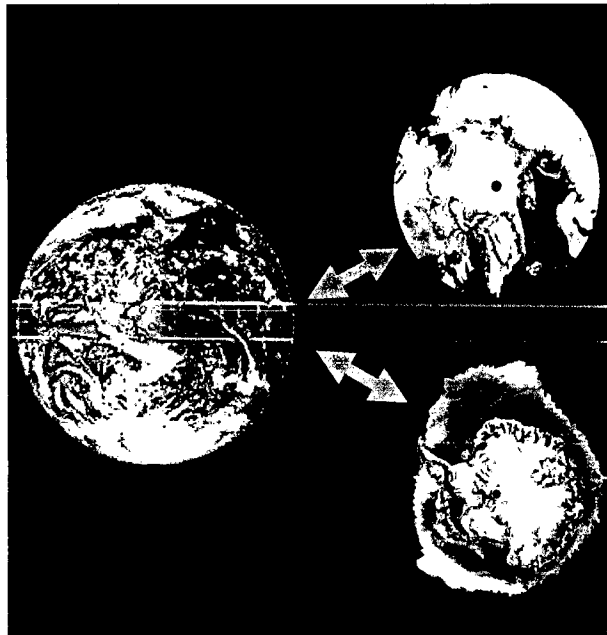
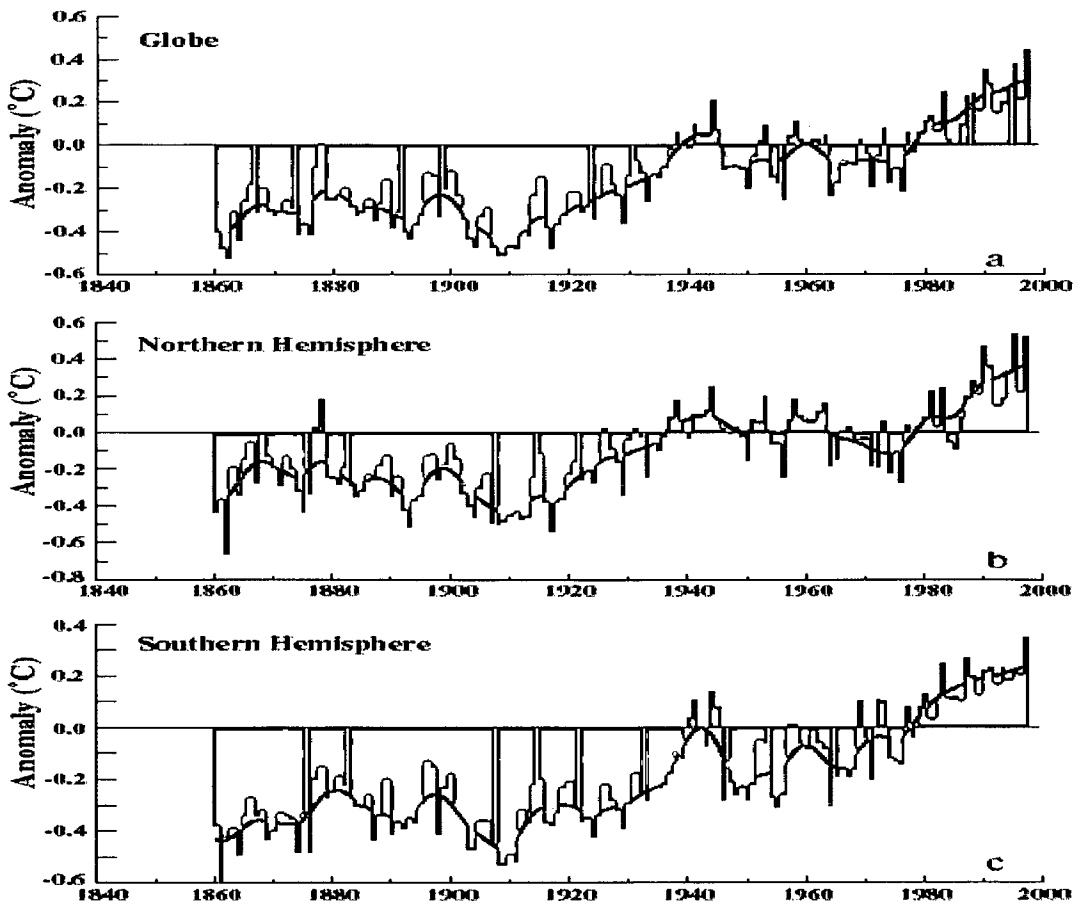


Fig 1.1: Global effect of polar Ice



1.2 Annual average of the combined land –air and SST anomalies (blue bars): (a) Global, (b)Northern Hemisphere, and (c)Southern hemisphere (Source: Hadley Centre for climate Prediction and Research, UK and Climatic Research Unit, University of East Anglia, UK)

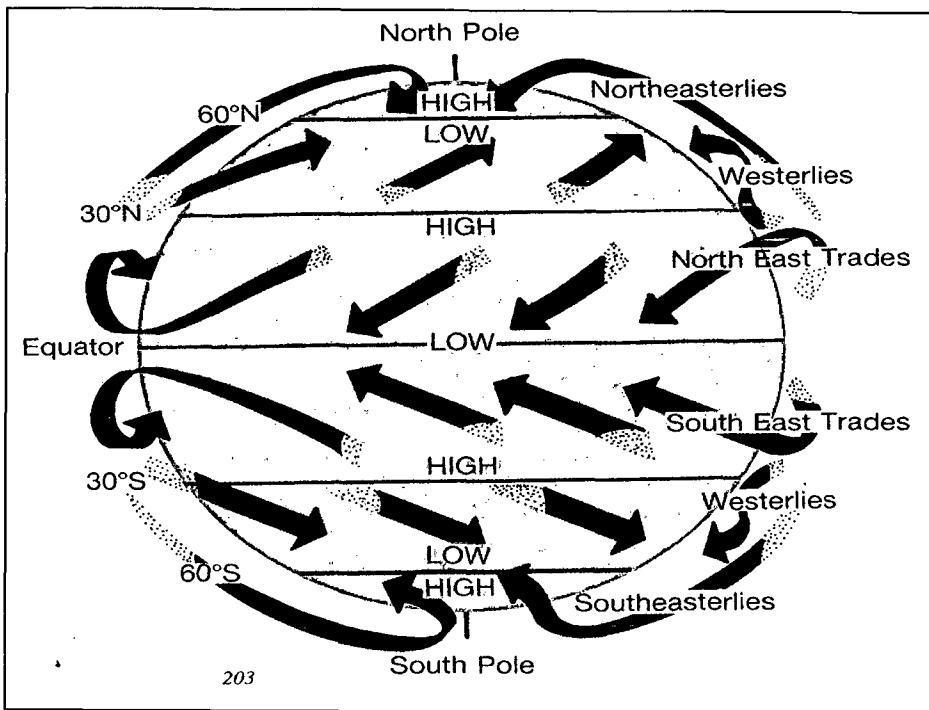


Fig 1.3 General Circulation pattern over the globe (Source: Antarctic Science Edited by - DWH Walton, 1987)

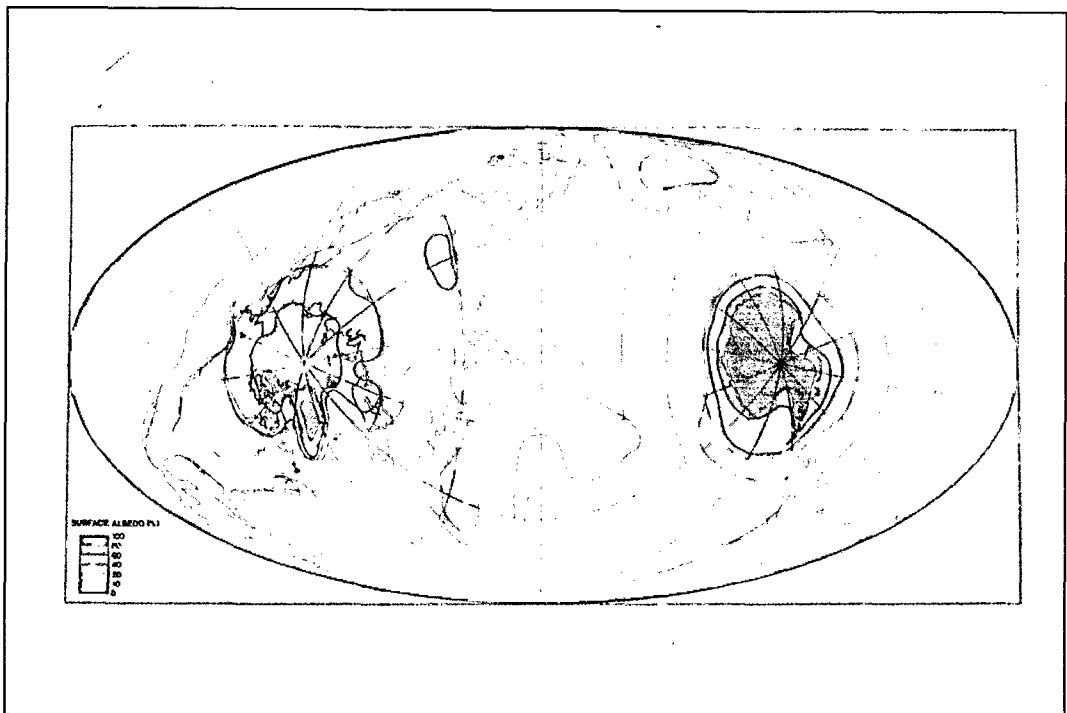


Fig 1.4 Globally albedo distribution (Source: Antarctic Science Edited by - DWH Walton, 1987)

CHAPTER -2

REMOTE SENSING AND POLAR ICE

2.1 INTRODUCTION

Remote Sensing is defined as the science and technology by which the characteristics of objects of interest can be identified, measured or analyzed without direct contact. Electro-magnetic radiation, which is reflected or emitted from an object, is the usual source of remote sensing data. However any media such as gravity or magnetic fields can be utilized in remote sensing. A device to detect the electro-magnetic radiation reflected or emitted from an object is called a "remote sensor" or "sensor". Cameras or scanners are examples of remote sensors. A vehicle to carry the sensor is called a "**platform**". Aircraft or satellites are used as platforms. The technical term "remote sensing" was first used in 1960's, and encompassed photogrammetry, photo-interpretation, photo-geology etc. Since Landsat-1, the first earth observation satellite was launched in 1972; remote sensing has become widely used.

The characteristics of an object can be determined; using reflected or emitted electro-magnetic radiation, from the object. Each object has unique and different characteristics of reflection or emission if the type of object or the environmental condition is different. Remote sensing is a technology to identify and understand the object or the environmental condition through the uniqueness of the reflection or emission.

Remote sensing is classified into three types with respect to the wavelength regions (see fig 2.1):

- (1) Visible and Near Infrared Remote Sensing
- (2) Thermal Infrared Remote Sensing and
- (3) Microwave Remote Sensing

The following figure is depicting the basic three types of remote sensing. The figure is showing radiation source, object and spectral radiance in these bandwidths, broadly their bandwidths and the sensors used for it.

Remote sensing can be performed using instruments mounted on ground-based towers, ships, helicopters, aircraft and satellite platforms utilizing all the regions of the electromagnetic spectrum. From satellite platforms, it offers the potential to repetitively and synoptically monitor vast areas on the earth. This technique becomes much more

convenient and efficient mode of study when we have to collect observations over the relatively inaccessible regions of the earth. In our study we use Remote Sensing observations from space for the study of ice covered surfaces, especially the sea ice surfaces, as found in the polar regions of the earth.

2.2 BASICS OF REMOTE SENSING

Remote Sensing is generally conducted from above the surface of the earth, either from within the atmosphere or from above the atmosphere. The gases in the atmosphere interact with solar irradiation and with the radiation from the Earth's surface. The incoming radiation will experience varying degrees of transmission, absorption, emission, and/or scattering from the atmospheric molecules depending on the wavelength of the radiation.

At some wavelengths, the atmosphere is almost transparent to the incident irradiation. At other wavelengths it is partly transparent. However, at some wavelengths, it highly absorbs the incident radiation and does not allow it to penetrate significantly. Figure 2.1 shows relative atmospheric radiation, transmission and absorption at different wavelengths.

Blue zones mark minimal passage of incoming and/or outgoing radiation, whereas, white areas denote **atmospheric windows**, in which the radiation doesn't interact much with air molecules and hence, isn't absorbed.

Most remote sensing instruments on atmospheric or space platforms operate in one or more of these windows by making their measurements with detectors tuned to specific frequencies (wavelengths) that pass through the atmosphere. However, some sensors, especially those on meteorological satellites, directly measure absorption phenomena, such as those associated with carbon dioxide, CO₂ and other gaseous molecules. The atmosphere is nearly opaque to EM radiation in part of the mid-IR and all of the far-IR regions. In the microwave region, by contrast, most of this radiation moves through unrestricted, so radar waves reach the surface. However, if it is raining, the raindrops cause backscattering that allows the rainfall to be detected.

Scattering is an important phenomenon in the atmosphere. Mie scattering refers to reflection and refraction of radiation by atmospheric constituents (e.g., smoke) whose dimensions are of the order of the radiation wavelengths. Rayleigh scattering results from molecules of the constituents gases (e.g., O₂, N₂, CO₂, water vapor etc.) which are much smaller than the radiation wavelengths. Rayleigh scattering increases with decreasing (shorter) wavelengths, causing more scattering of blue light (blue sky effect) compared to red. Particles much larger than the radiation wavelengths give rise to *nonselective* (wavelength-independent) scattering. Atmospheric backscatter can, under certain conditions, contribute as much as 80 to 90% of the radiant flux observed by a spacecraft sensor.

Remote sensing of the Earth mostly uses reflected energy in the visible and infrared and emitted energy in the thermal infrared and microwave regions to collect radiation that can be analyzed numerically or used to generate images whose variations contain information about the object surface from which they come. The data is generally collected over a number of spectral bands to get as much information as possible. This is called multi-spectral remote sensing.

2.3 SENSORS

The technique of remote sensing involves measurement of reflected or emitted radiation from a target surface through the use of a sensor mounted on a distant platform, such as an aircraft or a spacecraft. The subject of what sensors consist of and how they perform (operate) is important and wide-ranging.

Most remote sensing instruments (sensors) are designed to measure photons. The fundamental principle underlying sensor operation is based on the concept of the photoelectric effect. This says that there will be an emission of electrons when a negatively charged plate of some appropriate light-sensitive material is subjected to a beam of photons. The electrons can then be made to flow from the plate, collected, and counted as a signal. A key point: The magnitude of the electric current produced (number of photoelectrons per unit time) is directly proportional to the light intensity. Thus, changes in the electric current can be used to measure changes in the number or intensity of photons that strike the detector plate during a given time interval. The kinetic energy

of the released photoelectrons varies with frequency (or wavelength) of the impinging radiation. But, different materials that undergo photoelectric effect release electrons over different wavelength intervals. Each has a threshold wavelength at which the phenomenon begins and a longer wavelength at which it ceases.

The principal parameters measured through remote sensing can be classified into three categories: Spectral, Spatial, and Intensity. The instruments that are used to measure spatial information include imagers, altimeters and sounders. The instruments used for measuring spectral information are called spectrometers. The intensity information is obtained through radiometers, scatterometers and polarimeters. There are some instruments that measure both the spatial information and the intensity information. They are called imaging radiometers. Similarly, the instruments that measure spatial information and spectral information together are called imaging spectrometers. There are some instruments that measure both the spectral and the intensity information. They are called spectro-radiometers.

There are two broad classes of sensors called the Passive and the Active sensors. The passive sensors measure the energy that comes from an external source such as the solar energy reflected or the thermal energy emitted from the earth's surface. The active sensors generate their own energy and beam it outward. A fraction of this energy is sent back by the target and measured by the sensor as return signal.

Sensors can be non-imaging or imaging. Non-imaging sensors measure the radiation received from the target surface on a point-by-point basis, converts it into electrical signal strength and either records it directly or transmits it to the ground station. Imaging sensors such as photographic camera or a TV camera record the two-dimensional information about the target surface simultaneously for all the elements within a scene.

Radiometer is a general term for any instrument that quantitatively measures the EM radiation in some interval of the EM spectrum. When the radiation is in the form of visible light from a narrow spectral band, it is called photometer. If the sensor includes a component, such as a prism or diffraction grating, that can break radiation extending over a part of the spectrum into discrete wavelengths and disperse them at different angles to reach the detectors, it is called a spectrometer.

Sensors that instantaneously measure radiation coming from the entire scene at once are called imaging systems. The eye, a photo camera, and a TV vidicon belong to this group. The Field of View (FOV) of an imaging sensor is determined by the apertures and the optics used in the system. If the scene is sensed element by element (each equal to a small area within the scene) along successive narrow strips over a finite time, this mode of measurement is called scanning. Most non-camera sensors operating from moving platforms image the scene by scanning.

In case of a scanner, the target is static but the sensor sweeps across the sensed scene, moving systematically in a progressive sweep and also advancing across the target. The scanners are of two types: "mechanical" and "electronic". The mechanical scanners contain a mechanical component (e.g., a moving mirror or a moving antenna) that scans the scene element by element (see fig 2.3A). The electronic scanners have a linear array of detectors. These detectors simultaneously measure the radiation coming from the different elements of a strip on the object scene (see fig 2.3B). Therefore, in this case there is no need for mechanical scanning. The area covered by the scanners in the cross-track direction is called swath width.

The Cross-track mode normally uses a rotating mirror to sweep the scene along a line. The Along-track scanner uses an array of detectors to collect radiation from the entire line in the Cross-track direction at a time, thus avoiding the need for mechanical scanning.

Each scanned line is subdivided into a sequence of individual spatial elements that represent a corresponding square, rectangular, or circular area called ground resolution cell (called pixel when imaged by sensor) on the scene surface being imaged. During the process of scanning, the cells are sensed one after another along the line. For each cell, the radiation received by detectors over a short but finite duration is converted into a digital count and recorded or transmitted to the ground.

The aerial coverage of the pixel is determined by instantaneous field of view (IFOV) of the sensor system. The IFOV is defined as the solid angle extending from a detector to the area on the ground it measures at any instant. IFOV is a function of the optics of the

sensor, the sampling rate of the signal, the size of the detector, and the altitude above the target or scene. The image is then numerically represented by a two dimensional array of Digital numbers (DN), each representing the radiation coming from a pixel. Using these DN values, a "picture" of the scene is recreated on a film (photo) or on a monitor (image) by converting the DNs, pixel-by-pixel and line-by-line into corresponding gray level values.

Radiometers viewing the earth-surface can receive power mainly from the following three sources: the earth-surface, the atmosphere, the sun and also from the extra terrestrial sources. The radiation emitted by the earth-surface gets modified on its way to the satellite due to (i) absorption by the atmospheric gases and (ii) absorption & scattering by the liquid and the solid suspended particles present in the atmosphere. The emissivity of the surface is always less than unity; the power emitted by the surface corresponding to its physical temperature is always less than that emitted by a blackbody at the same temperature. The total upwelling radiance, $I_H(\gamma)$, received at an altitude H at frequency γ , can be written as the sum of the following three components -- (i) total radiation from the surface (land, ocean or ice surfaces) $I_s(\gamma)$, (ii) the upwelling radiation emitted by the atmosphere $I_{atm}(\gamma)$, and (iii) the down welling atmospheric radiation reflected from the surface $I_{atm}^r(\gamma)$ as shown in the following equation :

$$I_H(\gamma) = I_s(\gamma) + I_{atm}(\gamma) + I_{atm}^r(\gamma) \quad (2.1)$$

Fig. 2.4 schematically shows the viewing geometry of a scanning radiometer and also illustrates above three components of the signal entering the radiometer simultaneously.

Microwave region of the electromagnetic radiation varies in frequency between 1GHz to 300 GHz i.e. 300 mm to 1 mm in wavelength. A radiometer viewing the earth surface can receive power from the following three sources: the surface of the earth, the atmosphere and the sun. The radiometers collect thermal radiation in the microwave part of the spectrum mainly (i) emitted by earth surfaces [a], (ii) emitted by the atmosphere in the upward direction [d], (iii) emitted by the atmosphere in the downward direction but later reflected from the earth's surface in the upward direction [b] and (iv) the solar radiation which is reflected back from the earth surface to the satellite sensor [c] (see fig 2.5). Also satellite sensors (radiometers) sense the radiation from the cloud top and the radiation

reflected from upper atmosphere. At these long wavelengths no scattering takes place by the atmosphere, aerosols, haze, dust or small water particles in the cloud (if the cloud is not thick). Thus, microwave sensors are all-weather and day-and-night devices, although the radiation in 22 GHz is affected by the scattering caused by the water vapour present in the atmosphere and similarly the 85 GHz emission is affected by the scattering caused by the ice crystals present in the clouds.

On the other hand, there are certain disadvantages of the microwave sensors. The thermal emission per unit surface area from the earth is very weak at these wavelengths, so the signal received at the sensor is weak. To overcome the noise levels, signals from a large field of view must be received and integrated, thus giving a coarser spatial resolution. The emissivity of the sea/ice surface at microwave frequencies is a function of (i) the dielectric properties of sea-water/ice surfaces and (ii) the roughness of the surface. Since dielectric constant varies with (i) physical temperature of the surfaces, (ii) salinity/brine content, (iii) frequency and (iv) polarizations of the electromagnetic radiation; the observations of a multi-channel microwave radiometer would contain information not only about the surface, but also about the characteristics of the medium to certain depth. Figure 2.6 illustrates the absorption of microwave radiation by water vapour and oxygen. From which it is apparent that the 2-10 GHz range is the best for surface viewing. Below this, the galactic contribution is strong and above it the correction required for water vapour and oxygen becomes increasingly large. Rain remains a problem within the 2-10 GHz range.

2.4 INTERACTION OF ELECTROMAGNETIC RADIATION WITH OCEAN AND ICE SURFACES

Electromagnetic radiation interacts with the ocean/ice surfaces through the emissivity and roughness of the surface. Emissivities of the surfaces play an important role in parameter extraction from the passive microwave remote sensing observations. In this section, the detailed description of the emissivity of different surfaces (ocean/ice) is discussed.

2.4.1 Emissivity of Different Types of Earth Surfaces

Emissivity of a surface at a particular temperature is defined as the ratio of the radiant emittance of the body to that of the black body at the same temperature. Emissivity of the

surface changes with the type of the surface, angle of observation, frequency at which observation is taking place and roughness of the surface.

2.4.1.1 Emissivity of the Open Water Ocean Surface

The emissivity $\epsilon(\gamma, \theta, p)$ is a function of frequency (γ), incidence angle (θ) and polarization (p). The polarization can be either Vertical (V) or Horizontal (H). The $\epsilon(\gamma, \theta, p)$ can be defined in terms of specular reflectivity, $R(\gamma, \theta, p)$, as

$$\epsilon(\gamma, \theta, p) = 1 - R(\gamma, \theta, p) \quad 2.2$$

For a plane surface $R(\gamma, \theta, p)$ depends on the incidence angle (θ) and the complex dielectric constant (e_w) (Schanda, 1976), and can be written as follows

$$R(\gamma, \theta, H) = \left[\frac{\cos \theta - \sqrt{e_w - \sin^2 \theta}}{\cos \theta + \sqrt{e_w - \sin^2 \theta}} \right]^2 \quad 2.3$$

$$R(\gamma, \theta, V) = \left[\frac{e_w \cos \theta - \sqrt{e_w - \sin^2 \theta}}{e_w \cos \theta + \sqrt{e_w - \sin^2 \theta}} \right]^2 \quad 2.4$$

In the microwave region the dielectric constant ' e_w ' is a function of frequency ν , temperature T and salinity ' s ' (see fig 2.7). Fig 2.8 shows the general shape of the variation of ϵ_H and ϵ_V with viewing angle, although the exact position of the Brewster's angle at which ϵ_V peaks will vary with the value of e_w . As per the relation of emissivity ϵ and power reflection coefficient R given above, their graphs are complementary.

The complex dielectric constant for seawater can be given by Debye's equation as,

$$e_w = e_\infty + \frac{e_s e_\infty}{1 + i2\pi f t_r} - i \frac{\sigma}{2\pi f e_0} \quad 2.5$$

Where ' i ' is the imaginary number $\sqrt{-1}$, e_∞ is the electric permittivity at very high frequencies, t_r is the relaxation time, σ is the ionic conductivity and $e_0 = 8.854 \times 10^{-12}$ faraday m^{-1} is the permittivity of free space. e_s , t_r , σ are functions of the temperature and the salinity of the sea water (fig 2.9). This is important at radio frequencies. The dielectric constant and the emissivity behaviour at frequencies (50 GHz) have been studied in detail by Wilheit (1972), Pandey and Kakar (1983) and Hofer and Njoku (1981). Variation in

surface temperature will change the surface brightness temperature (Wilheit, 1978). From above discussion we conclude that

- i) The influence of salinity on emissivity is small, except for frequencies below 5 GHz, where it lowers the emissivity
- ii) The complex part of the dielectric constant is large, and exceeds the real part for frequencies above 20 GHz.
- iii) The emissivity for any specular surface at horizontal polarisation decreases with increasing incidence angle while for vertical polarization, it increases with incidence angle θ , until θ reaches the Brewster's angle θ_B , and then decreases rapidly between θ_B and 90° (Ulaby et al., 1982).

2.4.1.2 Emissivity of the Sea Ice Surface

Sea ice covers about one-ninth of the total area of world's ocean. The sea ice cover over the ocean is of special interest for applications in the field of climate change, oil exploration, shipping and marine navigation and for strategic operations. Sea ice can be divided into two major classes (i) first year ice (FY) and (ii) multiyear ice (MY). They differ in aspects related to thickness, salinity and the melt-season that they have survived.

The emissivity of sea ice depends upon the following factors:

- i) Sea ice thickness
- ii) Dielectric constant and the temperature profile of the ice layer
- iii) Thickness of any snow layer present on the top of the ice layer
- iv) The degree of inhomogeneity and anisotropy of the ice volume

i) Sea ice thickness

Layers of sea ice below the surface layer also contribute to its emissivity. It is found that the emissivity of sea ice increases with ice thickness up to 15cm for frequencies greater than 10 GHz and then remains constant (Ulaby et al., 1986).

ii) The Dielectric constant and the temperature profile of the ice layer

The dielectric constant of sea ice is a complex quantity. The real part of the dielectric constant gives the refractive index of the medium and the imaginary part gives the loss factor of the medium. The dielectric constant of sea ice is a function of the following:

- (a) Complex dielectric constant of pure ice
- (b) The complex dielectric constant of the brine pockets or inclusions
- (c) The fraction of brine volume and
- (d) The shape and orientation of the brine pockets or inclusions relative to the direction of the electric field of the EM wave propagating in the medium.

The dielectric constant plays an important role in the determination of the emissivity of any surface (see eq. 2.2 & 2.3). Though these two equations are valid for the open water ocean surfaces, but the same are true for the ice surfaces also. For a lossy medium (e.g., ice or seawater) the dielectric constant is a complex quantity given by the relation

$$\epsilon = \epsilon' - i\epsilon'' = \epsilon'(1 - i \tan \delta) \quad 2.6$$

where ϵ' describes the constant with respect to the free space, for example $\epsilon'=1$ for air and $\tan \delta$ is defined as the loss tangent. For pure ice, the real part of the dielectric constant, ϵ' , is constant at frequencies between 10MHz and 1000GHz, with $\epsilon' = 3.17$ (Ulaby et al., 1986), but the imaginary part (known as the loss factor) is up to several orders of magnitude smaller than that for water.

The dielectric properties of sea ice in the microwave range are governed by the presence of salt, brine pockets and air bubbles. As for any composite medium, it is not only the volume fraction but also the shape, the size distribution and the orientation of brine inclusions that determines the effective permittivity. The dielectric property of the sea ice also depends upon the temperature of the medium (sea ice), frequency, polarization and the direction of propagation of the electromagnetic wave. The dielectric loss factor, ϵ'' , covers a wide range of values, from 0.01 to more than 1.0. The loss factor decreases rapidly with decreasing temperature and increases with increasing salinity. First year (FY) sea ice has high value of ϵ'' (3 to 10 times) than the multi-year (MY) sea ice.

The dielectric properties of the ice determine the reflection coefficients at the air-ice and ice-water interfaces, the penetration depth of the medium, and the radiative

characteristics of the sea ice. When the penetration depth δ_p is significantly smaller than the slant distance traversed, the net contribution to the radiant emission from the underneath water may be ignored. If the ice thickness is more than 20 cm, there will be no signature of radiation coming from the seawater below the ice surface at frequencies higher than 10GHz. The MY ice is least lossy because its salinity is lowest. Penetration depth of MY ice is of the order of a few centimeters at 20 GHz and is deeper or shallower at lower or higher frequencies, respectively.

The major conclusions derived from the aircraft observations of sea ice in the microwave region are (1) there is a large contrast existing between the emissivities of sea ice and the open seawater (2) the contrast between the emissivities of FY ice and MY ice increases with frequency. It is also found that the emissivity of the first year ice is approximately frequency independent, whereas the emissivity decreases rapidly with frequency for MY ice.

2.5 REMOTE SENSING OF POLAR CRYOSPHERE: HISTORICAL BACKGROUND

Ground based observations of the Polar Regions present formidable logistic difficulties due to harsh, cold, windy, and inhospitable environmental conditions. Above all, the Polar Regions remain dark continuously for long durations. Thus, most of the Polar Regions and high altitude ice cover areas remain unexplored. Remote sensing from airborne sensors and satellites plays a valuable role in collecting information about these regions.

The remote sensing of the cryosphere started with the use of aerial photography. But to study the large areas synoptically, there was a need for a satellite-borne sensor. The first satellite sensors developed to view the large scale structure and the motion of the cryosphere, in particular, the sea ice, used the optical and the infrared channels (Sissala et al.,1972). Those sensors were placed onboard the early Nimbus, Tiros and Earth Resources and Technology satellite (ERTS, later renamed as LANDSAT).

By the late 1960s, it was felt that the sequential synoptic and repetitive observations are needed for sea ice/glacier monitoring in Polar Regions and also for climate studies. The satellite-borne visible sensors are capable of giving information about the ground only in

cloud free and well-illuminated conditions. The Polar Regions remain dark for several months of the year and remain cloudy very frequently in the remaining months.

The ability of microwave sensors to view the earth's surface day and night and in all weather conditions makes them suitable for the study of physical processes in the Polar Regions. Further, more microwave sensors onboard polar orbiting satellites make measurements frequently enough to obtain nearly complete polar coverage within a day or two, thereby enhancing the scope of the study of ice-ocean-atmosphere interactions.

2.1.1 Optical Remote Sensing of Cryosphere

Satellite based study of snow cover started with TIROS – 1, in 1960. Since then the potential of satellite study of snow cover is explored using more advanced sensors such as the Wide Field of View Sensor (WIFS) on the Indian remote sensing satellites (IRS-1C, 1D and P3 satellites. Now, the sensors like linear imaging self scanner (LISS II and III) on board IRS and Landsat TM, provide higher spatial/spectral resolution for more precise studies.

Since 1966, NOAA has mapped the aerial extent of snow cover in the Northern Hemisphere on a weekly basis using optical satellite imagery (e.g. AVHRR, GOES) (Matson et al., 1986). This data set is the longest satellite-derived record (>30 years) of the snow extent, and has been used as the basis for many analyses of snow cover variability and change on a hemispheric and continental scale (Robinson et al., 1993; Brown, 1995).

Using satellite infrared data, the surface temperatures of polar regions have been derived for the period of 1979 – 85, using the data from the Temperature Humidity Infrared Radiometer, onboard NIMBUS-7 (Comiso. 1983,1994). Satellite infrared systems provide a spatially coherent and continuous coverage in cloud free regions both day and night. Comiso (2000) has studied the surface temperature trends of the Antarctic using NOAA Advanced Very High Resolution Radiometer (AVHRR) data and reported a negative trend of $-0.042 \pm 0.067^\circ \text{C}$ per year inferred from the twenty years' record of the

satellite data. Also he found that inter-annual fluctuations of the temperatures lie in the range -0.177 to $+0.094^{\circ}\text{C}$ per year for the Antarctic ice sheet.

2.1.2 Passive Microwave Remote Sensing of Cryosphere

During late 1960s and 1970s, images of sea ice were acquired by satellite borne visible and infrared sensors. But, they proved useful only for the study of meso-scale phenomena in the cloud free regions. Surface observations can be taken, in all weather and day-or-night conditions, regularly and frequently only through microwave sensors at reasonable temporal and spatial intervals. The limitation of passive microwave sensors is the coarser spatial resolution, which restricts the delineation of smaller scale features of the ice pack. However, the integrated measure of the open water amount within the ice packs and the identification of ice types can be provided by these instruments. . USA started with a prototype of the Electrically Scanning Microwave Radiometer (ESMR) flown over the Arctic on an aircraft platform. The aircraft observations during the year 1967-1970 clearly demonstrated the ability of passive microwave sensors to distinguish between open water and sea ice. The 1970 observations also lead to a hypothesis that there are at least two types of radio-metrically distinct sea ice types: first-year ice and multi-year ice. This was confirmed during the Arctic Ice Dynamics Joint Experiments (AIDJEX) in subsequent wintertime aircraft expeditions (Gloersen et al., 1973; Meeks et al., 1974).

The first satellite passive microwave remote sensing of the atmosphere began with the Russian satellites Cosmos 243 and Cosmos 384 in 1968 and 1970 respectively. The great advancement in the polar cryospheric remote sensing took place by the full scale flight of ESMR onboard NASA Nimbus – 5 satellite during 1973 – 1976 (Gloersen et al., 1974 a,b).

Study of Cryosphere (particularly the study of Polar Regions) got the boost by the launch of the Scanning multi-channel microwave radiometer (SMMR) on board Nimbus – 7 (fig 2.10). This sensor provides the data from October 26th, 1978 to August 20th, 1987. It made the observations at four frequencies (6, 10, 19 and 21 GHz with both Vertical and Horizontal polarizations). The extent, concentration and area covered by the sea ice (including both, the first year ice, i.e. the ice that has survived for less than one full year and the multi-year ice i.e., the ice that has survived for more than a year or the ice that

has survived over the a summer melt season) have been studied using the SMMR data (Svendsen et al., 1983; Cavalier et al, 1984; Gloersen and Cavalieri, 1986; Comiso, 1986). Passive microwave satellite data have also been used to obtain surface temperature (Shuman et al., 1994). The detailed description and study of the SMMR ice data provide information such as ice growth, decay, inter- and intra- annual variation, and the ice cover on regional, hemispheric and global scales (Gloersen et al, 1992). This study has been continued by the defense meteorological satellite program (DMSP) series of satellites (F8, F10, F11, F13) using Special Sensor Microwave Imager (SSM/I) sensor since 1987 (fig 2.11). The difficulties experienced in combining SMMR and SSM/I data at geophysical parameter level have been realized. For the sensor-inter calibration an overlap period of one year is desirable (Cavalieri et al., 1999).

The launch of India's Oceansat – 1, multi-frequency scanning microwave radiometer (MSMR) extended the scope of this study further more. This sensor records the data from the earth surface and the atmosphere at four frequencies (6.6, 10.65, 18 and 21 GHz with both the vertical and the horizontal polarization). This data has been available in three spatial grid formats: Grid-1, grid-2 and grid-3 having spatial resolution of 150km × 150km, 75km × 75km and 50km × 50km respectively (ISRO, 1999). Important geological features like the Trans-Antarctic mountain ranges, Gamburtsev sub-glacial mountains, Wilkes and Aurora sub-glacial basins etc. have been captured by the MSMR (Vyas et al., 2000, 2001; Dash et al. 2001). The low-frequency channels available in MSMR give more opportunity for better study of different atmospheric, oceanic and cryospheric parameters; hence the complex atmosphere-ocean-cryosphere interaction can be better understood. Further, more near- simultaneous observations of MSMR and SSM/I give a better insight for the above study.

Significant progress is made towards understanding the microwave signatures of the ice sheets. The microwave signatures are strongly affected by the signal coming from beneath the surface and also depend on ice layer densities, brine content, snow temperature, snow wetness and accumulation rate (Steffen et al., 1999; Abdalati and Steffen, 1998). For 19 GHz and 37 GHz, the link between the microwave emissions and the accumulation rates in the dry snow area of Greenland ice sheet is significant; however the emissivity is also dependent on the extent of hoar (ice crystals forming a white

deposit) development. As a result, accumulation estimates based on passive microwave satellite data and field observations may not match well with each other. Variations in melt-extent have been detected by establishing melt- thresholds in the cross – polarized gradient ratio (XPGR). The XPGR, defined as the normalized difference between 19 GHz horizontal channels and 37 GHz vertical channel of the SSM/I, exploits the different effects of snow wetness on different frequencies and polarizations and provides a distinct melt-signal. Also, a possible relationship between the Antarctic sea ice cover and the ENSO has been reported by Kwok and Comiso (2002).

2.5.3 Active Microwave Remote Sensing of the Cryosphere

The microwave remote sensing of polar ice became very convenient with launch of an active sensor like the Synthetic Aperture Rader (SAR) on board European Remote Sensing Satellites (ERS – 1) in 1991, because of its day and night observation capability, and all weather operation. It operates at C-band (6 cm wavelength) which is found to have an enhanced sensitivity to surface roughness and moisture content (Elachi, 1982). These high resolution (~ 25 m) backscatter data are acquired along a 100 km swath, which is a limiting factor for regional and large scale climatic studies. Since 1995, the Canadian Radarsat has generated SAR data sets having a swath width of 500 km and a spatial resolution similar to that of ERS – 1 and 2.

Using X-band airborne SAR, Western Barents sea was mapped for the first time on 3 consecutive days during second Marginal Ice Zone Experiment in 1987 (MIZEX87) (Sandven et al., 1999). High resolution SAR data provides the detailed information on meso-scale ice edge calculation, including ice tongues and vortex pairs (Johannessen et al., 1992). It has also been used for the study of ice edge features and processes, classification of ice and for ice motion studies (Sandven et al., 1999). Again, satellite radar interferometry (SRI) technique provides an excellent tool for monitoring the ice flow velocities and studying the ice streams, which are indicators of the response of the ice sheets to the climate change or to the internal instability (Goldstein et al., 1993). Also, the signatures of ice are related to the structure of the snow pack, which varies with the balance of accumulation and melt at various elevations. These processes can be studied in more detail using SAR data acquired at regular intervals (Fahnestock et al, 1993). The boundary zones can be accurately located with the use of the high resolution SAR imagery.

2.5.3.1 Scatterometer

Prior to the advent of the space borne scatterometer, almost all the ocean wind measurements came from the merchant - ship observations. There are lots of doubts about the distribution and the quality of the data collected by these ships. spaceborne microwave scatterometers are proven to be the only instruments that give synoptic-scale ocean surface winds (both U and V components) under all weather conditions, day and night. Although the primary objective of scatterometer is to measure the wind vector over the ocean, recent studies show that it can be used for ice and land surface studies also (Long and Drinkwater, 1994 and 1999; Remund and Long, 1999; Nghiem and Tsai, 2001).

Using scatterometer data, three types of studies can be performed in the Polar Regions. Yueh et al. (1997) developed an algorithm to differentiate sea ice in open water background using scatterometer data. Also, the ice mass balance in the perennial ice zone of the Arctic has been studied by Kwok et al. (1999) using NASA Scatterometer (NSCAT) data. Enhanced resolution of NSCAT data has been used for mapping the Antarctic ice cover (Remund and Long, 1999). Information regarding the drift of sea ice in the Arctic is studied by using NSCAT and SSM/I data together (Liu et al., 1999). Drinkwater and Liu (2000, 2001) have studied the surface melting in Antarctica and Greenland using ERS scatterometer, Radarsat Synthetic Aperture Radar and SSM/I data..

2.5.3.2 Altimeter

Though the altimeters are designed to measure the sea surface height (SSH), but the performance of radar altimeter over ice surfaces is different than that over the ocean surfaces. Over the ocean surfaces the distribution of the heights of the reflecting facets are nearly gaussian, and the wave form of the echo has a characteristic shape that can be described analytically, as a function of the standard deviation of the distribution which is closely related to the ocean wave height. But the echoes from ice surface have unpredictable shape and have a larger variability due to uneven surface elevations. The detailed information about the properties of different surfaces can be obtained from Fu and Cazenave (2001) and Bamber et al., (1994). Kim et al. (2002) have studied the distribution of sea ice in the Weddell Sea using Topex/Poseidon data.

Electro-Magnetic Spectrum (The eye for observations)

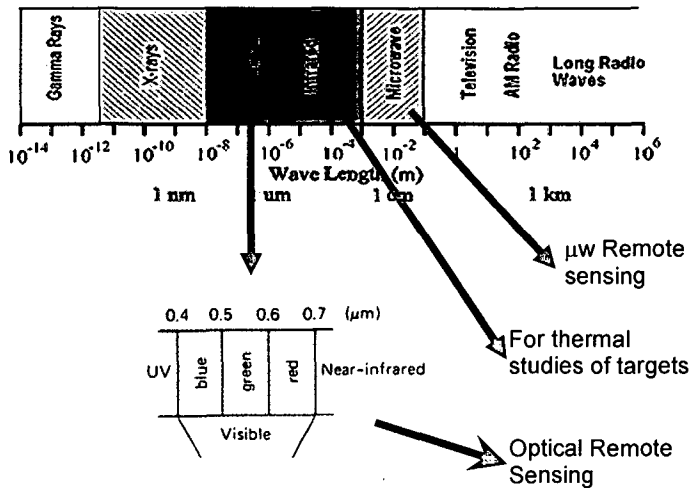


Fig 2.1: Electro-Magnetic Spectrum and different type of Remote Sensing

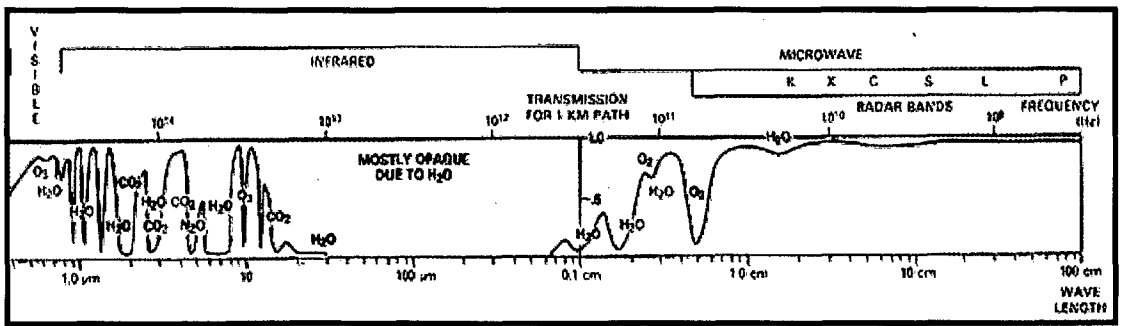


Fig 2.2: atmospheric radiation, transmission and absorption at different wavelengths

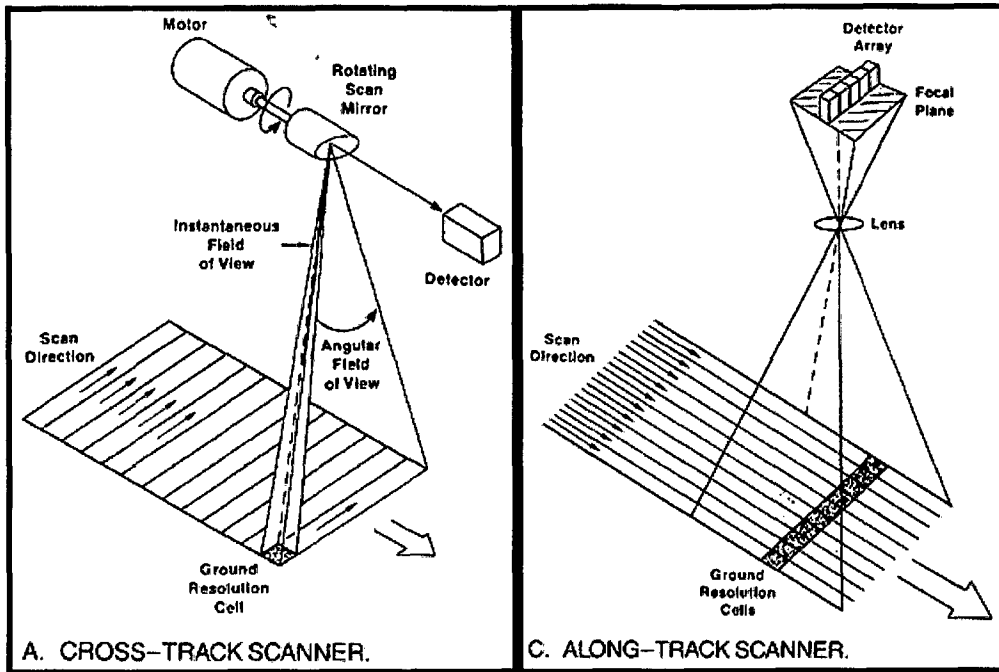


Fig 2.3: Cross-track and Along-track Scanning

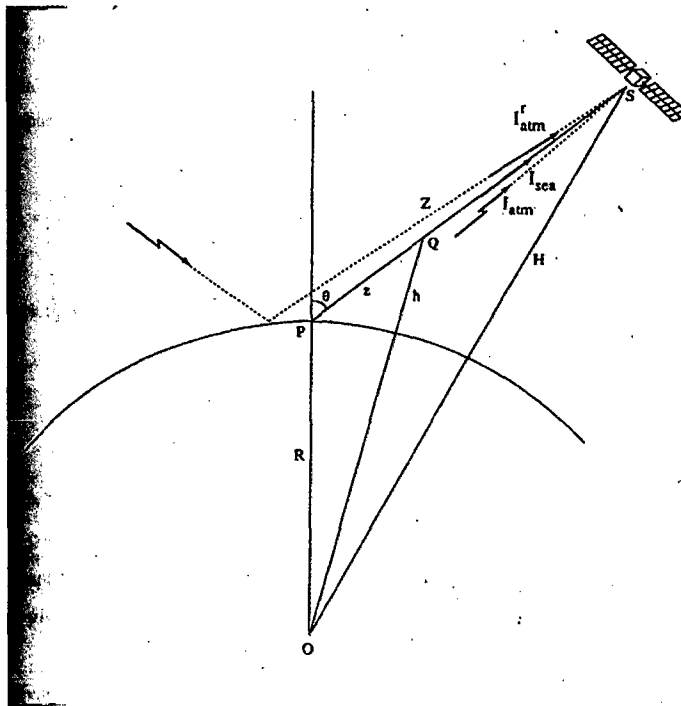


Fig 2.4 : Viewing geometry for the scanning radiometer. The diagram also shows the principal components for the signal received by a satellite radiometer viewing the earth surface (After Zavody et al., 1995)

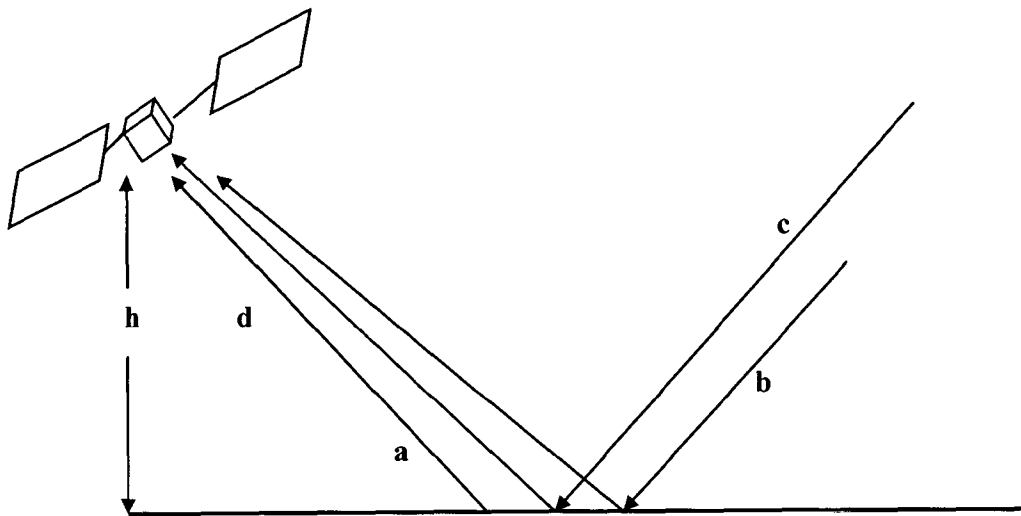


Fig 2.5 : Contributions from different sources reaching satellite sensor in case of microwave radiometer. Different terms are explained in the text (Dash, 2003)

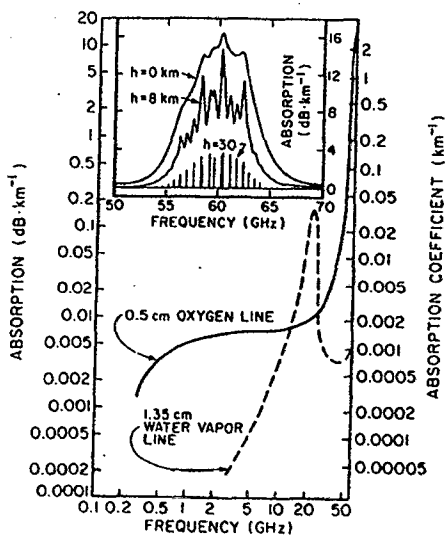


Fig 2.6 : Absorption of water vapour and Oxygen. Inset is a detailed expansion of Oxygen spectrum showing the effect of altitude on pressure broadening (After Maul, 1985)

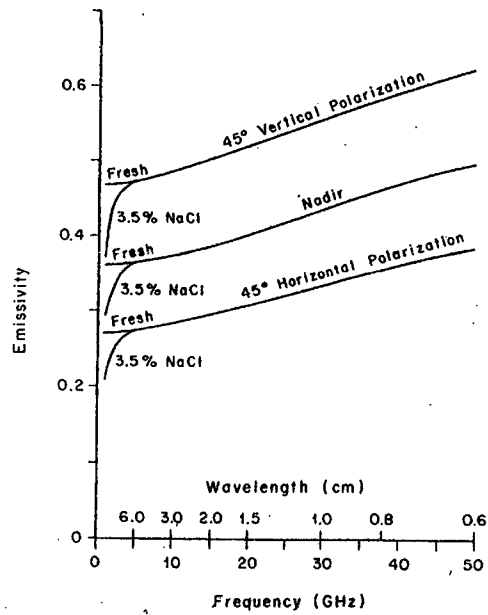


Fig 2.7: The emissivity of water (fresh and with 3.5% NaCl) as a function of radio frequency (Wilheit, 1972)

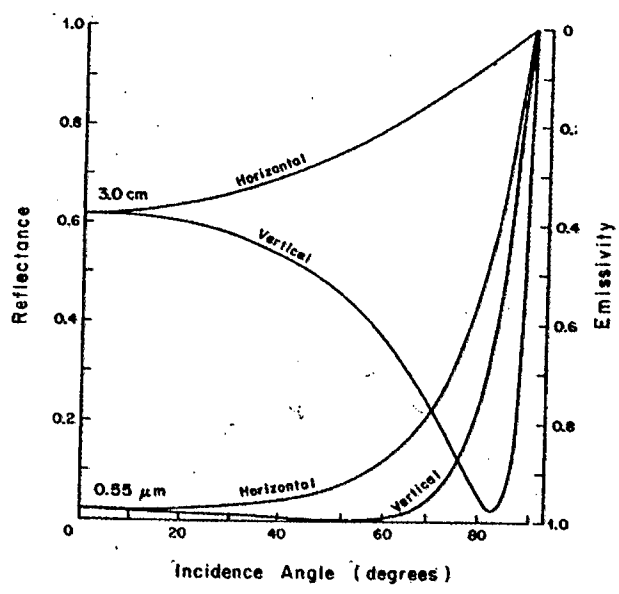


Fig 2.8 : Reflectance and emissivity of a plane sea-water surface as a function of incidence angle for two different wavelengths

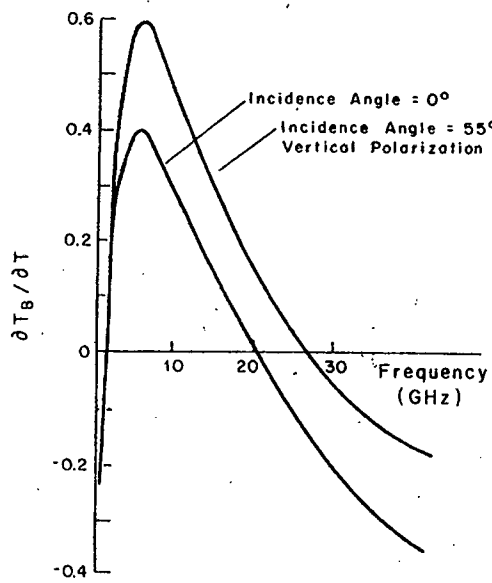


Fig 2.9: Changes in sea surface brightness temperature per change in surface temperature over the range 0 - 30°C, as a function of radio frequency (after Wilheit, 1978)

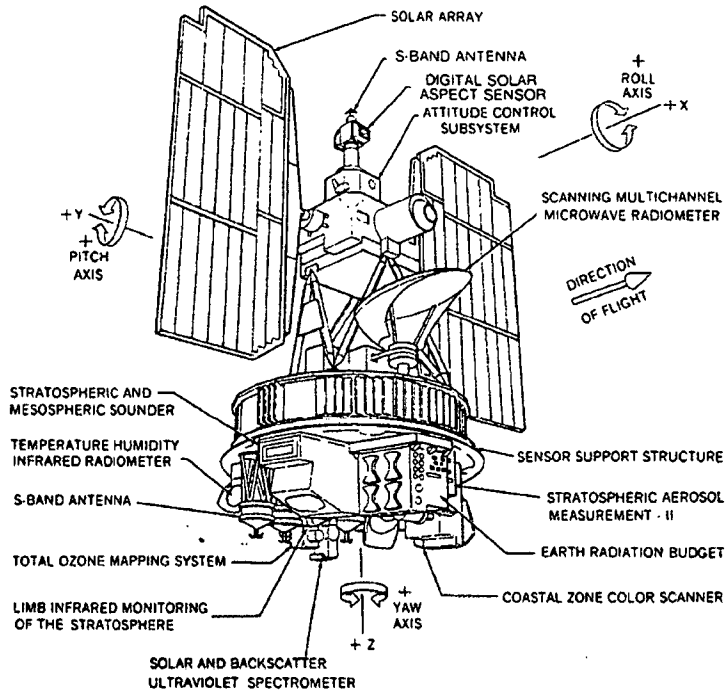


Fig 2.10: NIMBUS-7 with SMMR and a number of other instrument (Source: the NIMBUS-7 User's guide (1978) p. 2)

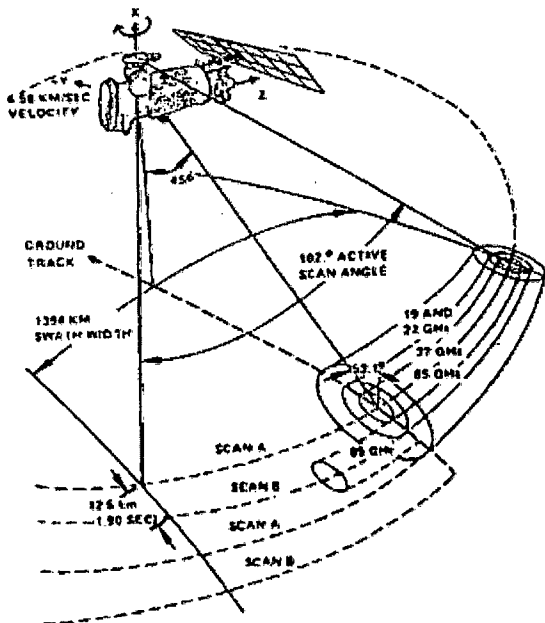


Fig 2.11: F08 SSM/I orbit and scan geometry (from Hollinger 1989)

CHAPTER -3

DATA DESCRIPTION

3.1 INTRODUCTION

In chapter 2 different techniques used for the study of polar cryosphere like passive and active remote sensing, altimetry and scatterometry are described. MSMR sensor onboard Oceansat-1 gives earth-surface information in terms of brightness temperatures after recording radiations emitted by the surface. In this chapter, we describe the sensors onboard OCEANSAT –1.

3.2 INTRODUCTION TO OCEANSAT – 1

Study of sea surface properties and related geophysical parameters require sensor systems which are different from other remote sensing sensors particularly in terms of spatial as well as radiometric resolution. India launched her microwave remote sensing satellite, IRS - P4 (renamed later as OCEANSAT – 1) in the series of Indian satellites, to address the oceanographic applications in a more concrete manner, on 26th May 1999. It was launched from the Shriharikota Range (SHAR). OCEANSAT - 1 is launched through the indigenously developed Polar Satellite Launch Vehicle (PSLV). Two payloads onboard Oceansat-1 are (i) the Ocean Colour Monitor (OCM), mainly dedicated to the study of biophysical properties of the oceans and (ii) the Multi-frequency Scanning Microwave Radiometer (MSMR) to study physical parameters of the ocean and the overlying atmosphere. Fig 3.1 shows the OCEANSAT –1 with the MSMR and the OCM.

3.3 THE ORBIT AND COVERAGE OF OCEANSAT – 1

OCEANSAT - 1 is dedicated to collect data for oceanographic, coastal and atmospheric applications. It is placed in a near-circular sun-synchronous orbit at an altitude of 720 km. The satellite crosses the equator in the descending node at 12 hours \pm 10 minutes. The track is controlled within \pm 1 km. of the reference ground trace pattern. The satellite takes the observation of whole globe with a repeat cycle of two days. The details of the orbit of OCEANSAT - 1 are given in the table 3.1 below (ISRO, 1999).

Table 3.1: Orbital details of OCEANSAT – 1

Altitude of the Satellite	:	720 km (near circular)
Orbital inclination	:	98.28°
Orbit period	:	99.31 min.
Distance between adjacent orbital ground traces	:	1382 km
Distance between successive ground traces	:	2764 km
Repetivity (coverage cycle)	:	2 days

3.4 SENSOR DESCRIPTION

Two payloads onboard Oceansat-1 are OCM and MSMR. OCM is a solid-state camera operating at 8 narrow spectral bands (see table 3.2) in the visible and near infrared bands. The basic concept behind this sensor is of push broom imaging mechanism using a linear array of charge coupled devices (CCD). The instantaneous field of view (IFOV) of the instrument is 360m having a swath width of 1420 km. To avoid the sun glint depending on the season, the electro-optic module has the provision to tilt the camera by $\pm 20^\circ$ in the along track direction. The signal from the oceans constitutes a very small fraction of the total radiance reaching the sensor aperture and the rest of it is contributed by the scattered radiation from the atmosphere. OCM has a 12-bit radiometric precision to cover the entire dynamic range of the observations from ocean to land. The major specifications of OCM are given in table 3.3 (ISRO 1999).

On the other hand, MSMR collects the data in microwave bands. It observes the earth's surface at four frequencies (6.6, 10.65, 18 and 21 GHz) with vertical and horizontal polarisation at each frequency. The capability of microwaves to penetrate the cloud makes MSMR a preferable option to take observations in all-weather conditions. Different earth surfaces and different atmospheric gases have different signatures at the above frequencies and polarizations. Suitable algorithms are developed (Gohil et al., 2000) to calculate different meteorological parameters such as sea surface temperature (SST), sea surface wind speed (SSW), cloud liquid water (CLW) and atmospheric water vapour (WV) using the MSMR brightness temperature (T_B) data. The major specifications of MSMR are given in table 3.4.

Table 3.2: Spectral band of OCM and their applications

Spectral Bands	Wavelength Range (nm)	Applications
C1	402 - 422	Yellow substance and turbidity
C2	433 - 453	Chlorophyll absorption maxima
C3	480 - 500	Chlorophyll and other pigments ($\leq 1.5 \text{ mg/m}^3$)
C4	500 - 520	Chlorophyll and other pigments ($\geq 1.5 \text{ mg/m}^3$)
C5	545 - 565	Suspended sediments (away from Chlorophyll and Gelbstoff)
C6	660 - 680	Second chlorophyll absorption maxima
C7	745 - 785	O ₂ absorption R-branch
C8	845 - 885	Aerosol optical thickness

Table 3.3: Major specifications of OCM

Parameter	Specifications
IGFOV at 720 km altitude	360m (across track)x 250m (along track)
Swath	1420km
No. of spectral Bands	8
Spectral range	402 - 885nm
Signal quantisation	12 – bit
Camera MTF (at Nyquist frequency)	> 0.2
Along track steering	+20°, 0°, -20°
Data rate	20.8 Mbits/sec.

Table 3.4: Major specifications of MSMR

Frequency (GHz)	6.6; 10.65; 18.0; 21.0
Spatial resolution (km ²)	105 x 68; 66 x 43; 40 x 26; 34 x 22
Polarisation	Vertical (V) and Horizontal (H)
Swath width	1360 km for all frequencies
Nominal incidence angle	49.7°
Radiometric temperature sensitivity	better than 1.0°K
Dynamic range	10°K - 330°K
Data rate	6.4 kbps
Antenna diameter	862 x 800 mm ²

3.5 TELEMETRY, TRACKING AND COMMAND NETWORK

Telemetry, tracking and command (TTC) network is responsible for housekeeping data reception from the satellite, in both the real time and playback modes, for (i) monitoring the health of the satellite/spacecraft, (ii) commanding the spacecraft and (iii) collection of range and range rate data through tracking.

Telemetry is responsible for continuously monitoring the health of the satellite. The reconfiguration, reorientation and repositioning of the satellite are controlled remotely through telecommands. The measurement of range and range rate of the satellite (i.e. to derive the position and velocity of satellite with reference to a ground station) is the job of tracking network. The functions of TTC for OCEANSAT-1 are carried out from ground stations at ISRO Tracking Centres (ISTRAC) at, Bangalore, Lucknow and Hyderabad in India and also from ISRO station at Mauritius. Also other external ground stations at Bears Lake (Russia), Biak (Indonesia) and Weilheim (Germany) provide their support to satellite operations and health monitoring and tracking. The Space Craft Control Centre (SCCC), located at ISTRAC is mainly responsible for spacecraft health monitoring, analysis, control, operational planning and network co-ordination.

3.6 DATA RECEPTION

The data from IRS-P4 is received at the National Remote Sensing Agency (NRSA), Hyderabad. The real time MSMR data and the OCM data in playback mode are received in X - band, while the real time MSMR data as well as the housekeeping data are received in S-band. Necessary information about the orbit and attitude as well as ancillary information required for application related data processing are also generated and incorporated in the payload data. The necessary system specifications are given in table 3.6.

Table 3.5: Receiving system specifications

Antenna	10m diameter (main reflector) 1.5m diameter (sub reflector)
Feed	X and S band
Polarization	Right Hand Circular (RHC)
Frequency bands	8025 - 8400 MHz (X-Band) 2200 - 2300 MHz (S-Band)
IF frequencies	375 MHz (X-Band) 70 MHz (S-band)
System G/T (dB/°K)	31.0 (X-Band) 19.5 (S-Band)

3.7 MSMR INSTRUMENT

MSMR is an 8-channel instrument receiving both horizontally and vertically polarized radiation at wavelengths 1.47, 1.67, 2.82 and 4.55 cm (ISRO, 1999). It is basically a dicke radiometer with fixed feed and scanning reflector. Microwave radiation from the earth and its atmosphere is collected by an off-parabolic reflector and is directed into a multi-frequency receiving horn, which distributes the various radiometric components to appropriate radiometers. Its antenna system consists of a parabolic reflector of 80 cm diameter and has an assembly of multi-frequency feed for all the four frequencies. Scanning is done by full rotation of the reflector. The reflector rotates at a constant angular speed of 11.173 rotations/min. This corresponds to a scan time period of 5.37 Sec. A conceptual diagram of the scanning geometry is given in fig. 3.2.1.

There are six receiver chains in the system. Two of them cater to 6.6 and 10.65 GHz, channel for vertical and horizontal polarisation data acquisition in alternate scans. Sufficient footprint overlap between 6.6 and 10.65 GHz channels allow such a configuration for data acquisition, which is not possible in the case of 18 and 21 GHz channels. However, for 18 GHz (V&H) and 21 GHz (V&H) data, four dedicated channels are used. For onboard calibration purpose two sky horns are used as cold source. One of them is functioning for 6.6 and 10 GHz frequencies and the other for 18.0 and 21.0 GHz frequencies. All six-receiver chains along with two sky horns are clustered around the

main feed in a compact assembly called the front - end feed assembly (FEFA). The basic aim is to minimize the radio frequency path loss prior to low noise amplification.

MSMR receivers are moderately stable with stability of 0.01 dB. It has Dicke type configuration, i.e., the receiver input is switched between the antenna and a reference noise source at ambient temperature. The switching rate is kept at 1 KHz. A rigid alignment is maintained by mounting the FEFA and reflector assembly including scanning motor on the CFPR. The function of the receiver assembly on FEFA is to carry out low noise amplification, down conversion to IF and square law detection. High gain base-band amplification and synchronous detection are carried out in a precision base-band processing system (PBPS). All of the inter-payload control operation, timing sequence generation and digitisation are done in DACS. The onboard integration time of PBPS is 18 ms. A 12-bit digitization is carried out at a sampling interval of 9 ms to avoid aliasing effect. The incoming microwave beams at constant angle of 43.33° from nadir, corresponding to an earth incidence angle of 49.7° at the OCEANSAT - 1 orbital altitude of 720km.

MSMR viewing geometry is given in fig 3.2 (a,b). The MSMR scanning arrangement results in a nearly circular intersection of the cone swept out by the oscillating optic axis with the surface of the earth. The swath of the observations across the sub-satellite track is about 1420km.

3.7.1 MSMR Data and Data Products

MSMR data products are routinely available from National Remote Sensing Agency (NRSA), Hyderabad. The data product is available for each day, (i.e. 24 hours) in a separate file. The details of the different types of data product available for MSMR are provided in the following subsections. Section 3.3.1 gives an over view of MSMR data products and the section 3.3.2 describes the MSMR data file structure

3.7.2 Overview of MSMR Data Products

The MSMR data products are available at five different levels. The products are generated starting from the raw data product level up to the monthly averaged product level. The five different products are

- 3.7.2.1 Raw data product
- 3.7.2.2 Antenna temperature data files (ATD product)
- 3.7.2.3 Brightness temperature data file (BTD product)
- 3.7.2.4 Geophysical Parameter data files (GPD product)
- 3.7.2.5 Monthly averaged product files (MAP product)

3.7.2.1 Raw data product

This product consists of the raw sensor data file (SDF) (i.e. raw MSMR data available at 5.37 seconds interval) and the orbit and the attitude data file (OATF) at one-second interval. Each individual file consists of 24 hours of data. For each day, totally there are four files. Among the four files two are header files and two are data files for SDF and OATF. The header files contain the relevant contextual information for the data files, which helps later on for processing and analyzing the data for different applications.

3.7.2.2 Antenna temperature data products

The raw data from MSMR is converted to antenna temperature data (ATD) using the ground and onboard calibration. An antenna temperature data file consists of data of all the passes that occur in one full day. Each channel of MSMR data is provided with 12 bit precision. The data stream is converted to temperature values after applying proper calibration using the ground calibration data (before the launch of satellite) and the onboard calibration data sets as well as the analog and the digital telemetry subsystems (ADTMS) data (Mishra et al. 2002). This data set gives the actual temperatures as observed by the antenna, i.e. the total radiation received by the antenna from all sources. In case of 6.6 GHz (H&V) and 10.65 GHz (H&V) the raw data comes in alternate scans, where as for 18 GHz (V&H) and 21 GHz (V&H) we get the ATD for all the scans.

In order to make the data set uniform, the missing scan lines in the 6.6 and 10.65 GHz channels are filled by the repetition of the data from the previous available scan line. The observed ATD is highly over sampled. To reduce the data volume, the consecutive samples of the scanned data are averaged and put as one sample. In addition to the temperature values, the latitude, the longitude and the incidence angle related information

is also provided for each grid cell. A data flag is also assigned to each grid cell, to indicate its data quality.

3.7.2.3 Brightness temperature data product

From ATD products, the brightness temperature (T_B) data are derived by applying the antenna pattern correction. A brightness temperature data (BTD) file consists of 24 hours of each output data cell. Here the cells are not same as the input scanned cells, but are uniformly gridded as per three different prespecified schemes. Square grids are generated along and across the sub-satellite track taking sub-satellite track as the central line. The BTD is available in three different spatial grids. The size of the grid cells in three schemes are 150km \times 150km, 75km \times 75km and 50km \times 50km. The brightness temperature (T_B) data are available in above three grids separately. A brief description about the data available in different grid is given below :

(a) Grid – 1

It is the grid with largest cell size available in the MSMR data products. This grid corresponds to 6.6 GHz frequency in terms of spatial resolution. The data from all the other high frequency channels like 10.65, 18 and 21 GHz are also provided in this grid. In addition to the latitude, longitude, incidence angle and the data quality flag for each grid cell are computed and provided along with the T_B data of the corresponding cell.

(b) Grid – 2

This grid has a spatial size of 75km \times 75 km, which fits to the spatial resolution of MSMR at 10.65 GHz frequency. As 6.6 GHz channel has poorer resolution, the T_B for 6.6 GHz is not available in this grid. The T_B for other higher frequencies and polarisations are available in this grid. Corresponding to each grid cell T_B , the latitude, longitude, incidence angle and the flag are computed and provided in the data set.

(c) Grid – 3

This is the smallest grid size available in the brightness temperature data file. It has 50 km by 50 km spatial extent corresponding to the resolution at 18.0 and 21.0 GHz

frequencies. This grid does not contain the T_B values at frequencies 6.6 and 10.65 GHz as they have poorer resolution. Hence T_B 's for only 18V, 18H, 21V and 21H channels are generated for this grid in the brightness temperature data sets. In addition to the T_B values the latitude, longitude, incidence angle and the data quality flag are computed and assigned to each grid cell. In the present study grid 2 and grid 3 T_B 's only have been used because of the finer resolution at which they are available.

3.7.2.4 Geophysical parameter data product

Geophysical Parameter Data products (GPD) are derived from BTD using suitable parameter retrieval algorithms. From the MSMR BTD only four GPD products (i.e. sea surface temperature (SST), sea surface wind (SSW), cloud liquid water (CLW) and total integrated atmospheric water vapour (WV)) are operationally available. The GPD products are available at all the three different grid-levels, which are same as the BTD grids described above. For the retrieval of SST 6.6 GHz channel serves as the prime channel although other channels are used. Similarly 10.65 GHz channel is used as the main channel for the SSW speed retrieval. 18 GHz and 21 GHz channels play the key role in the derivation of WV and CLW in the retrieval algorithm. All four GPD products are available in Grid - 1, i.e. 150 km \times 150 km resolution, where as SSW, WV and CLW are available on the grid 2 i.e. 75 km \times 75 km spatial resolution. In grid 3, only WV and CLW are available. It has a spatial resolution of 50km \times 50km. Latitude-longitude information is provided for the centre of each grid cell. Information about the quality of the data is provided for each grid cell by assigning the flag after quality control check.

3.7.2.5 Monthly averaged product

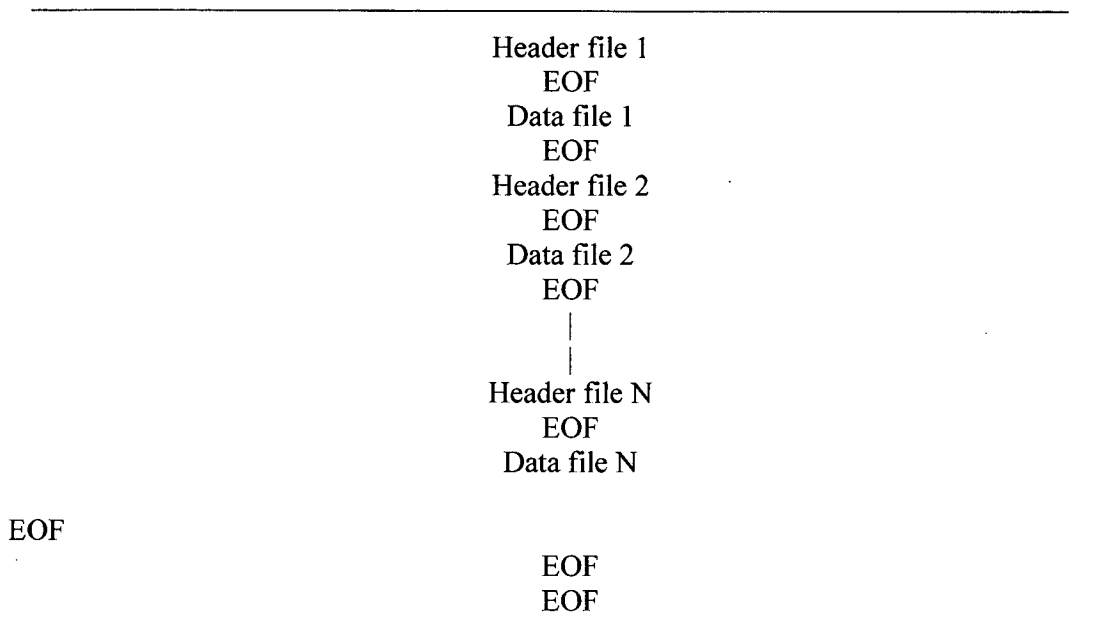
The monthly averaged product files contain the geophysical parameters such as SST, SSW, CLW and WV averaged over a month. This data is available on 1° \times 1° geophysical grid.

3.7.3 MSMR Data File Structure

Each of the data products described above comprises of multiple files in each data set. Each individual data product has a separate header file and a data file. The header gives the information about the date of creation of data, start-time, end-time, start- orbit, end-

orbit, number of orbits in the file etc. The header file consists of one ASCII record only for each data set. There is one end of file (EOF) marker after each file and three EOF markers after the last file. An elaborate data structure of MSMR is given in table 3.7.

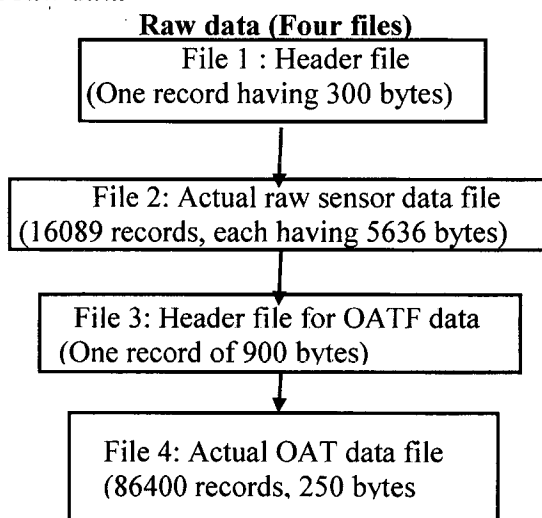
Table 3.6: MSMR data structure



(a) Raw data product file structure

Each raw data set contains four files, out of which two are header files and two are data files. The first file is a header file for the raw sensor data having one record of length 300 bytes. The second file is the actual raw sensor data file, having 16089 records. Each record has record length 5636 bytes. The third file is the header file for OATF. It has one record of record length 900 bytes. The fourth file contains the actual OAT data file. The OAT data file has 86400 records. Each record has record length 250 bytes (see chart 3.1).

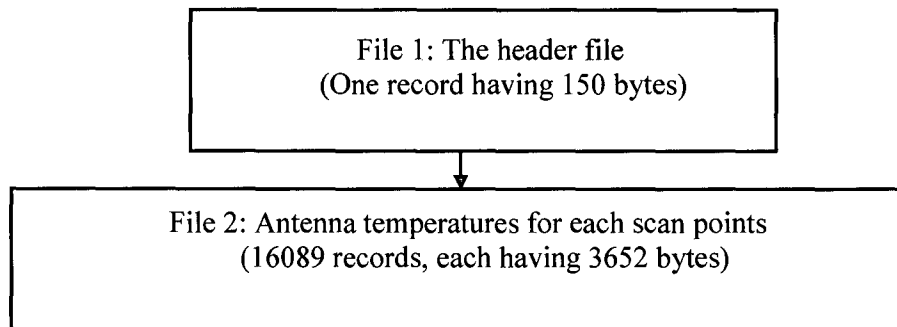
Chart 3.1: Chart of raw data



(b) Antenna temperature data file structure

The antenna temperature data product contains two files. The first file is the header file and the second file contains the antenna temperature values corresponding to each scanned point (after averaging by 2). The header file has one record having record length 150 bytes. Where as the data file has 16089 records having record length 3652 bytes (see chart 3.2).

Chart 3.2: File structure of the antenna temperature data product
Antenna temperature data file



(c) Brightness temperature data file structure

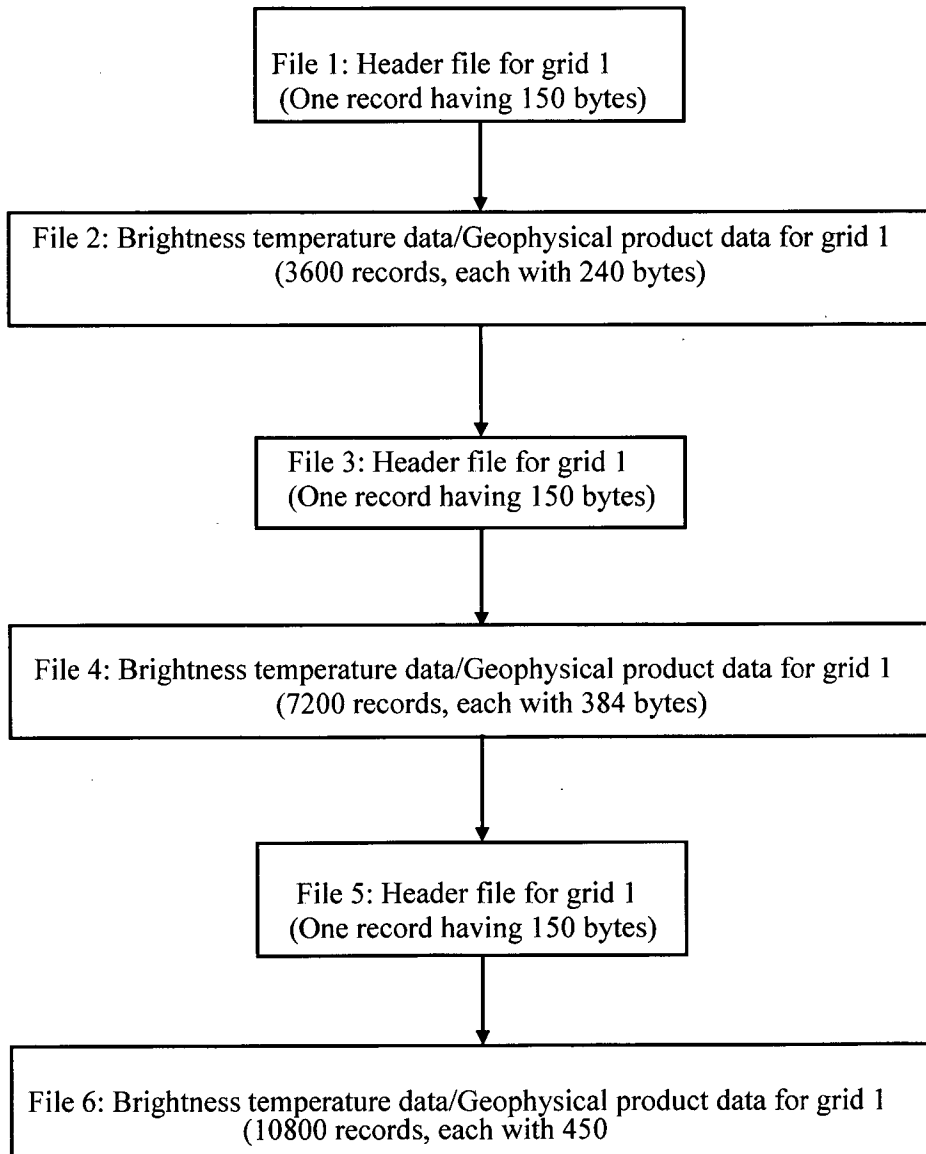
Brightness temperature data product has multiple header and image/data files corresponding to each grid size. There are six files in the BTD product. The first, third and fifth files correspond to header file for grid 1, grid 2 and grid 3 respectively. The second, fourth and sixth files correspond to grid 1, grid 2 and grid 3 data files respectively. Each header file contains one record having record length 150 bytes. Grid 1 data file i.e. second file has 3600 records, each record having record length of 240 bytes. Grid 2 data file i.e. 4th file has 7200 records each having record length 384 bytes. Sixth file in the BTD product set is the grid 3 data file. This file has a record length field 456 bytes. The number of records in this file is 10800 (see chart 3.3).

(d) Geophysical parameter data file structure

Corresponding to each grid size there are multiple header and data files for GPD product. The number of files in the GPD product set is same as BTD data product set. The first, third and fifth files correspond to header file for grid 1, grid 2 and grid 3 respectively. All the three header files have one record each with record length 150 bytes. In grid 1 all the

four geophysical parameters are available. It has 3600 records. Each record contains 240 bytes. Grid 2 data file has 7200 records. Each record contains 384 bytes. The lowest grid i.e. grid 3 file has 10800 records, with record length 456 byte each (see chart 3.3).

Chart 3.3: File structure for the brightness temperature/geophysical data product
Brightness temperature data/Geophysical product data



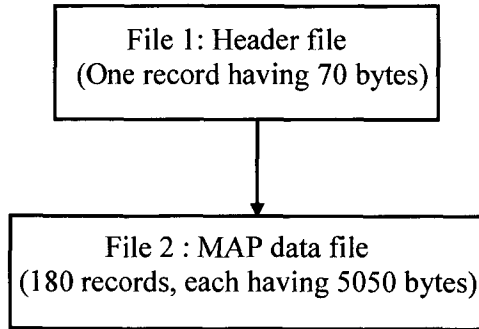
(e) MAP data file structure

It consists of only two files. The first file is the header file of length 70 bytes. The second file is the data file containing 180 records, each having length 5050 bytes. The total volume of the data for this product will be about 0.91 Mbytes.

Chart 3.4: File structure of MAP data product

MAP data

(Two files)



IRS - P4

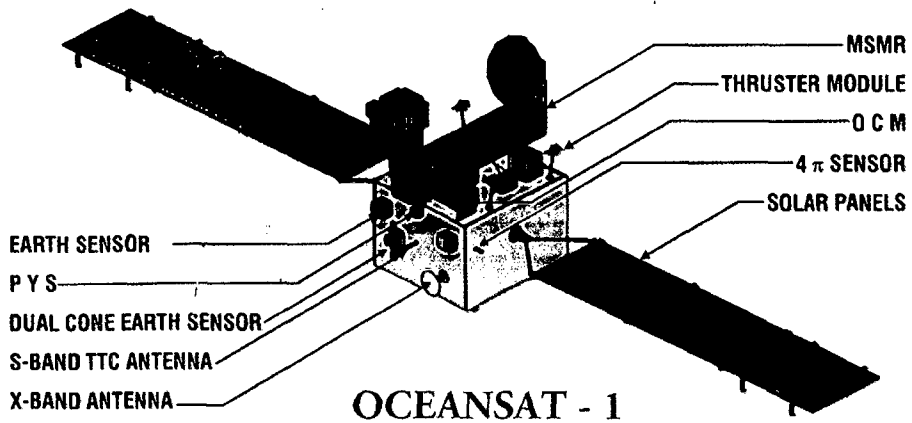


Fig 3.1 : Block Diagram of OCEANSAT-1

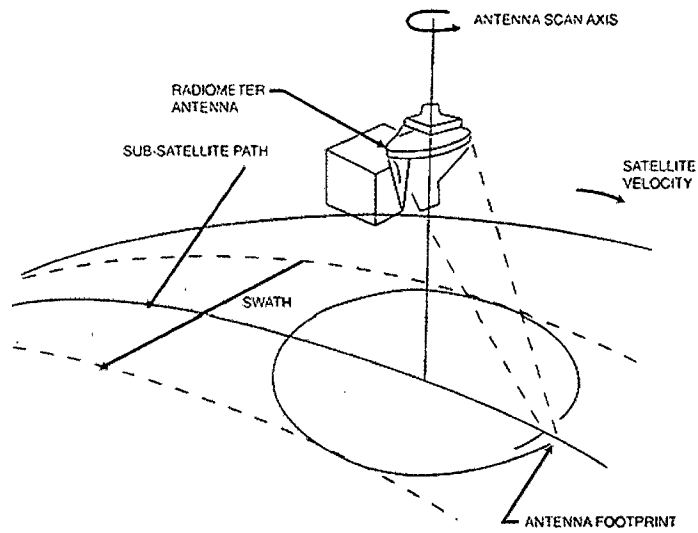


Fig. 3.2 (a): Viewing geometry of MSMR (Dash 2006)

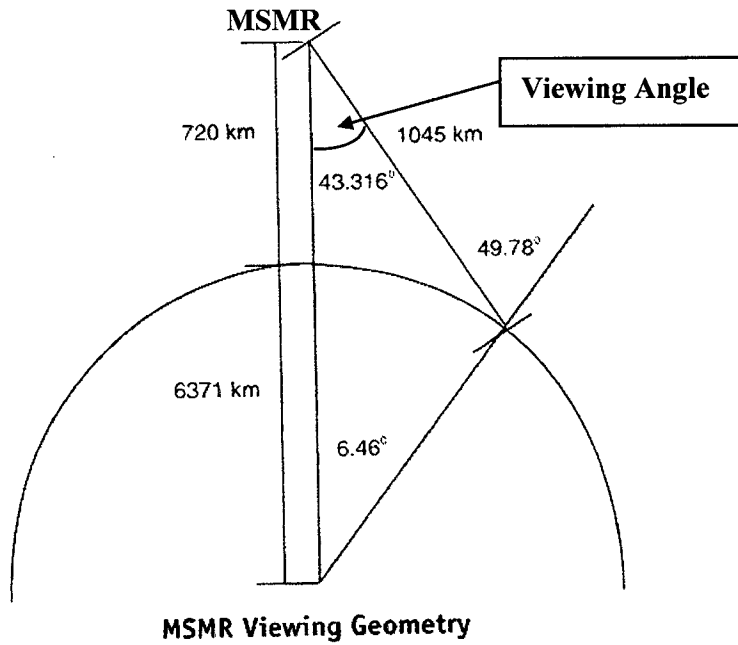


Fig. 3.2 (b): MSMR Viewing Geometry

CHAPTER -4

PROCESSING OF MSMR DATA FOR SEA ICE STUDIES

4.1 INTRODUCTION

In previous chapters we have described some aspects of remote sensing, with special emphasis on microwave remote sensing of polar cryosphere and also described the Oceansat-1 MSMR and OCM sensor specifications and data products. In this chapter we are going to describe the processing aspects of the MSMR data for the study of polar sea ice and projecting the data on polar stereographic projection for visualization.

4.2 EXTRACTION OF DATA

The basic requirement for research and development is the good data of the physical variables. Once the research problem has been identified and research plan is chalked out the important task is the collection, extraction and quality control of data. In remote sensing, the data is collected by the satellite or airborne sensors. The greatest problem in the satellite remote sensing is the calibration and the validation of data. The assurance and evaluation of the quality of data for OCEANSAT – 1 MSMR have been performed by several investigators, (see Mishra et al. 2002, Palsule et al. 2002, Mihir et al. 2003). On available data we apply different algorithms for the study of the sea ice.

4.2.1 Extraction of data for the region of interest

The immediate problems that follow the acquisition of raw data are the calibration and the validation of the data. The validation and calibration of the acquired MSMR T_B data and those of the geophysical products have been described by Sharma et al. 2002, Mishra et al. 2002, Palsule et al. 2002, Bhandari et al., 2002. In our study, the MSMR T_B data of the region of interest is extracted from the raw T_B data. We select the 18 GHz MSMR data for sea ice studies for the following reasons:

- ❖ 18 GHz channel has a spatial resolution (i.e. $50 \text{ km} \times 50 \text{ km}$) higher than the 6 and the 10 GHz channels, and equal to the 21 GHz channel (which is more sensitive to atmospheric water vapour).
- ❖ In lower frequency channels, the energy recorded by the radiometer may be contaminated by the water beneath the sea ice. This contamination is very less in case of higher frequencies like 18 GHz and 21 GHz. (Svendsen et. al .,1983)

- ❖ The contrast between different polarizations is more at higher frequencies, which help us to study different types of ice and their properties.
- ❖ 21 GHz channel being nearer to the water vapour absorption band (22 GHz) is more sensitive to columnar water vapour, so, for the ice extent calculation, the Brightness Temperature value in 18GHz channels are preferred. (Svendsen et. al.,1983)

For ice concentration studies we have used dual-channel data (10 GHz and 18 GHz) with dual-polarization (Vertical and Horizontal). The sea ice concentration analysis from the MSMR data will be discussed in detail in chapter 5.

4.2.2 Development of interpolation scheme to fill the data gap

As described in chapter 3, the MSMR radiometer collects data over a swath-width of 1360 km. The raw data acquired along the swath is transferred to an evenly spaced latitude-longitude gridding scheme with individual elements of 0.5 deg. X 0.5 deg. This process, coupled with the rejection of bad inferior quality data leads to several data gaps in the output. To fill the data-gaps, an interpolation scheme is developed, for which the following assumptions are made

- ❖ The variation of the emitted radiation observed by the MSMR is continuous and gradual in both the directions i.e. along the track and across the track of the satellite flight.
- ❖ There is no abrupt change in the signal between the two points of observation, either along track or across track of the satellite flight.
- ❖ We have assumed that the variation of T_B from one point to the other along the same scan line or along the track of the satellite is linear.

We interpolate both, along the track and across the track, using the linear interpolation technique, to fill the data gaps. The interpolation formulae can be given as

$$y(x) = y(a) + \frac{x-a}{b-a} [y(b) - y(a)] \quad 4.1.$$

where a and b are the time (positions) of the data set at the start and the end of the sampling increment being interpolated, and x represents the corresponding time(position) at which the interpolation is desired within the interval $[a, b]$. y represents the dependent variable, in this case, the brightness temperature.

4.2.3 Geographical gridding of the data

Satellite observations give data of the earth along the orbital track and across the swath. However, the data points do not lie along any well defined geographical referencing system. In order to study and analyze the data, it is very necessary that it is brought down from the satellite perspective view to a regular latitude-longitude grid structure. For this purpose, we use the weighted average method to calculate the effective brightness temperature (T_{Beff}) of the grid-cells at each grid intersection point (GIP).

All the observation points lying within one grid cell area centered on a GIP are considered in the computation of T_{Beff} . The weightage given to the T_{B} of any point within this area is proportional to $1 - r_i^2$, where r_i is the radial distance between the i^{th} point and that GIP. All the points under consideration are assigned weightages in this manner and then the weighted average of the corresponding T_{B} 's is taken. This gives the T_{Beff} for that GIP. The exercise is then repeated for all the GIP's in the scene.

$$T_{\text{Beff}} = \frac{1}{N} \sum_{i=1}^n \frac{1}{(r_i^2 - 1)} T_{\text{Bi}} \quad 4.2$$

where T_{Beff} is the effective brightness temperature at the grid point

r_i is the radial distance of the i^{th} point in units of grid cells, from the chosen grid cell centre

N is total number of observation points within the grid cell

T_{Bi} is Brightness temperature value at the i^{th} point

For our study purpose we have chosen the grid size to be $0.5^\circ \times 0.5^\circ$ geographical grid. For the temporal averaging we use the simple averaging method, for all the observations obtained during the 24-hour period of a given calendar data.

4.3 MAPPING OF MSMR DATA

For study of earth surface features there is need to choose proper projection. Map projection is a technique for projecting curved surface of the earth on a two dimensional plane. There are different types of projections available to map the earth's surface depending upon the capability of a projection, region of interest and the application under consideration. For example at mid- and low latitudes, Mercator projection is used for navigational applications. Generally for mapping the polar region, Polar Stereographic Projection is used.

4.3.1 Polar stereo graphic projection

MSMR T_B data over the polar region is projected using the polar stereographic projection. It can be done by considering the projection plane to be tangential to the earth's surface at one of the poles (North or South Pole), with vertex of the projection being the opposite pole. Each point on the earth can be represented on the projection plane by joining the vertex with the point on the earth's surface and extending the line to intersect the projection plane. The point of intersection gives the map coordinates for the given point on the earth. This concept is illustrated in the figure 4.1. In this figure the point 'P' on the earth's surface is projected on the polar plane at Q. The vertex is at B. The coordinates of each element on the projected map are determined as follows:

$$r = d \tan \alpha \quad 4.3$$

Where d is the diameter of the earth

α is the angular projection at the opposite pole, this can be expressed in terms of latitude ϕ as

$$\alpha = \frac{\gamma}{2} = \frac{1}{2}(90 - \phi) \quad 4.4$$

To study the Arctic (Antarctic) region the plane is passed at the geographic North (South) pole and the geographic South (North) pole is taken as the vertex.

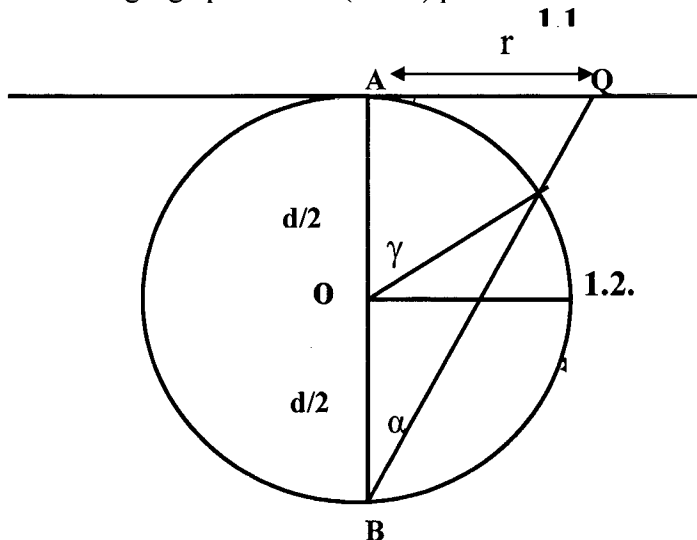


Fig. 4.1: The concept of polar stereographic projection

4.3.2 Mapping of MSMR data in the Polar-stereographic projection

To display the MSMR T_B data over the Antarctic, the gridding scheme (as described above) is used. The data is mapped on to a $0.5^\circ \times 0.5^\circ$ geographical latitude longitude grid. For multiple occurrence of data points in a single grid cell the effective average value of T_B is calculated and assigned to that cell. To reduce the random noise due to the receiver systems as well as due to the atmosphere, averaging of T_B for each grid cell is carried out for 6-8 day period approximately during the middle of each month. The results are considered as representative for the corresponding month. The data void-regions are filled with a special value (say -9999.0) indicating the undefined nature of their T_B . Suitable colour scheme is chosen to represent different ranges of surface radiance values at microwave frequencies. The continental boundary is overlaid on the image.

4.4 CALCULATION OF SEA ICE AREA

For calculation of sea ice extent, we have gridded the data into $0.5^\circ \times 0.5^\circ$ regular geographical latitude longitude grid. The sea ice extent calculation is done for different sectors of the Polar Regions. The ice boundary is defined by thresholding technique in case of MSMR data and by taking 15% sea ice as the ice boundary for SMMR and SSM/I data.

The observation periods of MSMR, SMMR and SSM/I data used will be described in chapter 7. Ice and water regions are examined and transect are selected across the water - ice boundary. Then graphs of T_B are plotted as one moves along the transect.

The boundary between sea ice and water is derived through inspection of steep slope regions on the graphs obtained (moving from north to south or vice versa) by the above method. These boundaries (one for 18 GHz vertical and another for 18 GHz horizontal polarization) are then used later on as discriminant function for classification between sea ice and open water. Once the boundary pixel is identified, we try to differentiate the land pixels from the ocean pixels. To differentiate the ocean area from the land area, a topographic file of the northern hemisphere is used. This topographic file is recast on another geographical grid having same spacing as that of the T_B data file. Each pixel of the data file and the topographic file is compared. If a pixel is identified as the ocean

pixel and it occurs inside the sea ice boundary, then the area of that pixel is calculated (taking the earth as an oblate spheroid).

The schematic diagram for the same is given below (see fig. 4.2). The above procedure is followed for all the pixels and finally the areas of the oceanic pixels are suitably added to calculate (i) the ice extent for different sectors in the polar and finally (ii) the total ice extent. This file is generated from the E-topo file available in the public domain (see fig 4.3) (www.ngdc.noaa.gov).

The area dA of a grid cell (see fig. 4.2) can be calculated using the following equation

$$dA = \int_{\theta_1}^{\theta_2} \int_{\phi_1}^{\phi_2} r^2 \cos \theta d\theta d\phi \quad 4.5$$

Where, r is the distance of the point from the centre of the earth.

θ is the latitude and ϕ is the longitude of the point

θ_1 and θ_2 are the initial and final latitudes (lower and upper boundary of the grid cell)

ϕ_1 and ϕ_2 are the initial and final longitude (lower and upper boundary of the grid cell)

Considering the earth as an oblate spheroid its radius at any latitude and longitude position was approximated using the following equation

$$r = \left[\frac{a^2 b^2}{a^2 \cos^2 \theta + b^2 \sin^2 \theta} \right]^{1/2} \quad 4.6$$

Where a is the equatorial radius of the earth (6378.140 km) and b is the polar radius of the earth (6356.755 km)

The area is calculated for all the months of the years for which the data are available.

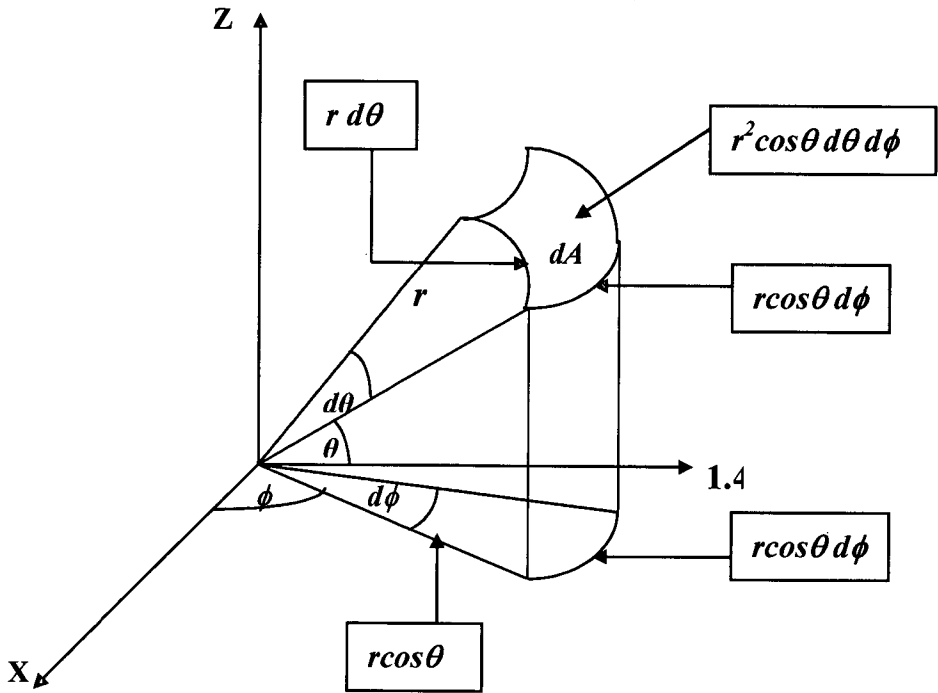


Fig. 4.2: Schematic representation of pixel area on the earth surface (Dash, 2003)

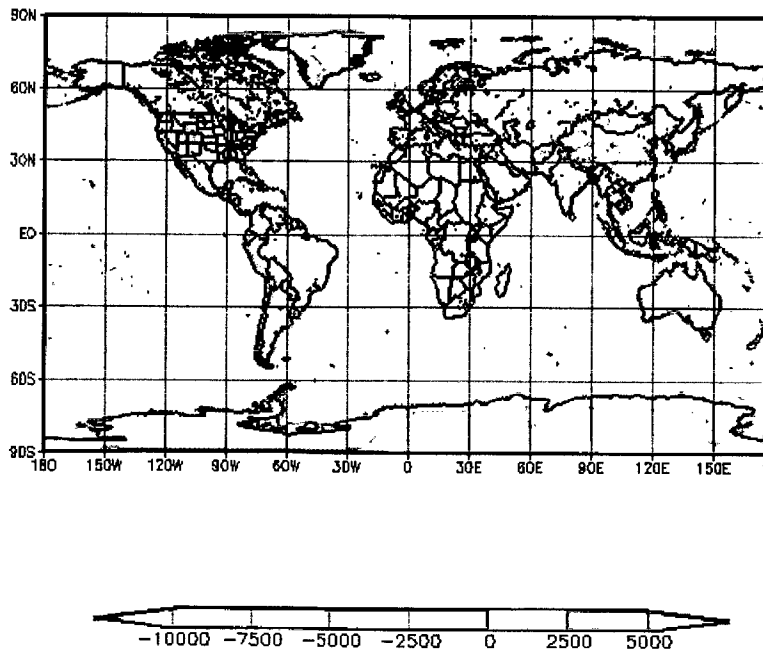


Fig 4.3: Depth/Elevation Map of the World

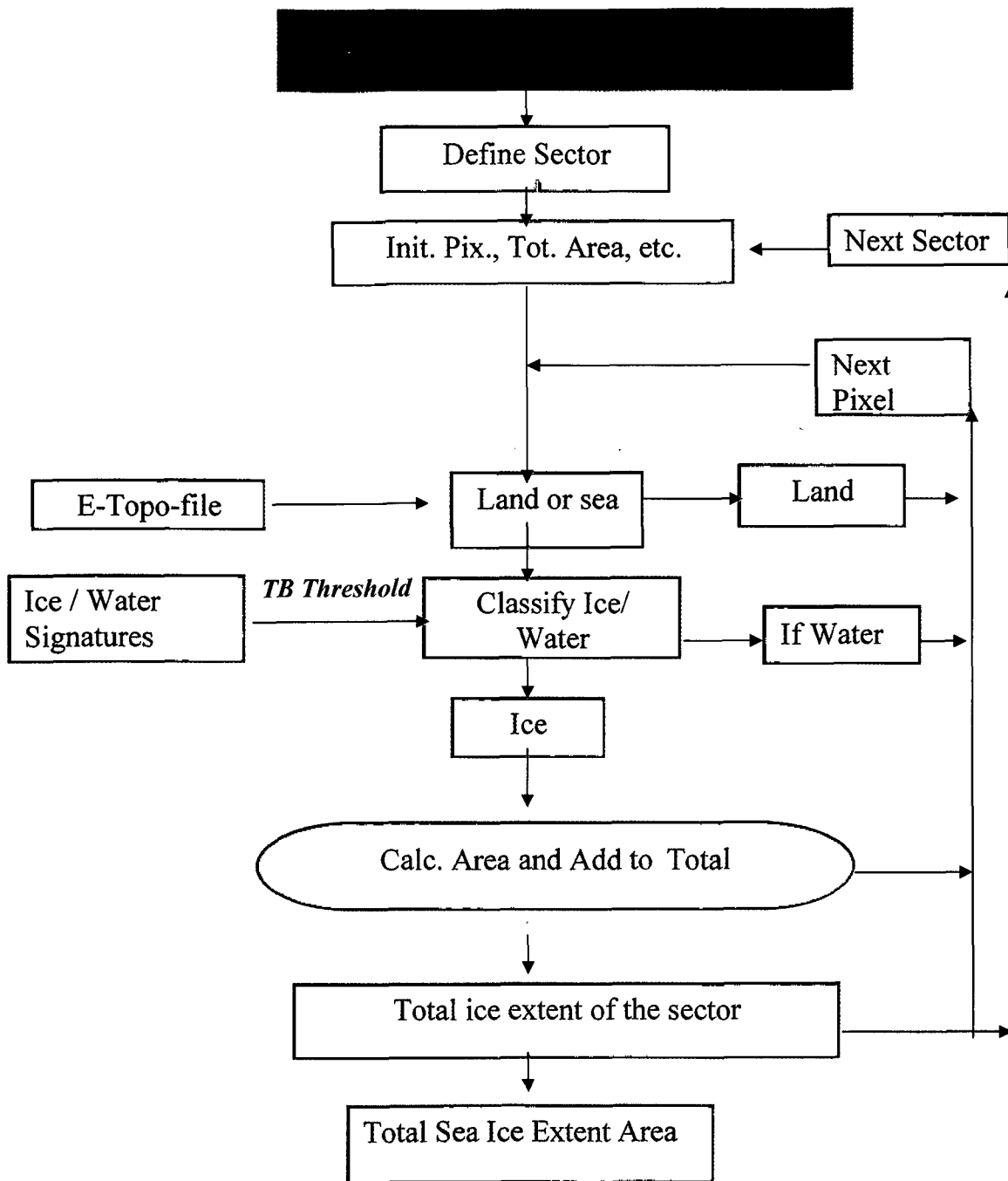


Chart 4.1: Area calculation Flow chart

CHAPTER -5

**INTER-COMPARISON OF MSMR
AND SSM/I OVER SOUTHERN
POLAR OCEAN (SPO)**

5.1 INTRODUCTION

In this chapter we attempt an indirect validation of the brightness temperature observed by MSMR over the South Polar Regions with near simultaneous measurements from SSM/I onboard DMSP series of satellites. For the study of the region of interest, first we have chosen data sets from both sensors for two different seasons during the 1999 -2000 period. T_B images are produced by using data sets from the two sensors for their comparative study. Based on regression analysis of MSMR observed T_B 's and SSM/I T_B 's, we have developed sea ice concentration algorithm for the Southern polar region. The MSMR SIC algorithm allows estimation of SIC with less than 10% rms error .The analysis brings out the very high level of compatibility in measurements produced by the two sensors .The inter-comparison with the near operational sea ice analysis from SSM/I paves the way for the continuous and reliable monitoring of polar ice with MSMR

5.2 INTER-COMPARISON

Passive Microwave remote sensing sensors are of all weather and all season capability for sensing the terrain. Specifications of MSMR, SMMR and SSM/I are explained in chapter 3. They have played a vital role in the study and monitoring of the inhospitable regions of both the Polar Regions. These studies have been carried out for monitoring of sea ice using PMR measurements from Nimbus -5 ESMR, Nimbus-7 SMMR and DMSP SSM/I (Glorsen et al .,1992, Parkison et al., 19990). Numerous investigations have been made to understand the observed short term and long term regional and hemispheric changes in sea ice characteristics in relation to climate and climate change. The MSMR data is used to study the spatial distribution and seasonal variability of sea ice characteristics over the polar sea ice regions.

Changing sea ice extent over polar region is of great importance in the context of future climate change. Important fact with PMR is that it scans large area of the earth in a short time so that any large scale change can be detected and monitored frequently. To get confidence in data quality we need inter-comparison of MSMR results with other sensors of higher resolution. Short overlap between different microwave sensors e.g. between SMMR and SSM/I during 1987 and between successive SSM/I sensors later on has played a key role in the inter-calibration of sea ice measurements from SMMR and

SSM/I over the Arctic and the Antarctic regions. As a result we have highly reliable time series of sea ice measurements over Arctic as well Antarctic region over a period of almost two and a half decades. Through inter-comparison of inter-annual variation of sea ice extent over polar region we can validate the MSMR data for future study of global warming.

5.2.1 Comparison of the Emissivity of Sea Ice and open water

Emissivity of any physical body is a function of polarization, frequency and angle of incidence of the radiation at the interface of the two media. Out of all these influencing factors, the frequency plays dominant role. In different atmospheric windows at the same physical temperature, the emissivity of the same body is different. Emissivity is dependent also on the nature of the medium itself. Emissivity changes depending upon whether the medium is homogeneous or heterogeneous.

In microwave range of the spectrum between 1-100 GHz, emissivity of water and ice shows very good distinguishability between them. Emissivity of pure water and saline water are different due to difference in their dielectric constants.

$$\text{Emissivity } e = \frac{Tb}{Ts}$$

For specular surface, if the reflectivity is $\Gamma(\nu, \theta, p)$ then

$$\text{Emissivity } e = 1 - \Gamma(\nu, \theta, p) \quad 5.1$$

Where ν is Frequency

θ is the Angle of Incidence

p is the Polarization either Horizontal (H) or Vertical (V)

Specular reflectivity (Ulaby et al, 1982) $\Gamma(\nu, \theta, p)$ for both horizontal and vertical polarization is given by :-

$$\Gamma(\nu, \theta, H) = \left| \frac{\cos \theta - \sqrt{\epsilon_w - \sin^2 \theta}}{\cos \theta + \sqrt{\epsilon_w - \sin^2 \theta}} \right|^2 \quad 5.2$$

and

$$\Gamma(\nu, \theta, V) = \frac{\left| \frac{\epsilon_w \cos \theta - \sqrt{\epsilon_w - \sin^2 \theta}}{\epsilon_w \cos \theta + \sqrt{\epsilon_w - \sin^2 \theta}} \right|^2} \quad 5.3$$

where H and V stands for horizontal and vertical polarization respectively.

ϵ_w is the dielectric constant of water with respect to air. In microwave region ϵ_w is a function of three quantities, frequency (f), surface temperature (Ts) and salinity in case of sea water. The frequency dependence of the dielectric constant of pure water is given by the well known Debye Expression as,

$$\epsilon_w = \epsilon_{w\infty} + \frac{\epsilon_0 - \epsilon_{w\infty}}{1 + j2\pi f\tau_w} \quad 5.4$$

where ϵ_0 is static dielectric constant of pure water

$\epsilon_{w\infty}$ High frequency limit of ϵ_w

τ_w Relaxation time for pure water in seconds

f Electromagnetic frequency

Magnitude of high frequency dielectric constant $\epsilon_{w\infty}$ was determined by Lane and Saxton(1952) to be approx. 4.9

Equation 5.4 can be expressed in the form of a complex quantity as

$$\epsilon_w = \epsilon_w' + j\epsilon_w'' \quad 5.5$$

where real and imaginary parts are as follows

$$\epsilon_w' = \epsilon_{w\infty} + \frac{\epsilon_{w0} - \epsilon_{w\infty}}{1 + (2\pi f\tau_w)^2} \quad 5.6$$

$$\epsilon_w'' = \frac{2\pi\tau_w f(\epsilon_{w0} - \epsilon_{w\infty})}{1 + (2\pi f\tau_w)^2} \quad 5.7$$

Emissivity of saline water:

Saline water contains dissolved salts. Sea water is a solution of different salts like sodium chloride and others. Salinity is expressed in parts per thousand by weight. We can determine emissivity of saline water by knowing dielectric constant and putting in the above equations 5.1, 5.2 and 5.3.

The real and imaginary parts of the dielectric constants of saline water solutions are given by :-

$$\epsilon'_{sw} = \epsilon_{sw\infty} + \frac{\epsilon_{sw0} - \epsilon_{sw\infty}}{1 + (2\pi f\tau_{sw})^2} \quad 5.8$$

and

$$\epsilon''_{sw} = \frac{2\pi f\tau_{sw}(\epsilon_{sw0} - \epsilon_{sw\infty})}{1 + (2\pi f\tau_{sw})^2} + \frac{\sigma_i}{2\pi\epsilon_0 f} \quad 5.9$$

Pure water ice and fresh water ice :-

Unlike liquid water whose relaxation frequency lies in microwave region the relaxation of pure ice lies in kHz region . the relaxation frequency f_{i0} of ice is 7.23 kHz at 0°C and decreases with negative temperature to 35 Hz at -66°C (Auty and Cole, 1952).

In microwave region quantity $2\pi f\tau_i = \frac{f}{f_0} \gg 1$.

Therefore Debye`s relaxation equation simplifies to

$$\epsilon'_i = \epsilon'_{i\infty}$$

and

$$\epsilon'' = \frac{\epsilon_{i0} - \epsilon_{i\infty}}{2\pi f\tau_i} = (\epsilon_{i0} - \epsilon_{i\infty}) \frac{f_{i\infty}}{f} \quad 5.10$$

Here i stand for pure ice.

Sea ice typically has emissivity of about 0.9 as compared to water whose emissivity is about 0.4 on the basis of the above analysis.

Sea ice (SI):

Sea ice is a heterogeneous mixture of liquid brine inclusions and air pockets interspersed within the ice medium. SI is divided into three categories which are given in the table below with its thickness and salinity profile.

Table 5.1: Types of Sea ice and their properties

Type SI	Thickness	Salinity profile
Young Ice (YI)	Less than 30cm	5-16% near the surface 4-5% in the bulk of ice, increases to 30% near the water interface.
First Year Ice (FYI)	30cm- 2m	Less than 1% at the surface
Multi Year Ice (MYI)	Exceeds 2m	2-3%in the bulk portion of the ice.

Average dielectric constant of a heterogeneous mixture is governed by the dielectric constant of the substances in the mixture, their volume fractions, their spatial distributions and their orientations relative to the direction of the incident electric field vector. All Theoretical models are developed for the study of SI by assuming either ellipsoidal particles (spheres, needles or discs) or confocal ellipsoidal shells.

Assuming brine inclusions spherical in shape Hoekstra and Capplino(1971) developed a model for modeling SI dielectric constant. Average dielectric constant is given by the expression :

$$\epsilon_{si} = \epsilon_i + 3v_b \frac{(\epsilon_b - \epsilon_i)}{(2\epsilon_{si} - \epsilon_b)} \quad 5.11$$

where ϵ_{si} is dielectric constant of sea ice .

ϵ_i is dielectric constant of pure ice.

ϵ_b is dielectric constant of brine inclusions.

v_b is volume brine fraction

Equation 5.11 simplified to real and imaginary parts as

$$\epsilon'_{si} \cong \frac{\epsilon'_i}{1 - 3\nu_b}$$

Where $\epsilon'_i = 3.15$ relative permittivity of pure ice.

since and on the assumption that for small values of ν_b

$$\epsilon'_b \gg \epsilon'_{si}$$

Loss factor $\epsilon''_{si} = \nu_b \epsilon''_b$ shows good agreement between observed and predicted value for FYI but not for MYI.

Vant et al (1978) conducted an extensive study of the dielectric behavior of sea ice in the 0.1- 40 Ghz range. Good agreement was found between the model results and the majority of the experimental observations of the dielectric behavior of sea ice.

Table 5.2: Spread of T_B 's for sea ice and open water from P4 - MSMR

Frequency (GHz) & Polarisation	Range of T_B (in K) for Open water	Spread of T_B (in K) for Open water	Range of (in K) T_B for Sea ice	Spread of T_b (in K) for Sea ice	Separation of ice from water (T_B (in K))
6 (V)	128 - 147	19	215-237	22	68
6 (H)	67 - 92	25	184 - 213	29	92
10 (V)	137 - 158	21	216 - 242	26	58
10 (H)	82 - 97	15	204 - 229	25	107
18 (V)	160 - 176	16	225 - 246	21	49
18 (H)	89 - 118	29	204 - 225	21	86
21 (V)	161 - 176	15	204 - 234	30	28
21 (H)	102 - 130	28	191 - 226	35	61

Next the data were processed to generate the histograms for all the four frequencies and two polarisations to provide 8 combinations. The histogram representing the T_B on x-axis and frequency of occurrence of that T_B in the study area on y-axis for all the eight channels are shown in the figure 5.1(A – H). The histograms are further analysed to compute the spectra of the polar oceanic surfaces, both as a function of frequency and as a function of wavelength.

The figures 5.1.1 (A), (B), (C), (D), (E), (F), (G) and (H) show the T_B distribution in the study area in the form of histograms for 6(H), 6(V), 10.65(H), 10.65(V), 18(H), 18(V), 21(H), 21(V) respectively. It can be observed that in each of them, two peaks/clusters are prominent and distinct. From this histogram analysis it is clearly seen that the peaks about the lower T_B values correspond to open water and the peaks about the higher T_B values correspond to the sea ice (as observed by Svendsen et al., 1983 and cavalieri et al., 1984). Table – 5.1 gives the features of the T_B variability, both in terms of the centre and the spread of the clusters. Svendsen et al., (1983) had also reported a similar type of separation between sea ice and open water in terms of their (water & ice) T_B values. Also the peak value of the T_B spectrum is plotted against the corresponding frequency and polarization (see fig. 5.2a). It is found that the spectra obtained from MSMR behave similarly with the spectra derived earlier by Cavalleri et al., (1984) for SMMR. Another exercise has been done for the calculation of emissivity of the ocean and sea ice surfaces. To derive approximate emissivity the temperature of the region selected above is considered to be at 0°C. The emissivity curves are shown in the fig. 5.2b. The pattern of the emissivity curves matches well with that obtained from the ground observations by Svendsen et al., (1983).

5.2.2 Comparison at brightness temperature level

MSMR onboard OCEANSAT-1 is a four frequency; eight channel dual polarised dicke switched passive microwave system, whereas SSM/I is a similar dual polarisation total power radiometer system operating at 19.35, 22.235, 37 and 85.5 GHz, with 22.235 GHz channel providing only vertical polarization information. For relative calibration of the MSMR observed brightness temperatures and the derived geophysical parameters (e.g., the sea ice extent and sea ice concentration) over the Polar Regions, the simultaneous SSM/I measurements over the Antarctic region are used.

Both MSMR and SSM/I are conically scanning multi-frequency passive microwave radiometers. However, there are several differences e.g. available frequency channels and their center frequencies, the incidence angle, the coverage swath, the maximum north and south latitude reachable and the local time of observations etc. While most of these are

minor differences as far as observing polar sea ice is concerned, these must however be kept in mind during the inter-comparison exercise. Since, 18/19 GHz channel is the most

suitable common channel between MSMR and SSM/I, in providing surface characteristics with reasonably good atmospheric transparency and with acceptably high spatial resolution, we have restricted our analysis to data from this channel. This channel is also common between the three most used passive microwave sensors for the sea ice research, viz. SMMR, SSM/I and MSMR. Moreover, for developing the algorithms for estimation of sea ice concentration, we have used T_B at 10 and 18 GHz channels of MSMR to derive the polarization and spectral gradient ratios (Gloersen et al., 1992) as independent variables. In order to inter-calibrate MSMR observed brightness temperatures with those from SSM/I, sample SSM/I data sets covering the summer and winter seasons over the Antarctic region were obtained from NASA, GSFC. The SSM/I 19.35 GHz T_B values available at 25 km resolution were first weight-averaged using a 2×2 pixel window and then re-sampled at $0.5^\circ \times 0.5^\circ$ resolution to make these observations compatible with the MSMR resolution of $50 \text{ km} \times 50 \text{ km}$ at 18 GHz. The MSMR observed T_B 's were then compared with near synchronous and co-located SSM/I T_B measurements. To study the behaviour of the T_B at the marginal ice zone, a transect along 15°W longitude and latitude ranging from 50°S to 70°S was taken for MSMR and SSM/I for 15-16 October, 1999. The T_B 's for all the MSMR channels, the T_B 's for the 19, 22, 37 GHz vertical channels of SSM/I and the T_B 's for 19, 37 GHz horizontal channels of SSM/I have been plotted against the latitude (see fig 5.3). It is found that both the sensors show similar behaviour except slight numerical difference in their T_B values (see fig 5.3). This variation is caused possibly due to the differences in their look angles and in their central frequencies.

Fig 5.4(a) shows a scatter diagram of MSMR T_B 's vs. SSM/I T_B 's for 18 H channels for the periods Oct. 15-16, 1999 and Feb. 15-16, 2000. The comparison is carried out for a small region ($68^\circ \text{S} - 76^\circ \text{S}$ & $35^\circ \text{W} - 60^\circ \text{W}$) in the Weddell Sea where one expects the ocean to be covered with sea ice, at least partially, in both the seasons. Fig 5.4(a) shows a histogram of T_B values over the southern polar ocean (South of 50°S) for Oct. 15-16, 1999 as observed from MSMR and SSM/I.

It is clear from the figure that there is a large scatter (see fig 5.4a) and there exists small biases due to the differences in the center frequency and in the incidence angle of the two sensors (Ulaby et al., 1982). The scatter partly results from the difference in the sensitivity of MSMR at 18 GHz and that of SSM/I at 19.35 GHz channel to the atmospheric contribution. Difference also arises due to slightly different surface emissivities at the two frequencies. Nevertheless the scatter clearly delineates the clusters related to open water and sea ice with varying degree of concentration. The presence of outliers can be attributed to the varying amounts of atmospheric WV and cloudiness between the sampling times of the two sensors, as their equatorial crossing time for SSM/I is 06:15 hrs local time corresponding to 12:00 hrs for MSMR at their ascending nodes. The histogram of the T_B 's (fig. 5.4b) from SSM/I and MSMR also shows a striking resemblance confirming the reliability of the MSMR data.

In addition to the pixel-level comparisons, we also generated T_B images over the Antarctic region from SSM/I data, after bringing down the resolution to 50 kms, for comparison with corresponding MSMR images. Fig 5.6 shows a comparison of the corresponding 18GHz (H) and 19GHz (H) T_B images that brings out the clear spatial correspondence between various sea ice and continental ice features. The correspondence is remarkably good for MSMR images obtained during two different seasons. This gives us a confidence in the use of MSMR data to study the variability of sea ice characteristics at inter- and intra-annual time scales.

5.3 DEVELOPMENT OF SEA ICE CONCENTRATION (SIC) ALGORITHM FROM MSMR DATA

In this section we describe the algorithm development for derivation of sea ice concentration (SIC) (percentage of sea ice cover in each pixel) using MSMR data. Here the SIC has been derived in two different ways. In the first method T_B values are directly used for the calculation of SIC. In the second method an attempt is made to calculate the SIC using normalized values of brightness temperatures. The SIC derived from the MSMR for a different period were then compared with the SIC obtained from SSM/I for validation purposes.

5.3.1 Development of SIC algorithm based on MSMR T_B 's

In this method the observed MSMR T_B 's are related to SIC using coefficients derived from the SSM/I sea ice concentration data, expressed in percentages. The SSM/I SIC has been derived from the T_B using the NASA Team algorithm (Comiso et al., 1997). SSM/I sea ice concentration data has been obtained from National Snow and Ice Data Centre (NSIDC), Bolder, Colorado. A multiple linear regression technique is applied to determine the coefficients that relate the observed MSMR T_B 's with the SSM/I SIC values. These coefficients are then validated for different regions and periods of observation to establish a regression model to project sea ice concentrations based on MSMR observations. The SIC values from SSM/I more or less serve as "truth" data, although not "ground truth" in the strict sense of the word. MSMR T_B 's over a few selected regions (described in table 5.2 (from Sl. No. 1 to 5)) all around the Antarctic continent are selected in the southern ocean so as to include maximum possible regional variability in the regression model. To take care of the seasonal variability in the model, the MSMR data for two distinct periods (15 August to 15 October 1999 corresponding to the peak in the ice extent and 15 January to 15 March 2000 corresponding to the minimum of the ice extent) are considered for the analysis.

They are selected so as to represent all the sectors in the Antarctic Ocean. 21 GHz channel is not used, because it gets affected by the presence of water vapour in the atmosphere. Instead, the 10 GHz channel is used in its place. The form of the regression model is given by equation (5.2).

$$\text{SIC} = a + b * T_{B(10V)} + c * T_{B(10H)} + d * T_{B(18V)} + e * T_{B(18H)} \quad 5.12$$

⊕

where, a, b, c, d and e are the derived coefficients

The values of the coefficients are found to be :

$$a = - 84.124$$

$$b = 0.53148$$

$$c = 0.424172$$

$$d = -0.193778$$

$$e = -0.043911.$$

Table 5.3: Regions selected for the development of SIC algorithm through multiple regression between MSMR T_B 's and SSM/I Sea ice concentration

Sl. No.	Regions	Latitude Range	Longitude Range
1	Weddell Sea	55°S – 75°S	30°W – 45°W
2	Indian Ocean	55°S – 65°S	30°E – 50°E
3	Pacific Ocean	55°S – 64°S	90°E – 100°E
4	Ross Sea	58°S – 70°S	150°W – 180°W
5	Bellingshausen and Amundsen Sea	60°S – 70°S	90°W – 120°W
6	Test area	55°S - 70°S	90°W - 135°W

In the above, we have used MSMR T_B 's from 10 and 18 GHz channels with horizontal and vertical polarizations. While 10 GHz channel has a better transparency to the atmosphere, it has a poorer spatial resolution of 75 km compared to 50 km of the 18 GHz channel. All relevant MSMR and SSM/I data were therefore brought to 75 km resolution before attempting the regression analysis. The model performance was validated against known sea ice concentrations in different regions and the error was found to be less than 7%.

Using the above regression model, we have generated SIC images over the entire Southern Ocean for two representative months of Sept. 1999 and Jan. 2000. It is found that the sea ice concentration calculated using the above algorithm is underestimating the SIC with that of SSM/I derived values by 10% at (higher concentration level) (see fig 5.5a) and overestimates by about the same value at (lower concentration levels). Fig 5.7 shows qualitative comparison between MSMR derived SIC and that obtained from SSM/I. To get the quantitative information about the accuracy of derived SIC, the SIC from test area (55°S to 70°S and 90°W to 135°W) is extracted from the above for two months period (September 1999 and January 2000) and then compared with the SIC

values obtained from SSM/I for the same region. Fig. 5.5 (a) shows a scatter plot between SIC derived from MSMR and the SSM/I observed SIC. It shows MSMR derived SIC has 97.84% correlation with that from SSM/I data (slope and intercept for the best fit line are 0.995 and 1.44 respectively). It can be seen clearly that MSMR derived SIC images faithfully portray all the features (qualitatively and quantitatively) observed in SSM/I images (see fig 5.7).

5.3.2 Development of SIC algorithm from MSMR Polarization and Spectral Gradient Ratios

In order to reduce the effect of additive and multiplicative errors in MSMR T_B 's, we have also followed a different approach of using the polarization (PR) and gradient (GR) ratios, defined below, following (Gloersen et al., 1992):

$$PR_f = \frac{T_{Bf}(V) - T_{Bf}(H)}{T_{Bf}(V) + T_{Bf}(H)} \quad (5.13)$$

where, f - the frequency, T_B - Brightness temperature
 V & H - Vertical and Horizontal polarization

$$GR(p) = \frac{T_B(18(p)) - T_B(10(p))}{T_B(18(p)) + T_B(10(p))} \quad (5.14)$$

where p - the polarization (Vertical or Horizontal)

Use of PR and GR also eliminates the effect of differences between center frequency of the 18/19 GHz channels of MSMR and SSM/I. Spatial averaging effect due to 25 km resolution of SSM/I vs. the 50 and 75 km resolutions of 18 and 10 GHz channels of MSMR would of course, affect the derived SIC estimates somewhat.

For estimating the PR and GR, we have once again made use of the 10 and 18 GHz channels of MSMR. The PR and GR estimates derived from MSMR data were regressed against the near-synchronous and coincident SSM/I SIC values. This regression was carried out over the areas mentioned above. The multiple regression equation is as stated below:

$$SIC = a_1 + b_1 * PR (10 \text{ GHz}) + c_1 * PR (18 \text{ GHz}) + d_1 * GR (H) + e_1 * GR (V) \quad (5.15)$$

where a_1 , b_1 , c_1 , d_1 and e_1 are the derived coefficients

The values of the coefficients are found to be

$$a_1 = 101.6459$$

$$b_1 = -14691.9$$

$$c_1 = 14297.2$$

$$d_1 = 13958.7$$

$$e_1 = -14216.3.$$

The above model has an inbuilt rms error of 7.57 % (sea ice cover within a resolution cell). The accuracy of SIC does not increase by use of PR-GR method, perhaps because of the spatial averaging effect to bring down to SSM/I resolution of 25 km to the MSMR resolutions of 75 km.

Based on the above PR & GR based algorithm, we have generated SIC images using MSMR data for the two seasons (Sept. 1999 and Jan. 2000). It is found that the sea ice concentration calculated using the above algorithm is underestimating the SIC with that of SSM/I derived values by 10% at the higher side and over estimates by the same amount at the lower side. The results are shown in Fig 5.8 along with the corresponding SIC images generated using SSM/I data. These images depicting the SIC over the Southern Ocean surrounding the Antarctica from the two sensors viz.

MSMR and SSM/I show very good feature-by-feature spatial correspondence in all the sectors. To assess the quality of the derived SIC, the SIC for the test area (55°S to 70°S and 90°W to 135°W) is extracted from the above two months processed data set, and compared with that derived from SSM/I for the same region. A scatter plot between SIC derived from MSMR and the SSM/I observed SIC. It shows MSMR derived SIC has 97.4% correlation with a bias of 1.90 with that of SSM/I data. It is observed that MSMR derived SIC values in the region of thick, multi-year ice in the Weddell Sea and Ross Sea Sectors are relatively lower. This could be attributed to the use of 10 GHz in case of MSMR as against 37 GHz used in SSM/I. Fig 5.9 shows Sea Ice Extent MSMR vs. SSM/I data for the Southern Polar Ocean (June 1999 – December 2000)

As more and more sophisticated PMRs are being launched, internationally there are ongoing efforts to improve the calibration procedures (Bhandari et al., 2000 and 2005, Desnos, 2002). The inter-comparison between MSMR and SSM/I data at the brightness

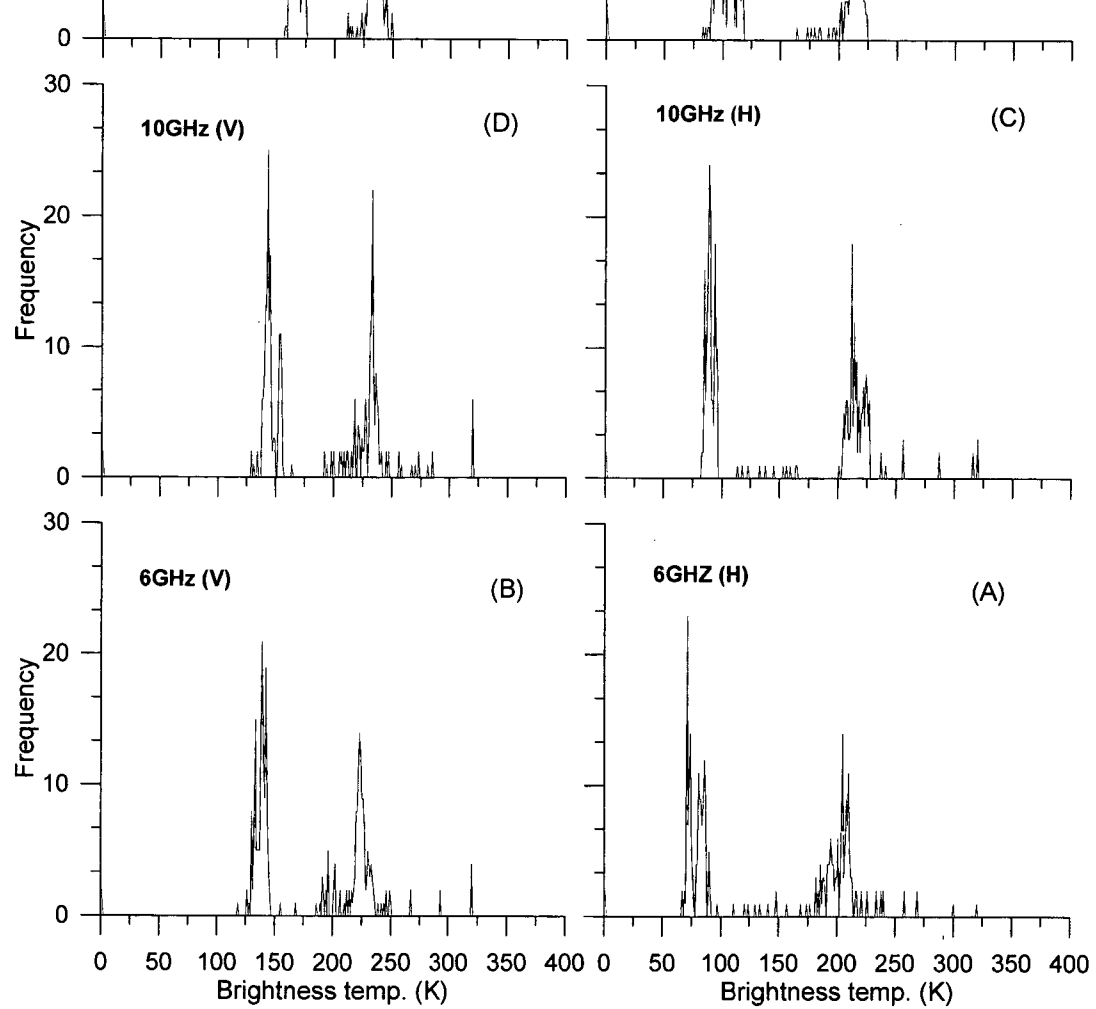


Fig. 5.1 (A-F): Frequency distribution of sea ice and open water- 90°W - 92° W (June 10-11, 1999)

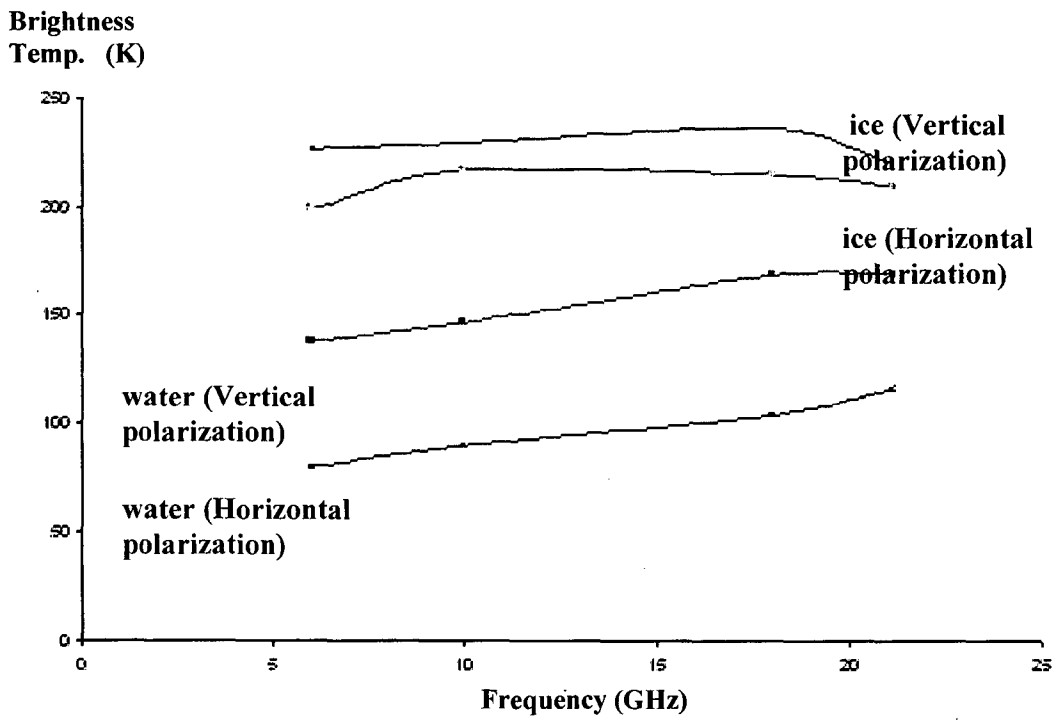


Fig 5.2 (a): Spectra of polar oceanic surfaces over the MSMR frequencies

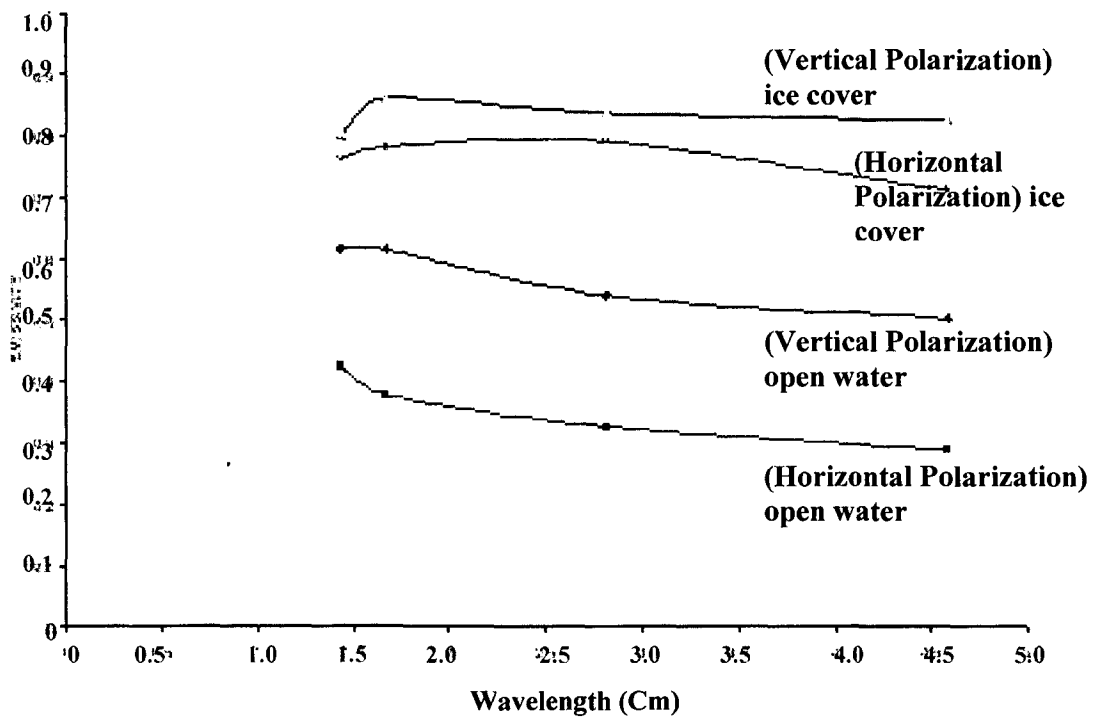


Fig 5.2 (b): Emissivity of polar oceanic surfaces over the MSMR wavelengths

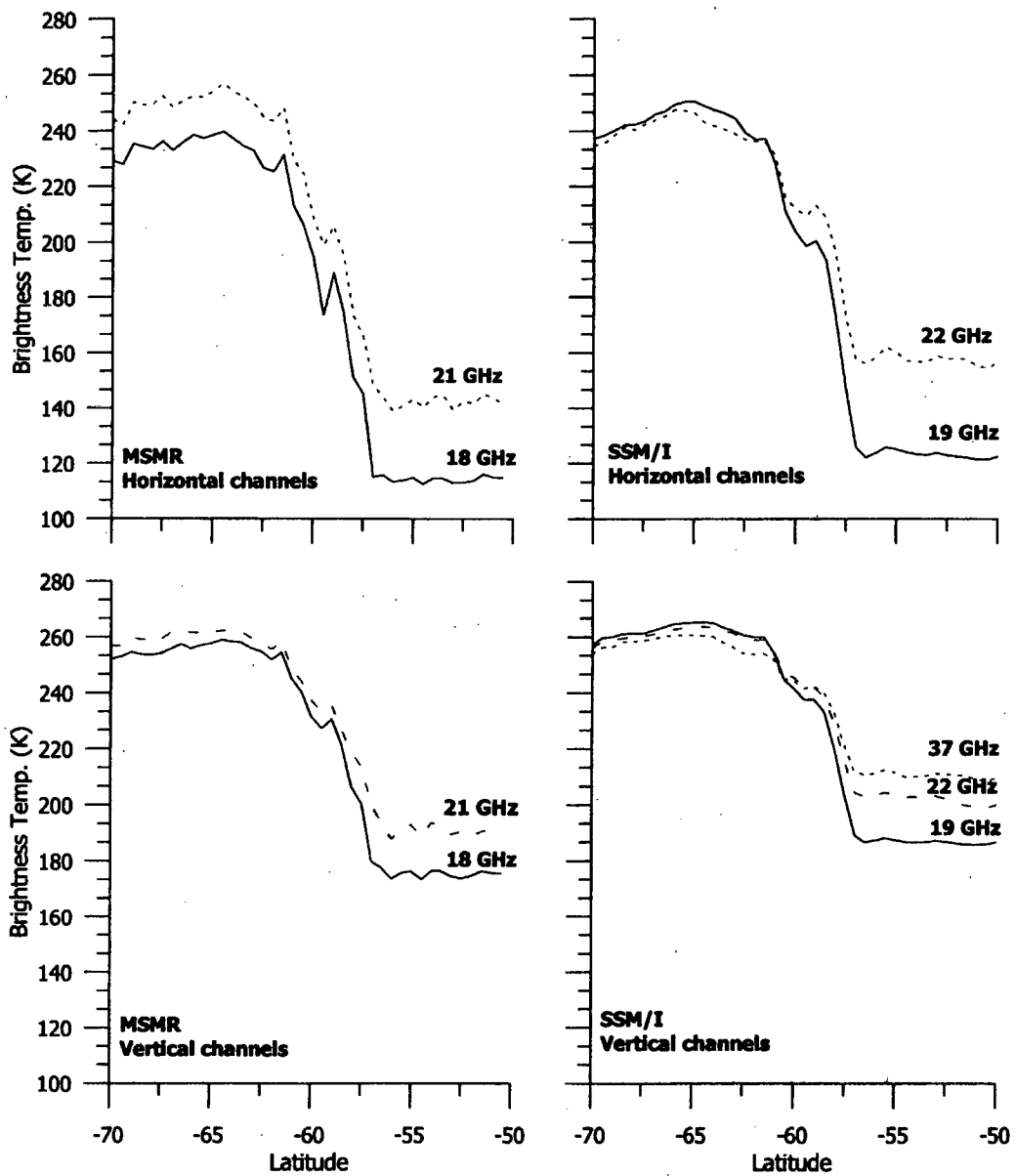
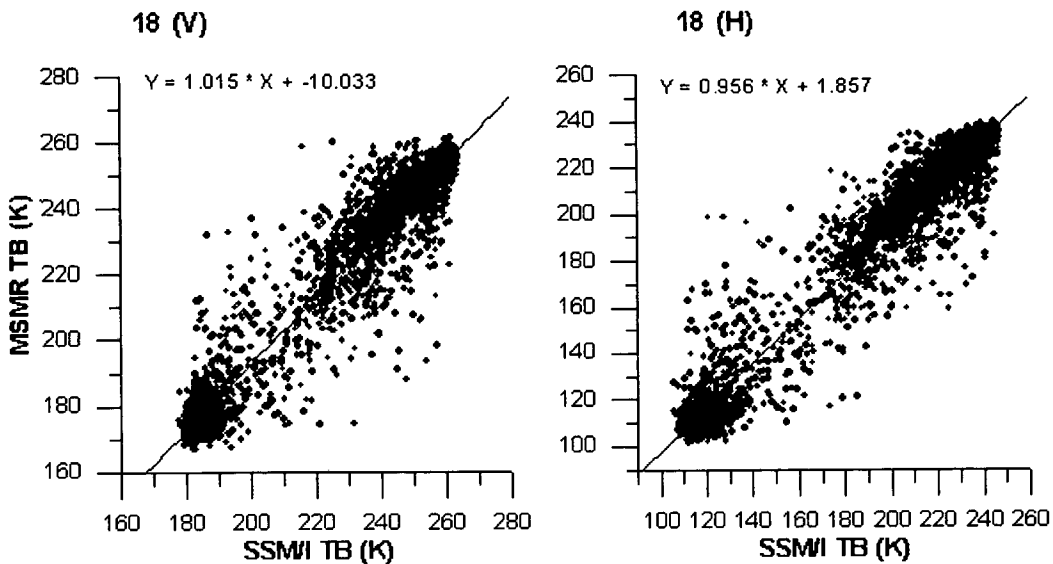
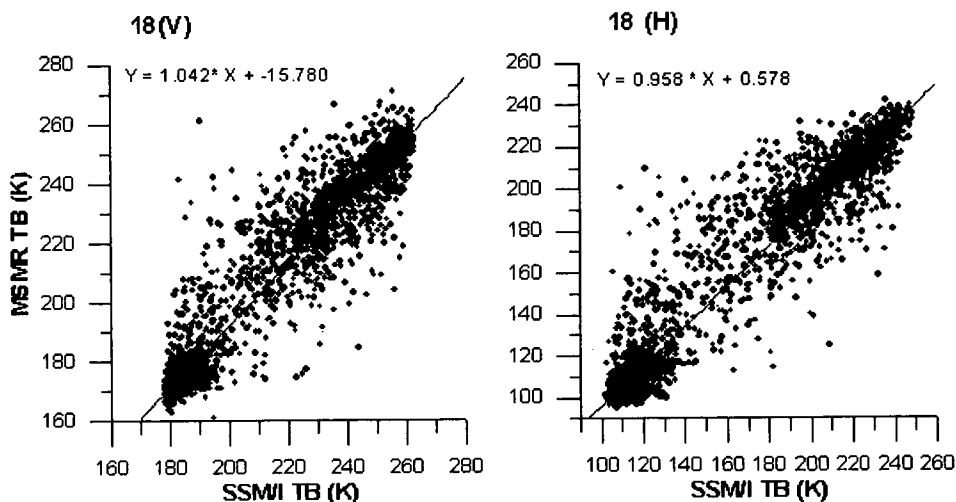


Fig 5.3 : Variation of T_B along a transect along 15° west longitude (Dash, 2003)



Fig

5.4(a): Scatter plot of MSMR (18GHz) vs SSM/I (19.35 GHz) T_B for Vertical and horizontal polarization for October 15-16, 1999



(b)

Fig 5.4(b): Scatter plot of MSMR (18GHz) vs SSM/I (19.35 GHz) T_B for Vertical and horizontal polarization for February 15-16, 2000

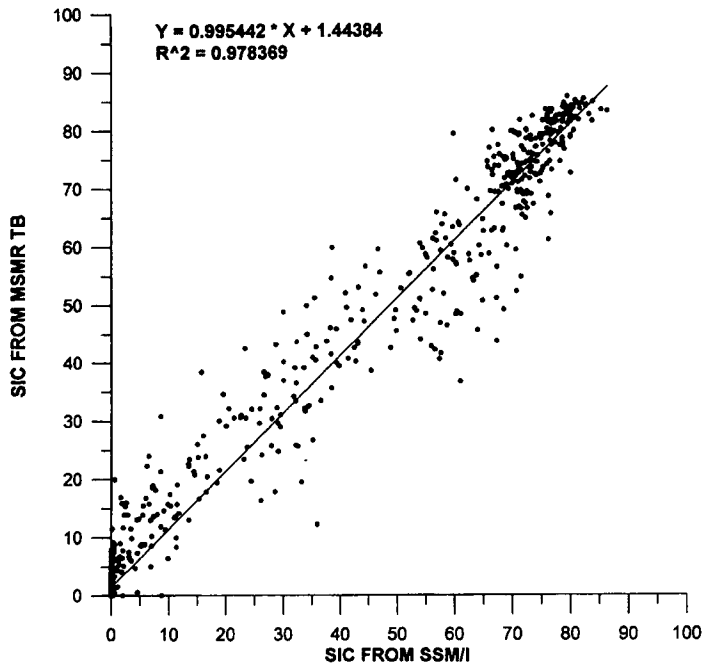


Fig. 5.5 (a) : Scatter plot between sea ice concentration (in%) derived from MSMR using T_B (on Y axis) and SSM/I sea ice concentration (on X-axis)

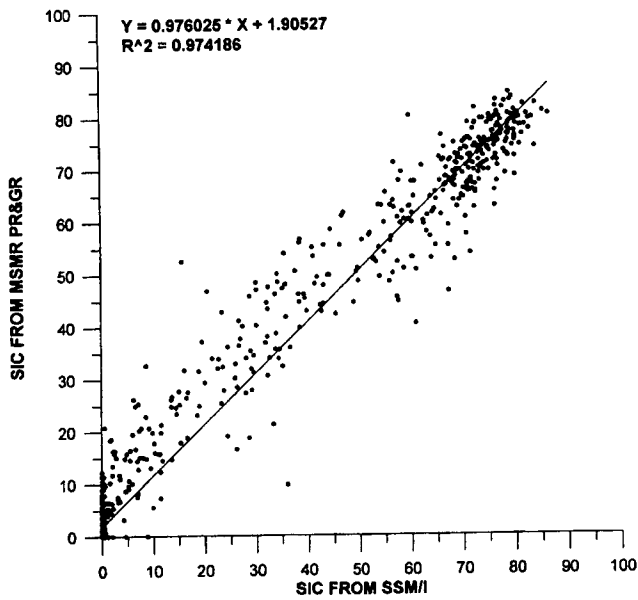
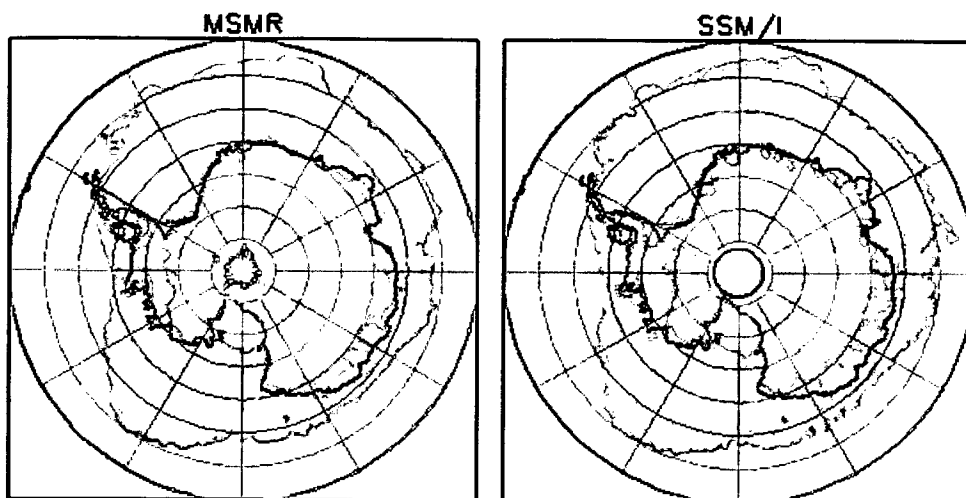


Fig. 5.5 (b) : Scatter plot between sea ice concentration (in%) derived from MSMR using PR & GR (on Y axis) and SSM/I sea ice concentration (on X-axis).

15-16 OCTOBER, 1999



15-16 FEBRUARY, 2000

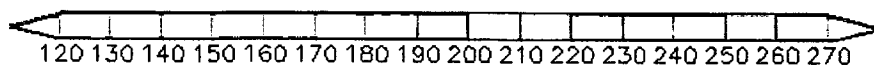
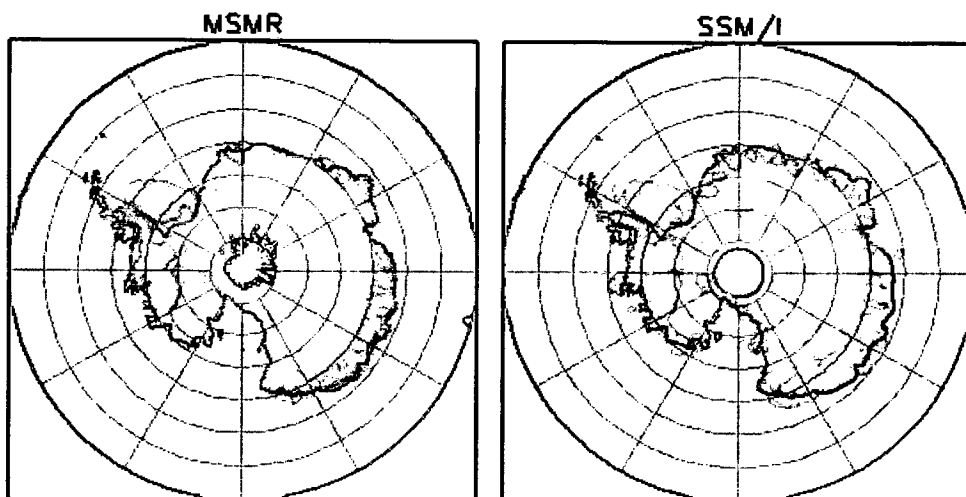
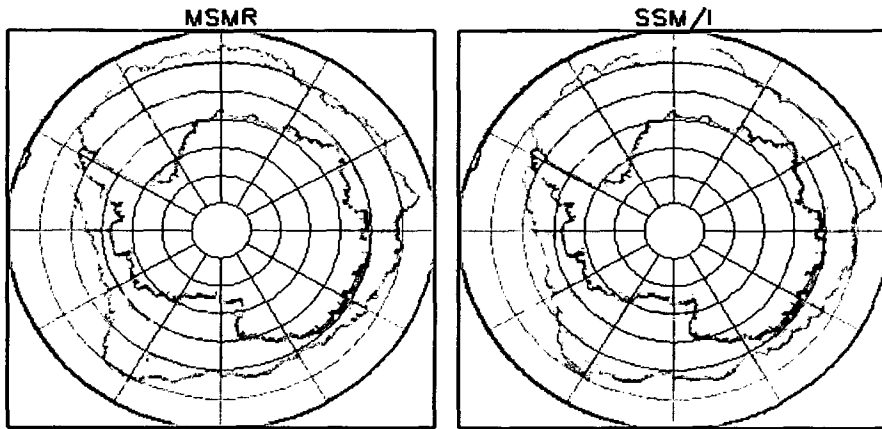


Fig 5.6: TB images over the Antarctic region from simultaneous MSMR (18H GHz) and SSM/I (19.35H GHz) channel

SEPTEMBER, 1999



JANUARY, 2000

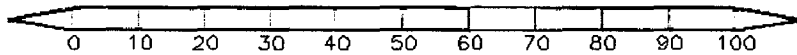
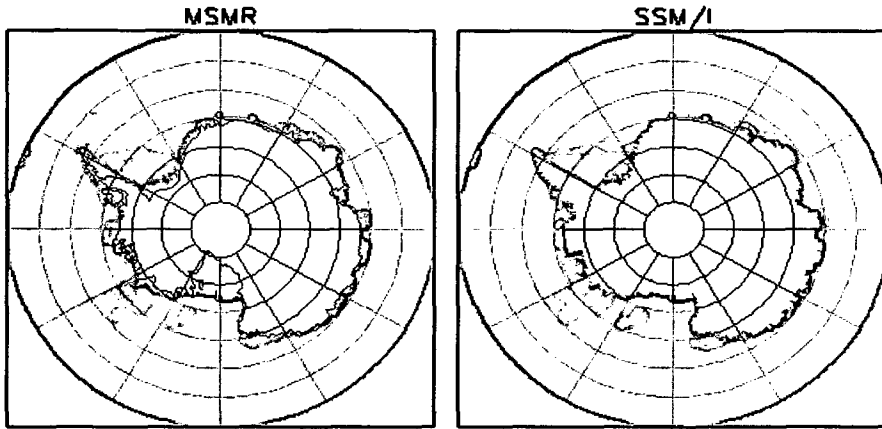
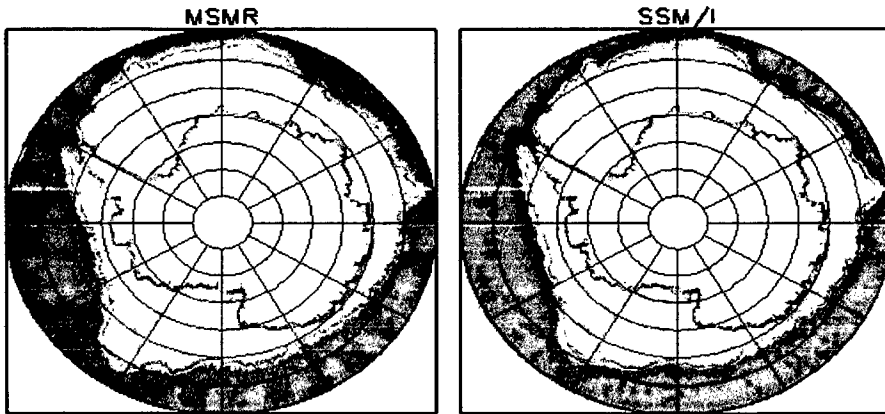


Fig 5.7: Comparison between monthly average Sea ice extent derived from MSMR Tb based algorithms and SSM/I for Sept. 1999 and Jan. 2000

SEPTEMBER, 1999



JANUARY, 2000

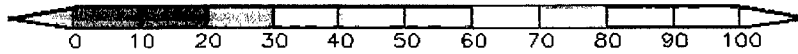
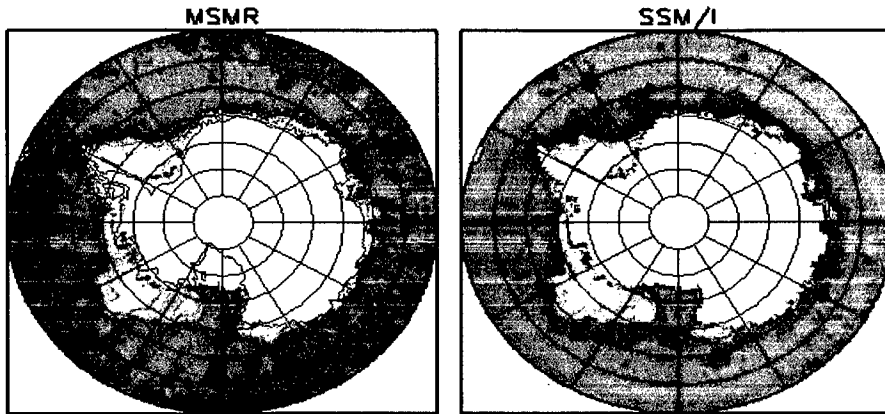


Fig 5.8: Comparison between monthly average Sea ice extent derived from MSMR PR & GR based algorithms and SSM/I for Sept. 1999 and Jan. 2000

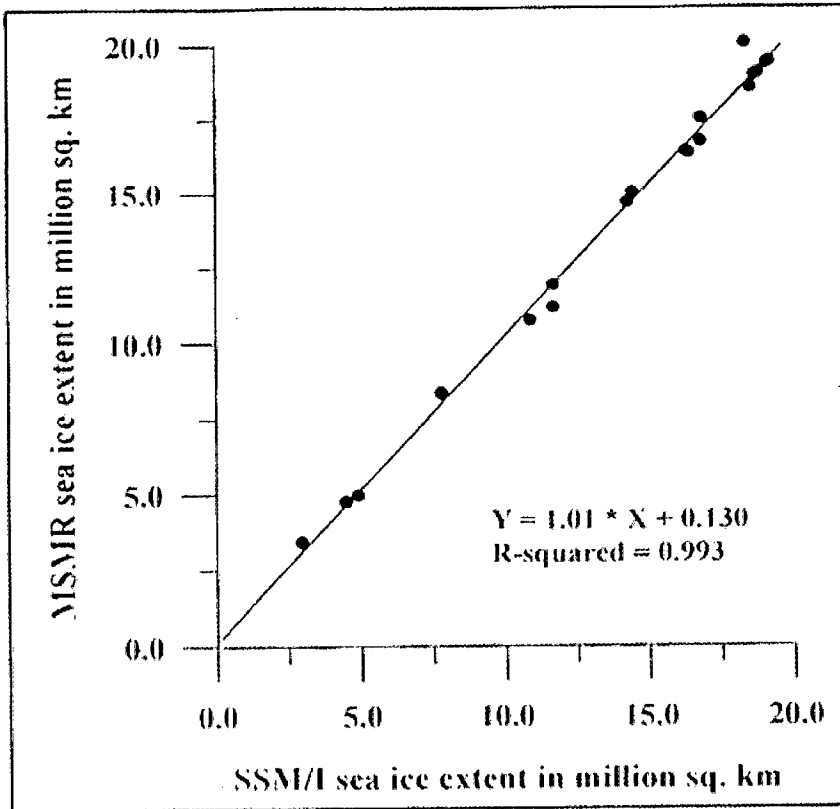


Fig 5.9: Sea Ice Extent MSMR vs. SSM/I data for the Southern Polar Ocean (June1999 – December 2000)

CHAPTER -6

SEA ICE COVER OVER THE SOUTHERN POLAR OCEAN (SPO)

6.1 INTRODUCTION

Antarctica, the frozen continent comprises of an area about $14 \times 10^6 \text{ km}^2$ and lies south of 60°S . The Antarctic ice sheet consists of three distinct morphological zones, the East-Antarctic (or the greater Antarctic), the West-Antarctic (or the lesser Antarctic) and the Antarctic Peninsula. It is surrounded by three major oceans of the world, the Indian Ocean, the Pacific Ocean and the Atlantic Ocean.

Several countries of the world have established their research stations in Antarctica. In 1981, India started her systematic and regular Antarctic research program by sending annual scientific expeditions. It established its first permanent base, named “Dakshin Gangotri” in 1983 and later on started another research station Maitri ($70^\circ 45' \text{ S}$, $11^\circ 45' \text{ E}$) (see fig 6.1). Since 1989 – 1990, multi-disciplinary research teams conduct round the year observations of geological, geophysical, biological and upper atmospheric processes from the new research station Maitri.

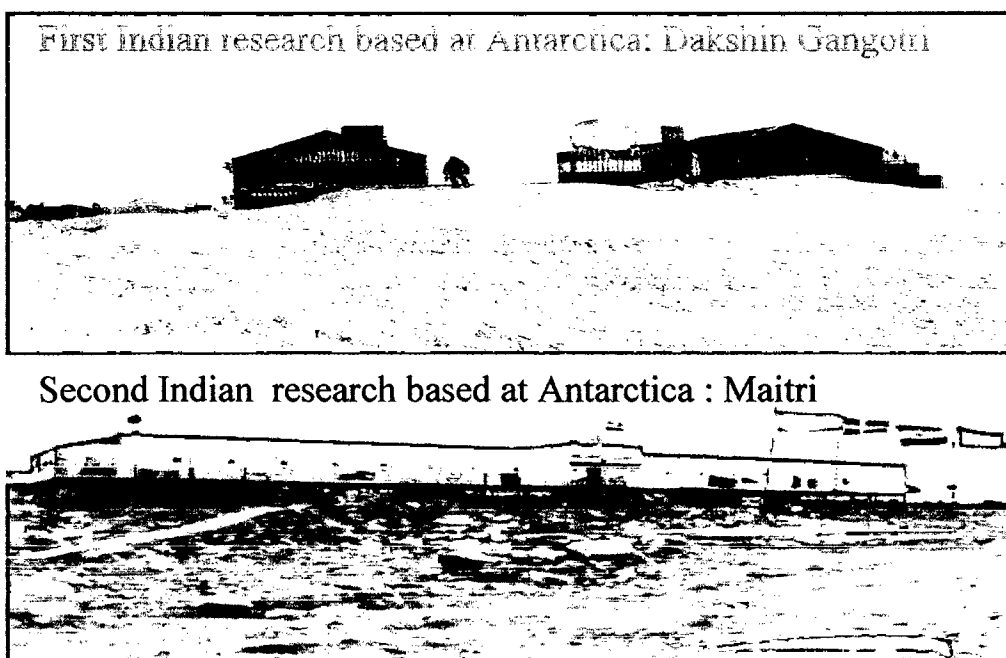


Fig 6.1: Indian Research base in Antarctica

The distribution of the sea ice around the Antarctic continent influenced by atmospheric & oceanic circulation and temperature in the South Pole (Zwally et. al, 1983). The large-scale circulation of the southern ocean is dominated by eastward flowing Antarctic circumpolar current (Frandy and Pillsbury, 1979). The Antarctic convergence, an oceanic

polar front characterized by large meridional gradients of temp., salinity and density, nominally lies between 50°S and 65°S. Near the APF, Ocean temperature s approach 6°C in summer and 4°C in winter (Gordon and Molinelli, 1982). Freezing of the ocean Surface during winter results in the formation of cold, highly saline sea water. The continual production of the ice in coastal polynyas, and its northward transport from the continental shelves, is an important mechanism for producing dense sea water (Zwally et. al 1985, C&M 1985). This dense water flows off the shelves between 70°-75°S, mixes with circumpolar deep water, and sinks to the bottom as Antarctic bottom water.(Gordon, 1974). In winter, sea ice extends as far as 2,200 km from the Antarctic continent, covering approximately $19 \times 10^6 \text{ km}^2$ of the Southern ocean. Antarctic sea ice cover, surrounded by Open Ocean and acted on by circumpolar winds, is generally more divergent then much of the Arctic sea ice cover.

In summer, the sea ice retreats to the coast along approximately 50% of the Antarctic coastline. The largest areas of summer sea ice cover the eastern Ross Sea, much of Bellingshausen & Amundsen seas and the western Weddell Sea.

The seasonal cycle of southern ocean sea ice is characterized by a minimum in the sea ice cover during February. This is followed by the expansion of the sea ice cover until it reaches maximum coverage during September and then rapidly decays from November to February.

6.2 DEFINING THE SECTORS IN THE SOUTHERN POLAR OCEAN

Southern Polar Ocean (SPO) has divided into five sectors for the study of sea ice by earlier investigators (Gloersen et al. 1992), (see table 6.1 and fig 6.2).

Table: 6.1: Sector location of the different sectors of Southern Polar Ocean

Sector	Longitudinal extent
Weddell Sea Sector	60°West - 20°East
Indian Ocean Sector	20°East - 90°East
Pacific Ocean Sector	90°East - 160°East
Ross Sea Sector	160°East - 130°West
Bellingshausen and Amundsen Sea Sectors	130°West - 60°West
Total	180 West – 180 East

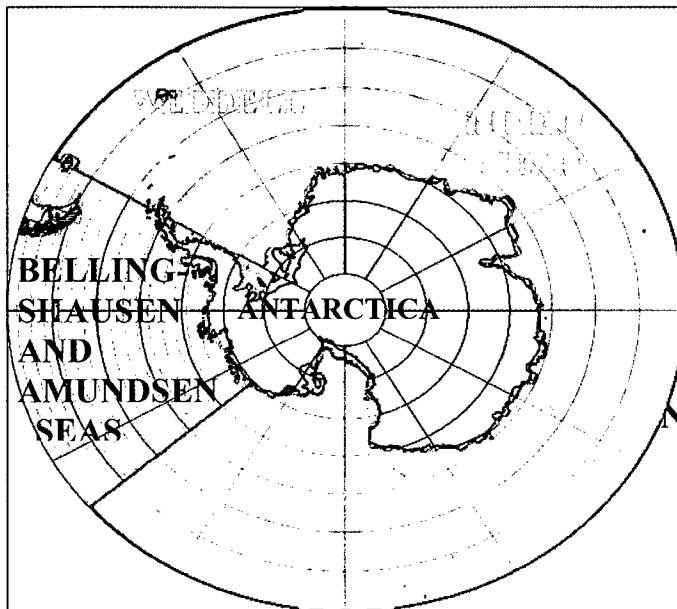


Fig 6.2: Base map of the different sector of the study area of Southern Polar Ocean

6.3 METHODOLOGY

Remote sensing of sea ice is most suited for the determination of parameters like the sea ice extent and the sea ice concentration. **Sea ice extent** refers to the area covered by sea ice from the continental boundary to the ice edge in the open ocean. However, ice-edge is not a perfect edge and lies in the marginal ice zone containing low concentration of ice interspersed with larger expanses of water. **Ice concentration** refers to the fractional ice-

cover lying within one resolution cell of the sensor. It is frequently defined in terms of percentage.

The wintertime sea ice boundaries in the Antarctic expand to 55° S and beyond. Therefore the lower boundary in the study region is kept at 50° S.

6.3.1 Channel Selection

The data from 18 GHz (H) channel of the MSMR payload onboard IRS -P4 have been used for this study. This data has the specifications (ISRO, 1999) as described in table 3.1.

The 18 GHz (H) channel is chosen because of

- a. Higher spatial resolution of 50 km. compared to 6 and 10 GHz channels.
- b. Lesser influence of water vapor compared to 21 GHz channels.
- c. Better distinction of sea ice features compared to 18 GHz (V).

6.3.2 Methodology to Process the Data

The data is available in binary format and is combined for all the 14.5 pass that occur on a given day. Each data point represents an average brightness temperature over an area of about 50-km x 50 km. However, this does not correspond to any standard geographic grid.

Software has been developed for gridding the data into a 0.5 ° x 0.5° latitude-longitude grid. Several data gaps are observed on displaying the gridded data through Image Display Software. The data is also likely to have a certain amount of noise. The methodology to process the data is outlined below.

1. At first the data in the binary form is converted into the brightness temperatures (T_B) in decimal form for the entire study area.

2. Then the data is mapped on to a $0.5^\circ \times 0.5^\circ$ latitude-longitude grid. For multiple occurrences of data points in a single grid cell the average value of the T_B is computed and assigned to that cell.
3. Then the data gaps are filled using a linear interpolation scheme in both the meridional and the zonal directions.
4. Next, to reduce the noise, averaging of the brightness temperatures for each grid cell is carried out over 4 repeat cycles of two days each.
5. The data are then mapped on to the polar stereographic projection.
6. This data is then displayed in image form using GRADS Software.
7. From GRADS display (see point 5 above), ice and water regions are examined and transects (straight lines across the water - ice boundary) are selected and graphs of T_B are plotted along this line.
8. The boundary between ice and water is derived through inspection of steep slope regions on the graphs obtained under point 6 above. This boundary (for 18 GHz horizontal polarization) is then used later on for distinguishing between ice and water. The optimal boundary between sea ice and open water is found to be at $T_B = 130$ K using this procedure.
9. The value as found above is then validated through the discriminant function analysis. The classification procedure used between the sea ice and the open water involved the supervised technique where previously known areas of open water and sea ice were taken and separate clusters of brightness temperatures were formed. The analysis was extended to include different seasons of the year. The optimal boundary (the discriminant function) between the two classes is found to be at $T_B = 130$ K, thus validating the value obtained under point no. 7 above.
10. As soon as a grid cell is identified as sea-ice, its area is computed for each grid cell and added to the calculation of total area.

The annual average is taken from October of the previous year to the September of the current year. This is because, the peak of ice cover occurs in the month of September, and the next cycle of the decay and the growth of the ice starts from October and goes up to September next. We have kept the same cycle under consideration for our analysis.

6.3.3 Details of Processing:

Brightness Temperature (T_B) maps over Southern Polar Ocean (SPO) is prepared from MSMR 18 GHz (H) observations for the period June 1999 - September 2001. These maps represent the average T_B for data collected between the 15th and the 22nd day (both days inclusive) of each calendar month. However, in the cases where problems of data non-availability existed, the dates have been slightly adjusted to keep the observation period constant as 8 days for the averaging process. The optimal boundary between sea ice and open water is found to be at $T_B = 130$ K (for 18 GHz (H)) through the steepest slope method and the discriminant function analyses as described at points. For the purpose of the analysis, the boundary of sea ice and open ocean region is considered to be lying at 15 % concentration level of sea ice in the marginal ice zone. The error in determining the area lying within the sea ice boundary is estimated to be within ± 8 %. The Maps have been generated for the MSMR operational period (June 1999 to Sept. 2001).

6.4 SEASONAL VARIATION (INTER-ANNUAL) OF SEA ICE EXTENT

In the Southern Polar Ocean, surrounding the Antarctic continent, the open water and the sea ice boundary can be clearly seen on the brightness temperature maps. Open water has the lowest T_B values due to its low emissivity. The T_B values less than 130 K in 18 GHz (H) channel are found to represent open water. Over regions known to be covered with sea ice, which has very high emissivity ranging from 0.5 – 0.9, different sea ice concentrations (i.e. the fractional sea ice cover within a resolution cell) show different T_B values that represent various levels of sea ice concentration.

It is also apparent that the build up and decay of sea ice cover lags in time with respect to the months of peak winter and summer. For example, the ice coverage is larger in **September / October** than in June, and less in February than in December. Most of the area of the southern ocean northward of 55° S is seen to be free of ice throughout the year.

During the MSMR observation period, the sea ice coverage is seen to have a minimum extent of 3.42 million km² in February 2000 and a maximum extent of nearly 20.07 million km² in **September / October** 2001. This compares reasonably well with the typical long-term average values reported in the literature (Comiso, 2000).

Intra-annual variation of the sea ice extent in different sectors of the Southern Polar Ocean are shown in figures for total SPO, Weddell Sea, Ross Sea, Indian Ocean, Pacific Ocean and the Bellingshausen sea sectors (Vyas et al 2003). It can be noted that the seasonal trend derived from MSMR is in good agreement with those derived earlier from SMMR (Gloersen et al., 1992).

6.5 SECULAR TRENDS OF SIE (INTRA-ANNUAL: COMBINATION WITH SMMR AND SSM/I RESULTS)

In figures 6.7-6.12, the MSMR derived sea ice extent estimates for 1999-2000 and 2000-2001 are presented in relation to SMMR and SSM/I derived values for the period 1978-2000. The data are fitted as two separate least squares lines, one considering only the SMMR and SSM/I values and the other after combining SMMR and SSM/I values with the MSMR estimate. The resulting trends are discussed below for different sectors of the Southern Ocean as defined earlier in **fig. 6.1 and Table 6.1**. With the exception of Weddell Sea, most other areas show positive trend of a few percent per decade in sea ice extent. This is noteworthy.

6.5.1 Weddell Sea Sector

The Weddell Sea sector lies between the longitudes 60° West to 20° East (see fig. 6.1). South Scotia and the Northern Weddell Oceanic Ridges serve as the northern boundary of the Weddell Sea. Its southern most portions is bounded by the Antarctic continent, the

western boundary is defined by the Antarctic Peninsula and at the eastern end, lies the West Indian ridges.

The Weddell Sea is identified as the major source of Antarctic bottom water. The bottom water formation process is greatly influenced by the large variability of the ice production in the region (Gordon, 1982). It is interesting to note that the winter of 1980, when the ice extent and area are the greatest, is followed by summer with the least ice extent in area. The sequence is suggesting of greater retention of oceanic heat during the winter, which may enhance the melting of summer (Fletcher, 1969). A number of studies of sea ice characteristics have shown the Weddell Sea to be a very dynamic region. The western part of the Weddell Sea remains ice covered during the entire year and most of the ice here is multi-year ice. The eastern Weddell Sea undergoes strong seasonal variability and is known to support formation of large Polynyas – regions of open water surrounded by sea ice. ESMR observations revealed the presence of such polynyas during the winters of 1974, 1975 and 1976. No polynyas were observed to occur during the SMMR period of observations. Weddell Sea is also known to be influenced by the ENSO phenomena and shows warmer and cooler temperature anomalies in an aperiodic manner (King and Turner, 1997; Comiso, 2000). Weddell Sea has also been identified as a major source of Antarctic bottom water and a region of deep vertical mixing (Gloersen et al., 1992).

During the 28-month period of MSMR observations, no significant polynya formation was observed in the Weddell Sea during the peak of winter. However, polynya like formations has been observed in the middle of the thick and dense sea cover during spring, which gradually expand and ultimately merge into open ocean at a later stage. This has been discussed later. Four different seasons images as observed by Oceansat-1 MSMR from June 1999- September 2001, are shown in fig 6.3 and SIE fig 6.4. The annual average sea ice extent over the Weddell Sea sector was estimated to be 4.2 million km² (see fig 6.5 (a) & (b)). This is compared with the SMMR and SSM/I estimates combined together for the years 1978-2000 in fig. 6.6(a, b). The figure (a) on the shows the trend obtained using only the SMMR and the SSM/I data. However, the MSMR data points are shown with error bars for comparison. The decreasing trend of the sea ice can be seen in this figure. The figure (b) on the shows the trend obtained using the SMMR, the SSM/I and the MSMR data together. Here, a trend reversal from positive to negative can be noticed. The variability of the MSMR estimate is approximately same as that of

SMMR and SSM/I. Inclusion of the MSMR estimate in deriving the secular trend results in a decrease of sea ice extent at a rate of -1.1% per decade.

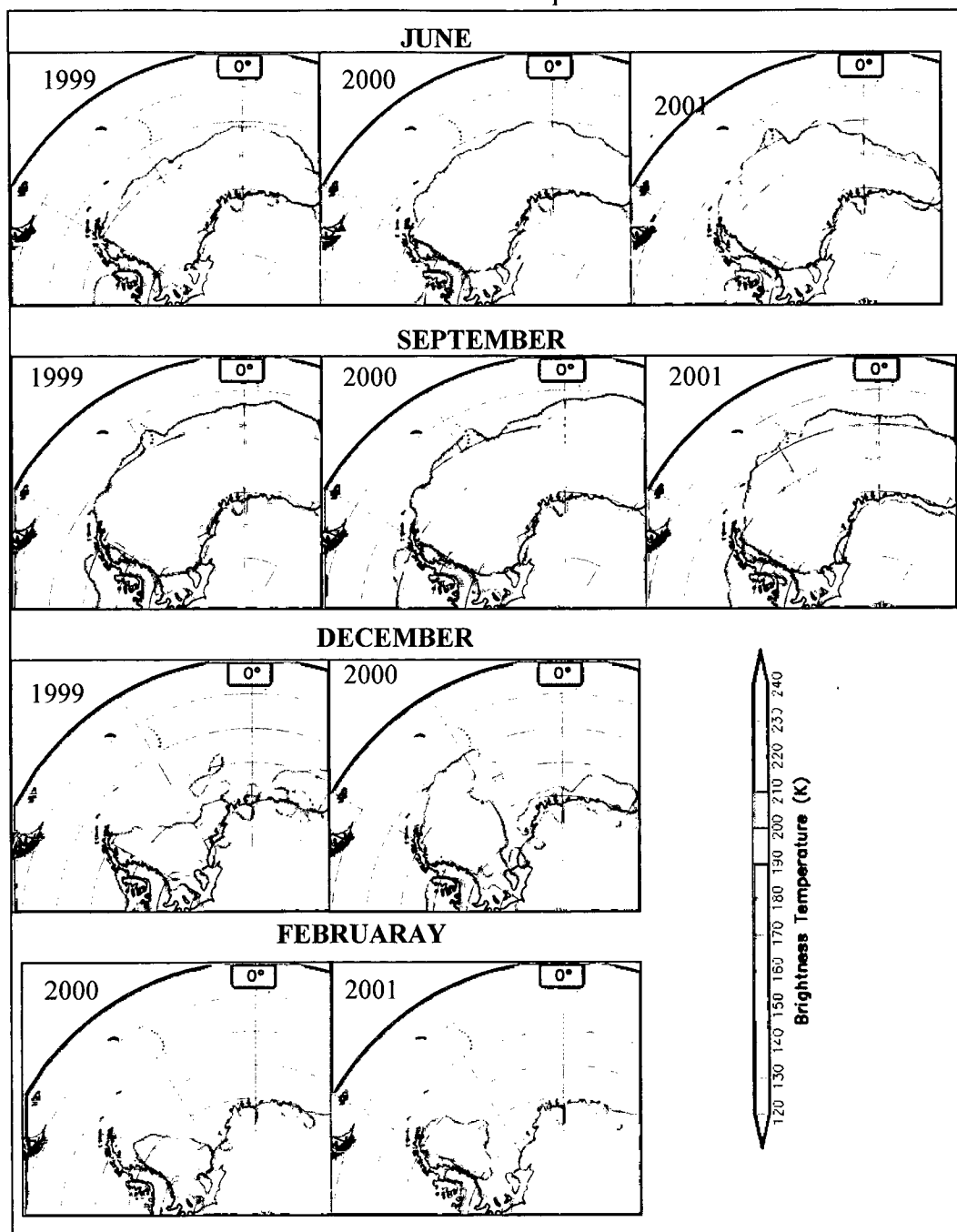


Fig 6.3: MSMR T_B images of different seasons in Weddell Sea Sector

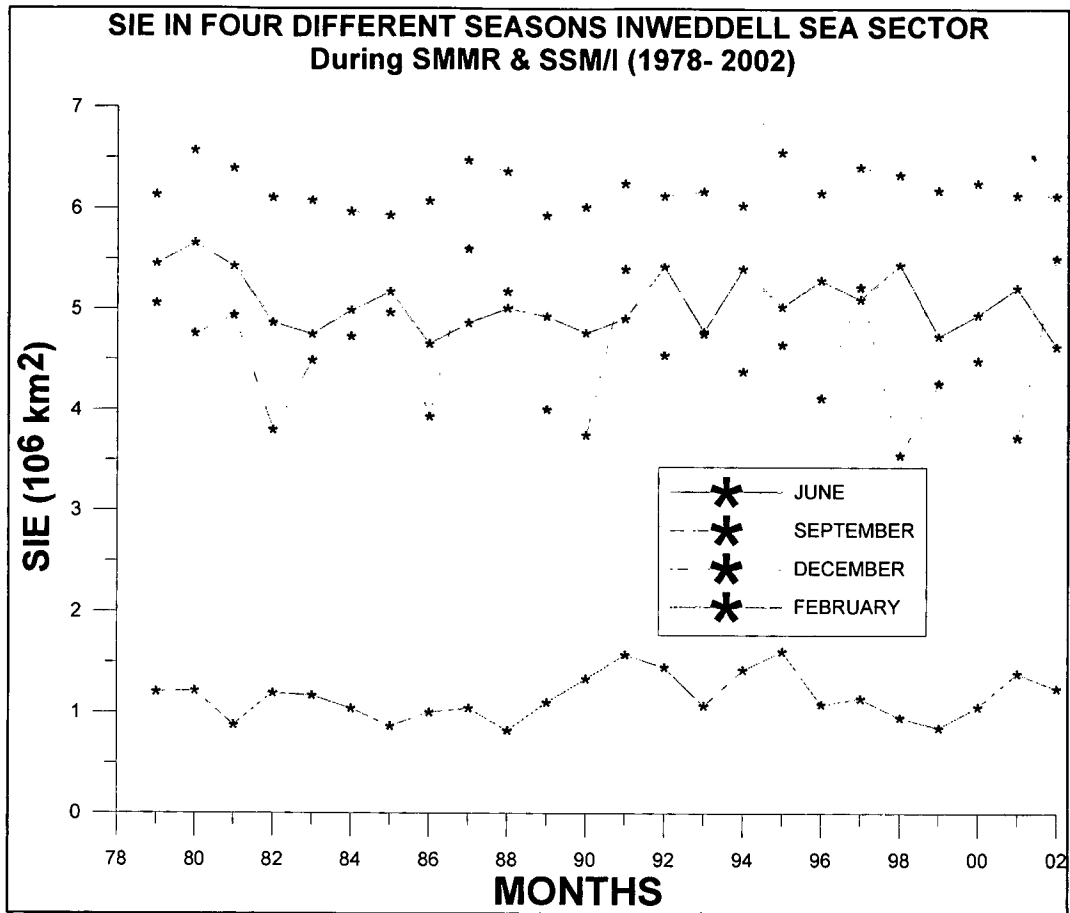


Fig 6.4: SIE in four different seasons in Weddell Sea Sector during SMMR & SSM/I period

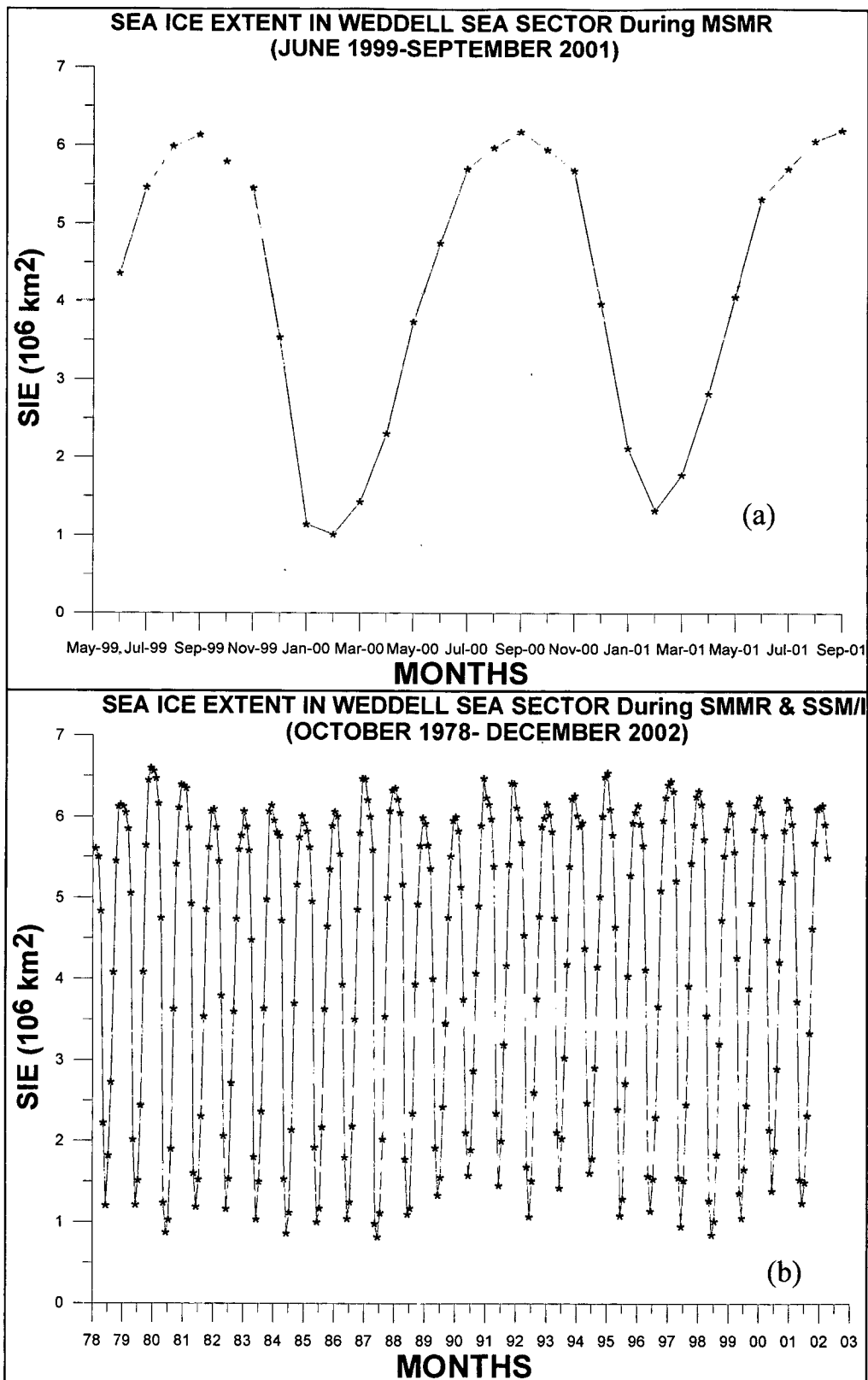


Fig 6.5: Monthly SIE in Weddell Sea Sector during MSMR period (a) and Long term monthly SIE in Weddell Sea Sector from SMMR and SMM/I (b)

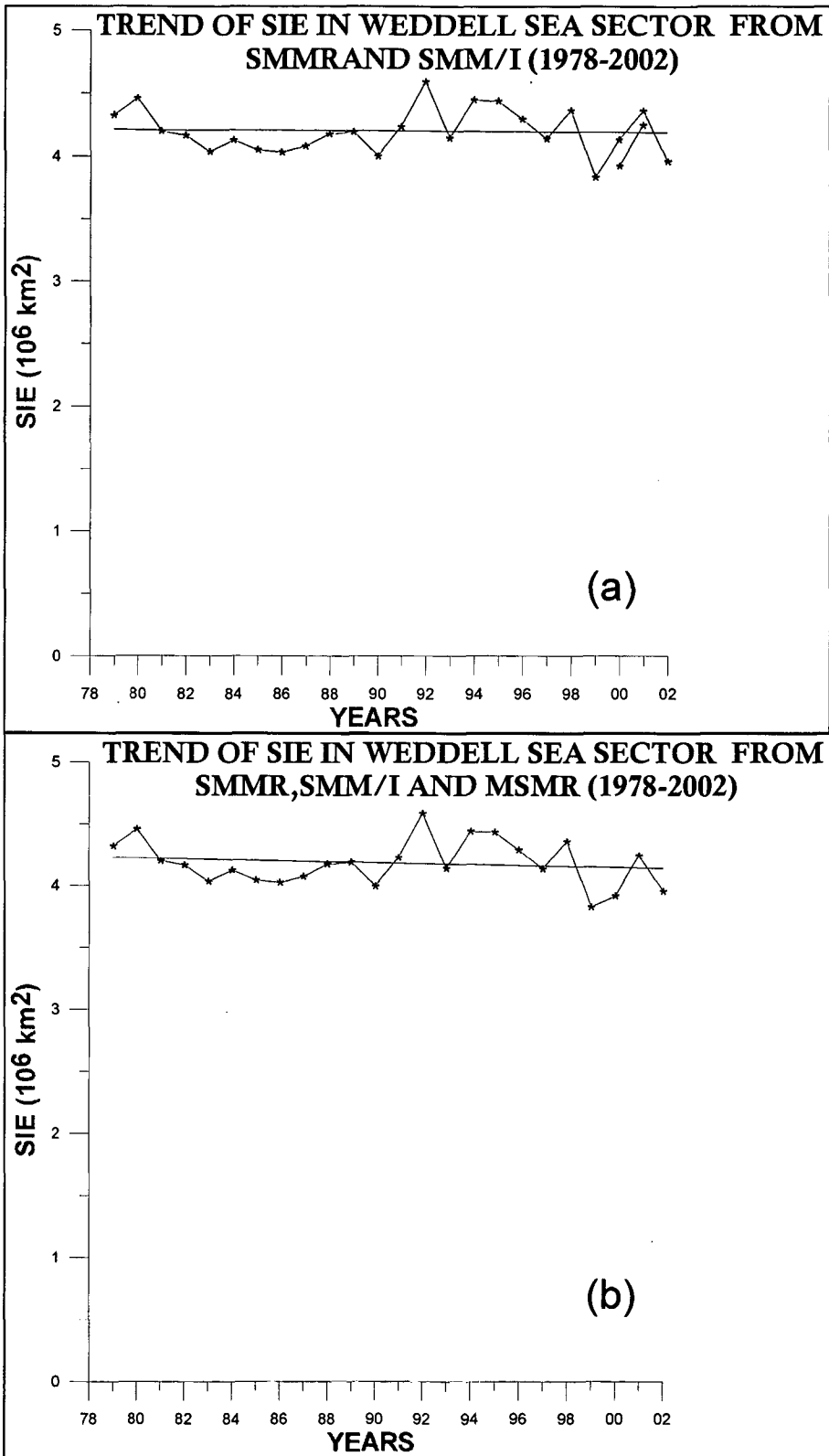


Fig 6.6: Yearly averaged SIE Trend in Weddell Sea Sector with SMMR and SMM/I (a) and SMMR and SMM/I with MSMR

6.5.2 Ross Sea Sector

The Ross Sea extends farther south than any other sector. In Southwest, the sea ice is bounded by the Ross Ice Shelf and the northernmost extension of the Trans-Antarctic mountains. Southeast part is bounded by the West Antarctic Ice sheet (WAIS). The shape of the edge of the ice pack in this sector is influenced by the ACC and the deflections of the current by the submarine topography (Zwally et. al., 1985).

The Ross sea sector is bounded by 160° East longitude and 130° West longitude. Like Weddell Sea, Ross Sea contains relatively cold water and a cyclonic gyre, which influences the formation of deep water near the front of the Ross Ice Shelf. The Ross Sea is a source of high-density bottom water, and a narrow boundary current along the continental slope of the eastern Ross Sea. The boundary current is a component of the global abyssal circulation. The volume of the shelf waters suggests that the source of one third of the total reservoir of the Antarctic bottom water can be attributed to the Ross Sea in the present day climate condition.

The brightness temperature maps, which are used to infer the sea ice extent clearly show that the sea ice extent moves towards north near 150° west longitude during the winter season. Four different seasons' images as observed by Oceansat-1 MSMR from June 1999- September 2001, are shown in fig 6.7 and SIE in fig 6.8 during SMMR & SSM/I Period. It is a clear indication of the influence of the ACC on the sea ice extent. The cyclonic ocean circulation in the Ross Sea influences the formation of open water near the front of the Ross Ice Shelf. Also near the front of Ross Ice Shelf, meso-scale Polynyas are formed during the spring as the pack ice opens to north, which can be clearly seen in T_b images of MSMR (see fig. 6.7).

The seasonal cycles of sea ice extent, sea ice area and open water within the ice packs, for SMMR and SSMI period from 1978 to 2002 and MSMR period, are shown in figs 6.9 (a), 6.9(b) respectively. The seasonal cycle of sea ice extent in this sector is different from that of other sectors. In this sector the growth of sea ice cover occurs rapidly for four to five months (March – July) followed by a slow expansion until September. The decay rate of sea ice is maximum from November to February. Similar results are also reported during the SMMR period (Gloersen et al., 1992). During January and February, the western portion of Ross Sea and the Ross Ice Shelf edge becomes ice free. Gloersen

et al. (1992) reported that in 1979 and 1980, the eastern portion of the Ross Sea Sector had considerably less ice than in other years.

The variations of sea ice extent from year-to-year for a given month in this sector show an anomalously low sea ice extent from January to August. The ice cover that sustains itself for more than a melt season, i.e. the minimum ice cover, during these 24 years of SMMR and SSM/I data analyzed is shown. For this sector, the minimum ice extent occurs during February. During the SMMR and the SSM/I period it is found that in 1979 and 1993 maximum ice cover occurs during July, whereas during the years 1981, 82, 84, 86, 91, 92, 95 and 1998 the maximum ice cover occurs in August. But for years 1980, 83, 85, 96 and 2000 the maximum ice cover occurs during October.

During winter, the open water present within few kilometers of the Ross Ice Shelf is strongly influenced by the synoptic weather systems. These synoptic weather systems force the sea ice to move away from the ice shelf (Zwally et al., 1985). During these periods the effect of cyclonic ocean circulation enhances the drifting of sea ice. The coastal regions and the open water areas during winter are predominantly associated with outlet glaciers and the katabatic winds coming from glaciers and ice sheets. The channeling of katabatic winds from the ice sheet causes frequent openings and closing of near-shore polynyas (e.g. Terra Nova Bay at 75°S and 165°E (Kurtz and Bromwich, 1985)). Ross Sea is another interesting region of the Antarctic with the presence of prominent Ross Ice Shelf. This area has been monitored very closely and several studies have indicated the breaking of some parts of the shelf. Recently, there have been reports of large icebergs detaching from the West Antarctic Ice Sheet on the southeast side of the Ross Ice shelf. One of the unique features that most of the MSMR T_B images in the atlas show is a distinct low T_B region on the Ross Ice Shelf with T_B values as low as 170 K. The cause of this persistent feature is not precisely known. However, it could be due to the difference in the crystal structure of the shelf ice or difference in the size of the snow grains present on the surface of the shelf. In other ice shelves also, such low T_B regions are observed.

MSMR study shows that the sea ice extent trend over the Ross Sea has changed from negative to positive. This is in contrast to the Weddell Sea ice extent trend, which has been observed to reverse from an increasing one to a decreasing one. The seasonal cycle of sea ice extent variation observed is largely similar to Weddell Sea (see fig. 6b). The

MSMR derived estimate of annual average sea ice extent over the Ross Sea sector is in consonance with the secular trend observed based on SMMR data (Gloersen et al., 1992).

This is compared with the SMMR and SSM/I estimates combined together for the years 1978-2000 in fig. 6.10(a, b). The figure (a) on the shows the trend obtained using only the SMMR and the SSM/I data We analyzed the annual averaged sea ice extent and sea ice area for years 1978 – 2002 using the SMMR, SSM/I and MSMR data. The trend analysis has been done using the linear least squares method for finding long-term changes.

Fig. 6.10 (a, b) shows the long-term variability of sea ice extent over the Ross Sea sector. The rate of increase in sea ice extent is found to be approximately 3.21 % per decade in the Ross Sea region during the period 1978-2002.

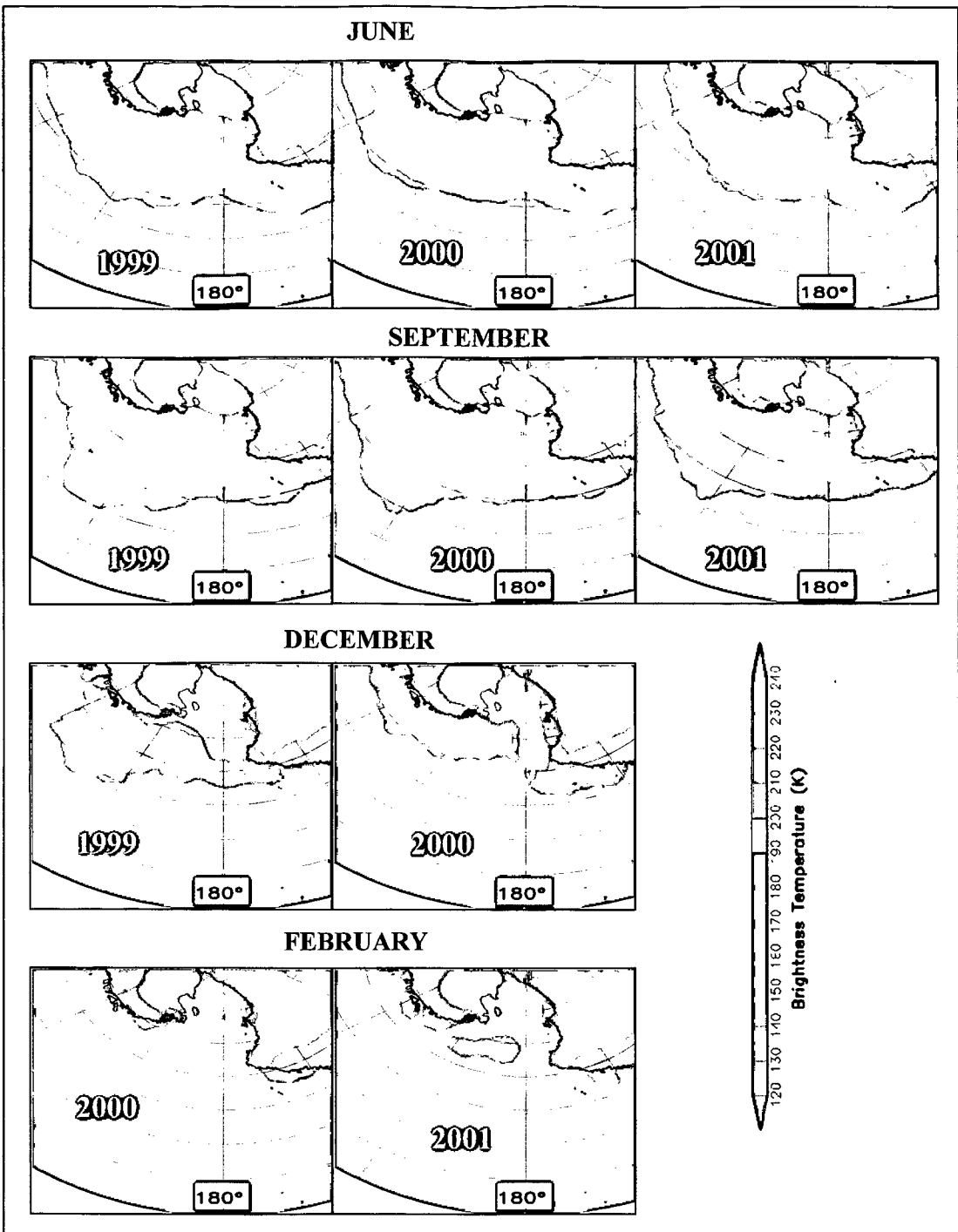


Fig 6.7: MSMR T_B images of different seasons in Ross Sea Sector

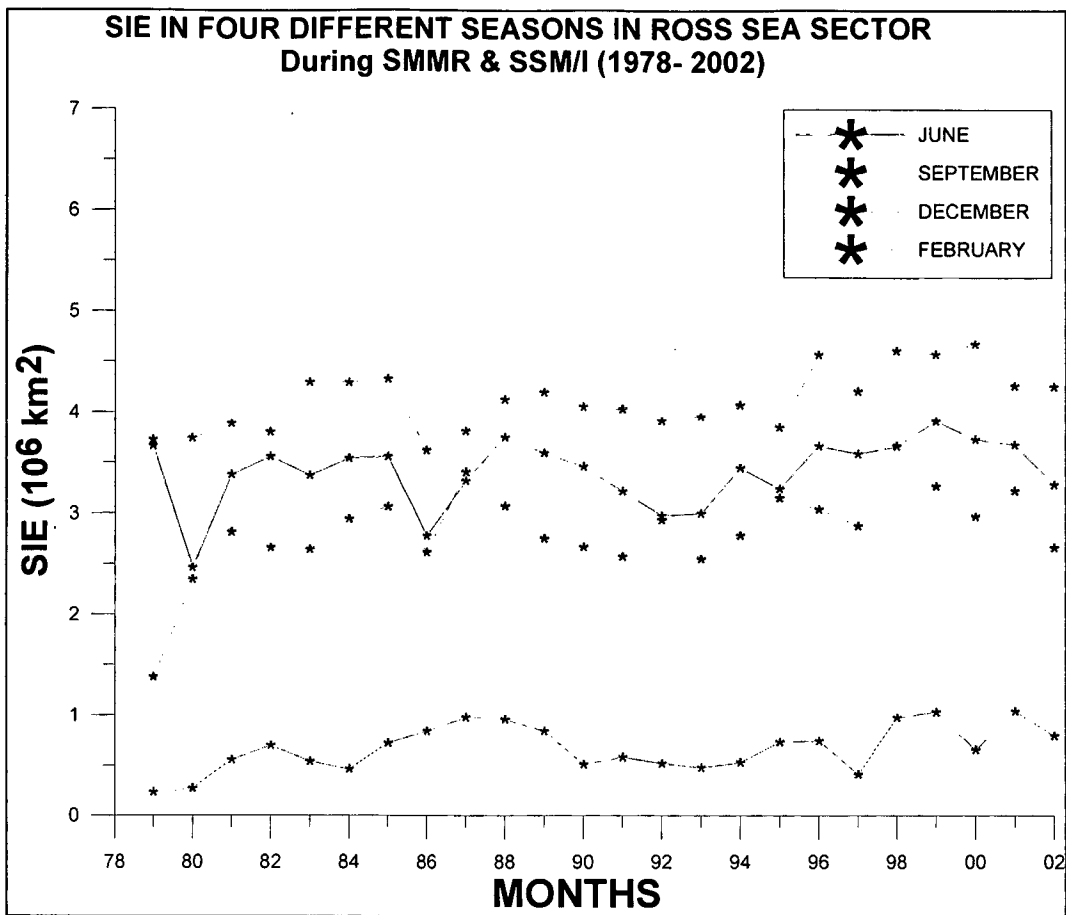


Fig 6.8 Four different seasons in Ross Sea Sector during SMMR & SSM/I period

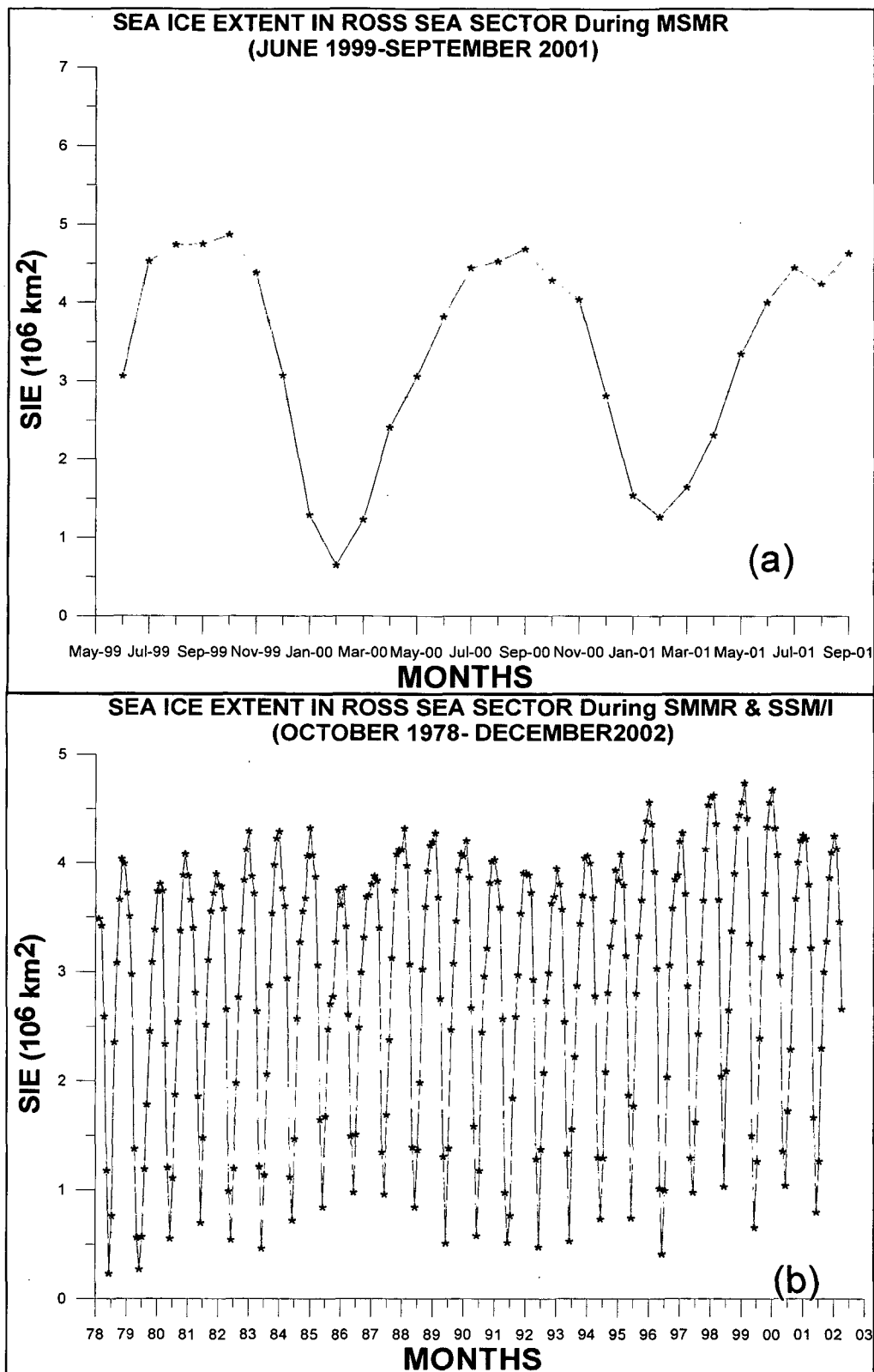


Fig 6.9: Monthly SIE in Ross Sea Sector during MSMR period (a) and Long term monthly SIE SMMR and SSM/I (b)

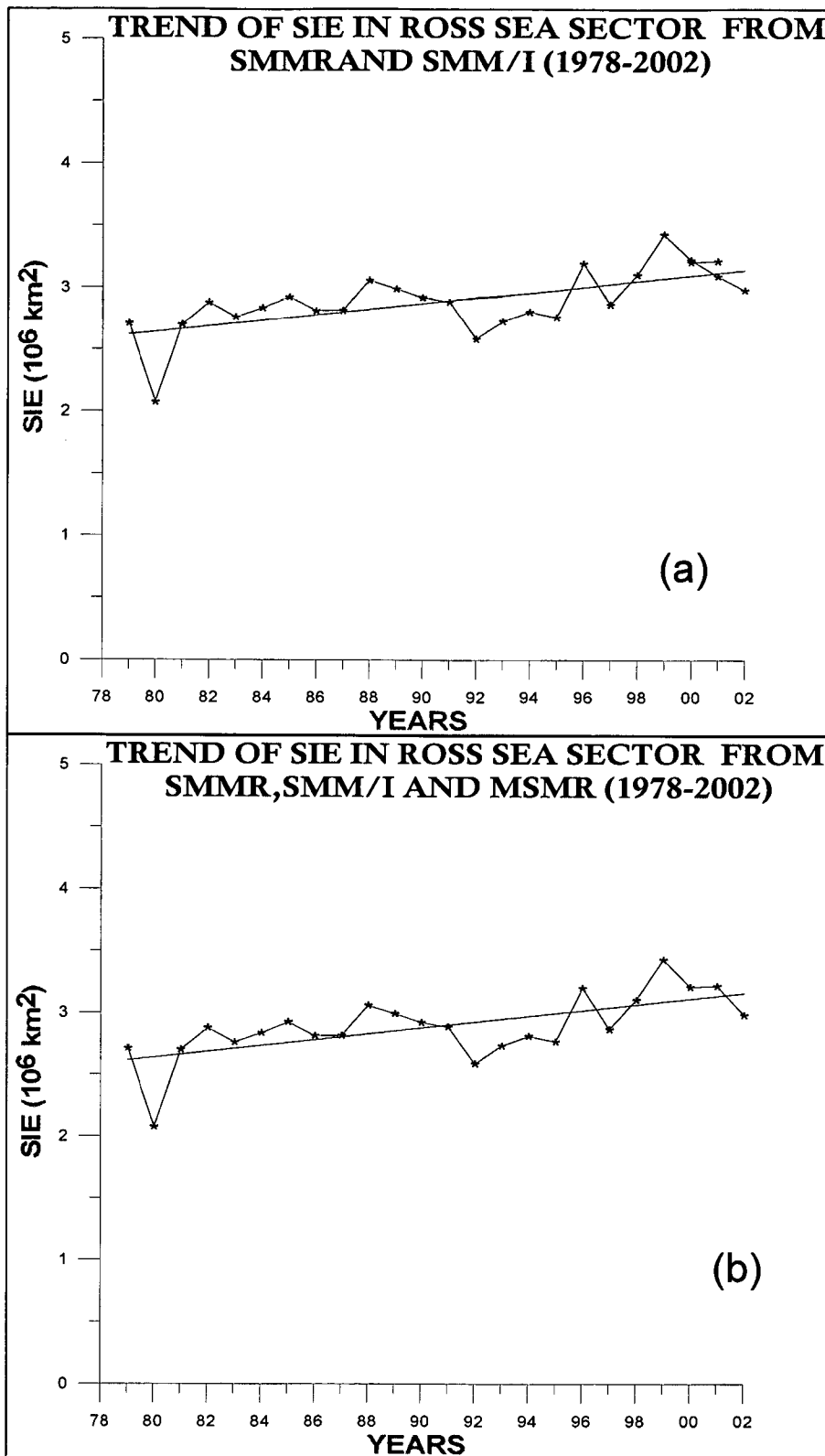


Fig 6.10: Yearly averaged SIE Trend in Ross Sea Sector with SMMR and SMM/I (a) and SMMR and SMM/I with MSMR (b)

6.5.3 Indian Ocean Sector

Indian Ocean is located at eastern edge of the Weddell Gyre. It is also the site of some isolated and relatively shallow pycnoclines near the coastal regions. (Gordon & Molinelli 1982).

Comiso and Gordon (1987) reported a recurring deep ocean polynya in the Cosmonaut Sea, located near 45° east longitude. This polynya has the same formation characteristics as large Weddell polynya observed during the ESMR period. Like Weddell Sea polynya, this polynya is preceded by an embayment and is located near a topographic rise. However, the lifetime of this polynya is less than one month. This polynya is categorized as the sensible heat polynya.

Wu et al. (2003) stated that heat required for forming and maintaining the Cosmonaut Sea polynya is at least 250 W/m² in winter and 135 W/m² in spring. Although the area of the Cosmonaut Sea Polynya is not large but in this region polynyas appear frequently. Spatial property distributions of the surface mixed layer, the subsurface temperature minimum layer and winter water are closely correlated with the seasonal warming and cooling, wind intensity, ice advance and retreat of seasonal sea ice cover, and the general circulation (Park et al., 1998). From the T_B images we are able to detect polynya like structure due to its low T_B values during July 2000 (near 65° S and 50°E) and during Nov. 2000 (near 65° S and 40°E) (see fig 6.11) Because of their small size and more inflow of sea ice these polynyas have shorter lifetime (for example the Cosmonaut Sea polynya). For a polynya to persisted throughout the winter, it should process a certain critical size (Comiso and Gordon, 1987). The Prydz Bay area exhibits the most saline, dense, deep winter water and appears as the site with the highest potential for the local formation of deep water in this sector (Park, 1998). This area is also the site where relatively large coastal polynyas occur in the Indian Ocean sector.

The T_B images of four different seasons are shown in fig 6.11. The SIE in the same seasons during the SMMR and SSM/I period shown in fig 6.12 (a). The SIE in MSMR period is shown in fig 6.13. The SIE in SMMR and SMM/I period is shown in fig 6.14 (a). The secular trend in SIE with SMMR and SMM/I and SMMR, SMM/I and MSMR is shown in fig 6.15 (a) (b) respectively.

The sea ice cover in these sectors is less than the Weddell Sea and the Ross Sea sectors. The Indian Ocean region shows a relatively moderate rate of long term increase of sea ice extent (2.65% per decade) although the annual average sea ice extent there is relatively low ($1.7 \times 10^6 \text{ km}^2$)

6.5.4 Western Pacific Ocean Sectors

Western Pacific Ocean extends from 90° East to 160° East, is the region south of Australia and New Zealand and is farthest from the pole. It is the warmest part of the SPO and has negligible ice cover throughout year.

This is the sector, which is farthest from the South Pole. The climatological records show that it is the warmest among the five Southern Ocean sectors described here. The sea ice extent is very less throughout the year in this sector. The monthly brightness temperature images of Southern Polar Ocean show that this sector is almost free of ice for the months of February and March.

Like other southern ocean sectors, this sector is also the site of many coastal polynyas. The coastal polynyas are created due to the effect of katabatic winds from adjacent mountains and glaciers. These polynyas are the key sites for the energy, mass and momentum exchange between the atmosphere and the polar ocean. Also these are the key sites of intense oceanic ventilation during winter and also serve as the source of cold and dense saline shelf water. The production of this dense shelf water by coastal polynyas is believed to be an important source of Antarctic bottom water (Gordon, 1974). During MSMR period some eddy structures are reported by Dash et al., 2001 in the Pacific Ocean sector.

The T_B images of four different seasons are shown in fig 6.11. The SIE in the same seasons during the SMMR and SSM/I period shown in fig 6.12 (b). The SIE in MSMR period is shown in fig 6.13. The SIE in SMMR and SSM/I period is shown in fig 6.14 (b). The secular trend in SIE with SMMR and SSM/I and SMMR, SSM/I and MSMR is shown in fig 6.16 (a) (b) respectively.

Pacific Ocean sector is the warmest among all the sectors of the Southern Polar Ocean. During the summer time the sea ice margin recedes towards the coast and most part of the coastline remains ice-free. SMMR derived sea ice extent analysis shows a negative trend

of $(-)$ $0.001 \times 10^6 \text{ km}^2/\text{year}$ (Gloersen et al., 1992). Vyas et al. (2003) reported average annual sea ice extent of $1.404 \times 10^6 \text{ km}^2$ estimated from MSMR data. The long-term trend over these seas appears to be negative.

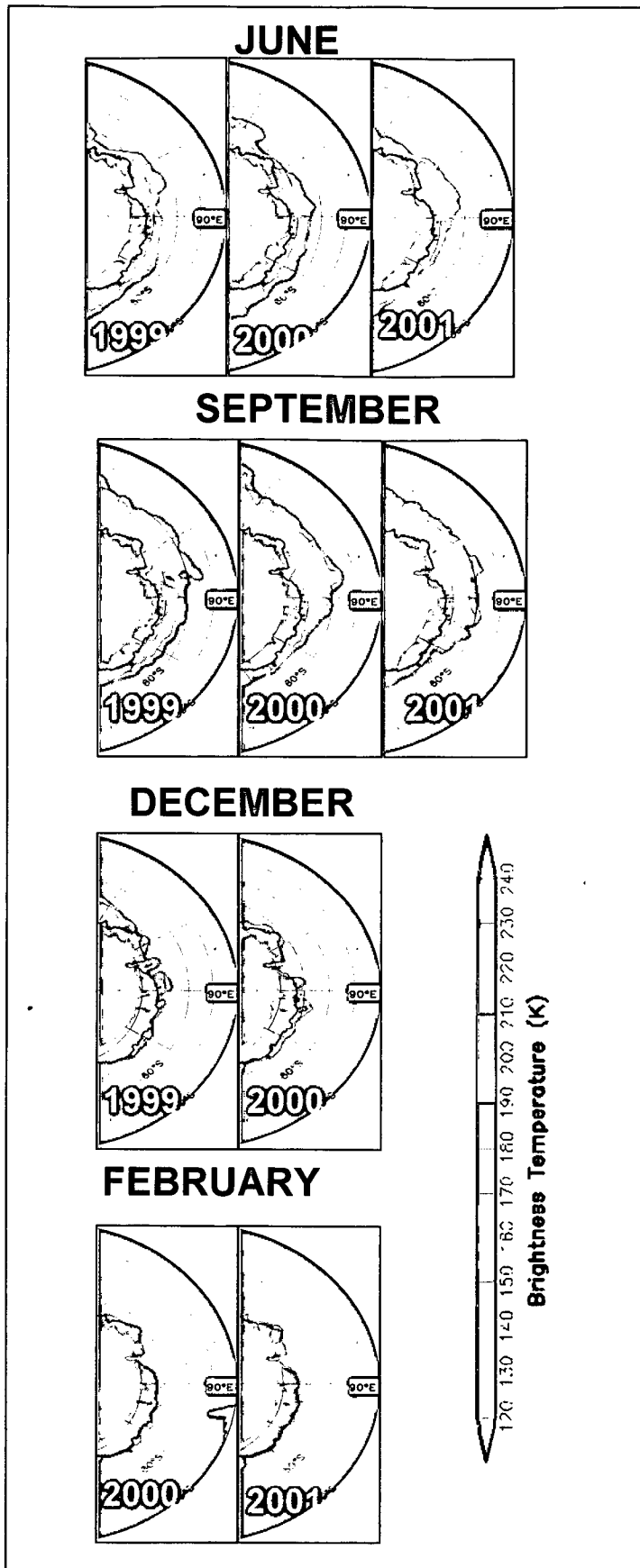


Fig 6.11 MSMR T_B images of different seasons in Indian Ocean and W. Pacific Ocean Sectors

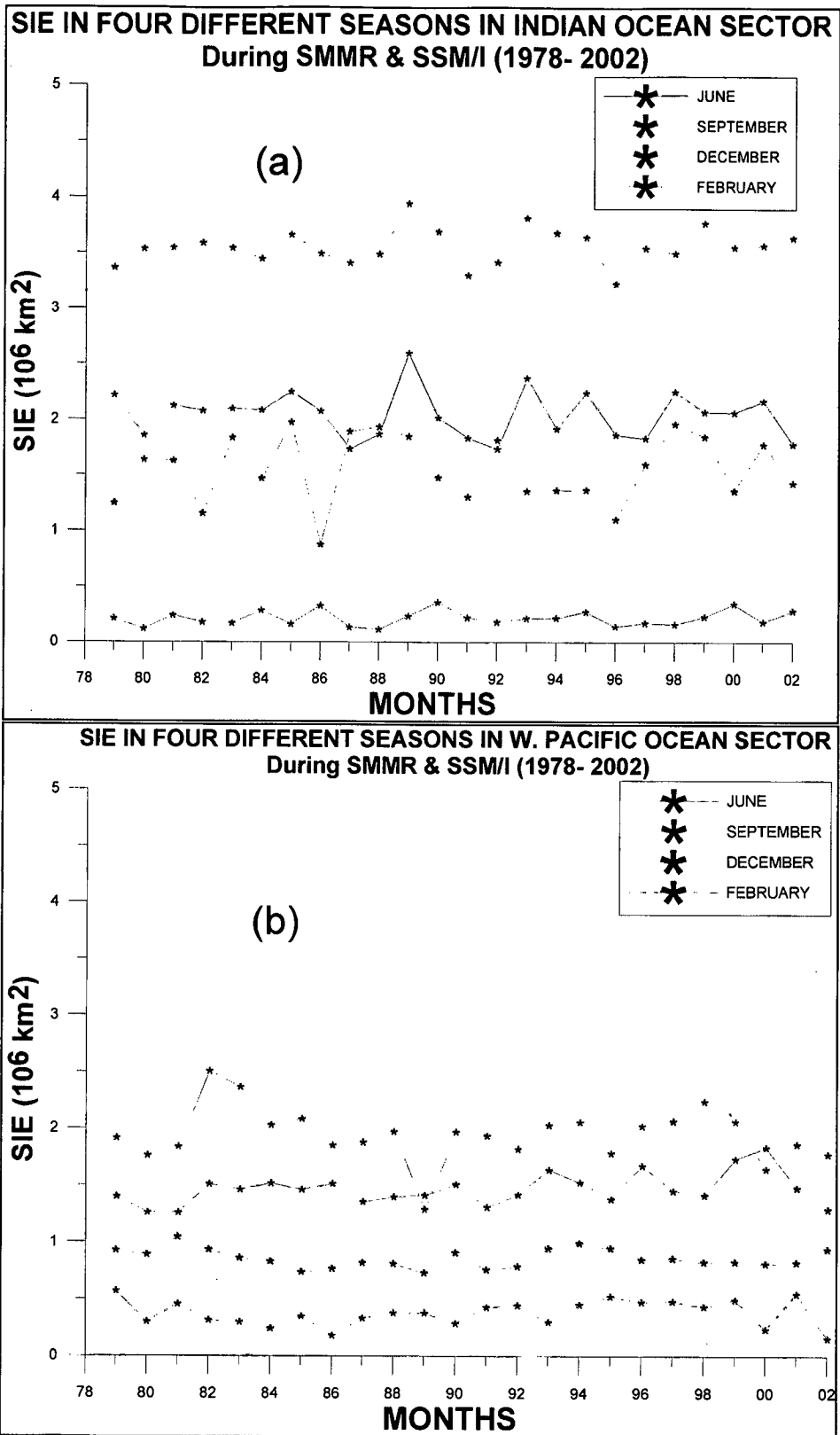


Fig 6.12 Four different seasons in Indian Ocean Sector (a) and W. Pacific Ocean Sector (b), during SMMR & SSM/I period.

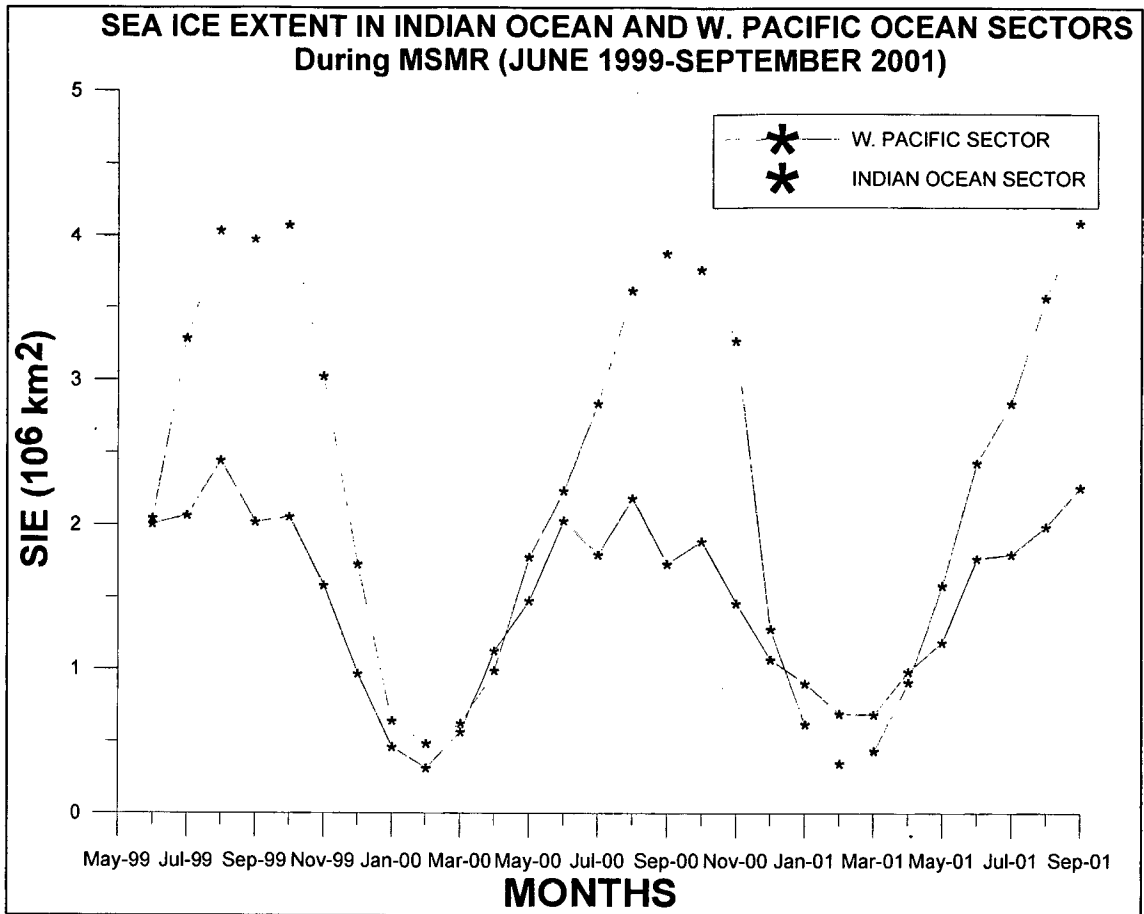


Fig 6.13: Monthly SIE in Indian Ocean and W. Pacific Ocean Sectors during MSMR period

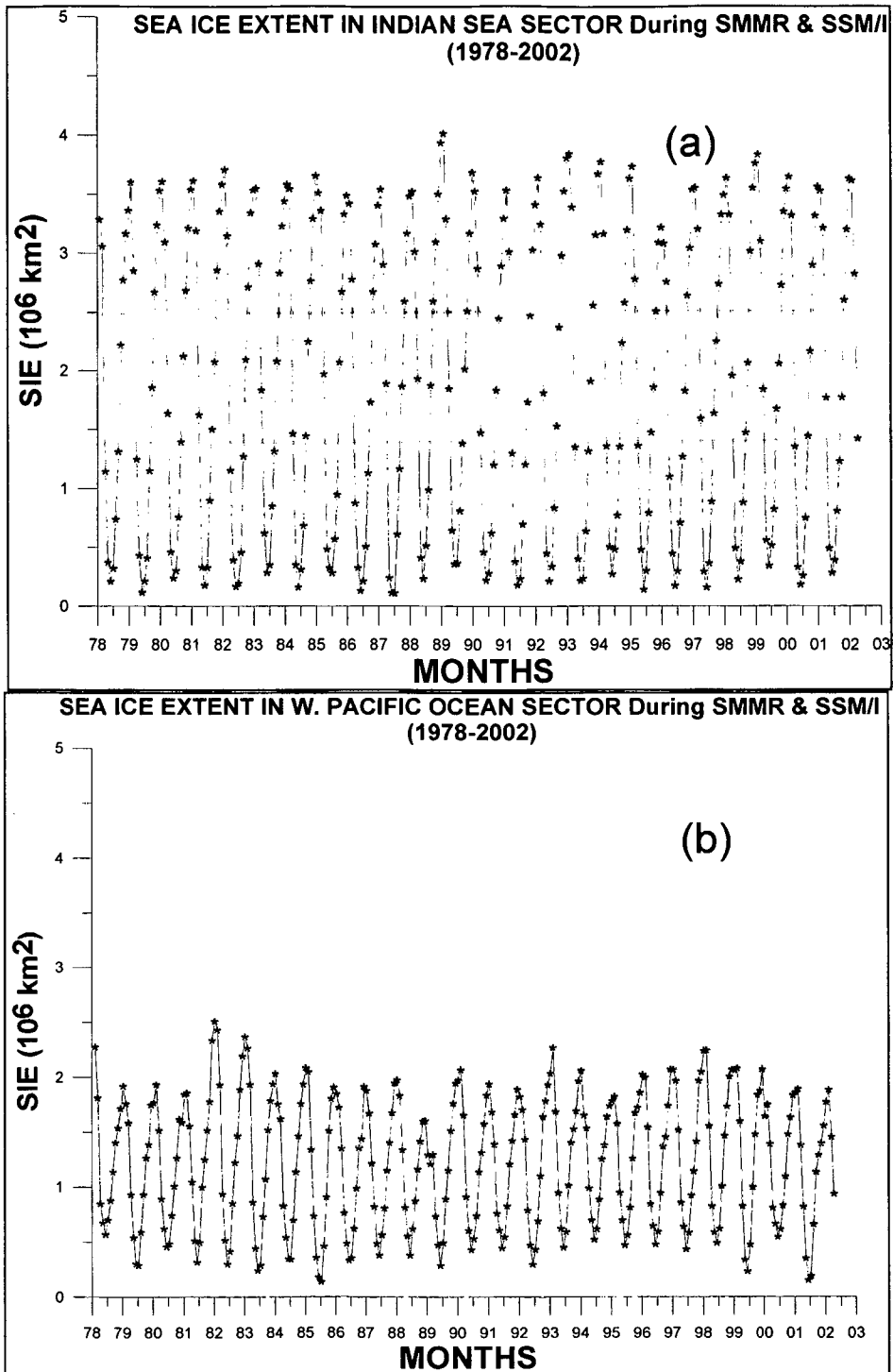


Fig 6.14: Long term monthly SIE in Indian Ocean sector (a) and W. Pacific Sectors (b) during SMMR & SSM/I period

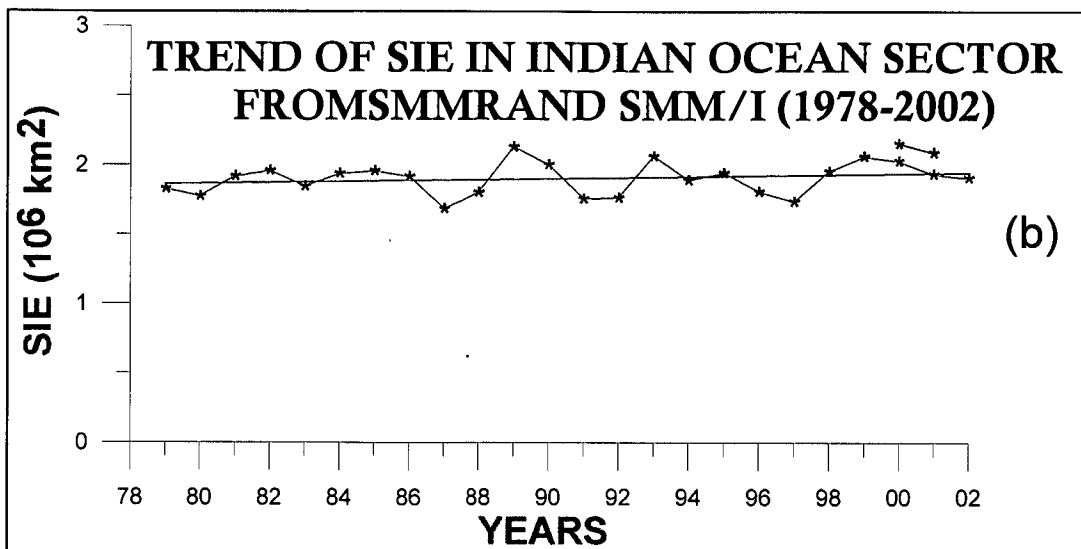
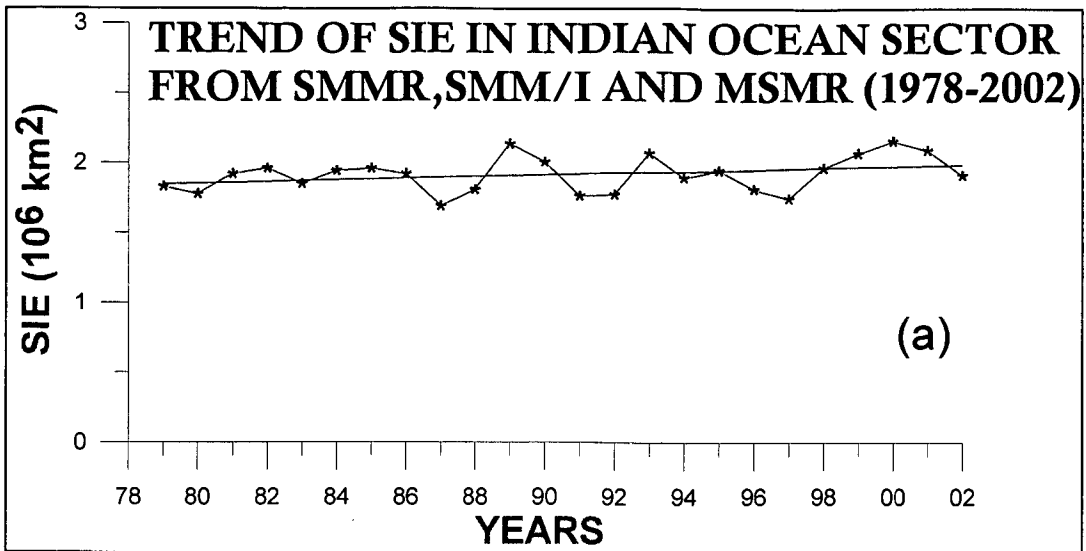


Fig 6.15: Yearly averaged SIE trend in Indian Ocean Sector with SMMR and SMM/I (a) and SMMR and SMM/I with MSMR (b)

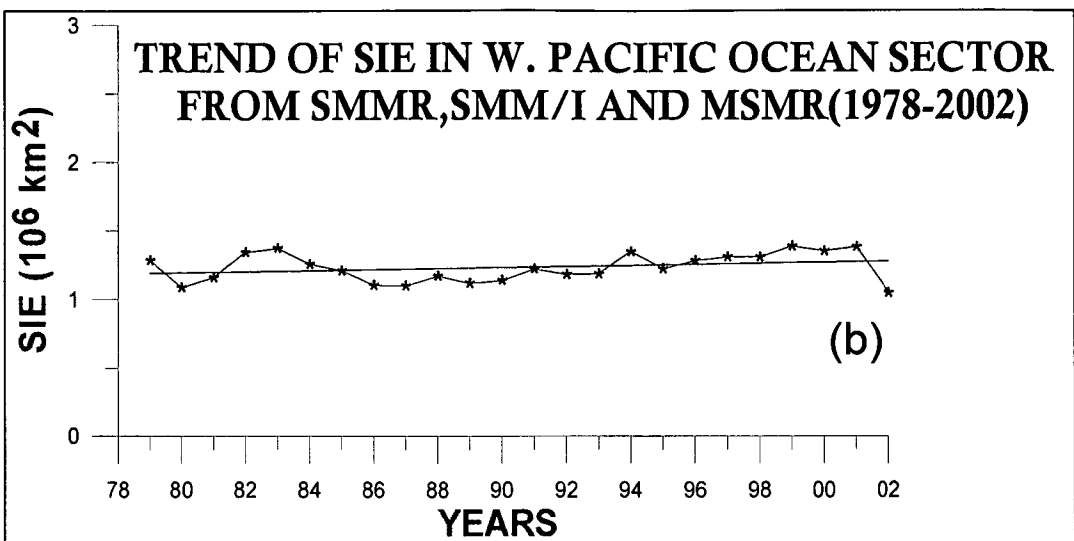
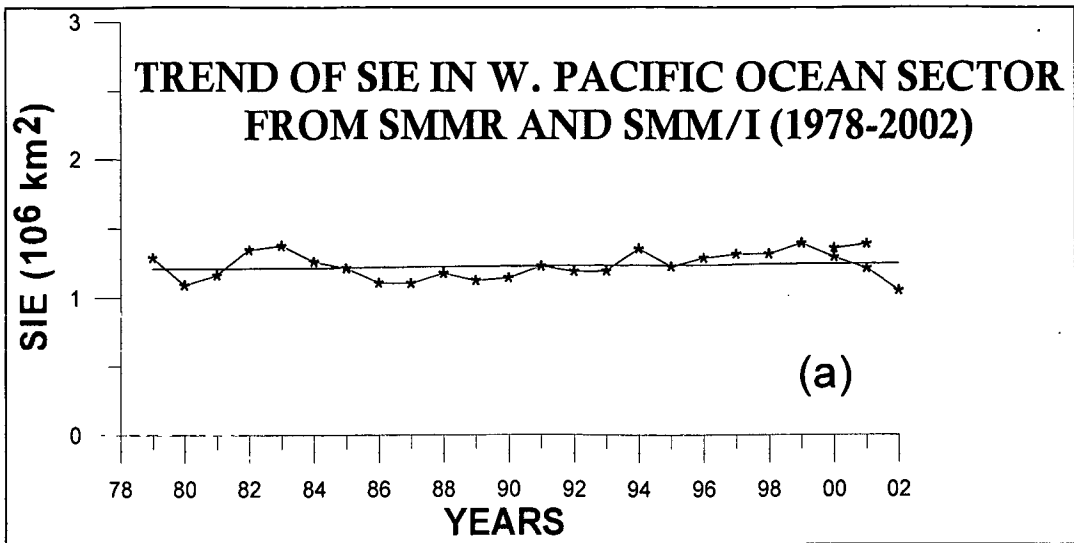


Fig 6.16 Yearly averaged SIE trend in W. Pacific Ocean Sector with SMMR and SMM/I (a) and SMMR and SMM/I with MSMR (b)

6.5.5 Bellingshausen-Amundsen Seas

Bellingshausen & Amundsen Seas (B &A Seas) have the largest ice cover during the summer and least seasonal variation among the SPO sectors. It may be due to the below freezing point surface temperatures prevailing round the year, partly caused by the North-South coastline of the Antarctic peninsula, which diverts the ACC.

Bellingshausen and Amundsen Seas sector is defined as the area between 130° W and 60°W. This sector is bounded by the Antarctic Peninsula on the east. It is characterized by strong stratification in Upper Ocean that contributes to the retention of large amounts of ice in summer. Antarctic Peninsula is mainly responsible for different processes taking place in this sector. After Weddell Sea sector, this sector has the second largest multi-year ice cover area (sea ice extent) among the five sectors described in this chapter. It has an average ice extent of 2.31×10^6 km². The reason for the Weddell Sea and the Bellingshausen and Amundsen Seas sector to have largest ice cover in summer is not known, but it may be due to the North-South coast- line of the Antarctic Peninsula, which pushes the circumpolar current northward. In this sector, the ratio of the average ice extent during the summer to that in winter is 1:4. This ratio is much higher than those for the other sectors.

The T_B images of four different seasons are shown in fig 6.11. During the MSMR period the sea ice extent is found to vary from a minimum of 0.89×10^6 km² during March 2000 to maximum of 2.963×10^6 km² during September 2000. The SIE in MSMR period is shown in fig 6.13. The SIE in SMMR and SMM/I period is shown in fig 6.14 (b). This is the region having the second largest multiyear ice area (the Weddell sea has the largest multiyear ice area). During November through January the melting is more. During the April-June months the formation is fast and then it becomes slower in successive months (June/July/August) the formation reaches its maximum in September

Bellingshausen and Amundsen seas sector is the sector where the least seasonal variation of sea ice has been observed. The SIE in the same seasons during the SMMR and SSM/I period shown in fig 6.12 (b). This sector shows prominent response to the ENSO phenomenon. During the El-Nino years there is a decrease in the sea ice area and sea ice extent anomalies (Kwok and Comiso, 2002). A study using the sea ice data spanning the

period from 1973 –1994, Jacobs and Comiso (1997) reported a decline in the sea ice extent in the Amundsen and Bellingshausen seas in the two decades following 1973.

They attributed the record decrease in the sea ice extent to more southerly surface winds and historic high surface air temperatures along the west coast of the Antarctic Peninsula. The sea ice trend for the SMMR period in this sector is found to be $(+) 0.004 \times 10^6 \text{ km}^2/\text{year}$ (Gloersen et al., 1992). A study by Kwok and Comiso, 2002 states that a decrease in sea ice extent and sea ice area anomalies occurred by $-15247.4 \pm 2212.3 \text{ km}^2/\text{year}$ and $-9844.8 \pm 1887.0 \text{ km}^2/\text{year}$ respectively.

The secular trend in SIE with SMMR and SMM/I and SMMR, SMM/I and MSMR is shown in fig 6.16 (a) (b) respectively. There was a decreasing trend in the sea ice extent during August for the years 1979 to 1983. But for the years 1983 to 1986 there was an increase in the sea ice extent during the above period and Gloersen et al. 1992). Similarly an increasing trend of sea ice extent is seen from 1992 to 1997 for the month of August. But, the over all trend shows a decreasing in sea ice extent.

The sea ice cover in these sectors is less than the Weddell Sea and the Ross Sea sectors. The long-term trend over these seas appears to be positive and with relatively high rate of increase in the Bellingshausen Sea (6.55% per decade)

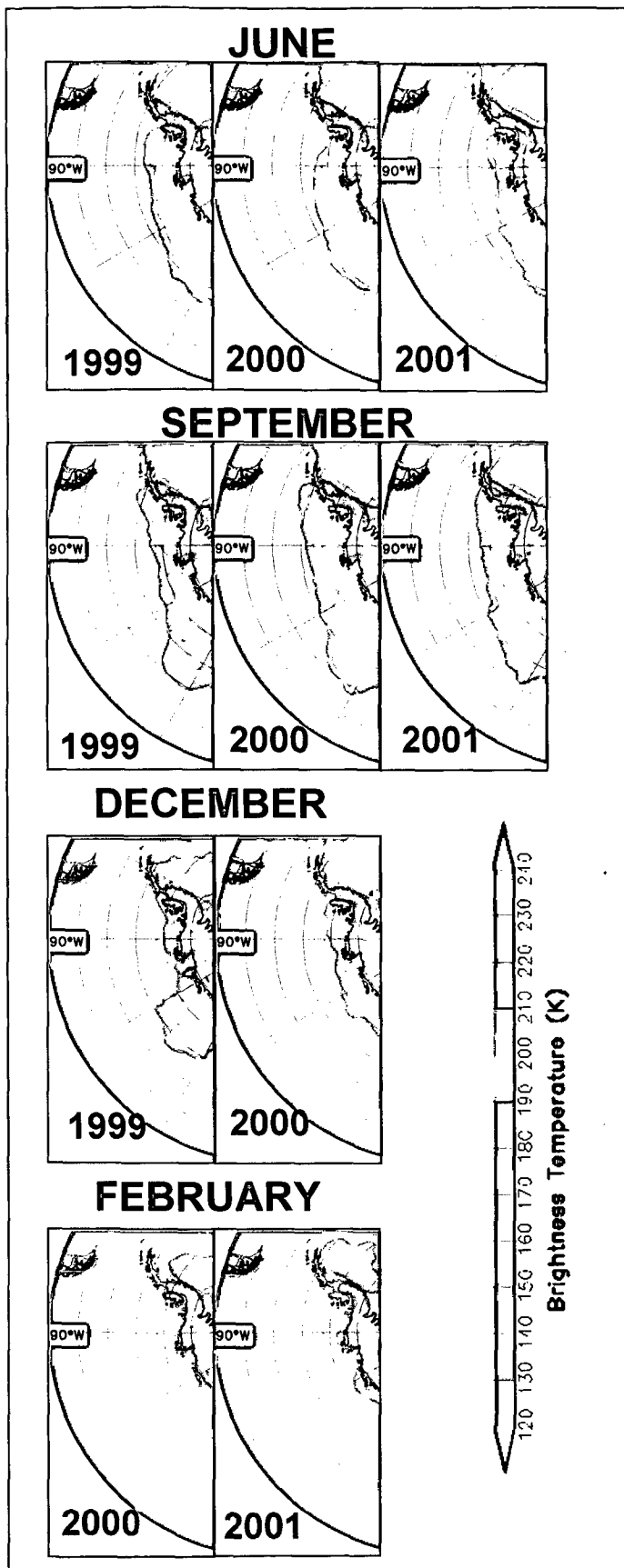


Fig 6.17: MSMR T_B images of different seasons in Bellinghousen & Amundsen Seas Sector during MSMR period

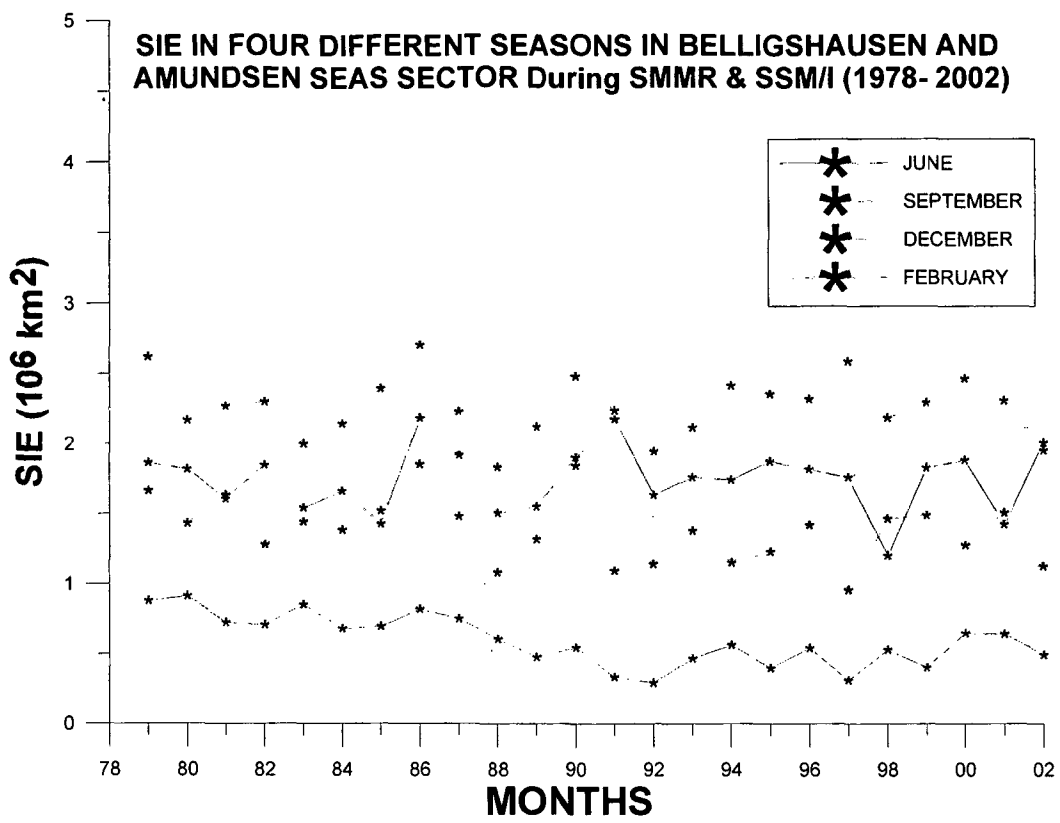


Fig 6.18 Four Different Seasons SIE in Belligshausen & Amundsen Seas Sector during SMMR & SSM/I period.

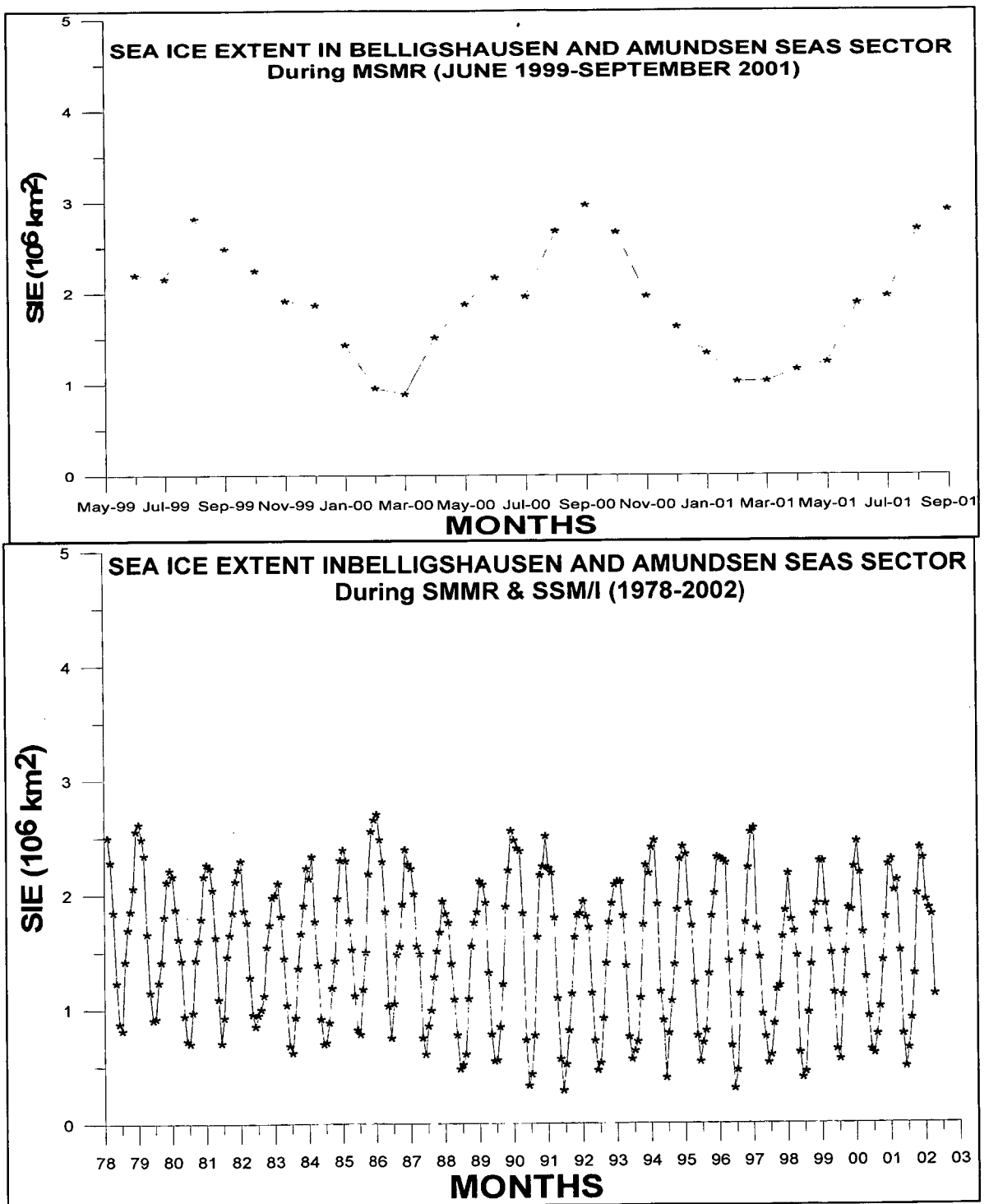


Fig 6.19: Yearly averaged SIE trend in Bellinghshausen & Amundsen Seas Sector from SMMR and SSM/I (a) and SMMR and SSM/I with MSMR (b)

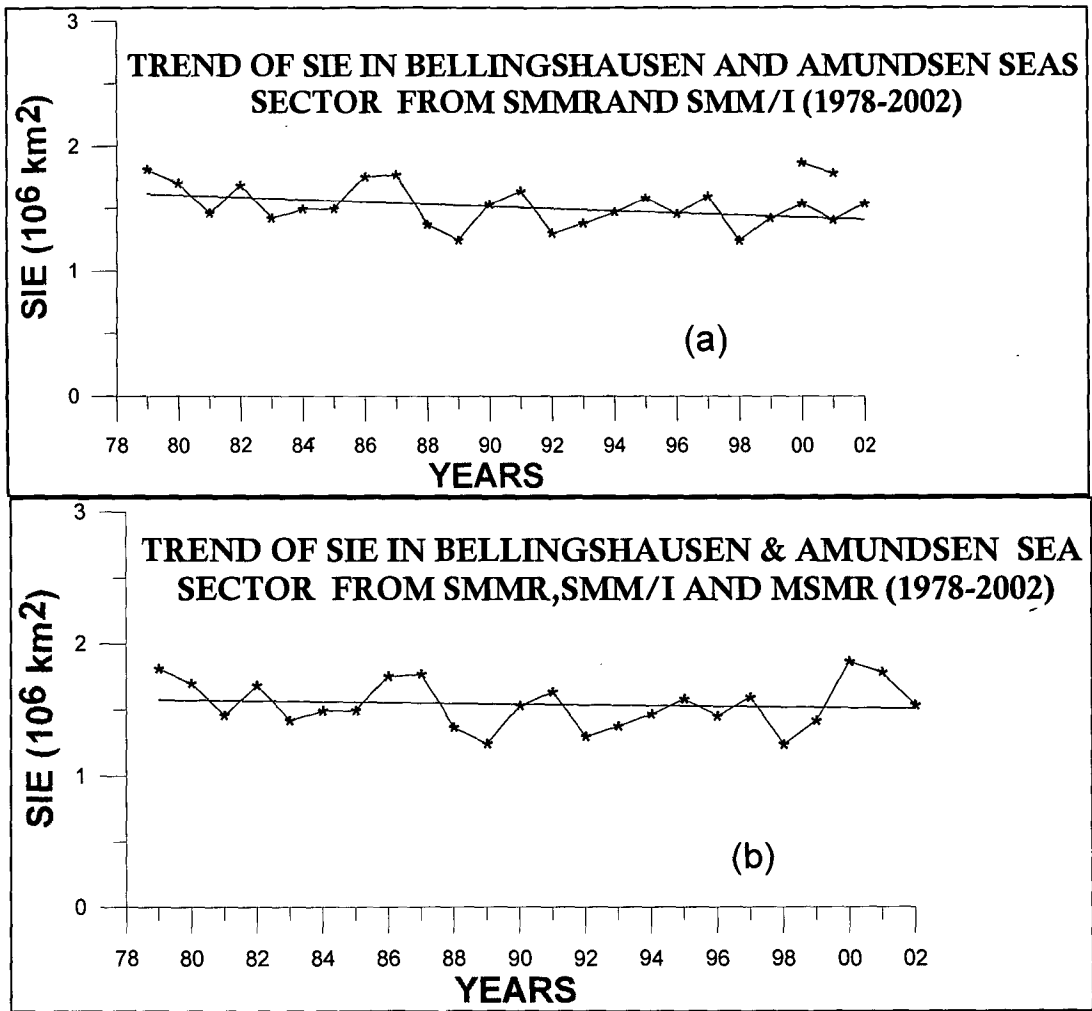


Fig 6.20: SIE Trend in Bellinghausen & Amundsen Seas Sector with SMMR & SMM/I (a) and SMMR, SMM/I & MSMR (b)

6.5.6 Southern Polar Ocean (as a whole)

Southern Ocean is the only Ocean, which connects the three major oceans and has no east-west boundaries. It is very important for climate studies, as it is the major source of the bottom water. A strong, deep eastward-flowing current known as the Antarctic Circumpolar Current (ACC) dominates the Southern Ocean. Average volume of water transported by ACC is 110 Sv (i.e. $110 \times 10^6 \text{ m}^3/\text{sec}$) (Pickard and Emery, 1993). Also it is the area of interaction between different water masses. It is an ideal area to study the interaction between ice, ocean, atmosphere and the lithosphere.

The brightness temperature maps serving as proxies to the sea ice cover are shown in fig 6.21. The seasonal variation of The SMMR and SSM/I (from 1978 to 2002) shown in fig 6.22. Fig 6.23 (a) shows the overall seasonal behaviour of the sea ice extent over the SPO obtained from the MSMR data. The sea ice extent varies from a minimum of about $3 \times 10^6 \text{ km}^2$ in February 2000 to a maximum of about $21 \times 10^6 \text{ km}^2$ in September 2001. Study of the changing behavior of the sea ice extent over the Antarctic region, based on a long term monitoring of the Antarctic Sea ice using passive microwave radiometry, has been attempted earlier systematically in the form of an atlas by Gloersen et al. (1992).seasonal cycle of ice extent, are presented in the and the average sea ice extent for the same is shown. The inter-annual variations in ice extent for different months are given in figs 6.23 (a) and (b), which facilitate a comparison of the month-by-month changes occurring in the sea ice extent. For MSMR period the seasonal cycle for year 1999-2000 and 2000-2001 is shown in fig 6.23 (a). Monthly sea ice extents (for SMMR + SSM/I period stated above) is shown in 6.23 (b).

(b)

The seasonal cycle of sea ice cover in Southern Ocean is characterized by minimum ice cover in the month of February. It is followed by expansion of the ice cover in successive months until the maximum ice coverage is reached during August to October. But, for most of the years (during 1978 to 2002), the maximum ice extent occurs during September. During MSMR period the sea ice extent is found to be maximum in August for 1999-2000 and in September for 2000-2001. The rapid decay of ice takes place from November through January. During February to March growth of ice area occurs in all the sectors except the Bellingshausen and Amundsen seas sector. The most rapid expansion of the ice cover occurs during the period from March to July. The ice growth in February to March is more rapid in the Ross Sea and Weddell Sea sectors than in other

sectors. A very interesting feature, namely slight decrease in sea ice extent or slower ice growth in July compared to other ice formation months, is marked in the Pacific Ocean and the Bellingshausen and Amundsen seas sectors during MSMR period. The cause of this is not known yet; it may be due to the influence of atmospheric circulation on the sea ice extent.

In their analysis, they found a very weak increasing trend over the period 1979-1987. MSMR observations (1999-2000 and 2000-2001) coupled with SSM/I observations (1988-2002) (see fig.6.24) suggest a continuation and strengthening of the secular trend observed during the SMMR period. This suggests an acceleration of the positive trend over the past one and a half decade. The present estimate of the trend is about 19,200 km² per year, which is approximately equal to 2.43% per decade. This is a rather weak trend but a consistent trend. Such a trend is also expected to result from the difference between the opposing trends observed in the Weddell Sea and Ross Sea sectors. The area weighted secular variations in other sectors are generally much smaller as compared to those in the above two sectors. Table-3 gives the summary of sea-ice extent and its rate of growth / decay in different sectors of the Southern Polar Ocean.

Extensive analyses of MSMR data have been carried out by Vyas and Dash, 2000; Vyas et al. (2001, 2003), Dash (2001), Bhandari et al. (2002a, 2002b) to study the characteristics of sea ice around the Antarctic region. MSMR estimates of sea ice extents over important regions of Weddell Sea and Ross Sea, as well as over the entire Antarctic Region, although covering a period of only 28 months, bring out the nature of seasonal and secular variations in a very consistent manner. The rates of change of sea ice extent covering a period of more than 20 years are estimated to be -1.1% per decade for the Weddell Sea, +3.21% per decade for the Ross Sea. It can be noticed that these trends are similar to those seen in the SMMR period (Gloersen et. al., 1992). The trend for the total Antarctic reported by Gloersen et al (1992) was almost negligible. However, that has now picked up and is approximately equal to +2.43% per decade for the entire region as a whole.

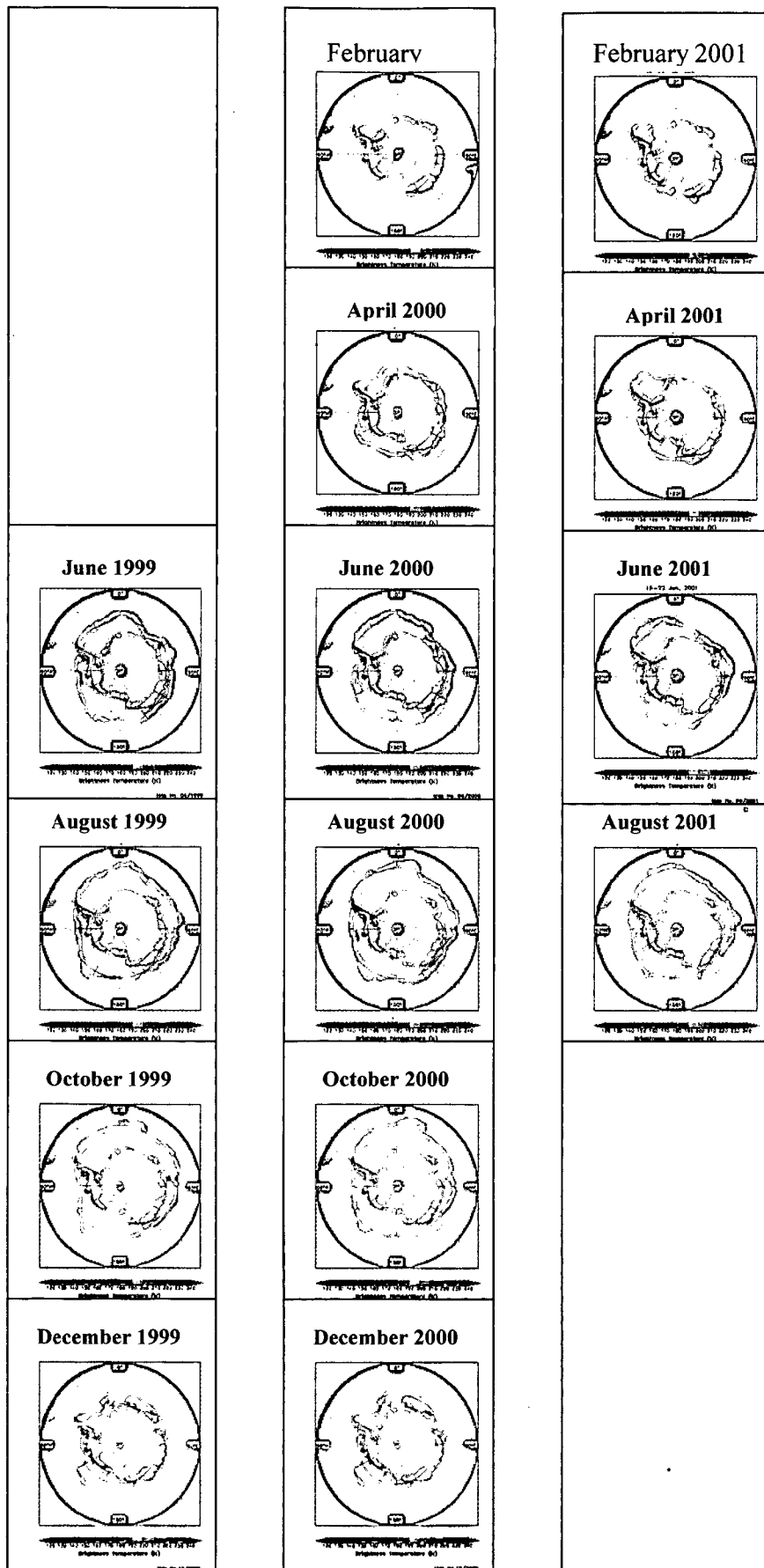


Fig 6.21: Seasonal and Inter-annual T_B Images of MSMR in the SPO

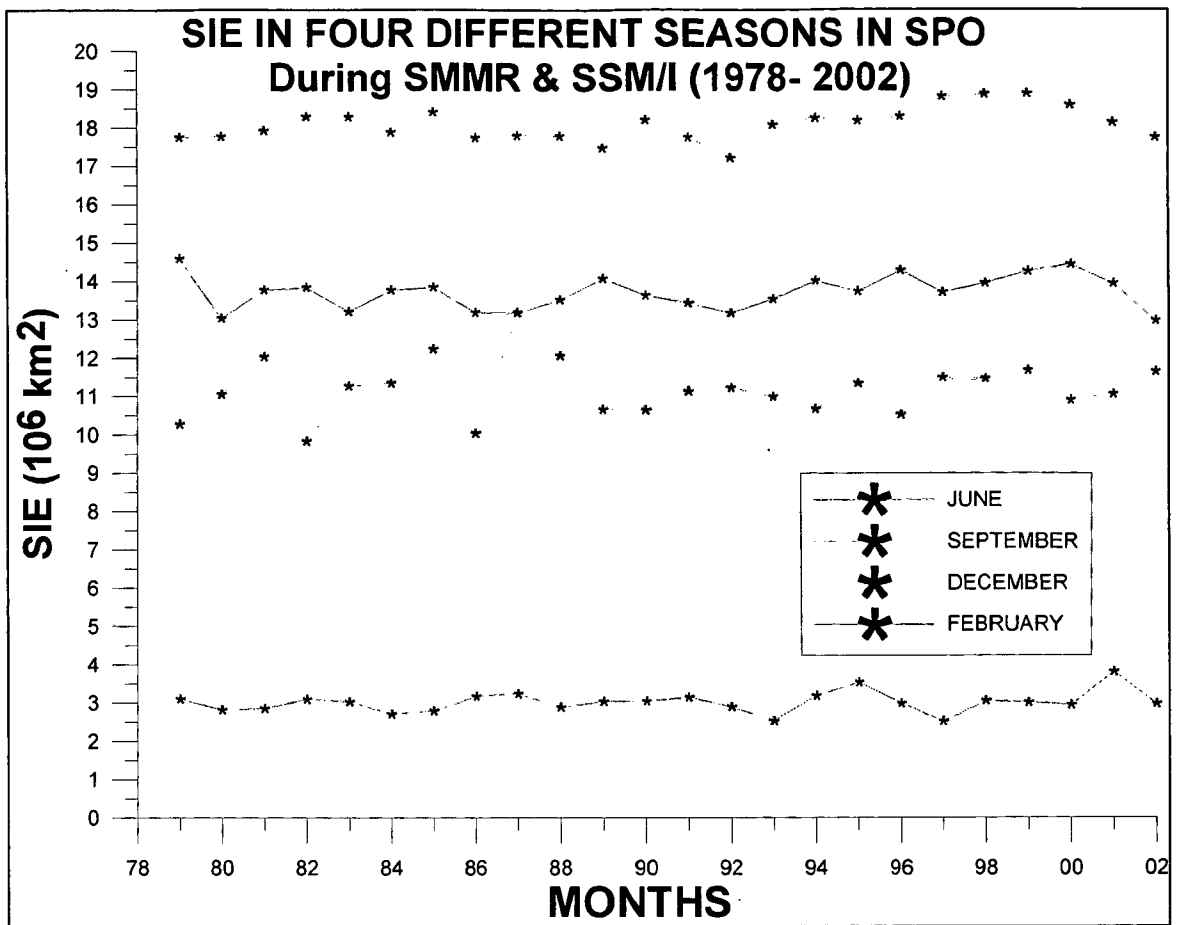


Fig 6.22: Four different Seasons SIE in the total SPO during SMMR and SSM/I period.

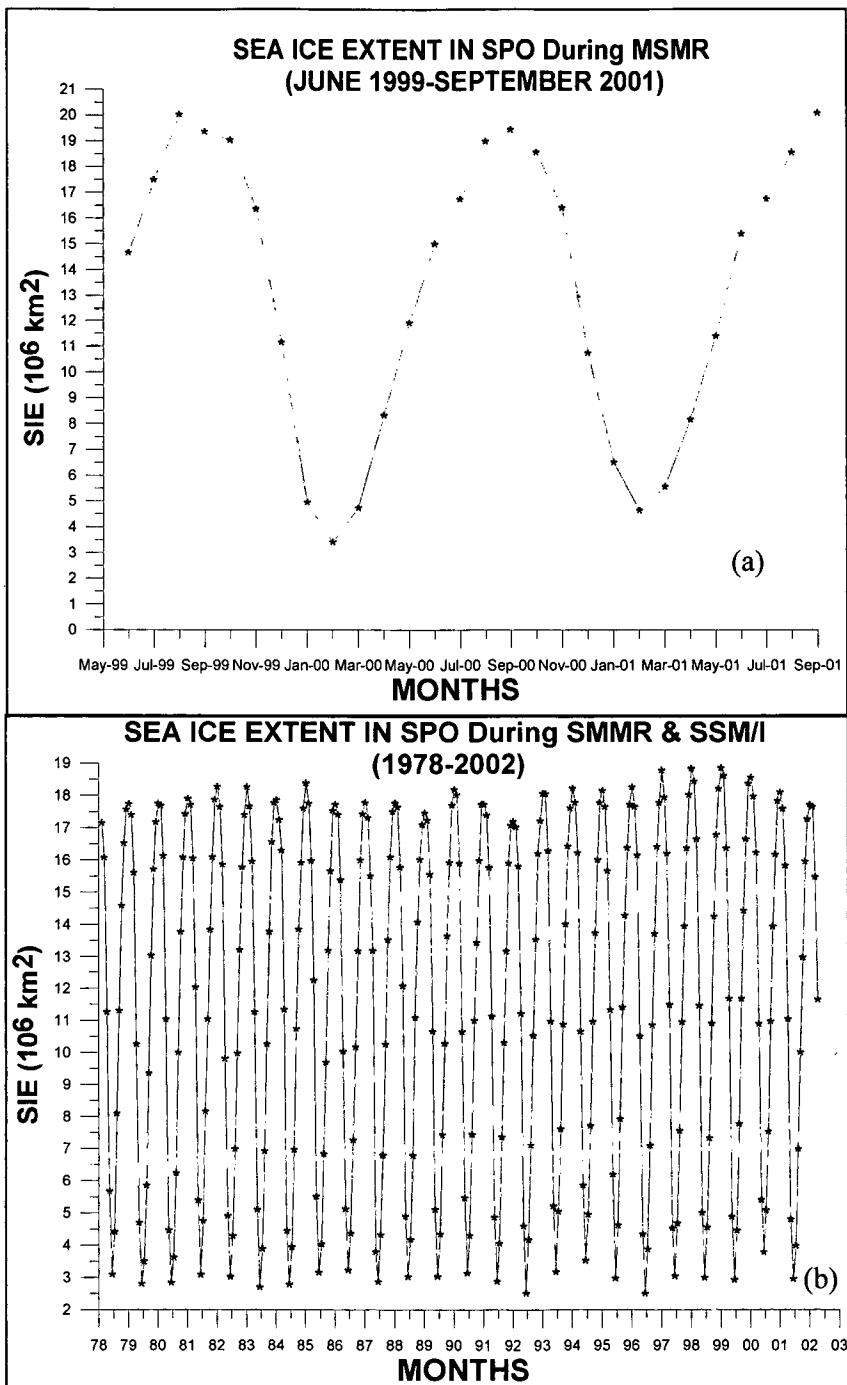


Fig 6.23: Monthly SIE in the total SPO during MSMR period (a) and long term monthly SIE from SMMR and SMM/I (b)

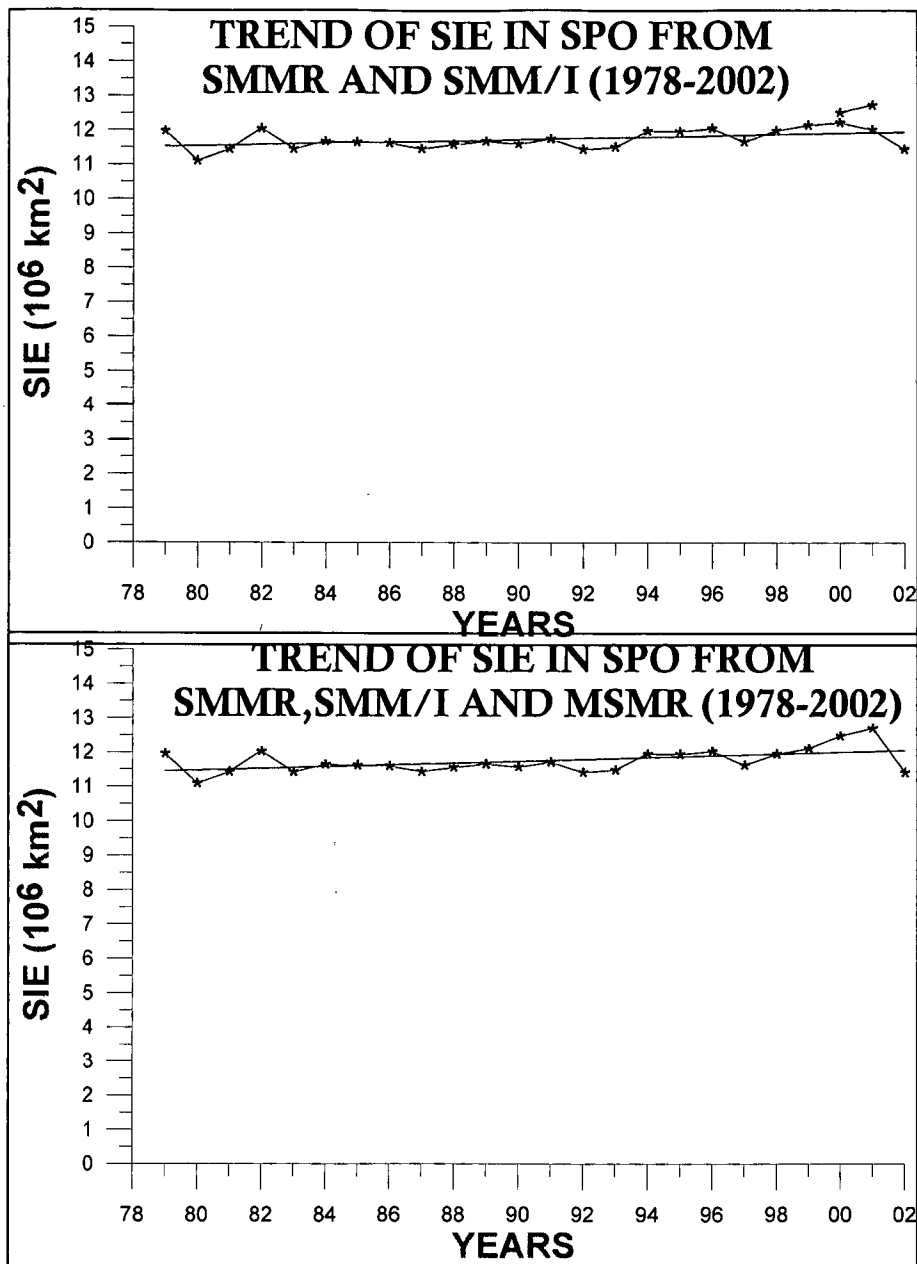


Fig 6.24: Yearly averaged SIE trend in the total SPO with SMMR and SMM/I (a) and from SMMR & SMM/I with MSMR (b)

Table –6. 2: Table of summary of ice extent and its rate of growth / decay in the SPO

Sl. No.	Sectors	Av. Sea ice Area in million km ² .	Rate of Annual increase or decrease per year (SMMR 1979-87 + SSM/I 1988-2002 period)	Rate of Annual increase or decrease per year (SMMR 1979-87 + SSM/I 1988-1998 + MSMR 1999-01 period)	% change per decade during 1978-2002	Remarks
1	Weddell sea	4.2	3,700 km ²	-4,600 km ²	-1.10	Slight trend rever from positive to negative.
2	Ross sea	2.8	-1,700 km ²	9,000 km ²	3.21	Trend reversal from negative to positive.
3	Indian Ocean	1.7	-300 km ²	4,500 km ²	2.65	Emergence of a positive trend.
4	Bellingshaus en and Ammundsen Sea	2.0	10,100 km ²	13,100 km ²	6.55	Slight increase in the positive trend.
5	Pacific Ocean	1.3	4,300 km ²	7,200 km ²	5.54	Slight increase in the positive trend
6	Total	12.0	16,100 km ²	29,200 km ²	2.43	Increase in the positive trend.

6. 6 TIME EVOLUTION OF THE MELTING PROCESS OF SEA ICE AS OBSERVED BY MSMR

We study the process of melting of sea ice from the images generated by MSMR, we find a strange phenomenon that the process of melting starts from the middle of the pack ice lying somewhere between the continental boundary and the marginal ice zone. Normally one would expect that the melting would start in the beginning of summer at the boundary of the ice in the relatively lower latitude zone where the prevailing temperatures would be higher compared to the higher latitude regions.

For a proper study, the MSMR data from 15 September to 15 March were processed at weekly interval for 1999-2000 and for 2000 - 2001. The images of the sea ice thus obtained were studied to see how the melting process gets initiated and how it progresses (See fig. 6.25 to 6.28).

An image represents the sea ice condition during the period 8-14 November, 1999. Here, no ice melting is observed. As we go over to the image of 15-22 November, we find that some ice starts melting at the point indicated by "A" (lying in the Weddell Sea) on the image. Here, the ice concentration has started reducing and thereby the brightness temperatures have started going down. In the third image, which belongs to the time period 24-30 November, further melting has taken place and the ice concentration is considerably reduced at point A. A new melting region has also emerged at point B in the Ross Sea. In the next image, which pertains to the period December 1-7, further melting has taken place and at A and B and fresh melting has started at D in the Pacific ocean sector. It is interesting to note that at all these points, the melting process starts in the middle of the high concentration ice zone. The areas melting in this way, look like polynyas that expand with time. As the season advances, we notice that these polynya-like structures grow in size and finally reach the marginal ice zone where they merge into the open ocean sometime in the month of December-January. Similarly, when we study the weekly interval images from the same season in the year 2000-2001, we find similar process taking place; albeit at some places the process of melting gets advanced or delayed by about a week.

Why this process of melting starts in the middle of the high concentration ice zone and not in the relatively warmer sea ice boundary zone, is still not well understood.

Coastal, or latent heat, polynyas form around Antarctica when strong persistent katabatic winds blow from the continental ice onto the sea ice. The winds push the sea ice offshore and expose the relatively warm ocean surface waters to the cold Antarctic atmosphere. The warm waters rapidly lose heat to the atmosphere (the heat flux can be 10-100 times that of ice-covered ocean; Gordon 1990) and freeze, resulting in the formation of large quantities of sea ice. The sea ice is then blown further offshore by the katabatic winds. The result can be a region of almost continual ice production. As the water freezes, brine is rejected into the underlying water column, increasing the local water density. The increased density, combined with heat loss to the atmosphere, results in intense mixing, and the very cold, oxygenated water is injected into the deep and bottom ocean where it is known as Antarctic Bottom Water (AABW) (Gordon & Comiso 1988, Gordon 1990, Smith *et al.* 1990).

The less common open ocean polynyas have characteristic diameters of 100km and are driven by the upwelling of warm ocean water, which maintains a large opening in the pack ice. Because the atmospheric heat loss from the open-ocean polynyas goes into cooling of the water column, they are sometimes called 'sensible heat' polynyas; because the heat loss from coastal polynyas goes into ice growth, they are called 'latent heat' polynyas.

The open-ocean polynyas generally occur away from the coast, and are driven by the upwelling of warm sea water. These polynyas are self-maintaining, in that as heat is lost to the atmosphere at the surface, the surface water becomes denser and sinks, driving future convection. The convection ceases when the atmosphere warms in spring, or if sufficient fresh water, either produced locally by melting, or advected into the region, places a low-salinity cap on the convection.

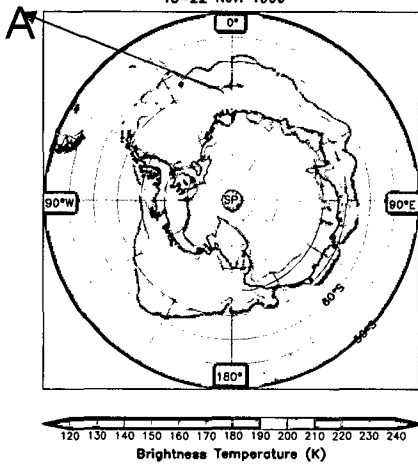
The polynya-like formations that we see on the MSMR images in the months of November-December do not belong purely to either of the two categories. They form in spring and not in winter, so the initiation of the formation process takes place due to

increasing solar insolation. The question is that why they don't initiate in the marginal ice zones where higher solar insolation is received during the same period of the year. The possible reasons could be the vigorous air sea interaction in these zones or the convective overturning of the water column below that lead to excess heat input at these places resulting into the earlier initiation of the melting process there. We can sum up that they originate in the middle of the ice zones by the joint effect of the solar insolation, supply of heat through oceanic thermal convection and / or the influence of atmospheric winds.

BRIGHTNESS TEMP. MAP OF THE ANTARCTIC

OCEANSAT-1 MSMR 18 GHz(H)

15-22 Nov. 1999

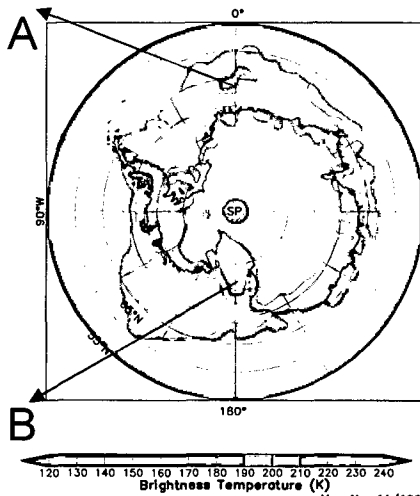


Map No. 11/1999

BRIGHTNESS TEMP. MAP OF THE ANTARCTIC

OCEANSAT-1 MSMR 18 GHz(H)

24-30 Nov. 1999

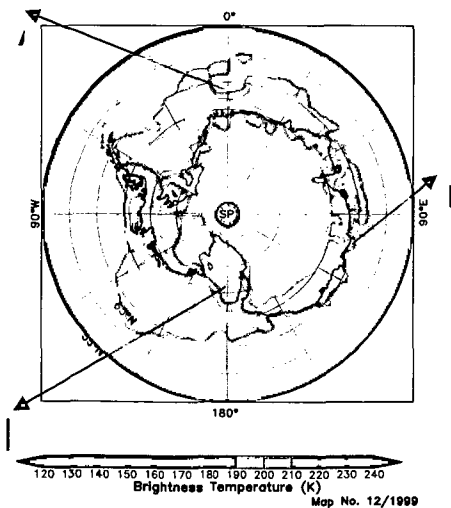


Map No. 11/1999

BRIGHTNESS TEMP. MAP OF THE ANTARCTIC

OCEANSAT-1 MSMR 18 GHz(H)

01-07 Dec. 1999

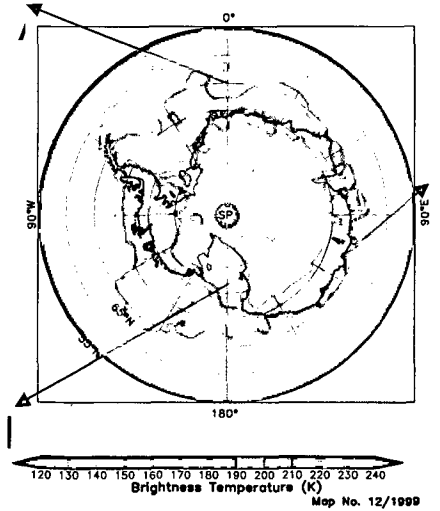


Map No. 12/1999

BRIGHTNESS TEMP. MAP OF THE ANTARCTIC

OCEANSAT-1 MSMR 18 GHz(H)

08-14 Dec. 1999

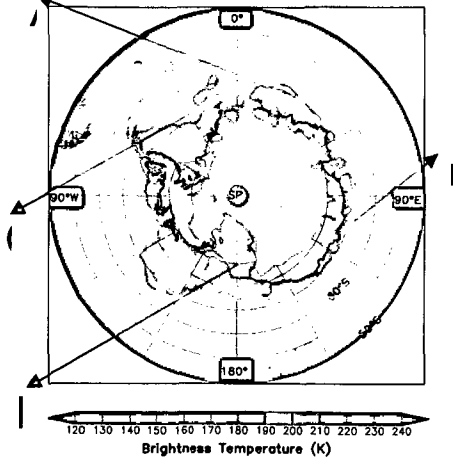


Map No. 12/1999

BRIGHTNESS TEMP. MAP OF THE ANTARCTIC

OCEANSAT-1 MSMR 18 GHz(H)

15-22 Dec. 1999

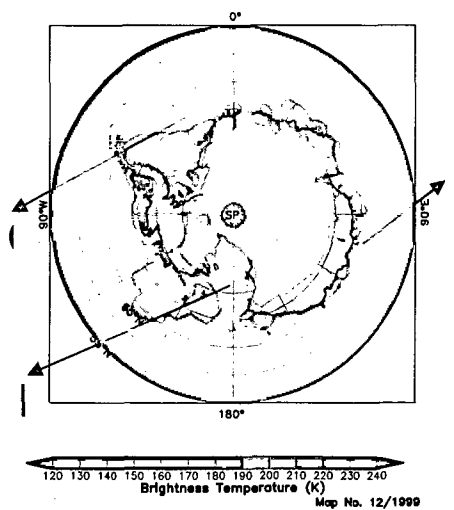


Map No. 12/1999

BRIGHTNESS TEMP. MAP OF THE ANTARCTIC

OCEANSAT-1 MSMR 18 GHz(H)

23-28 Dec. 1999



Map No. 12/1999

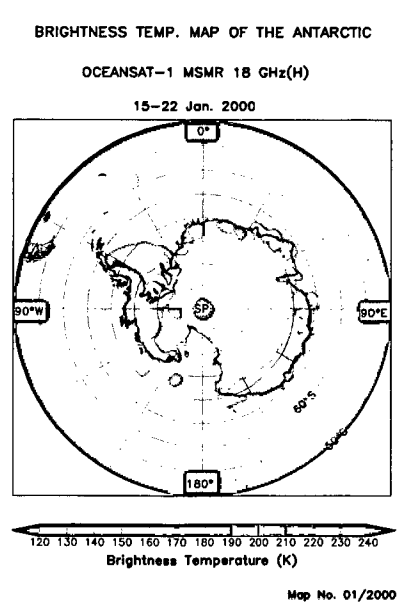
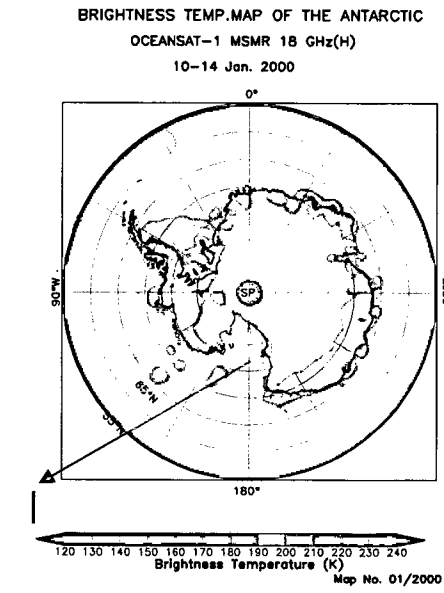
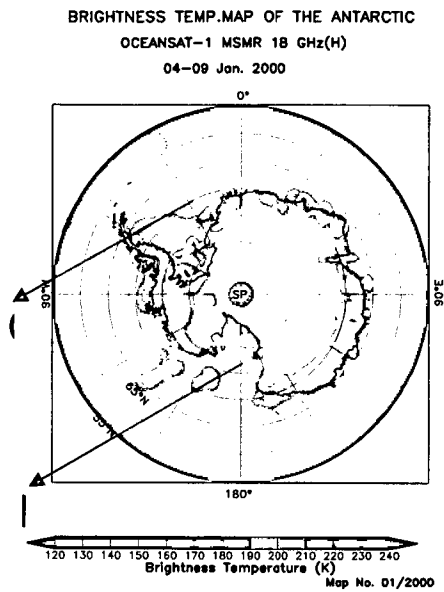
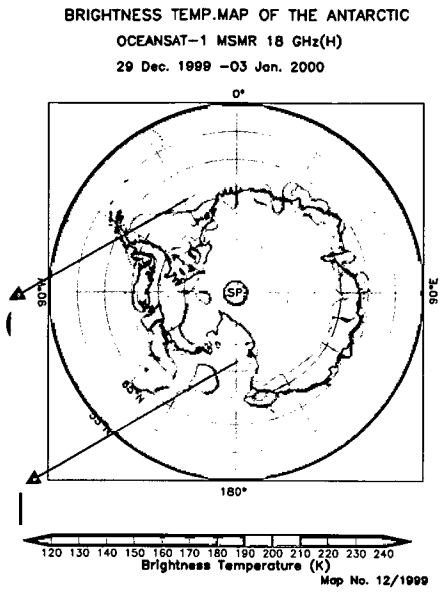
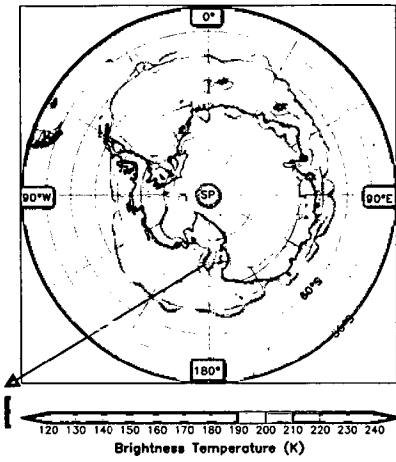


Fig 6.25 (b)

OCEANSAT-1 MSMR 18 GHz(H)

15-22 Nov. 2000

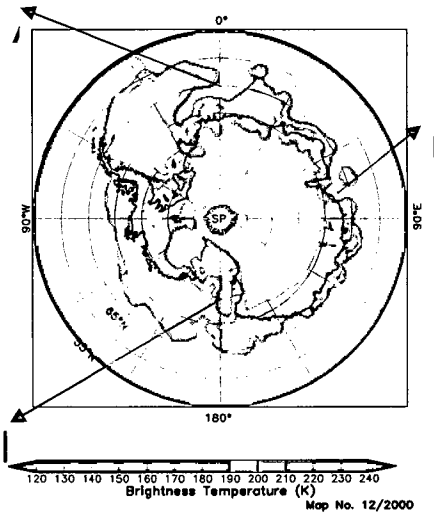


Map No. 11/2000

BRIGHTNESS TEMP.MAP OF THE ANTARCTIC

OCEANSAT-1 MSMR 18 GHz(H)

01-07 Dec. 2000

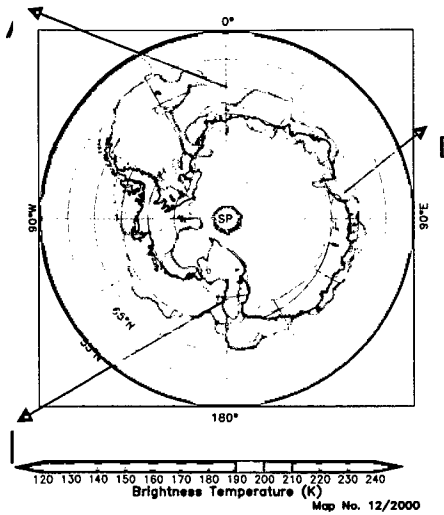


Map No. 12/2000

BRIGHTNESS TEMP.MAP OF THE ANTARCTIC

OCEANSAT-1 MSMR 18 GHz(H)

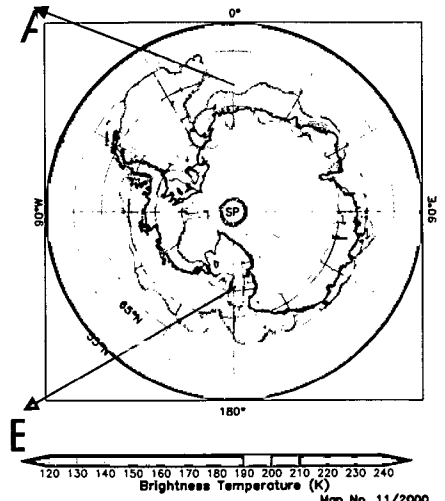
08-14 Dec. 2000



Map No. 12/2000

OCEANSAT-1 MSMR 18 GHz(H)

23-30 Nov. 2000

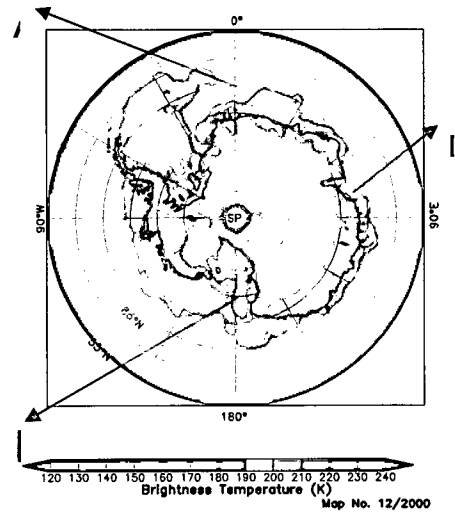


Map No. 11/2000

BRIGHTNESS TEMP.MAP OF THE ANTARCTIC

OCEANSAT-1 MSMR 18 GHz(H)

08-14 Dec. 2000

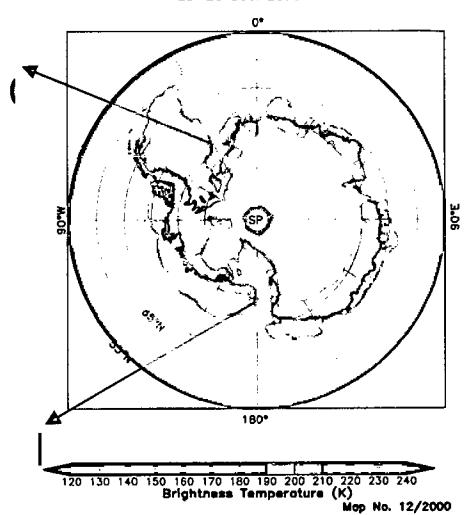


Map No. 12/2000

BRIGHTNESS TEMP.MAP OF THE ANTARCTIC

OCEANSAT-1 MSMR 18 GHz(H)

23-28 Dec. 2000



Map No. 12/2000

Fig 6.25 (c)

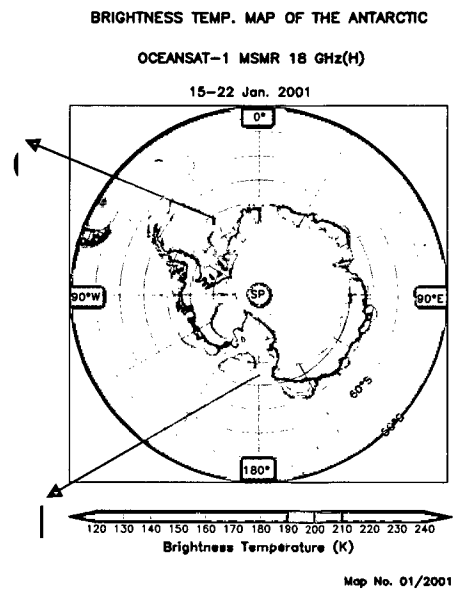
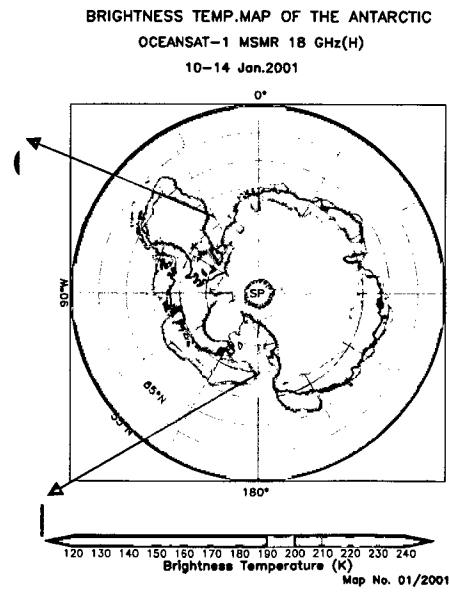
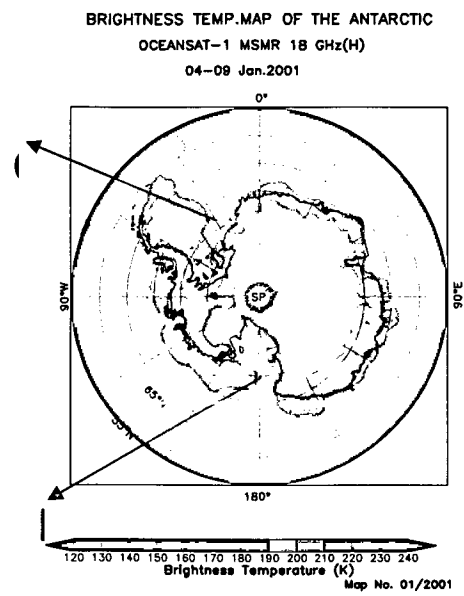
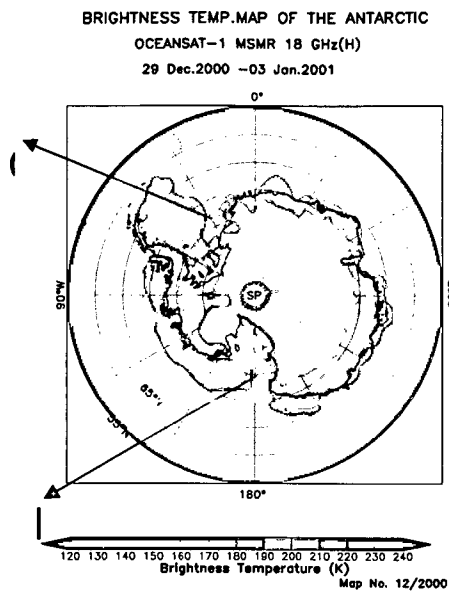


Fig 6.25 (d)

Fig 6.25: Evolution of melting process in the SPO during MSMR period (a,b,c,d)

CHAPTER -7

SEA ICE COVER OVER THE NORTHERN POLAR REGION (NPR)

7.1 INTRODUCTION

In previous chapter the sea ice in the SPO was discussed. This chapter is related to the sea ice in the North Polar Region (NPR). The NPR ice is a very important component of the earth's environment. Unlike the Antarctic, large human populations inhabit the NPR. This region has severely cold climate. Prolonged hours of daylight and darkness prevail here in summer and winter respectively. Large parts of land and ocean remain covered here with snow and ice throughout the year. The prevailing hostile environment has shaped the life style of the people living in these regions.

It is well known fact that Sea Ice cover over both the Polar Regions plays a major role in global as well as regional climate system. For instance, it works as an effective insulator between ocean and atmosphere. It restricts exchange of heat, mass momentum and chemical constituents. In winter, atmosphere is cool but sea remains relatively hot, so transfer of heat takes place from only open water and thin ice layer regions of ocean. In this way ice disturbs the thermodynamic cycle between ocean and atmosphere. An atmospheric change due to different causes (whether it is anthropogenic or natural) also affects the ice coverage extent in both the Polar Regions. So it can be said that the sea ice extent is a sensitive indicator of climate change.

Another role of SIE in climate system is due to its surface albedo. Surface albedo of water is only (10-15%) (Lamb, 1982), whereas sea ice albedo is around 80% (Greenfell, 1983). If there is fresh snow cover on sea ice then albedo increases up to 98% (vowinckel and orvig 1970). Due to higher albedo of SI in polar region, amount of solar radiation absorbed by the earth's surface is decreased considerably. This also contributes to the unequal distribution of energy in the lithosphere; it also contributes in disturbing the heat balance in the system. Insolation and albedo effects have important implications for climate change scenarios because they contribute to positive feedback mechanism (Kellogg, 1975).

Sea ice processes effects directly oceanic circulations by the rejection of brine during ice growth in winter. High density water goes down and starts convection driving the thermohaline circulation of the ocean. In addition to its importance in climate processes,

Sea ice plays an important role in the oceanic biome including location of certain fisheries and species. In this way we see, sea ice processes take part in climate change on global as well as regional scale.

For nearly two and a half decades, satellite data derived sea ice products are available. By observing these one cannot conclude about time scale of the climate change on global as well as regional basis. The existing satellite records have been used for the study of SIE in the polar region (Vyas, et al 2003; Bhandari, et al., 2005; Campbell et al., 1984; Parkinson et al., 1987; Gloersen and Campbell, 1988, Parkinson and Cavalieri, 1989, Budd, 1975; Kukle and Gavin, 1981; Zwally et al, 1983). Gloersen and Campbell (1988), using both ESMR, and SMMR data sets studied the sea ice extent variations on global scale.

7.2 SECTOR DEFINITION OF THE OCEAN IN NORTHERN POLAR REGION (NPR)

In the Northern Polar Region, most of the Seas are bounded by land like Arctic ocean, Baffin bay, Hudson bay and Canadian Archipelago. Bering Sea, Greenland Sea, Kara & Barents seas and Sea of Japan & Okhotsk are open to oceans. At the end of melt seasons about 60% of sea ice still remains in the Arctic region compared to 13% in the SPO (Gloersen, 1992).

“Gloersen et al. (1992)” define the sectors in terms of no. of grid cells, each having a fixed size in terms km x km. We have defined the sectors in terms of geographical latitude-longitude boundaries, with grid cells each having a 0.5 deg. x 0.5 deg. size. So, the boundaries defined by us differ slightly from those defined by them. Consequently the sector areas calculated by them and those calculated by us also differ slightly.

The distribution of the sea ice cover in the Arctic region in the six sectors Arctic Ocean, Bering Sea, Seas of Japan & Okhotsk, Greenland Sea, Kara & Barents seas and North American sector which include Baffin bay/Davis Strait/Labrador Sea, Gulf of St. Lawrence, Hudson bay and Canadian Archipelago (table 7.1). For making study convenient in large northern hemisphere region between 45°N and 90°N it has been divided into six different sectors (fig 7.1 & Political Map is shown in fig 7.2).

Their geographical locations is given in the table 7.1. These six sectors are Arctic ocean, Bering sea, Greenland ocean, Kara and Barents sea, Japan and Okhotsk sea and North American sector (includes Hudson Bay, Baffin Bay, Davis strait Labrador sea and Canadian Archipelago). We have calculated the real areas of these sectors including open water and ice extent in these sectors. Area calculation calculation algorithm is described in detail in chapter 6. Out of these six sectors Arctic Ocean has the largest area of all. Its area is $6.9029 \times 10^6 \text{ km}^2$.

Table 7.1: Definition of Sectors in the North Polar Region

Sr. No.	Name of the Sector	2.9 Latitude		2.10 Longitude	
		From	To	From	To
1.	Bering Sea Sector	56.0° N 52.0° N	66.0° N 56.0° N	163.0° E 172.0° E	203.0° E 195.0° E
2.	Seas of Japan and Okhotsk	45.0° N 45.0° N	63.0° N 60.0° N	140.0° E 127.0° E	160.0° E 140.0° E
3.	Kara and Barents Seas	65.0° N	81.0° N	17.0° E	102.0° E
4.	Greenland Sea	57.0° N 62.5° N 71.5° N	62.5° N 71.5° N 81.0° N	315.0° E 315.0° E 315.0° E	340.0° E 355.0° E 17.0° E
5.	N. American Sector				
5A		45.0° N	82.0° N	270.0° E	315.0° E
5B		55.0° N	78.5° N	247.0° E	270.0° E
5C		65.0° N	76.5° N	236.0° E	247.0° E
6.	Arctic Ocean				
6A		76.5° N	90.0° N	236.0° E	247.0° E
6B		78.5° N	90.0° N	247.0° E	270.0° E
6C		82.0° N	90.0° N	270.0° E	315.0° E
6D		81.0° N	90.0° N	315.0° E	16.0° E
6E		81.0° N	90.0° N	16.0° E	102.0° E
6F		70.0° N	90.0° N	102.0° E	163.0° E
6G		66.0° N	90.0° N	163.0° E	203.0° E
6H		68.0° N	90.0° N	203.0° E	236.0° E

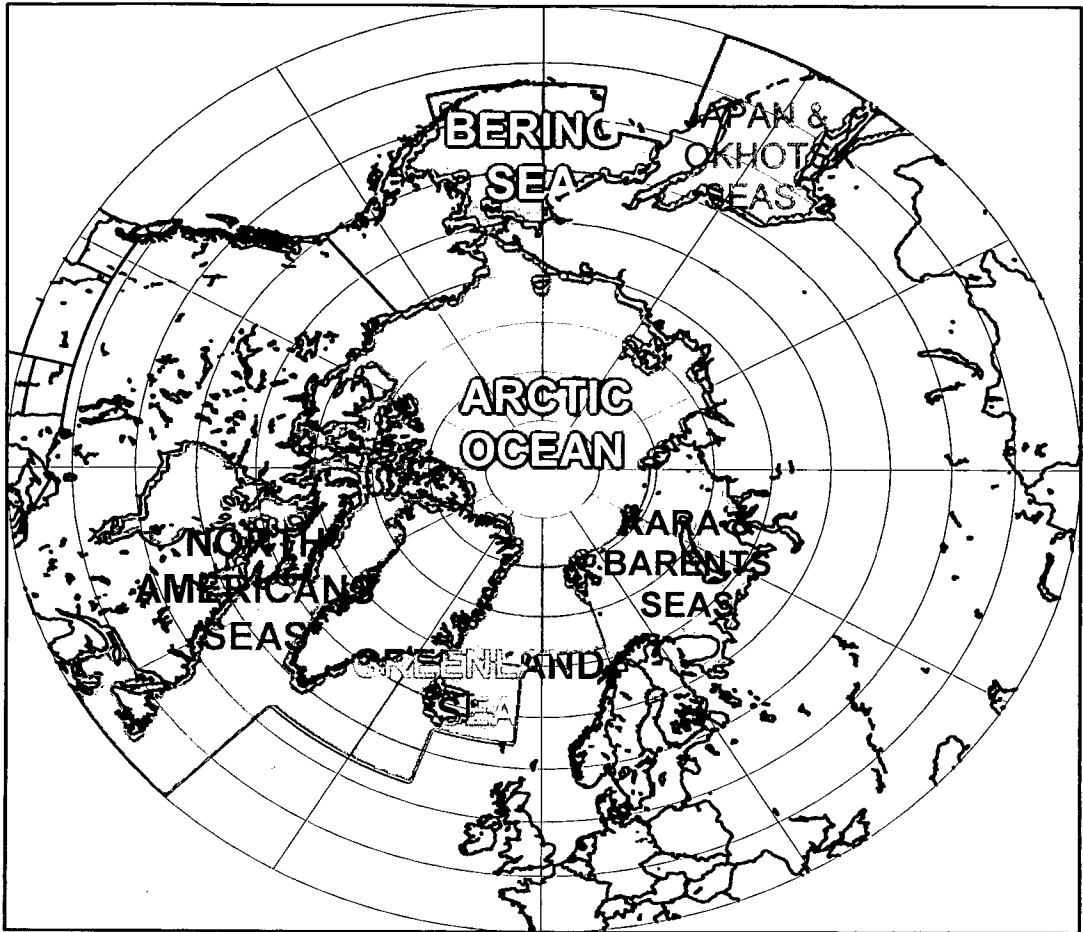


Fig 7.1: Base map of the different sectors of the study area of the Northern Polar Region



Fig 7.2: Political Map of the Northern Polar Region

7.3 METHODOLOGY

For the study of SI in the NPR, we have adopted the methodology as we have earlier used for the study of the SPO, described in detail in section 6.3 of the previous chapter. Minor differences are described below.

The wintertime sea ice boundaries in the NPR expand to much lower latitudes than in the SPO. Therefore the lower boundary in the study region is kept at 45° N. The classification procedure used between the sea ice and the open water involved the supervised technique where previously known areas of open water and sea ice (through SSM/I SIC maps) were taken and separate clusters of brightness temperatures were formed. The analysis was extended to include different seasons of the year. The optimal boundary (the discriminate function) between the two classes is found to be at $T_B = 150$ K.

To reconfirm the validity of the above threshold, 4 transects were taken across the ice-water boundary at longitudes 0°, 90° E, 180° E, 270° E. The variations of the T_B along the transect were plotted and the T_B at the center point of the steep slope at the ice edge was determined for each of the transects. Then the average of the T_B 's at the four center points was taken and rounded off to the nearest integer. This also confirmed that $T_B = 150$ is the optimal boundary for the classification of open water and sea ice in the NPR.

The annual average is taken from October of the previous year to the September of the current year. This is because, the less of ice cover occurs in the month of September, and the next cycle of the growth and the decay of the ice starts from October and goes up to September next. We have kept the same cycle under consideration for our analysis.

Fig. 7.3: T_B Images shows monthly variation of sea ice in the NPR as observed by MSMR from June 1999 to September 2001. Fig 7.4 puts into perspective the MSMR T_B images of corresponding months in the years 1999, 2000 and 2001 for ease of comparison.

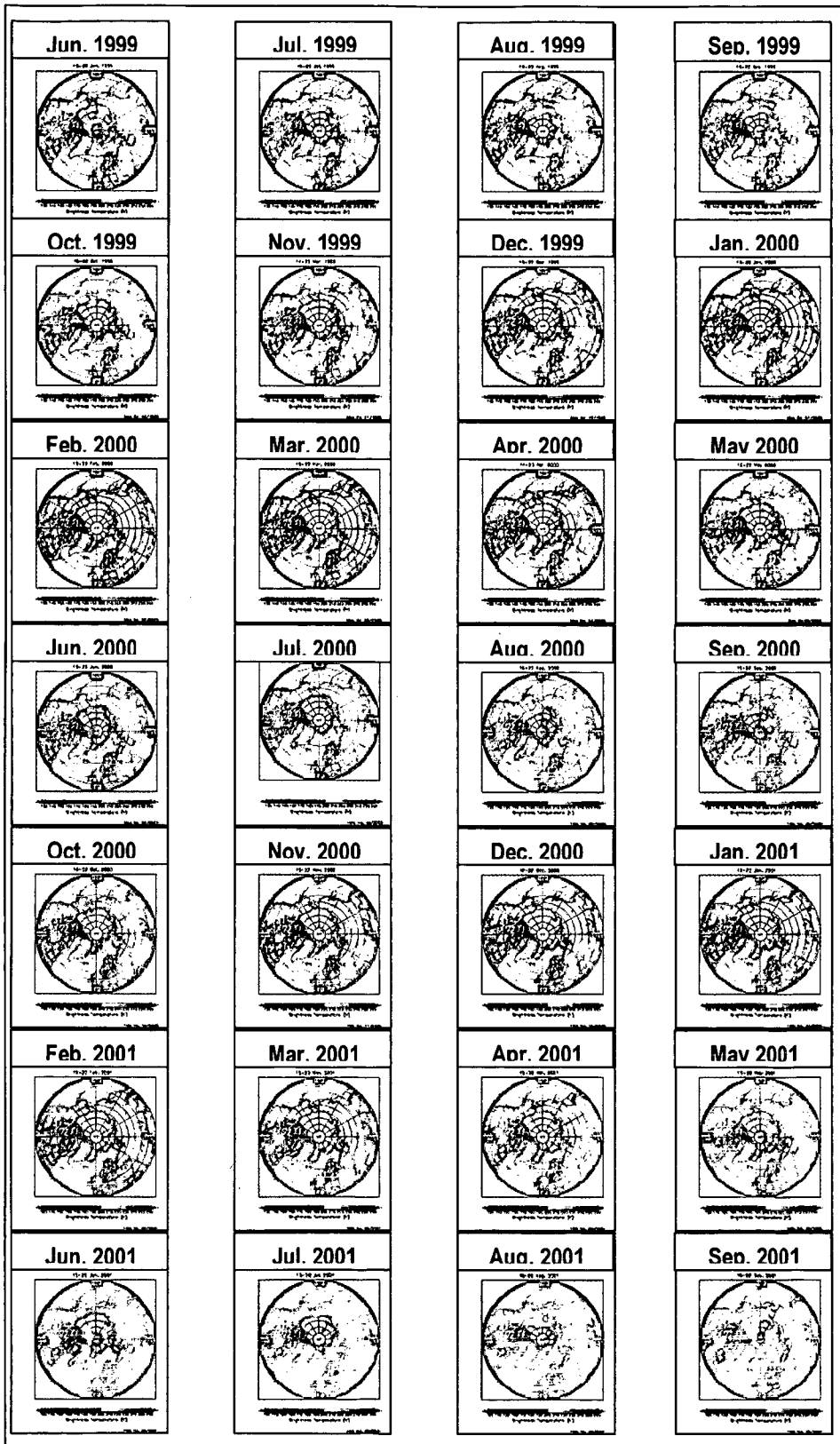


Fig. 7.3: Brightness Temperature Maps from MSMR – Total set at a glance.

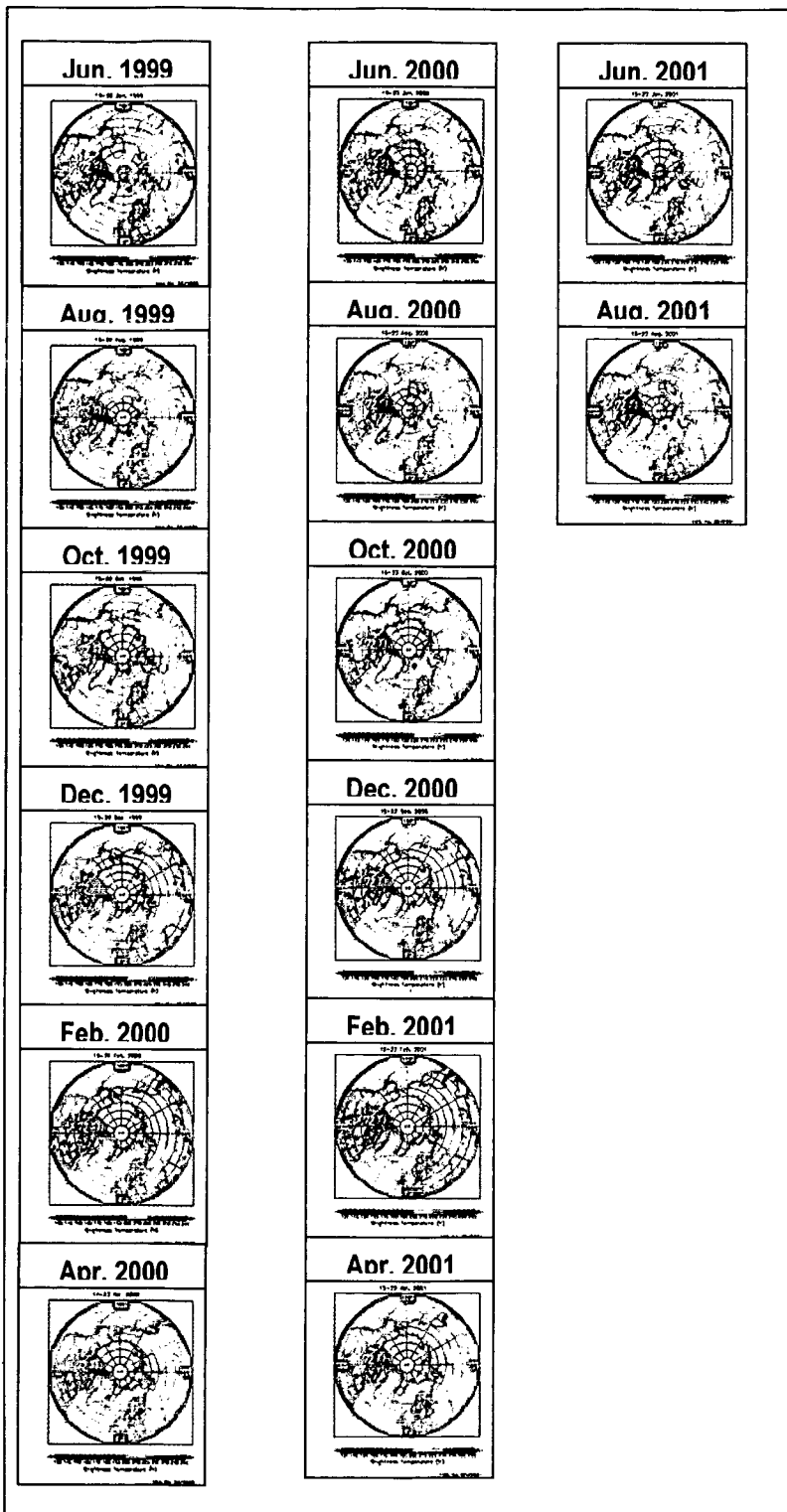


Fig 7.4: MSMR T_B Images Seasonal and Inter-annual variation of Sea Ice in the NPR

7.4 INTER-COMPARISON OF MSMR & SSM/I DATA

Space-borne sensors are ideal for monitoring the polar ice and its seasonal and inter-annual variability. Microwave data over these regions is available for more than two and a half decades now. The monthly sea ice extents derived from the MSMR and SSM/I sensors during 1999-2001 have been compared in the NPR also as we did earlier for SPO as described in chapter 5. The Oceanic region, lying within the Arctic Ocean is considered in this study. In this study also it is found that the MSMR results agree well with those obtained from SSM/I data (fig 7.5). The monthly sea ice is determined from June 1999 – September 2001 by the classification of ice and open water through the thresholding technique. Data of 18GHz (H) channel of MSMR was used for this study. For purpose of comparison and validation, SSM/I concentration data for the period of June 1999- September 2001 was processed and results are shown in fig 7.6. It is found that the results obtained from MSMR data agree well with those obtained from SSM/I data.

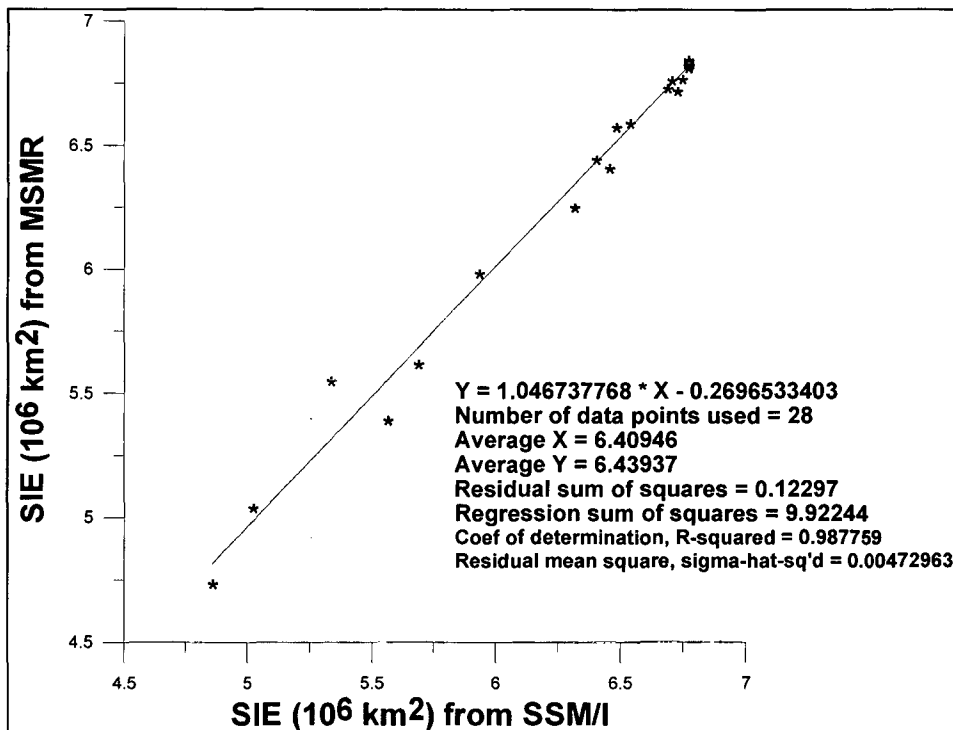


Fig 7.4: Inter-Comparison in SIE in the Arctic Ocean Sector between MSMR & SSM/I during June 1999- September 2001

7.5 INTER-ANNUAL VARIATION OF SEA ICE EXTENT

For the study of Arctic region sea ice, we have used the time series of SIE, SIC and open water area of last two and a half decades obtained from the three sensors SMMR, SSM/I and MSMR. SIE is taken as the area lying from the coastline to the boundary between the ice infested seawater and open sea water in the marginal ice zones (Dash et al .2003). We have assumed 15% SIC as the boundary between the open water and the sea ice cover. The ice extent includes both the area covered by the ice packs and the area covered by the intermittent water. The open water within the ice packs is the actual area covered by water lying in between the ice packs, available within the ice extent boundary.

$SIE = SIA + \text{open water within the ice packs.}$

For examining interannual variability of SIE and SIA we have calculated both of these for the whole region and also for the individual sectors. All these are calculated year by year and month-by-month for each year. The year-by-year and month-by-month variability for each sector is discussed in the following sections.

7.5.1 Bering Sea

Bering Sea has an area of 2,274,020 km². It is the northern part of the Pacific Ocean lying between between Siberia and Alaska. It Sea is surrounded by the Bering Strait on the north, by the Aleutian islands on the South, by the Siberian coast on the west and by the Alaskan coast on the east. Ocean currents moving in the NW-SE direction across the sea, help in limiting the further growth of ice in winter time. Ice begins to grow in early autumn. By November, the ice starts appearing along the northern coast lines. By March it covers the major part of the Bering Sea. From June Bering Sea Ice starts rapidly melting and in June, and in September, it remains completely ice-free.

Winter and summer sea ice extent cycle of last 24 years is given in Fig (7.2.2). Max extent in March varies from 0.65x10⁶ km² in 1995 to 0.95 x10⁶ km² in March 1984. The seasonal cycle of sea ice extents for the last 24 years reveals a considerable inter-annual variation. (Comiso 2000)

The T_B images of four different seasons are shown in fig 7.6. The SIE in the same seasons during the SMMR and SSM/I period shown in fig 7.7 (a). The SIE in MSMR period is shown in fig 7.8. The SIE in SMMR and SMM/I period is shown in fig 7.9 (a). The secular trend in SIE with SMMR and SMM/I and SMMR, SMM/I and MSMR is shown in fig 7.10 (a) (b) respectively.

This interannual variability in seasonal growth of the Bering Sea ice cover is associated with interannual changes in the position of the Aleutian Low (Cavalieri and Parkinson, 1987). Study of interannual variability in SIE is explained in the light of meteorological and /or oceanographical influences previously (Johnson 1979, Gratz 1983).

7.5.2 Seas of Japan and Okhotsk

Seas of Japan & Okhotsk are located approximately between 50° - 60° N and are bounded largely by Kamchatka peninsula, Siberia, Sakhalin island, and Kuril island chain. The sea of Okhotsk (area: 1,528,100 sq km), remains free of sea ice from July to October. Sea ice starts forming in November and covers most part of the sea in March. It remains up to May and then starts melting. The Sea of Japan, located further South, has a very small area at its northern which is covered by ice, that too only during December to March. Seas of Japan & Okhotsk remain ice free in summer.

Seas of Okhotsk and Japan have the peak of the ice extent in March. They are ice free in summer. The sea ice cover begins to form in late November in some of the coastal locations in the northeastern and northwestern sea of Okhotsk. The ice cover then slowly expands in the north and gradually forms along Sakhalin Island in December and along the Kamchatka peninsula coast in January-February. Then the ice advances to cover the center of the sea of the Okhotsk. This coverage remains up to the middle of March. Then, the ice starts retreating from the central parts, which continues up to April. By June, the ice remains only in the northern coastal areas.

The warm saline water of the Kamchatka current moving northward along the Kamchatka peninsula in the west causes the strong east west asymmetry in the ice cover. The warm water flow delays ice formation in the autumn and winter and speeds up ice decay in

springs. (Glorosen et. al 1992) General feature of annual cycle of sea ice distribution is that the ice forms first in cold, shallow low salinity water and then drifts in the direction approximating the basically counter clockwise current pattern of Okhotsk gyre.(Parkinson and Gratz 1983).

The T_B images of four different seasons are shown in fig 7.6. The SIE in the same seasons during the SMMR and SSM/I period shown in fig 7.7 (b). The SIE in MSMR period is shown in fig 7.8. The SIE in SMMR and SMM/I period is shown in fig 7.9 (b). The secular trend in SIE with SMMR and SMM/I and SMMR, SMM/I and MSMR is shown in fig 7.11 (a) (b) respectively.

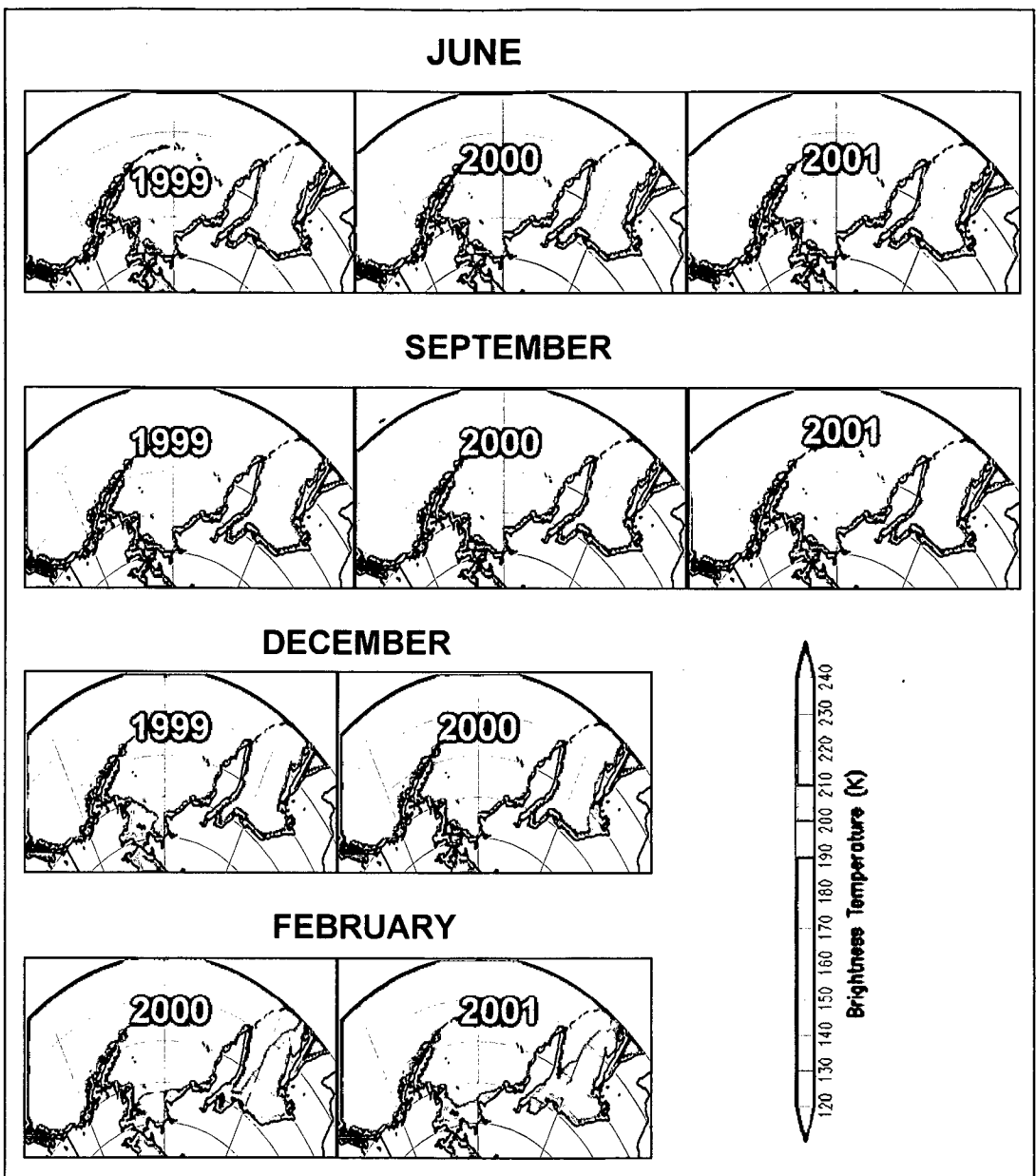


Fig 7.6: MSMR T_B images of different seasons in Bering Sea and Japan & Okhotsk Seas Sectors

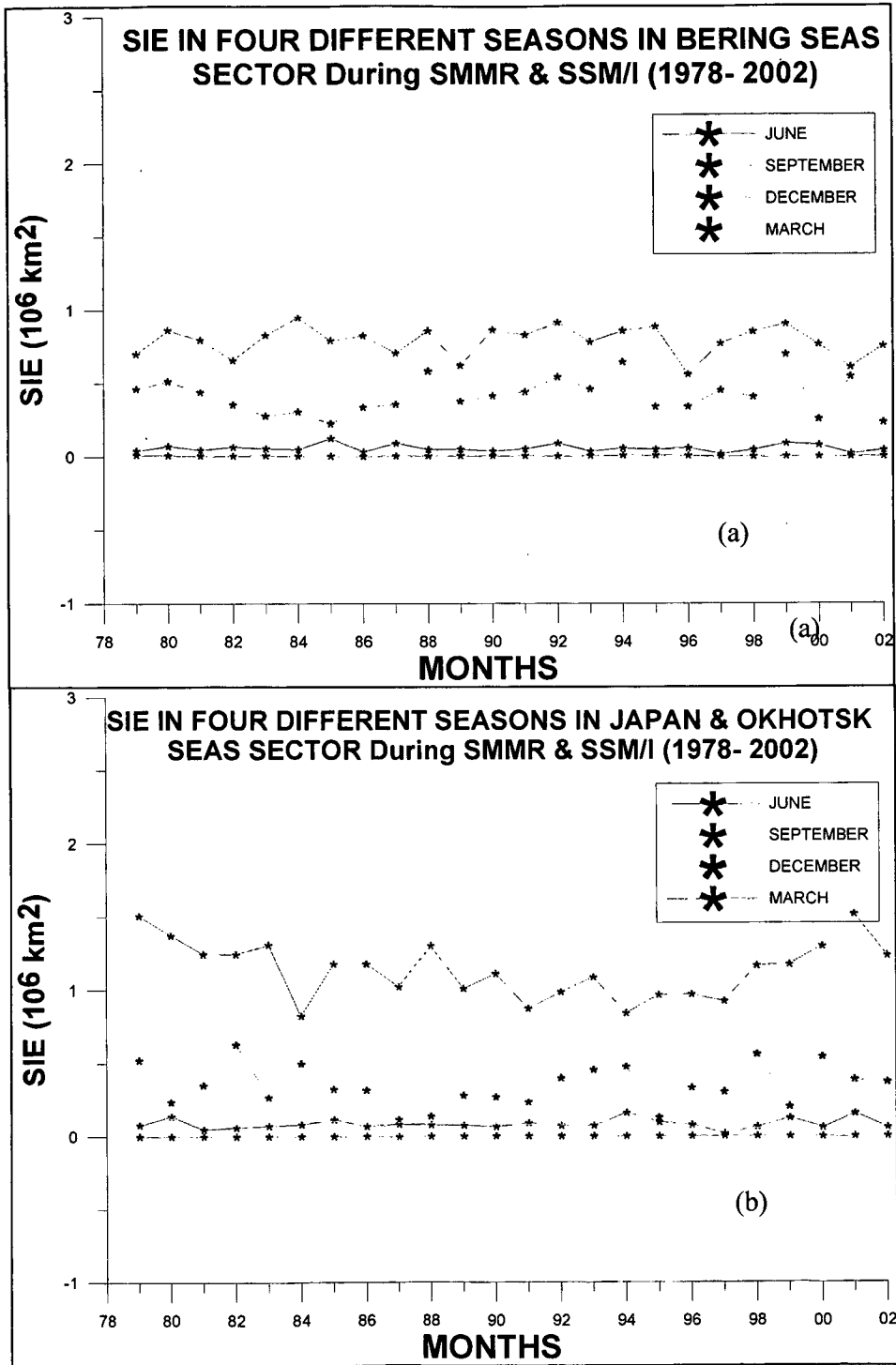


Fig 7.7: SIE in four different Seasons in Bering Sea (a) and Japan & Okhotsk Seas (b) Sectors during SMMR and SSM/I Period

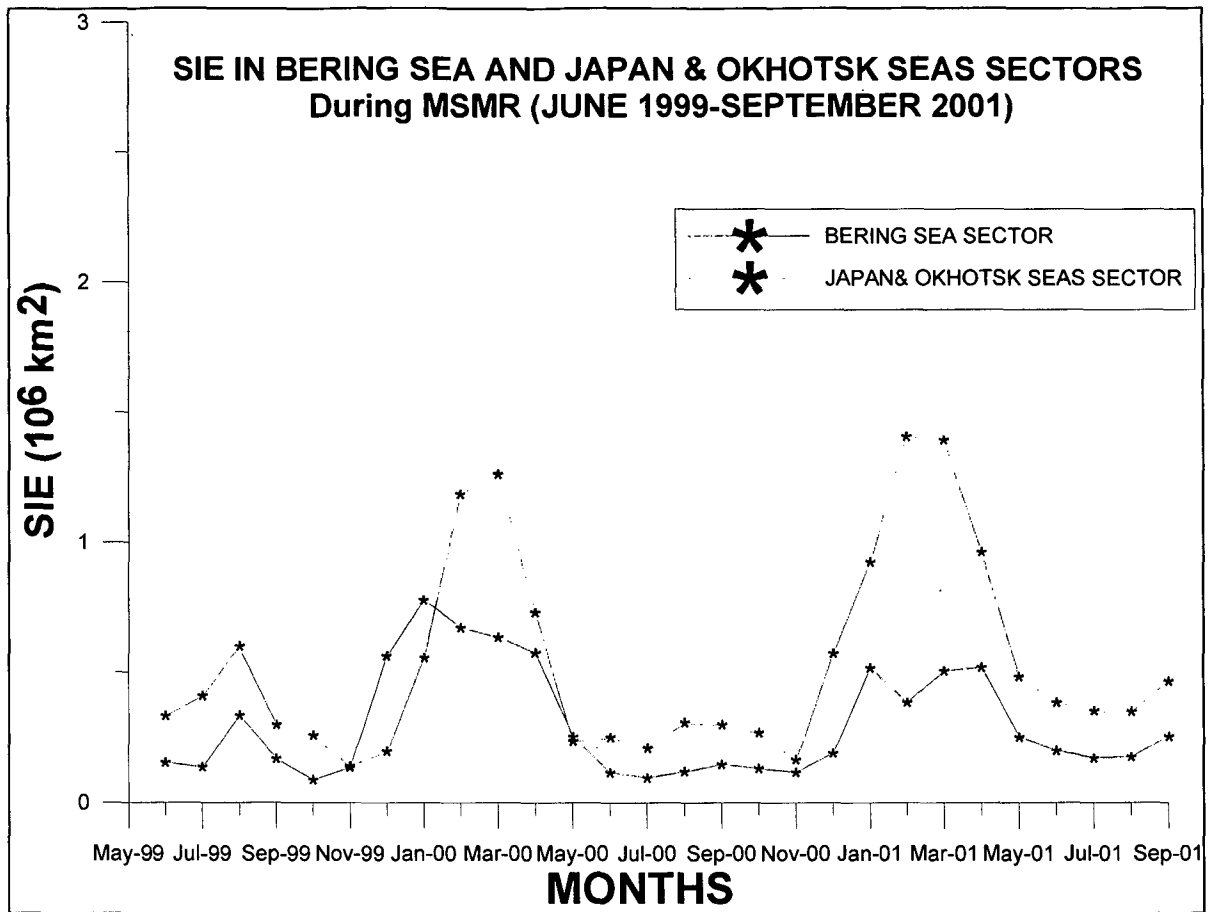


Fig 7.8: The monthly SIE in Bering Sea and Japan & Okhotsk Seas Sector during MSMR period

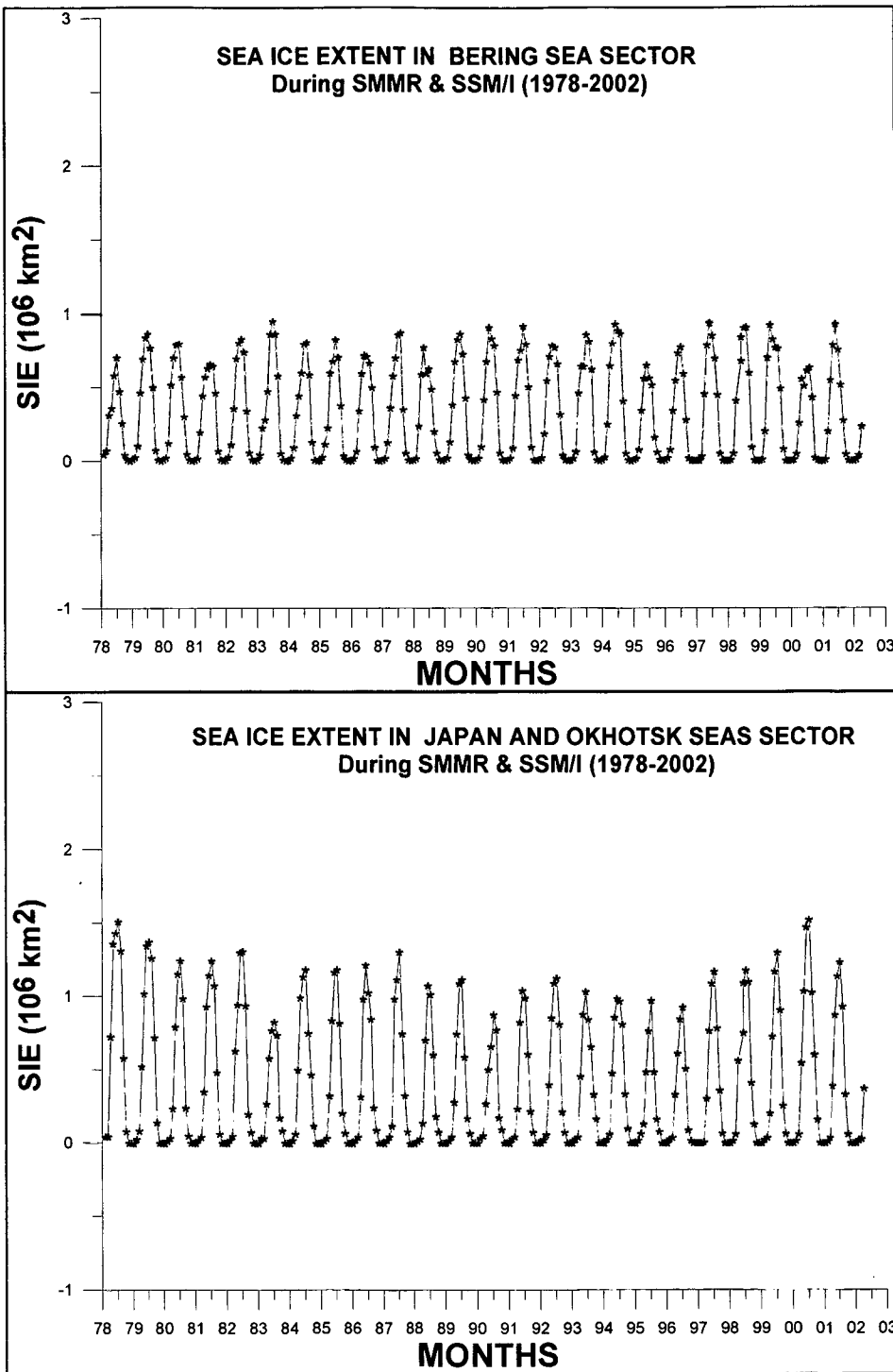


Fig 7.9: Long term monthly SIE in Bering Sea Sector (a) and Japan & Okhotsk Seas Sector (b) from SMMR and SSM/I

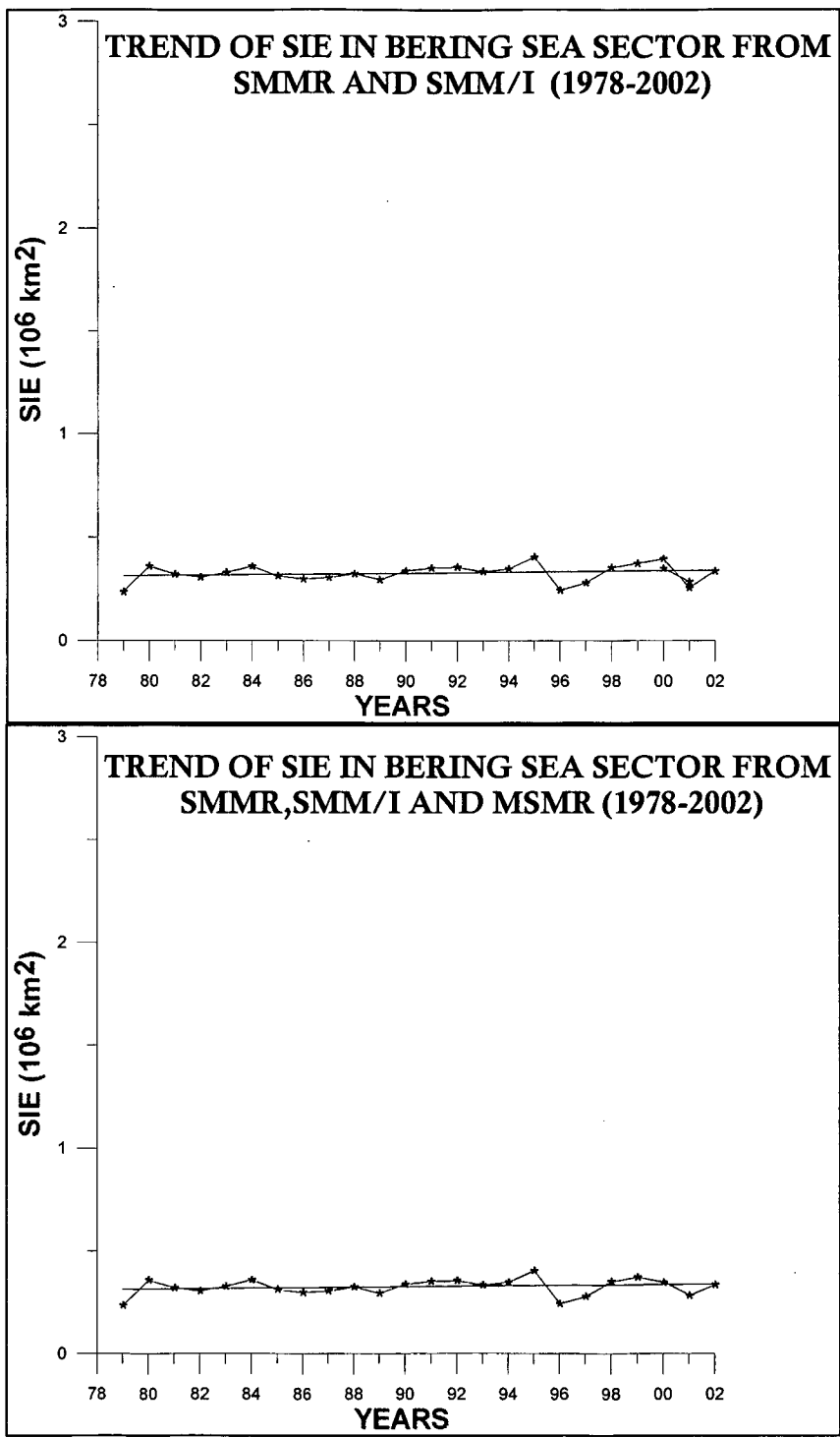


Fig 7.10: Yearly averaged SIE trend in Bering Sea Sector from SMMR and SMM/I (a) and from SMMR and SMM/I with MSMR (b)

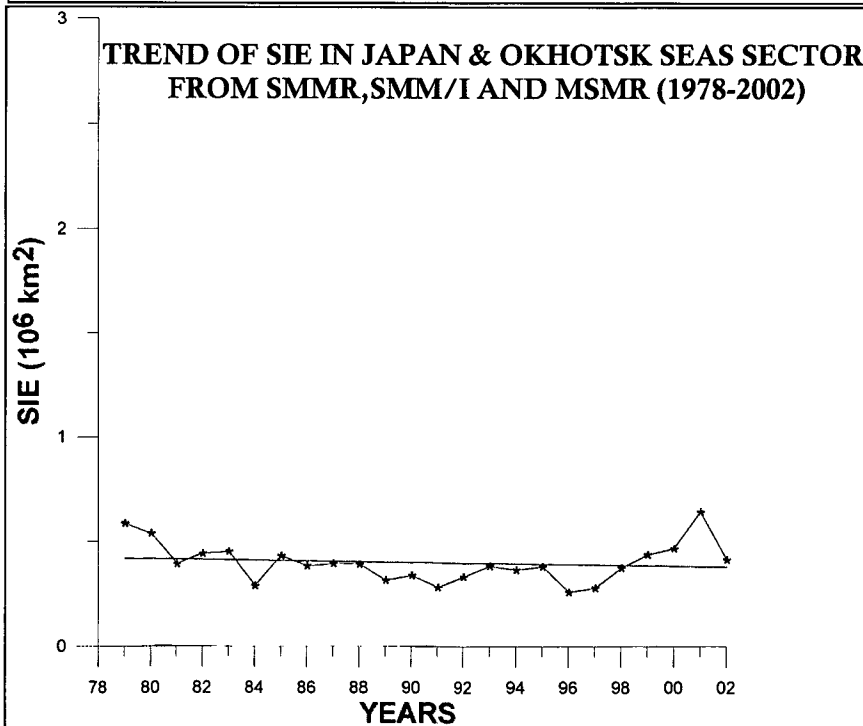
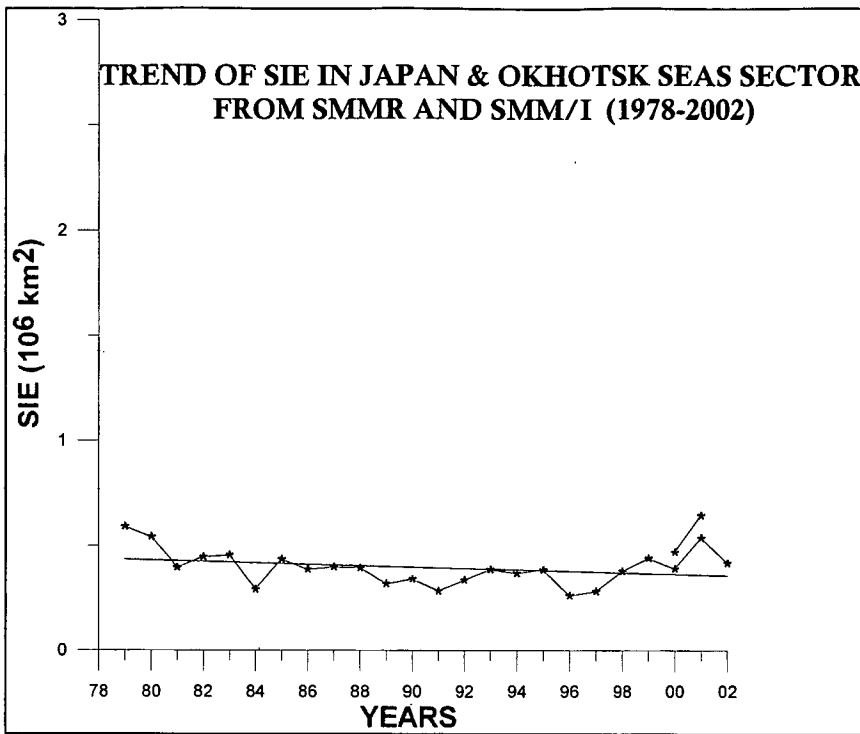


Fig 7.11: Yearly averaged SIE in Japan & Okhotsk Seas Sector with SMMR and SSM/I (a) and SMMR, SSM/I and MSMR(b)

7.5.3 Greenland Sea

The Greenland Sea is surrounded by Greenland Island, the Arctic Ocean and the North Atlantic Ocean, northeast of Canada, Svalbard and Jan Mayen Islands. It lies between the Arctic Ocean and the Atlantic Ocean and allows free movement of water between the two oceans. Its geographical location is given in the table 7.1. Its geographical area as per our sector definition is 3.0453 Msqkms .

The T_B images of four different seasons are shown in fig 7.12. The SIE in the same seasons during the SMMR and SSM/I period shown in fig 7.13. Rapid oscillations in SIE are observed throughout the observation period. Greenland Sea ice extent is very much variable in nature in winter as well as in summer (fig 7.13).

MSMR observed averaged monthly sea ice extent is plotted for the 28 months' period of data availability. Between 1979 –2002 the inter-annual variations in the spatial distribution of sea ice extent is shown in fig 7.14 (a). We have studied sea ice extent with the help of passive microwave data (SMMR, SSM/I, MSMR) available over a period of 24 years from 1978-2002. SMMR and SSM/I observed SIE is plotted in fig 7.14(b).

The secular trend in SIE with SMMR and SSM/I and SMMR, SSM/I and MSMR is shown in fig 7.15 (a) (b) respectively. During the 24-year observation period, the local winter maximum was maximum in 1994 and it was minimum in 1999, the variation being 60 %. (Comiso et al. 2000) On shorter time scale there appears to be oscillations with a period of about a month superimposed on the annual cycle . On observing the time series plotted, minimum ice area is found in Sep.2002 which is about 0.23 Msqkms.

MSMR observations of 28 months from June 1999 to sep.2001 reveal the same scenario of decreasing trend if we consider the three consecutive summers of 1999, 2000 and 2001. There is similarity between SSM/I and MSMR observations in the three summers and two winters during this period. Some pockets of the Greenland Sea show presence of the sea ice through out the MSMR observation period suggesting that these regions contain multi year ice.

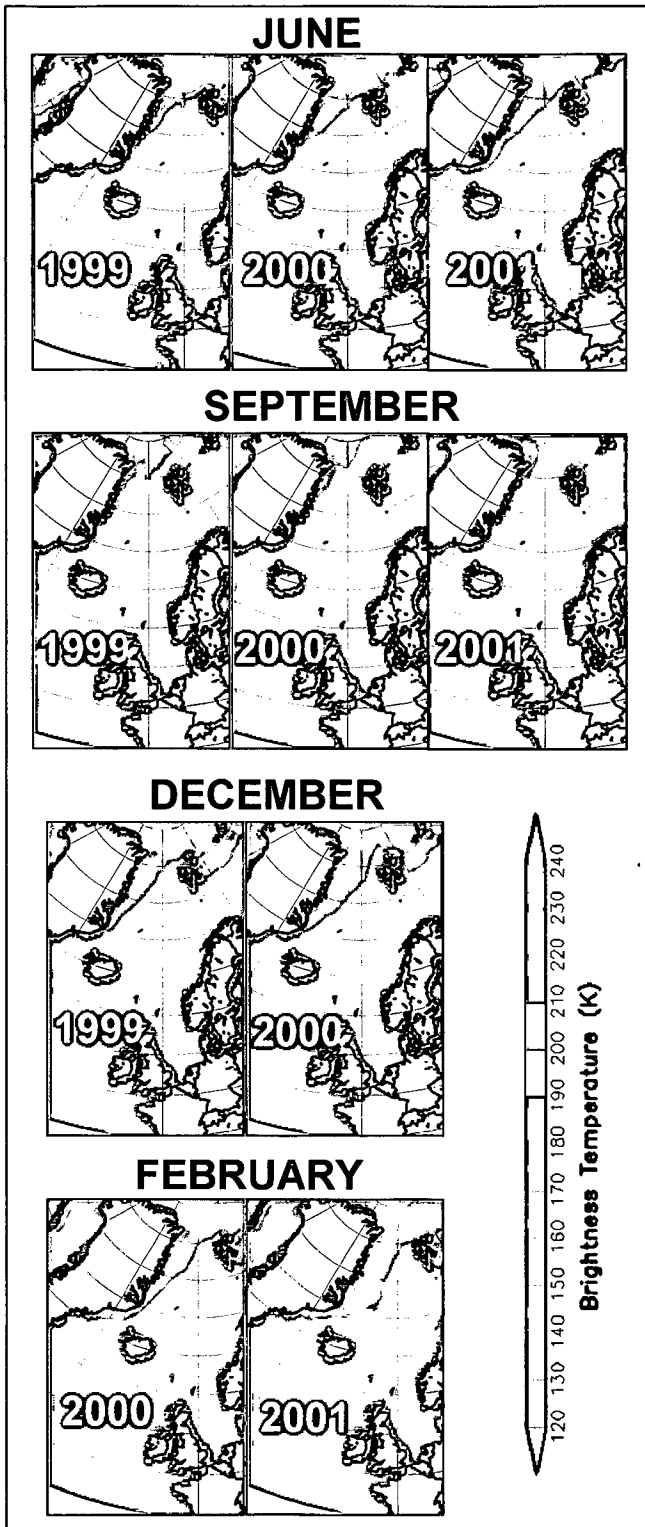


Fig 7.12: MSMR T_B images of different seasons in Greenland Sea Sector

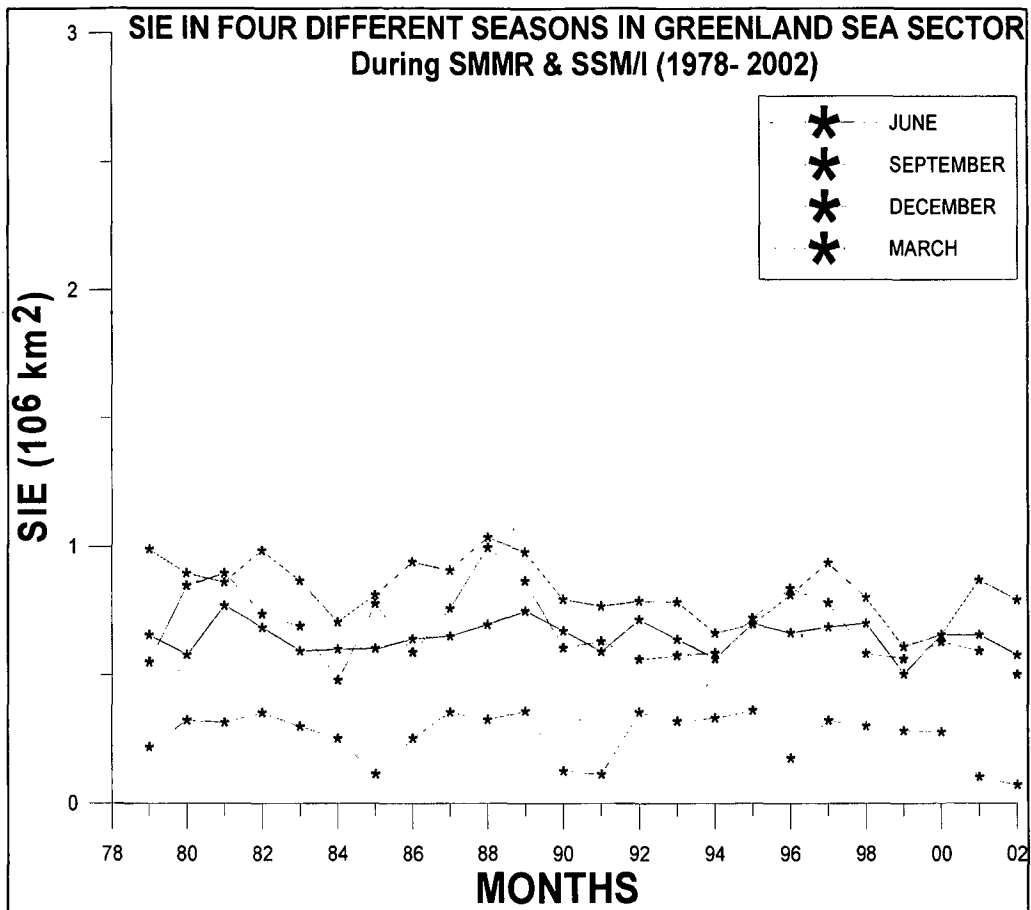


Fig 7.13: SIE in four different Seasons in Greenland Sector during SMMR and SSM/I Period

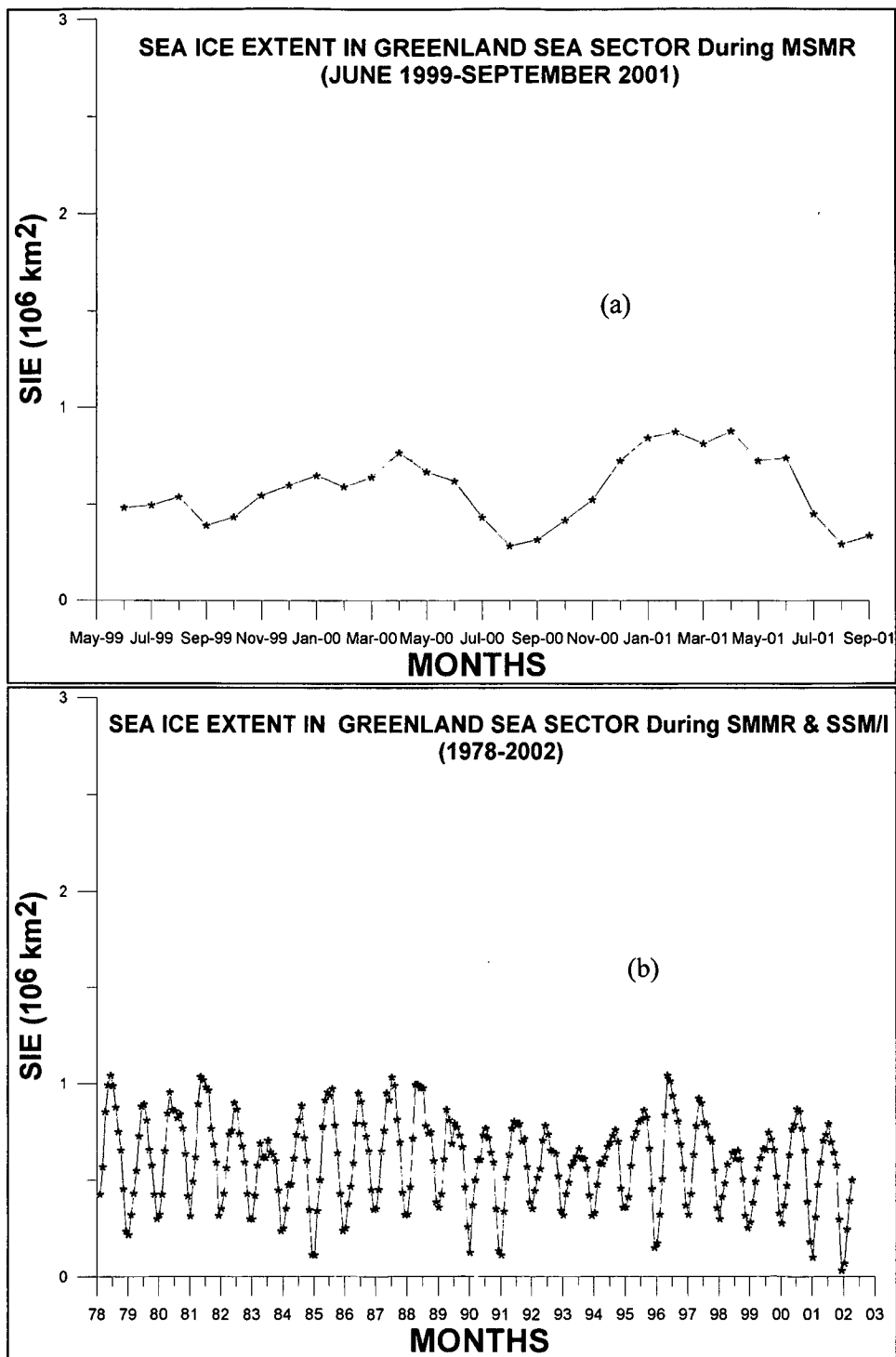


Fig 7.14: The monthly SIE in Greenland Sea Sector during MSMR period (a) and SMMR & SSM/I period (b)

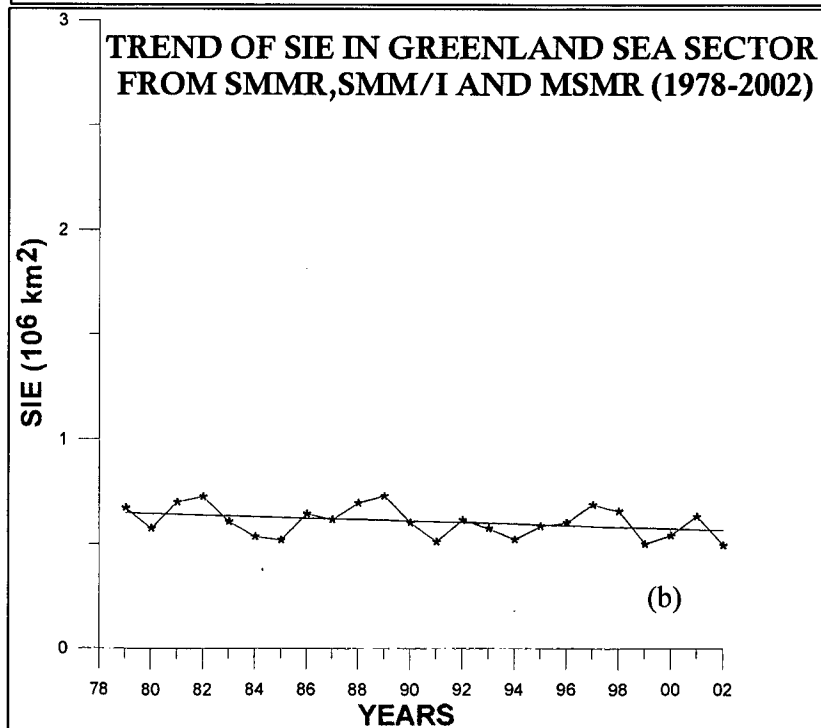
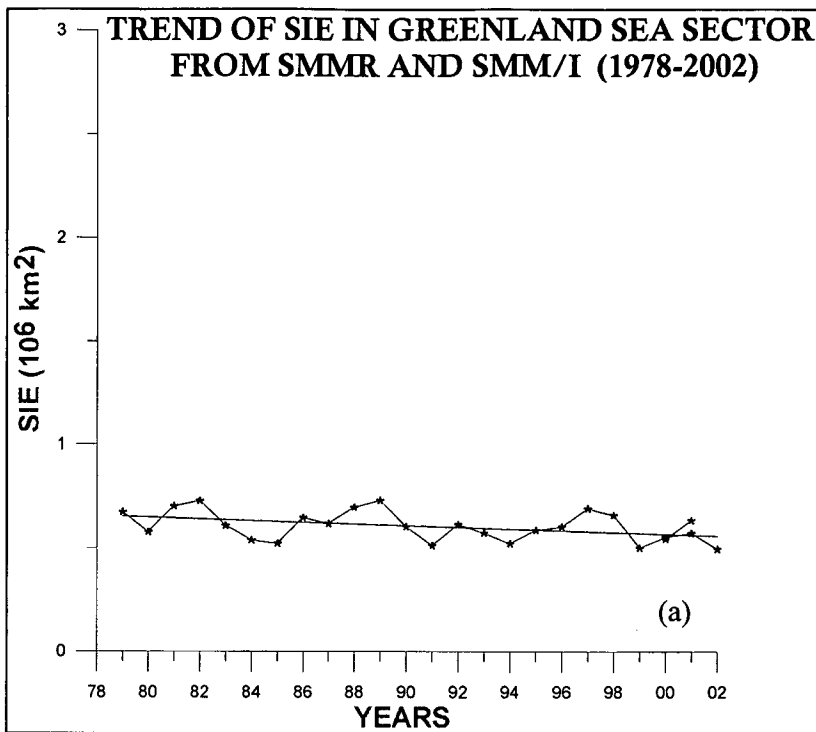


Fig 7.15: Yearly averaged SIE in Greenland Sea Sector with SMMR and SSM/I (a) and SMMR, SSM/I and MSMR (b)

7.5.4 Kara and Barents Seas

The Kara & Barents seas are located in the north of Scandinavia and western Russia and are separated by the island of Novaya Zemlya, which acts as a barrier between the cold Arctic waters in the Kara sea and the warmer waters in Barents sea under the weak influence of the Norwegian current. As a result Kara sea contains high concentration sea ice cover for most part of the year whereas the Barents sea remains mostly ice free. (Gloersen, 1992).

Kara Sea is a shallow sea with an average depth 128 m. It receives fresh water from the Siberian rivers, and is important for fishing. It is navigable only during August and September.

Barents Sea lies North of Norway and European Russia and is partially enclosed by Franz Josef Land on the north, Novaya Zemlya on the east, and Svalbard on the west. The sea was named after Willem Barentz, the Dutch navigator. To some extent, it remains under the influence of the North Atlantic Drift so that its ports remain mostly ice free throughout the year.

The T_B images of four different seasons are shown in fig 7.16. The SIE in the same seasons during the SMMR and SSM/I period shown in fig 7.17. The SIE in MSMR period is shown in fig 7.18 (a).

The yearly sea ice cycle is shown in the fig 7.18 (b). A time series of data between 1978 to 2002 is plotted against time in years. It shows minimum ice coverage in September which lies in its northernmost portion. During the autumn the ice edge moves southwards and by December, covers almost entire sea. Ice cover remains up to May and starts melting close to the coastline in June.

The secular trend in SIE with SMMR and SSM/I and SMMR, SSM/I and MSMR is shown in fig 7.19 (a) (b) respectively. The Kara sea south of 75° N is largely free of ice By August and the ice edge further retreats northward in September.. The Barents sea is almost free of ice in August and September. From October the ice edge starts moving

southward and gradually reaches 75° N in December.. In December ice growth proceeds westwards from Novaya Zemlaya and by March the ice covers most of the sea, east of 45° E. By observing combined KBS, the total sea ice extent shows an average seasonal sea ice cover expanding from a minimum of $0.7 \times 10^6 \text{ km}^2$ in September to a maximum of $1.9 \times 10^6 \text{ km}^2$ in March. Some MYI is transported into the Kara and the Barents seas from the central Arctic. (Glorsen et. al 1992.).

Maximum ice extent in the Kara and Barents seas shows sharp interannual variations. The maximum ice extent is observed in March 1998 and March 1979. Minimum ice extent is observed in March 1979 and March 1981. The spatial variation in Barents sea closely follows the variation in temperature from summer to winter. Variation in Kara sea is observed less due to very little variation in sea temperature. It happens due to advection of heat from Kara to adjacent Arctic Ocean. (Comiso et. al 2000).

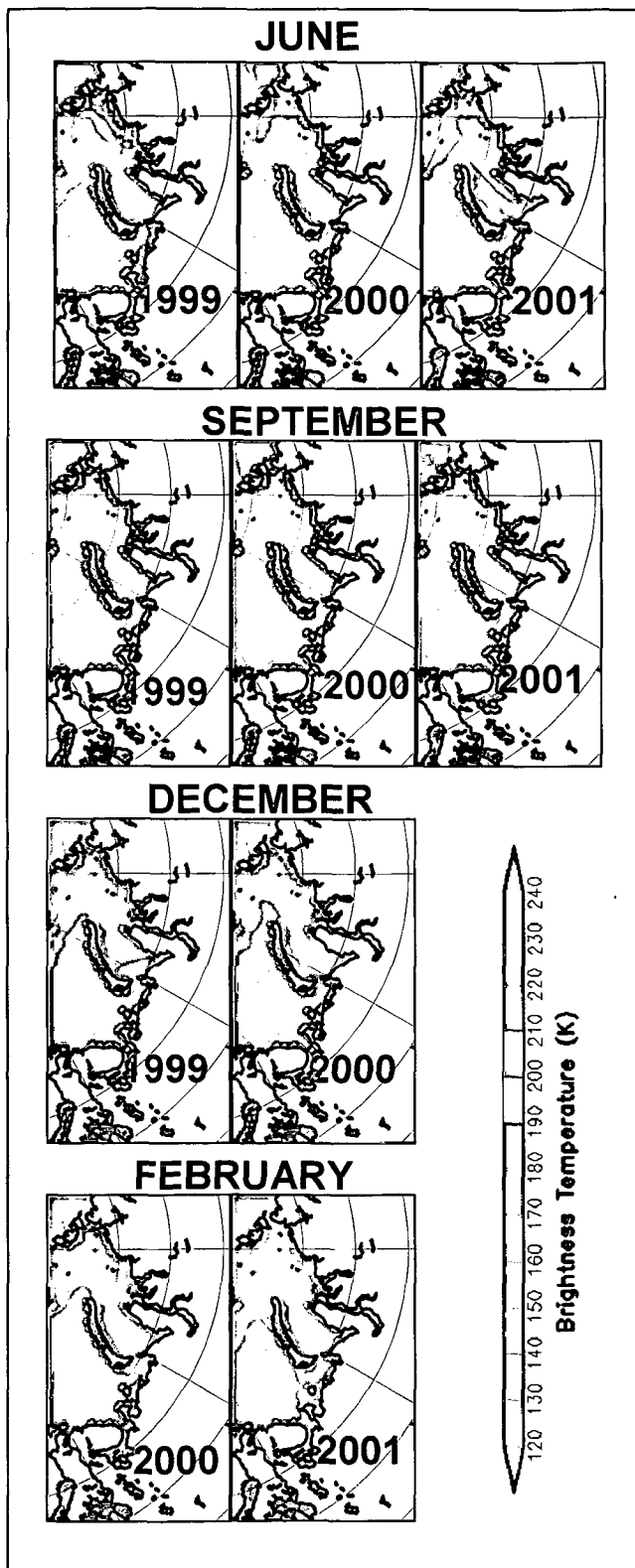


Fig 7.16: MSMR T_B images of different seasons in Kara and Barents Seas Sector

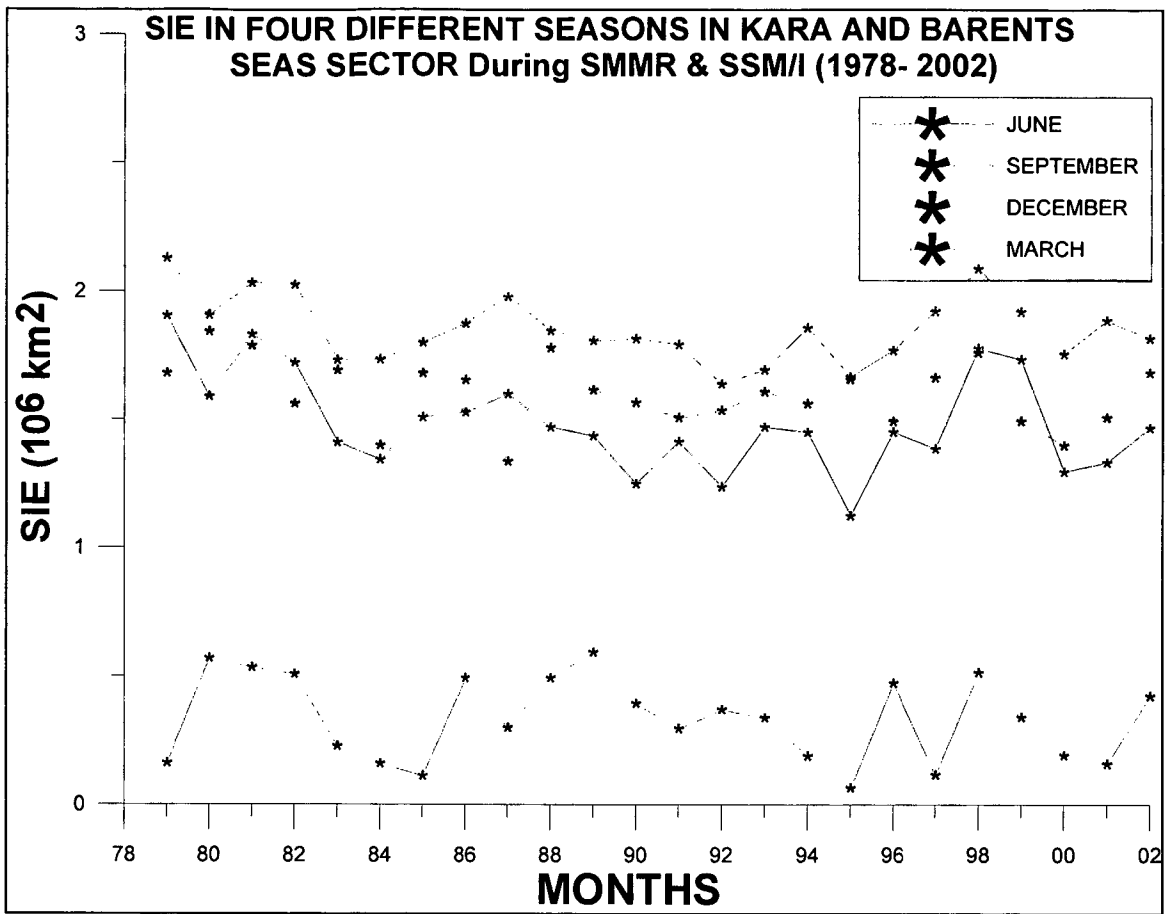


Fig 7.17: SIE in four different Seasons in Kara and Barents Seas Sector during SMMR and SSM/I Period

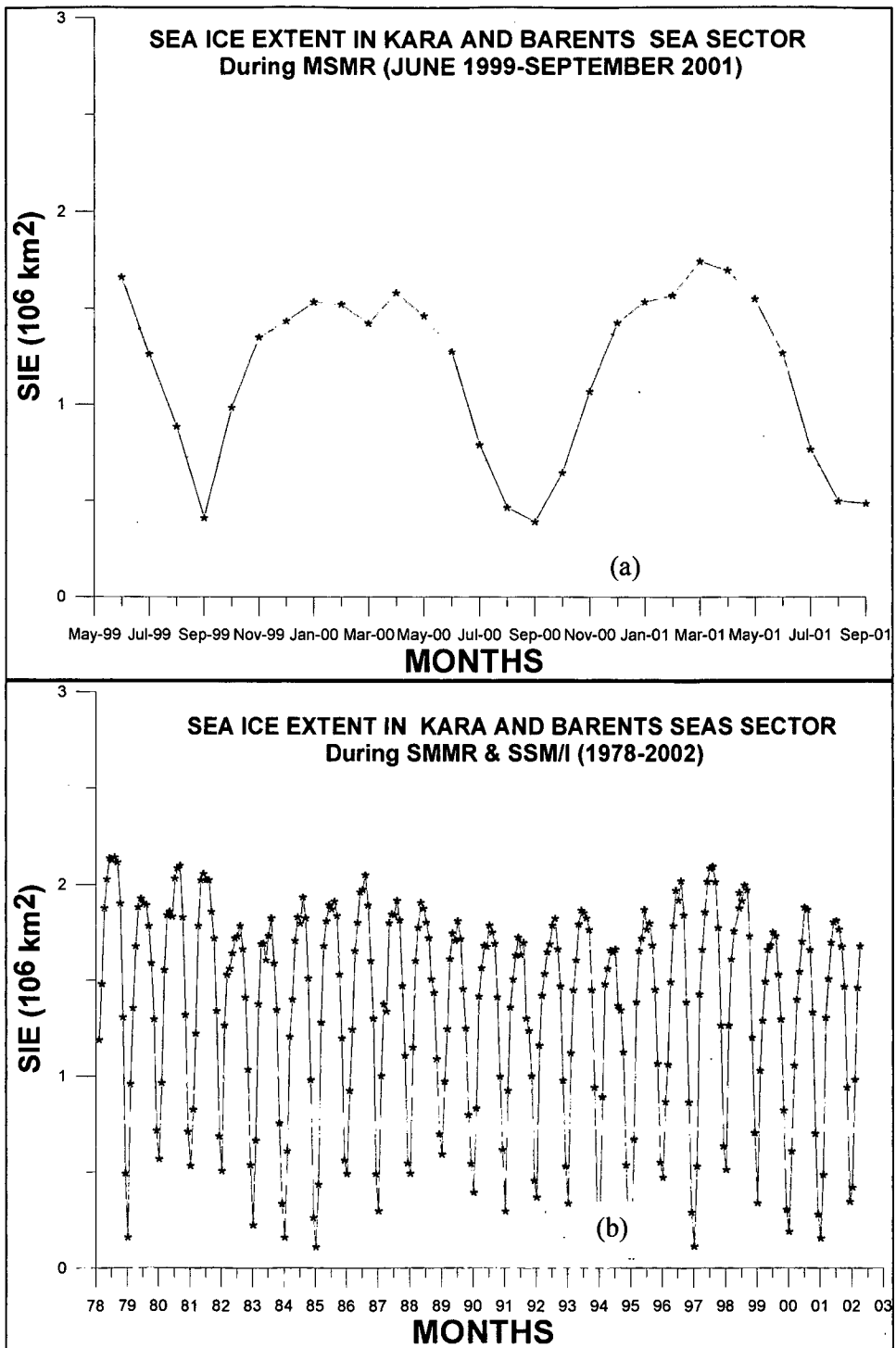


Fig 7.18: The monthly SIE in Kara and Barents Seas Sector during MSMR period (a) and long term in SMMR & SSM/I period (b)

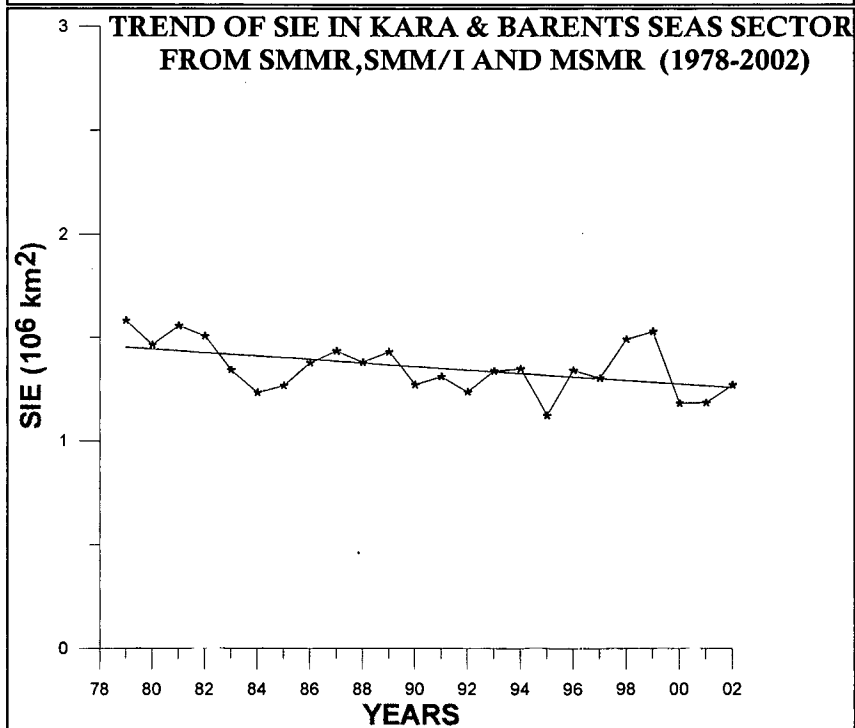
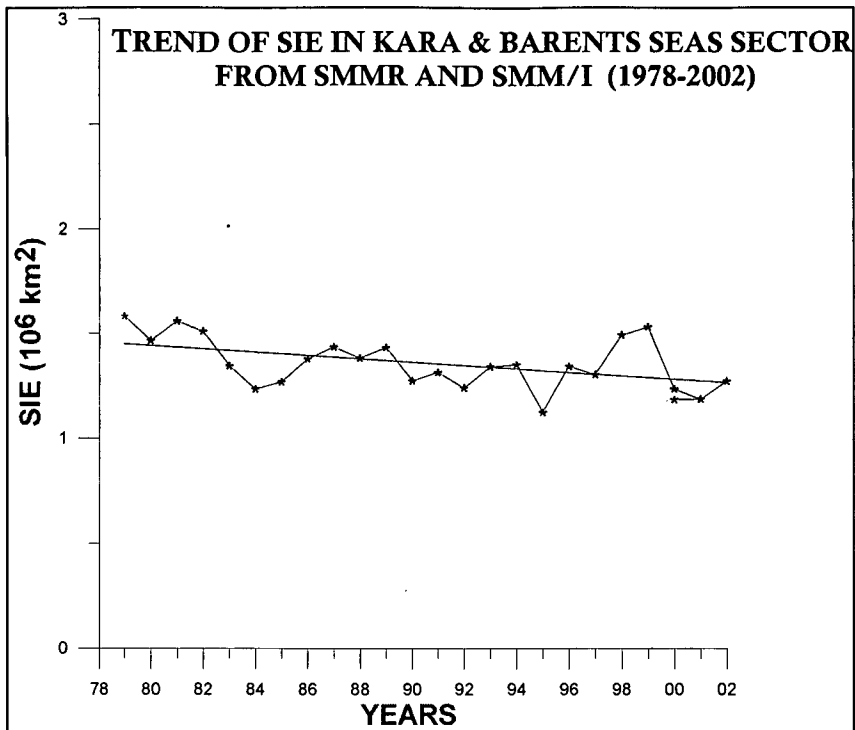


Fig 7.19: Yearly Averaged SIE in Kara and Barents Seas Sector with SMMR and SSM/I (a) and SMMR, SSM/I and MSMR (b)

7.5.5 North American Sector

The North American sector includes two large regions. The first one includes Baffin Bay, Davis Strait and Labrador sea areas and the second one includes ocean north of Alaska and Canada surrounding the Canadian Archipelago. It also includes the Hudson Bay and the Gulf of Lawrence.

Baffin Bay, Davis Strait and Labrador area is bounded on the north-east by Greenland, on the north-west by Baffin Island and on the south-west by Newfoundland. The region is open to the Atlantic Ocean on the south-eastern side and is connected to the Arctic Ocean through several narrow passages in the north.

The Canadian Archipelago is a group of islands and channels that go from the Canadian coastline to about 84° N. On its north and northwest lies the ice-covered Arctic Ocean. Its geographical location is given in table 7.1.

Canadian Archipelago is geographically a very complex region. It is a complex system of interconnecting of shallow channels, straits, bays, islands, and peninsulas where different types of sea ice are found. The morphology and the dynamics of the sea ice in this area are therefore very complex and the situation gets further complicated by the presence of grounded ice. The ESMR observations (Parkinson et al 1987) show significant inter-annual variability in ice types occurring throughout the Archipelago. Ice velocities found in these channels and straits as high as 58 km /day in Lady Ann strait and between 20 and 30 km/day in Amundsen gulf (Ramseier et al, 1975). From aircraft analysis it is found that the advection of ice takes place southward through the channels of the northern islands in the eastern sector of the Archipelago and further eastward throughout Jones and Lancaster Sound into Baffin Bay (Dumbeer et al.1981). The Canadian Archipelago region has the highest ratio of coastline length to the ice area of all the regions.

Hudson bay is located in northeastern Canada. It is surrounded by land on all the sides, except that it is linked on the northeastern side by Hudson strait to the Atlantic Ocean and via a complex passage to the Arctic Ocean through the Canadian Archipelago. Hudson Bay is almost ice covered for six month of the year from December to May. Ice

starts melts out during June-July-August. The decay is very fast the growth is also very rapid during October-November-December.

Gulf of St. Lawrence is bounded by Canadian landmass. It is connected to Labrador Sea by Strait of Belle Isle and to the Atlantic Ocean by Cabot Strait.

The T_B images of four different seasons are shown in fig 7.20. The SIE in the same seasons during the SMMR and SSM/I period shown in fig 7.21. The SIE in MSMR period is shown in fig 7.22 (a). The yearly sea ice cycle is shown in the fig 7.22 (b). The secular trend in SIE with SMMR and SSM/I and SMMR, SSM/I and MSMR is shown in fig 7.23 (a) (b) respectively

A time series of data of 24 years is analyzed for the ice extent coverage of the North American Sector as a whole. It is found that there are inter-annual variations in total ice extent in summers as well as in winters. This is different from the behaviour of the Arctic Ocean in which wintertime sea ice extent does not change.

We see the summer minimum observed in 1981 is $0.4 \times 10^6 \text{km}^2$ decreased to $0.27 \times 10^6 \text{km}^2$ in 1998. After 1998, it increased to $0.4 \times 10^6 \text{km}^2$ in the year 2002 (see fig 7.21 & 7.22 (b)). As far as winter minima are concerned, we find high year to year fluctuations. The highest wintertime coverage is found in March 1993 and the lowest winter extent is observed in March 1981. Finally the extent remains more or less constant at $3.4 \times 10^6 \text{km}^2$ in last five years of observations (i.e., in 1998, 1999, 2000, 2001 and 2002). The MSMR observations of June 1999- September 2001 show similarity with SSM/I observations.

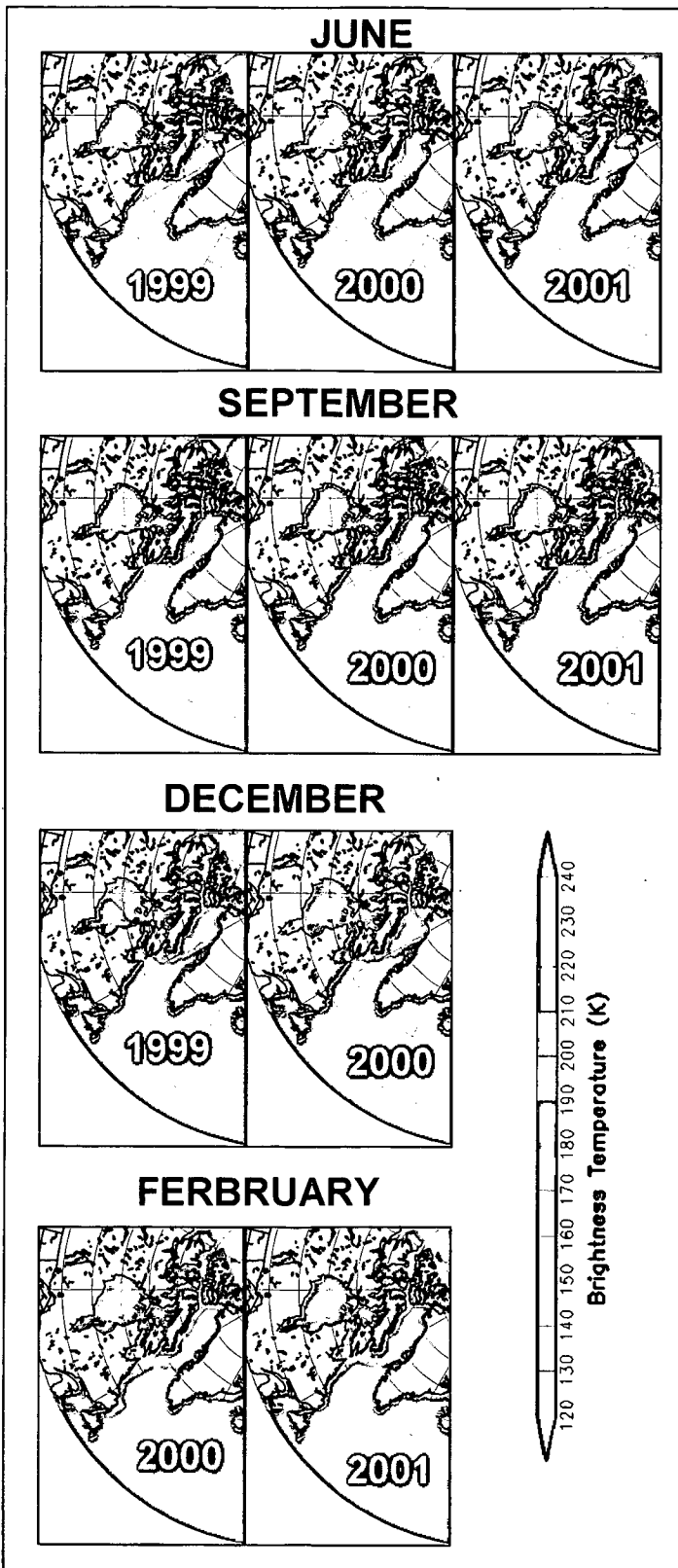


Fig 7.20 T_B Images of four different Seasons in North American Seas Sector during MSMR period

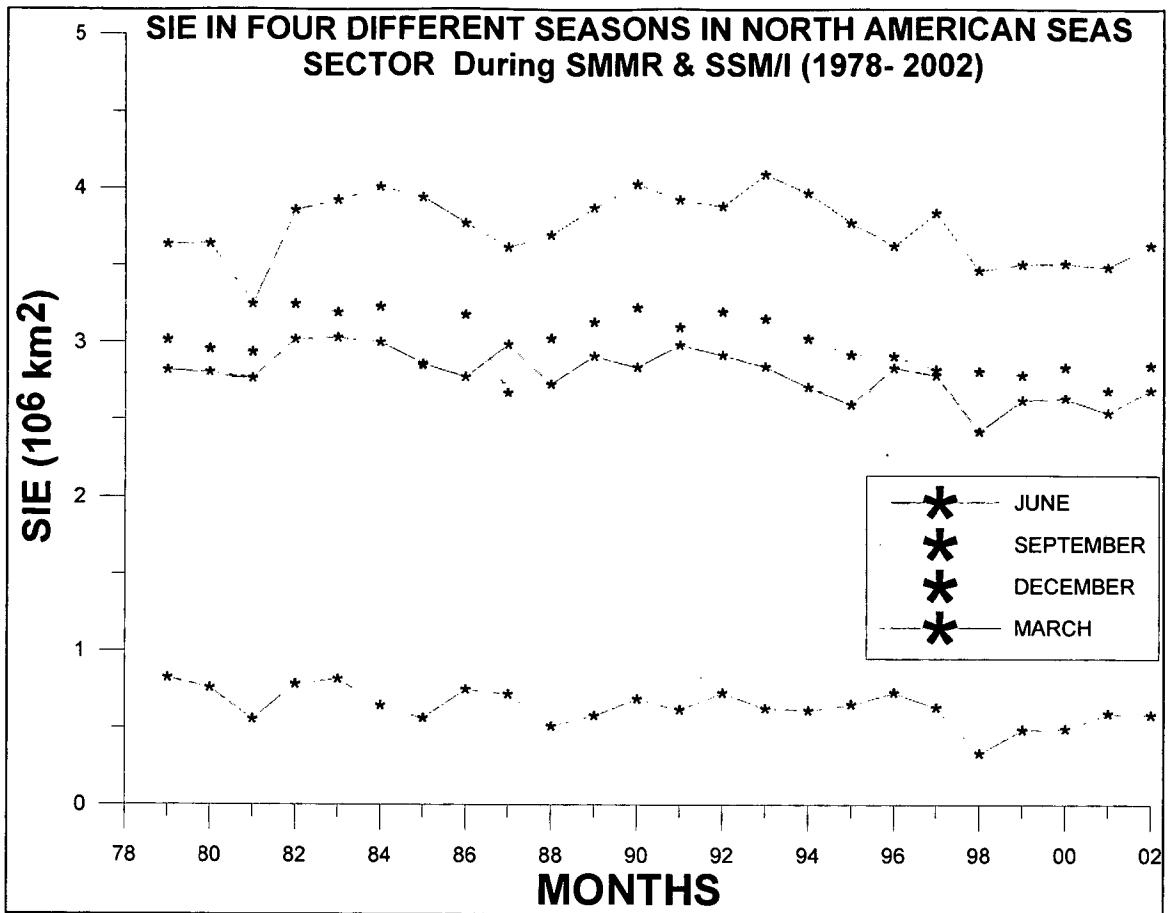


Fig 7.21: SIE in four different Seasons in North American Seas Sector during SMMR and SSM/I Period

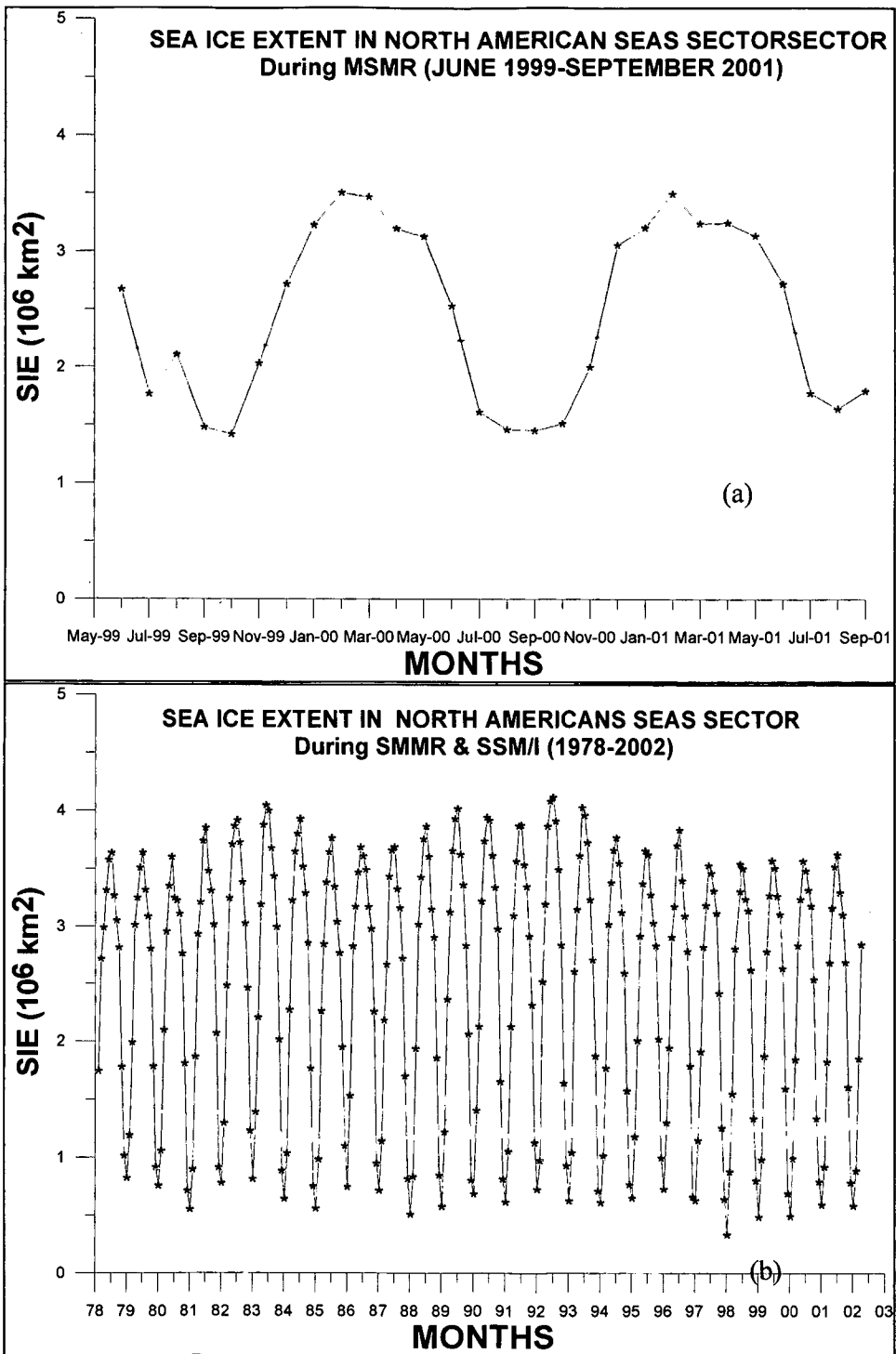


Fig 7.22: The monthly SIE in North American Seas Sector during MSMR period (a) and SMMR & SSM/I period (b)

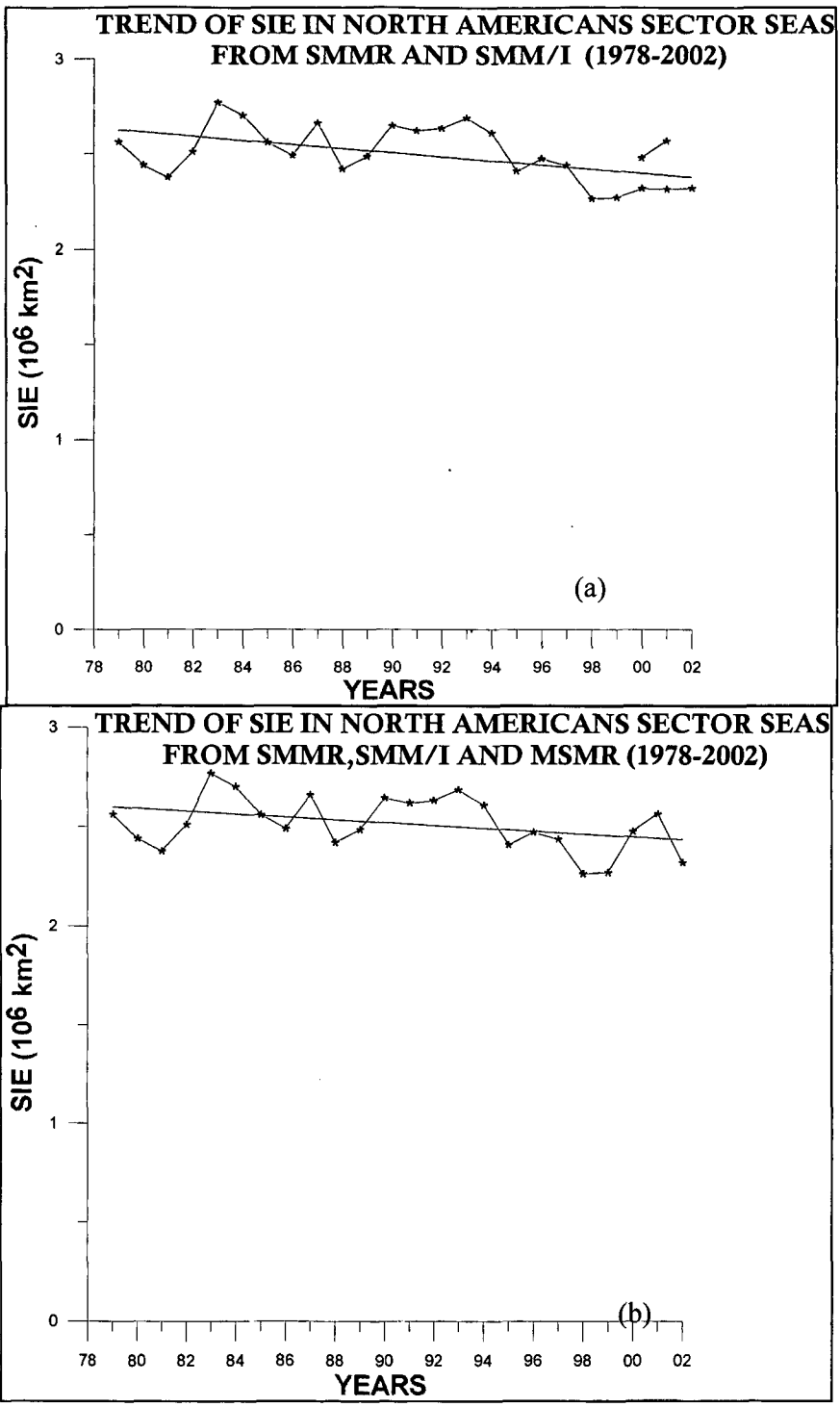


Fig 7.23: Yearly averaged SIE in North American Seas Sector with SMMR and SSM/I (a) and SMMR, SSM/I and MSMR (b)

7.5.6 Arctic Ocean (AO)

Geographical location of the Arctic Ocean ice cover is as per sector definition given in table 7.1. Arctic Ocean (AO) is divided into two basins Canadian basin & Eurasian Basin by the Lomonosov ridge, which extends from North Pole to Siberia. AO touches North American sector Seas, Greenland Sea, Bering Sea and Kara and Barents seas.

During the course of the year, a large variety of the sea ice types exist throughout most of the Arctic Ocean, ranging from nilas and frazil to all stages of first year ice and multi year ice (Glorosen, 1992). The distribution of the sea ice and open water is important for the polar heat budget studies. In winter, the fluxes of the of heat and water vapor through open water within the pack can be orders of magnitude greater than through surrounding pack ice (Badgley, 1996). The heat flux through thin ice is much greater than through thick ice (Maykut, 1978). Open water absorbs more solar radiation than sea ice in summer.

Arctic Ocean remains fully covered by Sea ice from November to May each year. It starts reducing from June to Mid September. Central Arctic Ocean always remains covered by the more than 60% sea ice. The inter-annual variability in the ice pack position at the time of September minimum has two principal modes – (i) the Siberian mode, when the ice pack remains distant from the Alaskan coastline and the (ii) the Alaskan mode, when the ice pack comes close to Alaskan coastline.

From November to March, the sea ice occupies almost entire Arctic Ocean. Average ice concentration in summer is around 79%. Maximum ice extent is observed in the month of March. The decreasing trend starts in April and goes up to September. During winter season, this sector is full of ice every year and there is no significant change from one year to another.

As for as inter-annual variability is concerned, the winter minimum exhibits year to year variability. It shows minima in 1980, 1984 and 1985 and maxima in 1979 and 1986. In winter season large changes are observed in T_B due to snow cover on ice surface which has higher emissivity.

In total life span of MSMR there are three summers: 1999, 2000 and 2001. The warming season in the northern region starts in April and the melting of snow gradually accelerates until September and then onwards starts decreasing. Correspondingly the seasonal trend of sea ice extent decreases from April to September and then again starts rising. Ice extent area of AO at the time of summer maximum are $4.7912 \times 10^6 \text{ km}^2$, $5.0276 \times 10^6 \text{ km}^2$ and $5.1998 \times 10^6 \text{ km}^2$ respectively.

The T_B images of four different seasons are shown in fig 7.24. The SIE in the same seasons during the SMMR and SSM/I period shown in fig 7.25. The monthly SIE in MSMR period is shown in fig 7.26 (a). The yearly sea ice cycle is shown in the fig 7.26 (b). The secular trend in SIE with SMMR and SSM/I and SMMR, SSM/I and MSMR is shown in fig 7.27 (a) (b) respectively

SSM/I observations show increasing trend in the same period in the AO SIE. But in the last week of September 2002, SSM/I observations show drastic decrease in SIE to $4.45 \times 10^6 \text{ km}^2$. (Comiso et. al, 2004) In only one year this drastic change in SI cover is found. The highest decrease in SIE is observed in 2002, 1990 and 1995 summers. The inter-annual variations are possibly driven by the inter-annual variations in the temperature regime. If this variation is monitored on a longer time scale it gives indications about the trend in the climate change, if any.

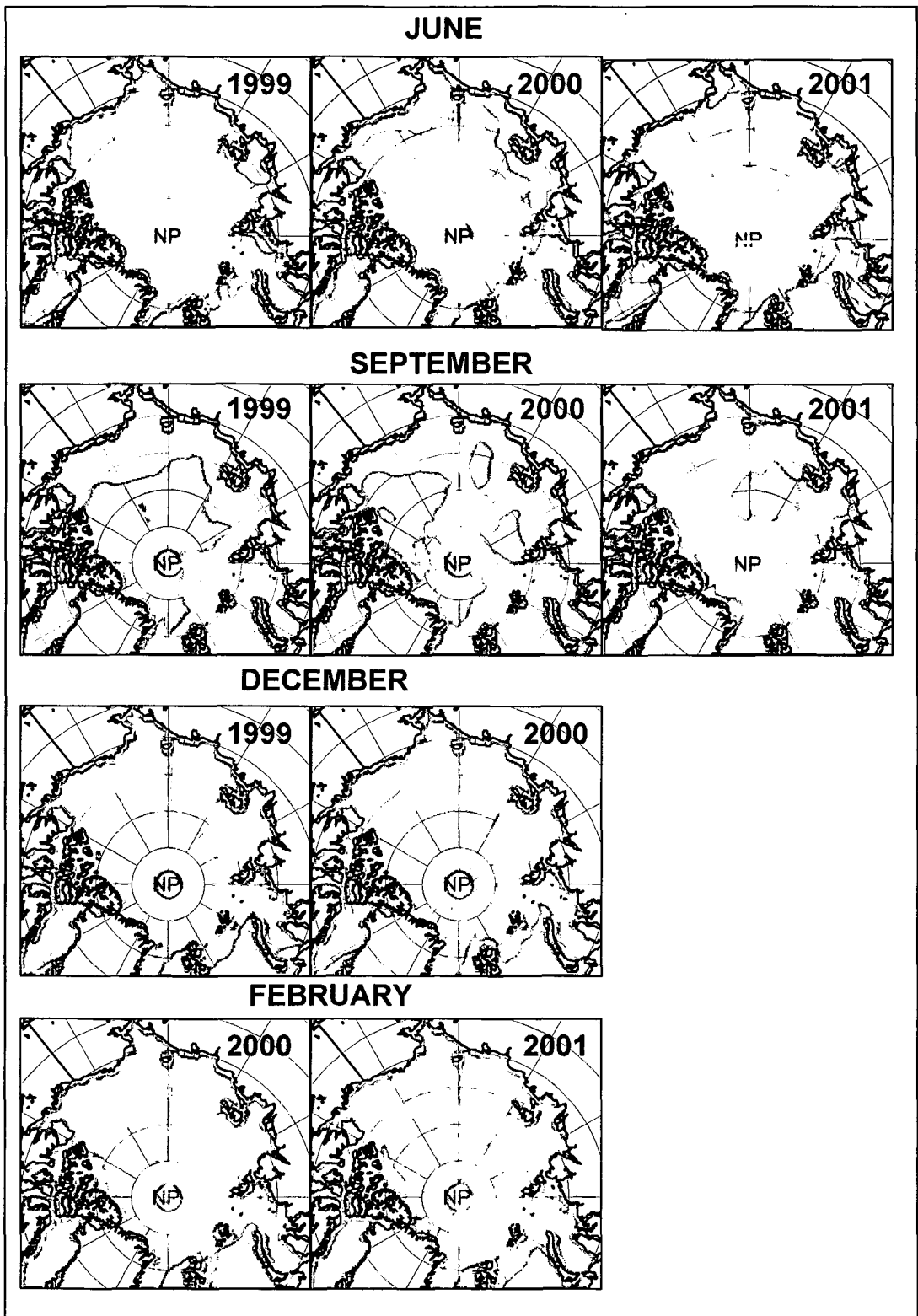


Fig 7.24: T_B Images of seasonal variation in Arctic Ocean Sector during MSMR period

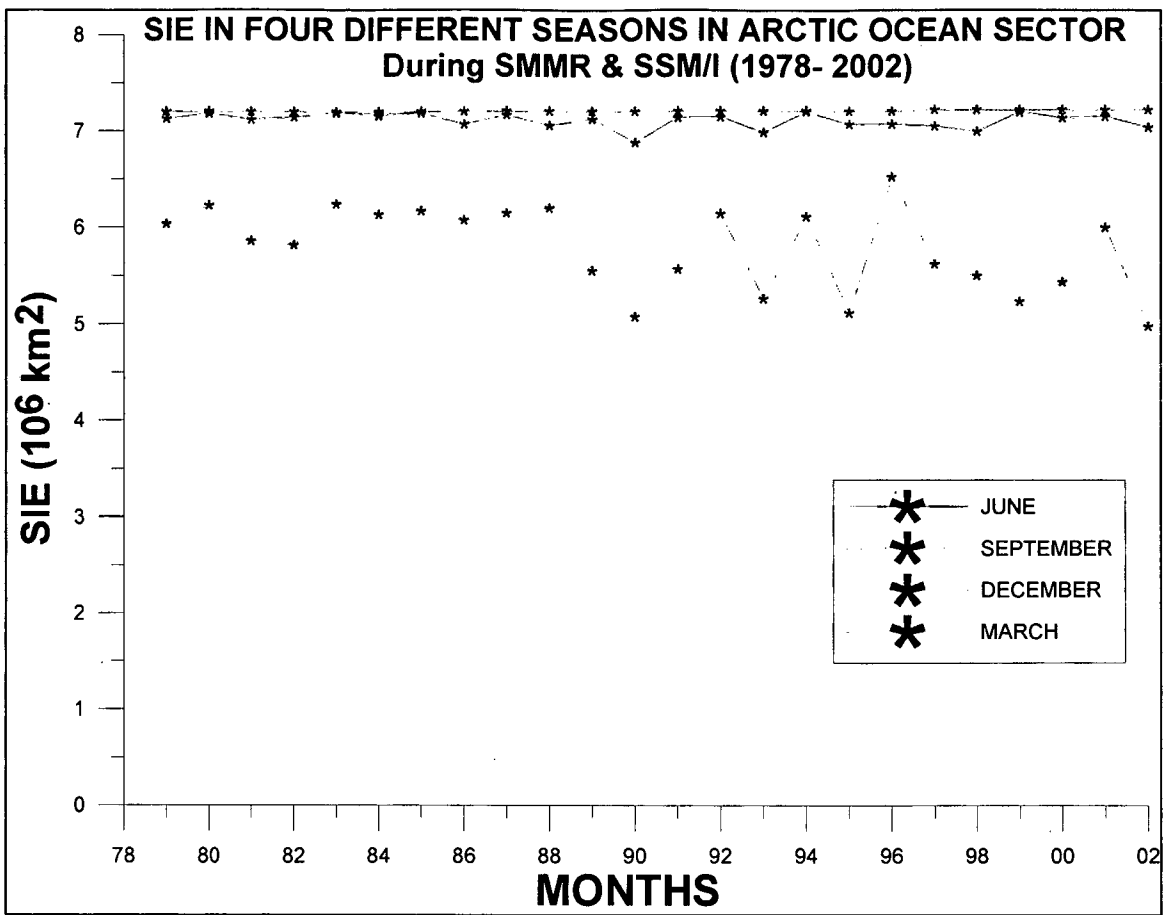


Fig 7.25: SIE in four different Seasons in Arctic Ocean Sector during SMMR and SSM/I Period

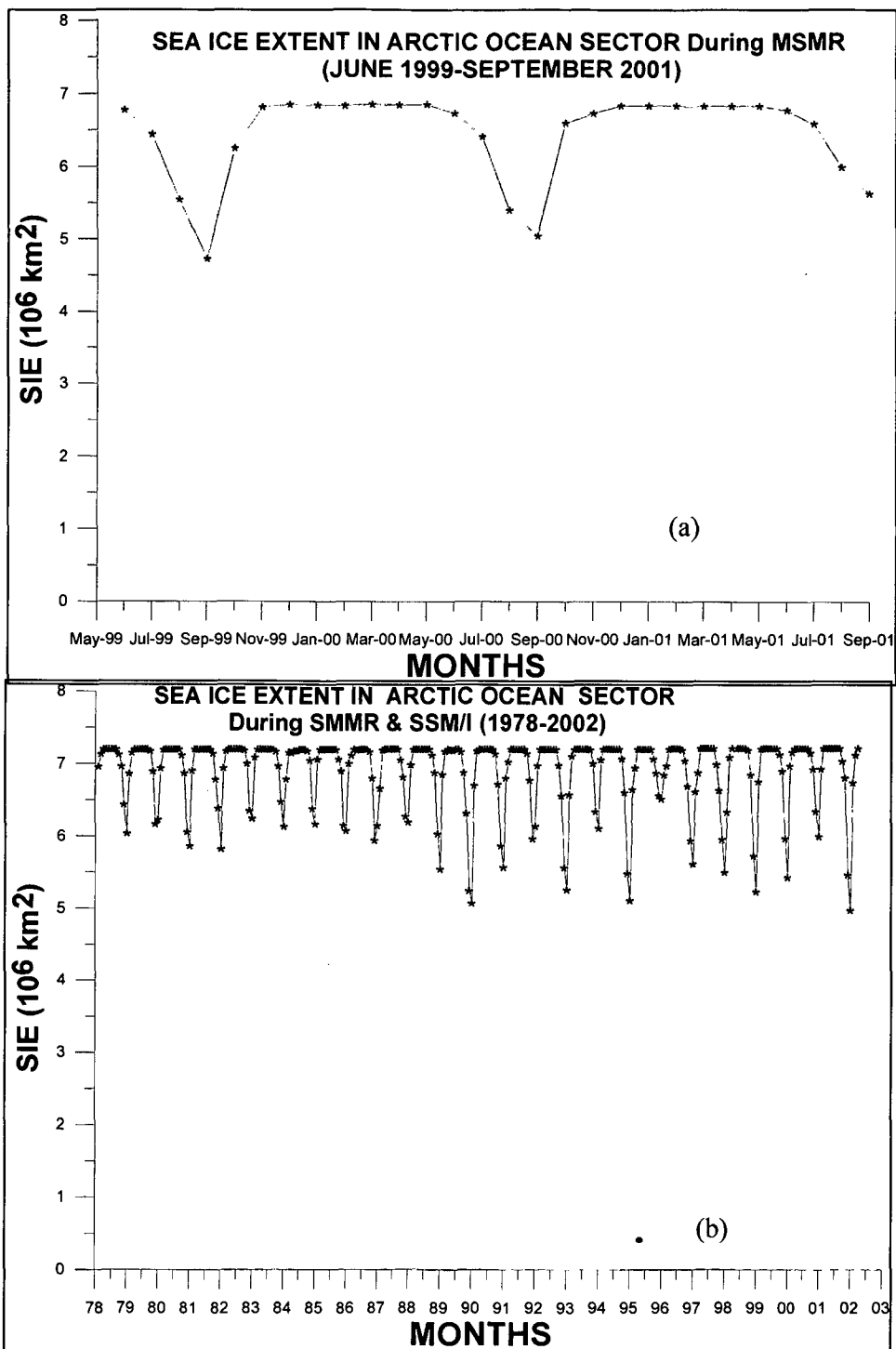


Fig 7.26: The monthly SIE in Arctic Ocean Sector during MSMR period (a) and long term SIE from SMMR & SSM/I period (b)

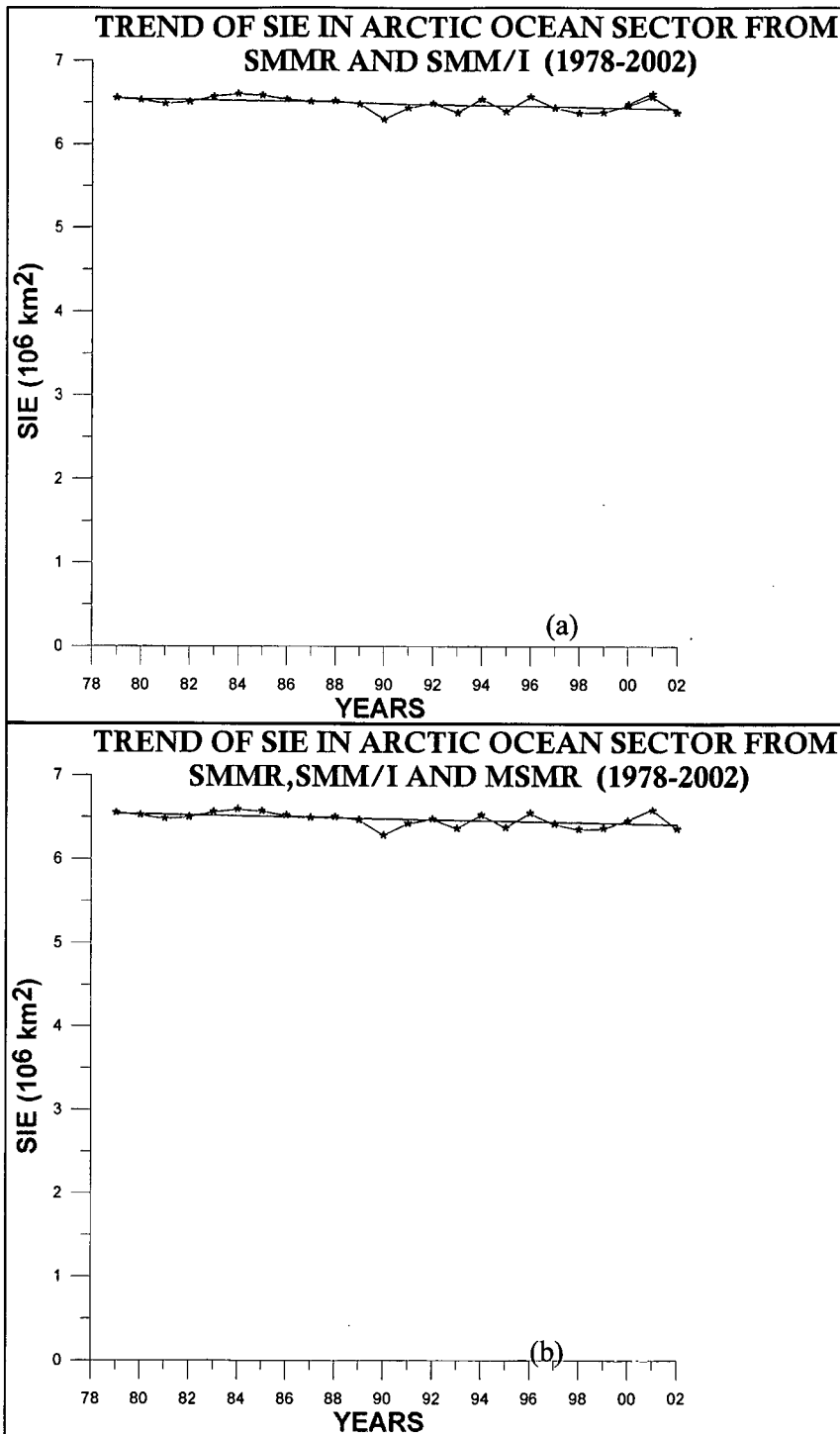


Fig 7.27: Yearly averaged SIE in Arctic Ocean Sector with SMMR and SSM/I (a) and SMMR, SSM/I and MSMR (b)

7.6 NORTH POLAR REGION (AS A WHOLE)

In the previous section we have discussed six different sectors individually in the North Polar Region. Their regional characteristics in brief and ice extents in summer and winter have been described. Interannual variability of SIE is explained for each of the six sectors defined in section 7.1. In this section we will discuss about the ice extent variation collectively in whole of the North Polar Region as observed by SMMR, SSM/I and MSMR derived sea ice cover.

7.6.1 Intra-annual Range of Ice Coverage

During the period 1978 - 2002 SMMR / SSMI observations, the average seasonal cycle of sea ice in the North Polar Region had ice extents ranging from a minimum of $7.0 \times 10^6 \text{ km}^2$ in September to a maximum of $15.4 \times 10^6 \text{ km}^2$ in March (Parkinson et al., 1999). In fact, minimum ice extent consistently occurred in September in each of the 24 years, and maximum ice extent occurred in March in all the years except 1981, 1987, 1989, and 1996, when it occurred in February.

Figure 7.28 illustrates the intra-annual range of ice coverage by presenting monthly average ice extent images of MSMR T_B for March, June, September and December of MSMR period.

Figure 7.29 is based on data from each of the 25 years and presents the average September ice cover, with more than 15% ice concentration. In the individual years, the September ice is generally observed mostly to the Arctic Ocean and the Canadian Arctic Archipelago, whereas the March ice is seen to extend into the entire Arctic Ocean, the Canadian Arctic Archipelago, Hudson Bay, and the Kara Sea, plus large portions of the Sea of Okhotsk, the Bering Sea, Baffin Bay, the far western Labrador Sea, the western Greenland Sea, and the northern Barents Sea.

The monthly SIE in MSMR period is shown in fig 7.30 (a). The yearly sea ice cycle is shown in the fig 7.30 (b) Time series observations show that in 1996, the March ice was less extensive than the average over the 1979-2002 periods (fig 7.30 (b)). The individual years show noticeable differences in some regions very little difference in some other

regions as compared to the 25-year-average distributions. The spatial distributions of the ice are related to different elements of the climate system in a complicated way. Some examples are given below:-

1. Waters on the north and west coast of Norway remains ice free even in peak winter in spite of the high latitudes due to the warmth brought by the Gulf Stream and its extension, the Norwegian Current.
2. Similarly, the extension of ice along the east coast of Greenland is in largely due to the south-flowing East Greenland Current.
3. The full ice cover over Hudson Bay in winter, in spite of its relatively low latitudes compared to most of the other ice-covered regions, results from its location in the middle of a continent, which causes colder winters and warmer summers than those in open oceans at the same latitudes.

7.6.2 Interannual Variability of Ice Coverage

Inter-annual variability generally refers to variation with respect to time, but the variations in the spatial distribution from year to year are equally important. Fig. 7.30 (b) presents monthly average ice cover for the 25 year period from 1978 to 2002. It shows the areas that are variable regarding the presence or absence of ice (on a monthly average basis) in the particular month. In all cases, ice is assumed to be present if the calculated ice concentration is at least 15% and absent if the calculated ice concentration is less than 15%. The region from 88°N to 90°N, where the Oceansat-1 orbit prevented collection of MSMR data, is assumed to be ice covered to at least 15% ice concentration, and hence is colored white. This assumption is well justified, as all the ice concentration levels in close proximity of this region (88°N to 90°N) are much higher than 15% throughout the observation period. The secular trend in SIE with SMMR and SMM/I and SMMR, SMM/I and MSMR is shown in fig 7.31 (a) (b) respectively.

In the central Arctic, there is very little variability. The regions of variability are found in the outer margins of the ice packs. However, in the month of June, ice begins to

break up, and in some regions the process of breaking up starts from the middle of the pack. Therefore, in June, the variability no longer remains restricted to the marginal ice zones. As a matter of fact, the process of monthly averaging masks many temporary openings and closings of the polynyas. Hence, for the study of the evolution of polynyas, weekly averaging would be more suitable.

Fig. 7.30 shows monthly average SIE vs Time in Year. Here one can see the variability in the annual cycle of ice cover over the observation period of 25 years. From the mean value of $7.0 \times 10^6 \text{ km}^2$ we see the highest deviation in year 2002 summer which had sea ice cover of $6.0 \times 10^6 \text{ km}^2$. Deviation from mean in decreasing order is in The years 2002, 1995, 1990, 1993 show deviation from the mean in decreasing order. In winter also, the interannual variation of sea ice cover is observed in the north polar region. Maximum ice extent of $16.2 \times 10^6 \text{ km}^2$ is observed in March 1979 (see fig. 7.30). MSMR data for the three summers of 1999, 2000 and 2001 shows good agreement with SMMR and SSM/I observations for ice extent in the north polar region .

Several areas show negative trends in the length of the sea ice season, which could be caused either by a warming trend of the climate or by increased advection of ice away from the specific region. However, the trends do not appear to be uniform nor monotonous. For example, there was a very thin ice cover in September, but September 1996 had very dense and wide spread ice cover.

Sea ice extents and their trends have also been calculated from the 25-year data set, and analyzed both regionally and hemispherically by Parkinson et al. (1999). The ice extents agree very well with the length of the sea ice season, and show an overall negative trend of -3.0% per decade over the 25 years for the Arctic as a whole. The largest ice extent decrease is observed in the Kara and Barents Seas (-10.5% per decade) and in the Seas of Okhotsk and Japan (-20.1% per decade). Ice extent increase is found in the Baffin Bay/Labrador Sea and in the Bering Sea. However, the ice extent decreases for the north polar region as a whole. For the Kara and Barents Seas and the Seas of Okhotsk and Japan, the results are statistically significant at a 99% confidence level. The increase in the Baffin Bay/Labrador Sea and the Bering Sea are not statistically significant (Parkinson et al., 1999). The trends in the length of the sea ice season and the ice extents complement each other extremely well, giving the same overall picture of where the ice cover is increasing and where it is decreasing

(Parkinson et al., 1999). The sea ice season results provide spatial detail and the ice extents provide the temporal detail, and thus, if both are taken together, we get a more comprehensive picture of the whole process.

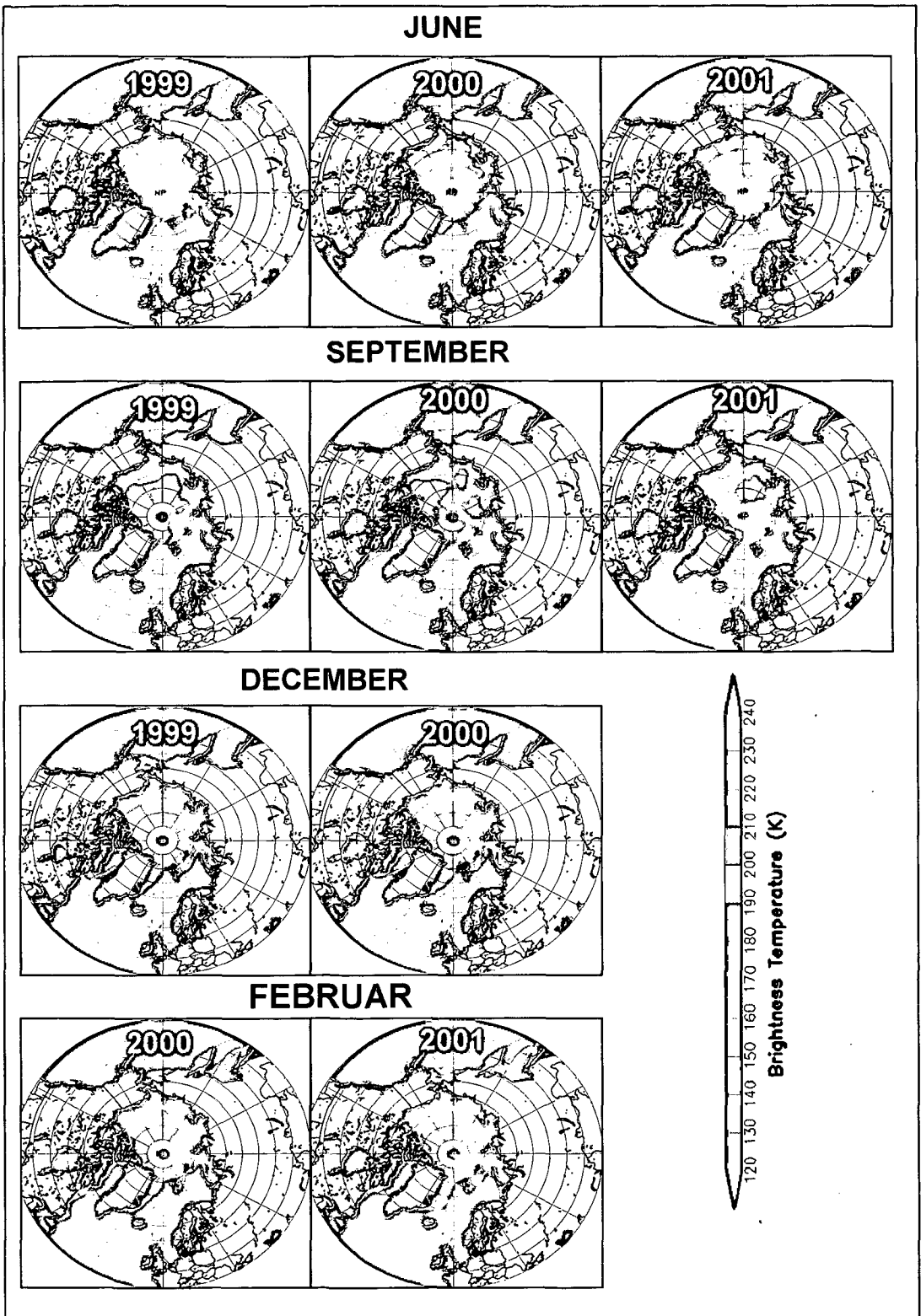


Fig 7.28: T_B Images of seasonal variation in the total NPO during MSMR period

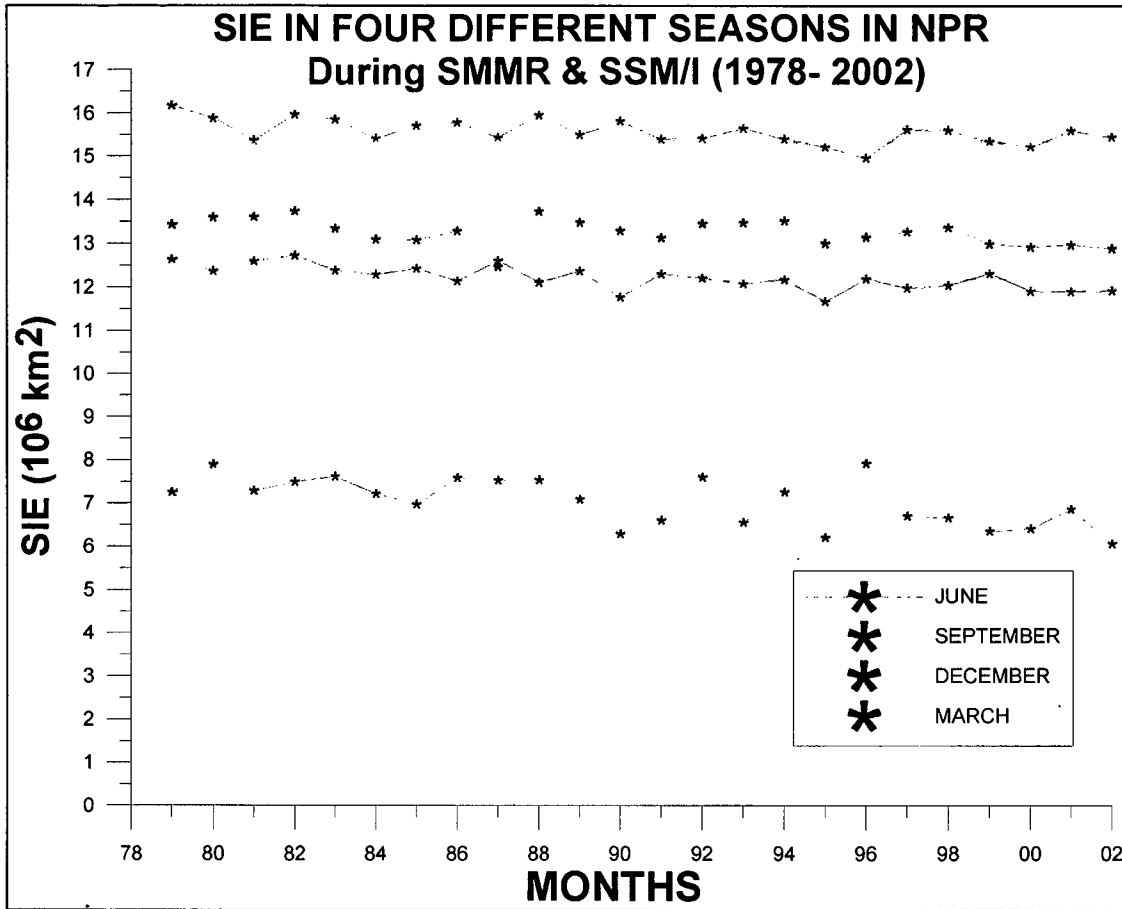


Fig 7.29: SIE in four different Seasons in the total NPR during SMMR and SMM/I Period

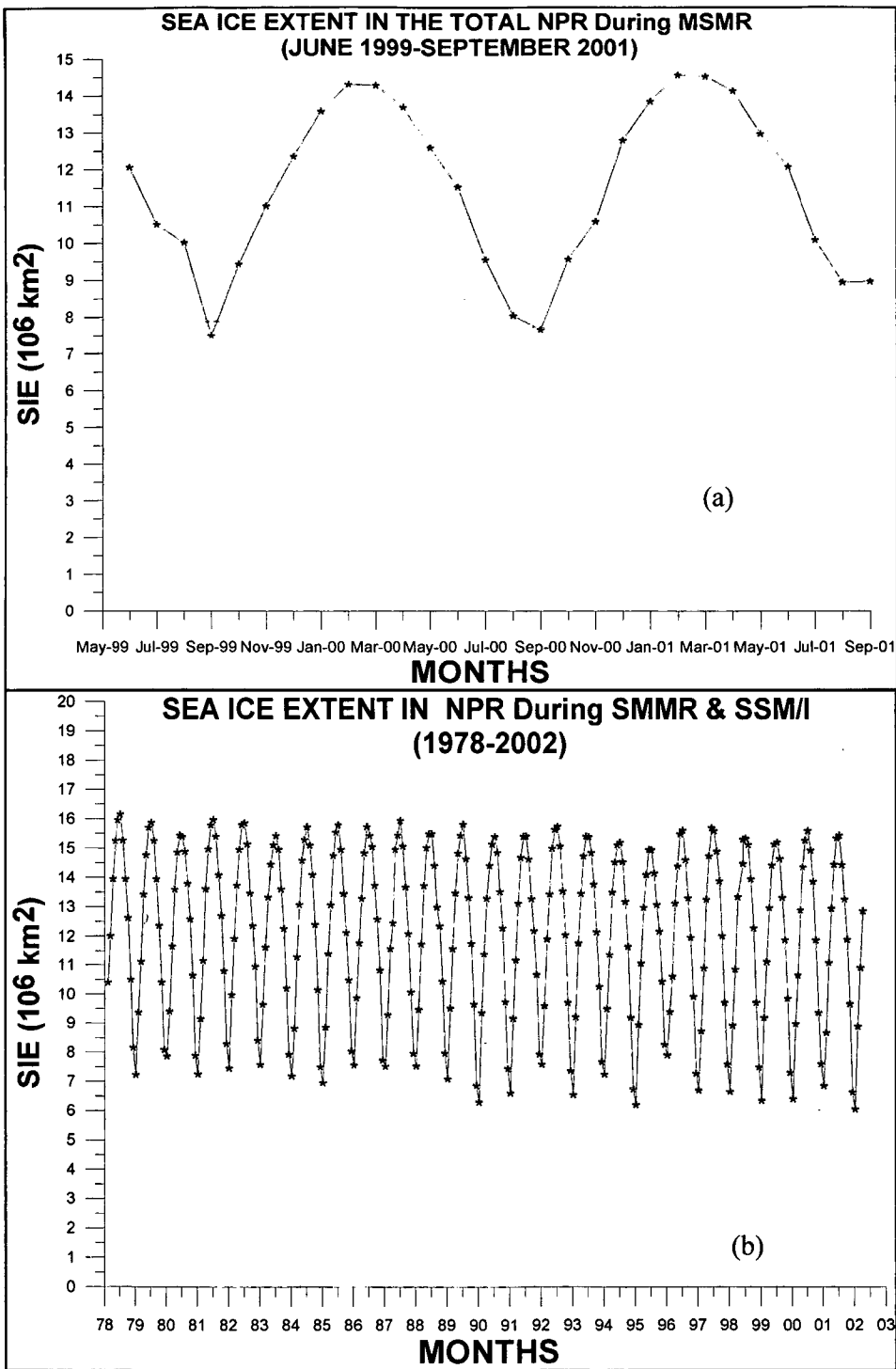


Fig 7.30: The monthly SIE in the NPR during MSMR period (a) and long term from SMMR and SSM/I period (b)

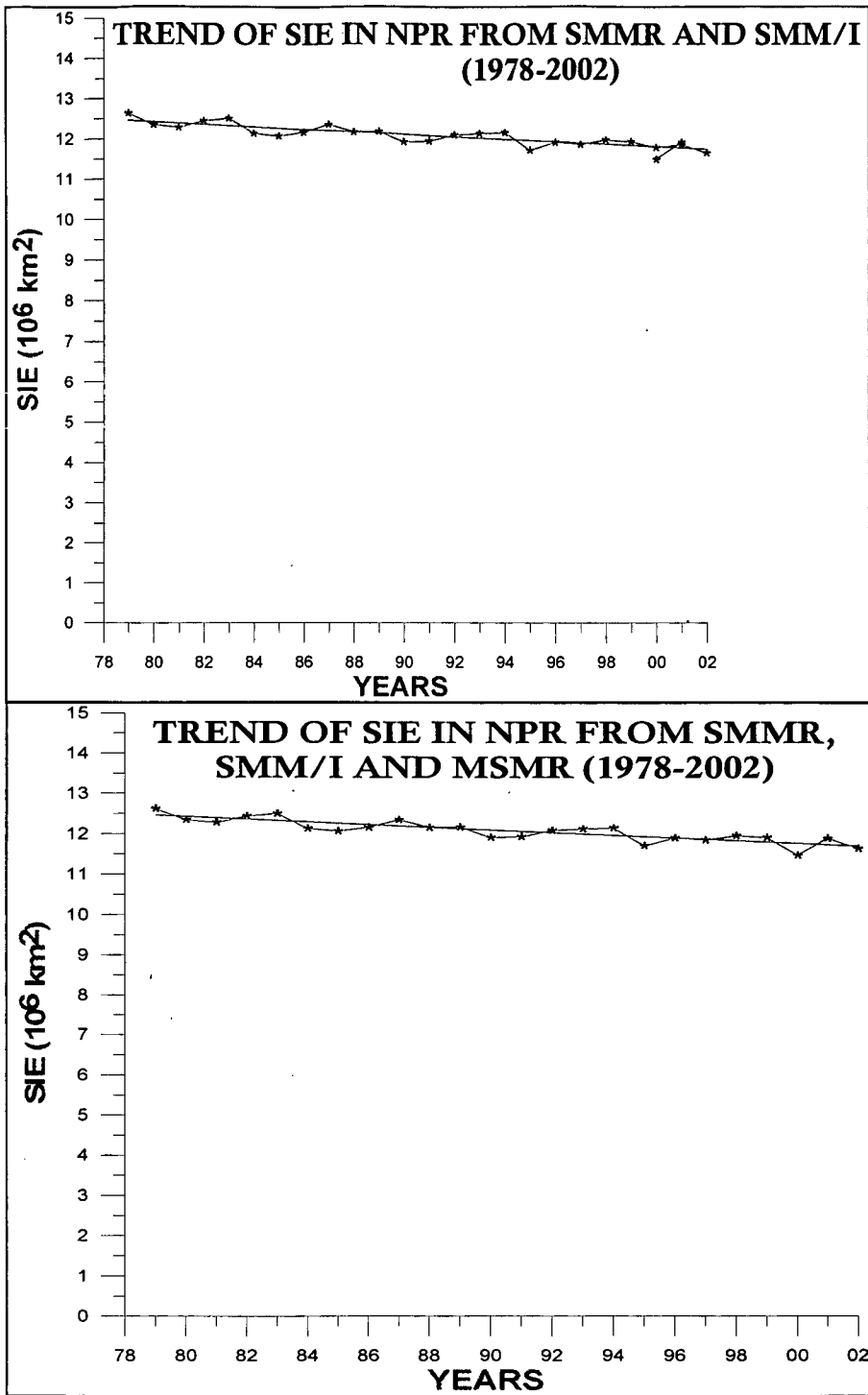


Fig 7.31: Yearly averaged SIE in the NPR with SMMR and SSM/I (a) and SMMR, SSM/I and MSMR (b)

CHAPTER -8

GLOBAL SEA ICE COVER

8.1 INTRODUCTION

It is well known that the long-term variation of sea ice is an indicator of climate change. Long-term changes in sea ice extent or area, covering a sizable portion of the world ocean can easily influence the climate. In turn, the climate change also influences the sea ice cover with a positive feed back factor, thus enhancing the climate change. This phenomenon can provide us a sensitive indicator to the changing climate. Thus monitoring the sea ice cover of the earth through satellites help us in deriving a useful quantitative measure to assess the extent of climate change.

For nearly two and a half decades, satellite derived sea ice products are available, but they are not yet enough to provide a conclusive evidence of any significant change in the climate. The existing satellite record has been examined for change in the sea ice extent and sea ice area in both the Antarctic (Budd, 1975; Kukla and Gavin, 1981; Zwally et al., 1983) and the Arctic (Campbell et al., 1984; Parkinson et al., 1987; Gloersen and Campbell, 1988, Parkinson and Cavalieri, 1989). Gloersen and Campbell (1988), using both ESMR and SMMR data sets, studied the sea ice extent extrema on a global scale. The data they used were not corrected for the instrumental drifts and orbital errors. Further, Gloersen and Campbell (1991 a, b) have extended their study using the corrected SMMR data.

Two of the important features of polar sea ice cover brought out by the satellite observations are the large seasonal and regional variability. Another characteristic is the low year-to-year variability for each hemisphere as a whole, in spite of the large regional variability. Those regions and sectors showing the largest interannual variability are the areas particularly susceptible to large scale atmospheric or oceanic forcing (Cavalieri and Parkinson, 1987; Niebauer, 1988; Enomoto and Ohmura, 1990). These regions are located in seasonal sea ice zones.

The Arctic and the Antarctic act as global heat sinks and provide the same thermodynamic function. However, in many aspects they are opposite and the contrast plays a key role in establishing their regional climates, and also that of the globe as a whole. The most obvious difference is the distribution of the land and sea in the two

hemispheres. The Arctic consists of an ocean surrounded by the continents, whereas the Antarctic contains a continent surrounded by the ocean. There is very little land between 40° and 60° S, and therefore very energetic westerly circulation can build up, in contrast to north where the presence of continents allows only moderate flow to develop. The Arctic oceanic basin has coherent but restricted circulation whereas, in the Antarctic, the circumpolar current prevails which interchanges large amounts of mass and heat with the surrounding seas.

The earth is closest to the sun during the Antarctic summer and most distant in Arctic summer. The Antarctic atmosphere receives about 7% more solar energy in the southern summer than the Arctic during the northern summer. The Antarctic is away from industrial activity, and hence, its atmosphere contains almost no pollutants or dust to reflect, absorb or scatter incoming radiation. The Arctic suffers more in this respect since it lies within the same circulation system as the major industrial areas of the world. The long term mean temperature for the southern hemisphere is about 1.6°C lower than northern hemisphere.

However, the Arctic is warmer and it is also generally more cloudy. Because it is warmer, there is relatively more melted in the Arctic. This tends to reduce the albedo of the surface, resulting in a typical summer value of 0.65 for the Arctic ice compared with 0.90 for the Antarctic ice. The northern ice is thus more efficient in absorbing the solar radiation, and consequently the temperature difference is further accentuated and the melting process gets strengthened.

8.2 COMPARISON OF THE SEA ICE IN THE SOUTHERN & THE NORTHERN POLAR REGIONS

Sea ice, over Antarctic and Arctic regions, is an important component of the Earth's climate system and plays a significant role in modifying the exchange of heat, momentum and moisture in the ocean-ice-atmosphere system. Long-term changes in sea ice, covering tens of Millions of square kilometers (mskm) of the ocean, can influence the climate

system. Sea ice covers about $17.5 - 28 \times 10^6 \text{ km}^2$ area of the global ocean, which is around 3-6% area of the earth's surface. Sea ice cover doubles in the Antarctic and multiplies five times its size in the Arctic from summer to winter (Zwally et al., 1983, Parkinson et al 1987 and Gloersen et al., 1992). Sea ice is the most expansive and maximum seasonally varying geophysical parameter on the earth's surface.

Climate change can influence the sea ice cover and this can serve as a sensitive indicator of changing climate. Knowledge of the high-resolution spatial distribution of sea ice is also of immense value in optimal and safe navigation in the polar oceans. Passive and active microwave measurements from space have turned out to be very useful tools to study and monitor ice conditions in the polar region (Gloersen et al. 1992; US-GCRP 2001, Bingham and Drinkwater 2000).

The Physiographical difference between the two polar regions is also very important. Antarctic is a continent which is surrounded by southern ocean which is well connected with the Indian, Pacific and Atlantic oceans. On the other hand, the Arctic is a predominantly oceanic region surrounded by land with very few passages connecting it with world's other oceans. Arctic Ocean has one third area with depth below 100m and its mean depth is 1800m (Wadhams, 2000) and on the other hand, southern ocean's depth lies in the range between 4000-6000m.

Arctic sea ice extent is minimum ($\sim 9.3 \times 10^6 \text{ km}^2$) in September and maximum in March ($\sim 15.7 \times 10^6 \text{ km}^2$). Sea ice is extending up to about 44°N in the Sea of Japan. First year ice in the Arctic is $\sim 7 \times 10^6 \text{ km}^2$ and multiyear ice cover is $\sim 9 \times 10^6 \text{ km}^2$ (Gloersen et al, 1992). Antarctic sea ice is minimum ($\sim 3.6 \times 10^6 \text{ km}^2$) in February and maximum ($\sim 18.8 \times 10^6 \text{ km}^2$) in September/October. In the Southern Ocean, sea ice is found between $55^\circ - 70^\circ\text{S}$, the first year sea ice covers $\sim 15.5 \times 10^6 \text{ km}^2$ and multi year ice covers $\sim 3.5 \times 10^6 \text{ km}^2$ (Comiso). Frazil type texture of sea ice 5-20% in the Arctic (Turker et. al. 1978) and 50-60% in the Antarctic (Langel et. al., 1989).

Ocean heat flux is the fundamental difference between the Arctic and the Southern ocean is the presence of fresh mixed layer overlying the pycnocline in the Arctic. This is caused by the inflow of fresh water from large rivers, mainly from Siberia. The fresh mixed layer is very stable and prohibits any significant heat fluxes from the much warmer Atlantic water underneath. An average heat flux is 4 W/m^2 . The 'Atlantic layer' at the depth of 200-300m is $1-2^\circ\text{C}$ warm. This heat would be sufficient to melt all the ice during the summer (Barry et al., 1993). In the southern ocean no rivers enter the seas and therefore, the mixed layer is much saltier and not well stratified. Mean ocean heat flux amount is about 40 W/m^2 .

Snow has a thermal conductivity between $0.1-0.3 \text{ W/m/K}$ (Massom et. al, 2001). It acts as a strong thermal insulator. Ice with thin snow cover grows faster than the one with a thick snow cover. Mean snow thickness of the Arctic sea ice reaches about 0.3 m in spring (Warren et. al. 1999). Thicker snow cover is found over Antarctic sea ice. Western Weddell Sea mean snow thickness can be thicker than 0.5m (Massom et. al, 2001). Arctic sea ice thickness varies from 3-5 m in comparison to the Antarctic 0.5-0.6 m (Wadhams, 2000). Salinity of sea ice is generally low in the coastal regions of the Arctic and high in those of the Antarctic.. Several large open ocean polynyas have been observed. in the Antarctic. Polynyas observed in the Arctic are comparatively fewer than those observed in the Antarctic. (Parkinson et al 1987)

Antarctic and Arctic sea ice characteristics have been monitored on more or less a continuous basis since 1973 using space based passive microwave radiometers Nimbus-5, Nimbus-7 onboard DMSP satellites. A detailed analysis of the Arctic and Antarctic sea ice over the 1978-1987 SMMR observation period was made by Gloersen et al. (1992). In addition to the strong seasonal and inter annual variability, their analysis revealed secular trends in the sea ice extent over different regions of the Antarctic. The region of Weddell Sea was found to have the strongest decreasing trend in the sea ice extent over the SMMR observation period. Ross Sea, on the other hand, displayed a slightly weaker but positive trend in sea ice extent. Other sectors of the Antarctic showed weaker and statistically insignificant trends. Antarctic region as a whole did not show any significant long-term variations, partly due to the fact that contrasting trends in different regions balanced each other.

Using the SSM/I data available since 1987, Miles et al.(1996) have reported an absence of any reliable long-term trend in the sea ice extent over the Antarctic. Vyas et al. (2001,2003), made combined use of SMMR, SSM/I and MSMR (onboard oceansat-1) from 1978-2001 and found that the Antarctic sea ice is slowly increasing and is exhibiting a small accelerating trend in the later years.

In contrast to this, the sea ice changes over the Arctic region indicate a consistent and significant long term decrease in sea ice cover and sea ice thickness. Numerous studies based on combined use of data from different microwave radiometers over the Arctic, covering the 20 year period (1978-1998), show a significant *decrease* of 0.7 Million sq km or about 7% in the sea ice extent (Johannessen et al. 2000). This is in conformity with the results of climate modeling studies which predict enhanced warming in the northern polar region due to increased greenhouse gas emissions (Mitchell et al. 1995).

In our previous chapter, we have discussed the seasonal variation of sea ice extent, sea ice area and open water within the ice packs in different sectors of the Southern Polar Ocean and the Antarctic as a whole. In this chapter we will discuss the interregional comparison of sea ice extent, sea ice area and open water within the ice packs in Southern Polar Ocean using annually averaged SMMR, SSM/I and MSMR derived sea ice products. Similarly a comparative study will be presented for both the hemispheres based on annually averaged sea ice products derived from SMMR and SSM/I data. Finally, we will present the summary of the global sea ice cover

8.3 SEASONAL CYCLE ON A GLOBAL SCALE

We will now examine the sea ice parameter for the globe as a whole. The variation in the Antarctic and the Arctic sea ice extent, sea ice area and open water within the ice packs are described by different researchers (Kwok and Comiso, 2002; Bjorgo et al., 1997; Gloersen et al., 1992). A summary of Arctic and Antarctic sea ice record from 1978 - 2000 is shown in figs 8.1, 8.2 and 8.3. All the three parameters shown (sea ice extent, sea ice area and open water within the ice packs) exhibit double peaked maxima in their annual behaviour. These curves reflect the variation in the relative phases of oscillations in the Arctic and the Antarctic sea ice cover and their year-to-year changes in the shape

of oscillations. A dip in the crust is formed due to coinciding of the southern maximum with the northern minimum in the months of August-September. This gives rise to double peak maxima in the curves can be seen in fig. 8.1. The double peak maxima in the global sea ice area oscillations are more or less symmetrical for the years 1979,1982,1984, 1989 and 1996. These interannual variations in the shape of the global ice cover oscillations (Gloersen and Campbell, 1988, 1991) may be explained by the large regional interannual variabilities that occur in the ice extents of each hemisphere (Parkinson and Cavalieri, 1989; Parkinson et al., 1987). The amount of sea ice decreases in some regions while increases in others, possibly because of corresponding shifts in the average weather patterns in those regions. The hemispheric asymmetries in the global ice cover may be due to different atmospheric and oceanic circulation patterns prevailing in the two hemispheres. It could also be because of the quasi-landlocked nature of the Arctic and the open ocean nature of the Antarctic region. However, further investigations are needed to explore and explain this phenomenon.

8.4 GLOBAL SEA ICE TREND AND TEMPERATURE

In the previous sections we have described the linear trends of sea ice extent in different sectors of the Antarctic and for the Southern Ocean as a whole. The annual and interannual trends in the Arctic have been studied by different authors (Zwally et al., 1983; Gloersen and Campbell, 1988; Parkinson and Cavalieri, 1989, Bjorgo et al., 1997). Bjorgo et al. (1997) found a decreasing trend of sea ice extent (4.5% per decade) and sea ice area (5.7% per decade) in the Arctic, which is higher compared to the decrease in sea ice extent (2.4% per decade) stated by Gloersen and Campbell, (1991) for the SMMR period.

The linear least squares fit trend analysis (see fig. 8.3) for the sea ice extent over the whole globe is $(-)$ 0.014×10^6 km²/year. The sea ice area also shows a negative trend of $(-)$ 0.0159×10^6 km²/year. But the open water within the ice packs is found to have an increasing trend of $(+)$ 0.0029×10^6 km²/year.

The decreasing trends show that the melting of sea ice in the Arctic is more prominent than the growth of sea ice in the Antarctic. The regression analysis of global sea ice cover is given in table 8.3.

Through use of MSMR data, it is found that there is a slightly accelerating trend in the Antarctic sea ice cover, as determined by analyzing the satellite derived sea ice cover over a period of 22 years beginning from 1979. The maximum positive and maximum negative deviation in the long-term trend in the sea ice extent and sea ice area around Antarctica appears to occur with an interval ranging between 5-8 years. This seems to be directly associated with Antarctic Circumpolar wave (ACW) / Antarctic Circumpolar Current (ACC). The sea ice cover during the SMMR period (1979 – 86) practically shows absence of any trend. The data from SSM/I period (1987 – 1998) shows a slightly increasing trend (Hanna and Bamber, 2001), inclusion of MSMR data (1999 – 2000 & 2000 – 2001) to the SMMR and SSM/I data shows slight acceleration in the increasing trend (Vyas et al., 2001, 2003). The reasons for this increasing trend are not yet clear and are open to investigation. Notwithstanding the increasing trend in the Antarctic, the global sea ice cover is found to be reducing. This shows the dominating effect of green house gases induced global warming, over the natural processes.

The Claims of global warming are often accompanied by graphs showing the difference (i.e. anomaly) between global average temperatures and the long-term average during 1961-90 inclusive.

These global averages might imply that warming is uniform around the world but this is far from the truth. A comparison of the temperature anomalies in the northern and southern hemispheres shows some significant differences and perhaps the differences between the two hemispheres provides some interesting clues about warming.

Three points stand out:

- ◆ the anomalies in the northern hemisphere are usually much higher than the anomalies for the southern hemisphere
- ◆ the temperature anomaly in the northern hemisphere is generally increasing but the anomaly for the southern hemisphere changes little

- ◆ the greatest anomalies for the northern hemisphere often occur during the northern winter.

The temperature anomaly in the northern hemisphere has increased more rapidly than that for the southern hemisphere since 1985. Typically the January anomaly is an annual peak for the northern hemisphere although at times December or February are higher. Note that in 1998 both hemispheres had temperatures well above the long term average for an extended period and this meant that global temperatures were higher than normal (Climate Research Unit at the University of East Anglia, in the UK).

The area of positive anomalies in surface temperature are shown to be precisely where negative anomalies in the sea ice cover (Comiso et. al. 2002).

Table: 8.1: Global Polar Sea ice trend

Name of the Physical Variable	Mean ($\times 10^6$ km ²)	Trend ($\times 10^6$ km ² /year)	95% confidence limit ($\times 10^6$ km ²)
Sea ice extent	24.18	-0.014	24.122 – 24.443

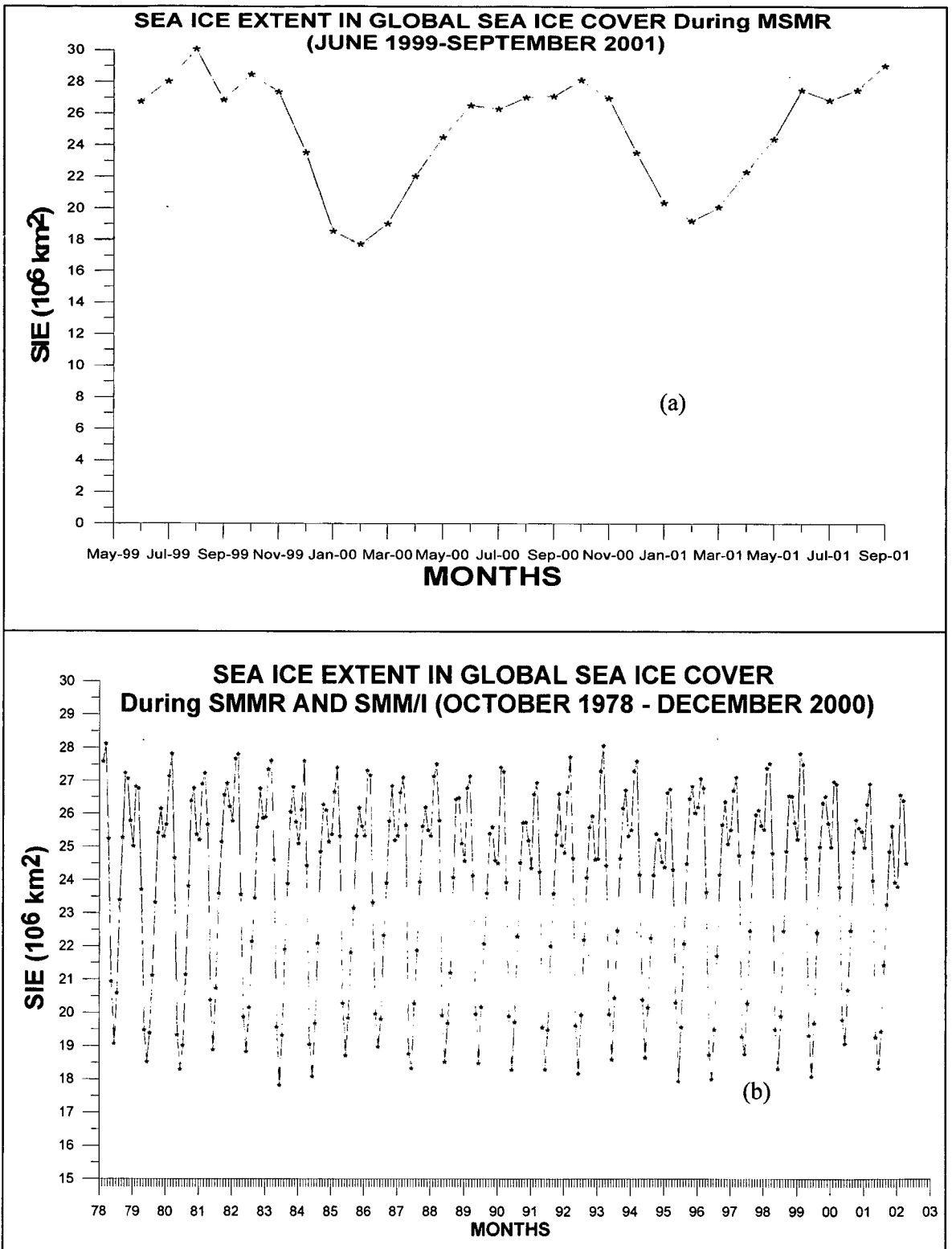


Fig 8.1: The monthly SIE in the NPR during MSMR period (a) and long term from SMMR and SSM/I period (b)

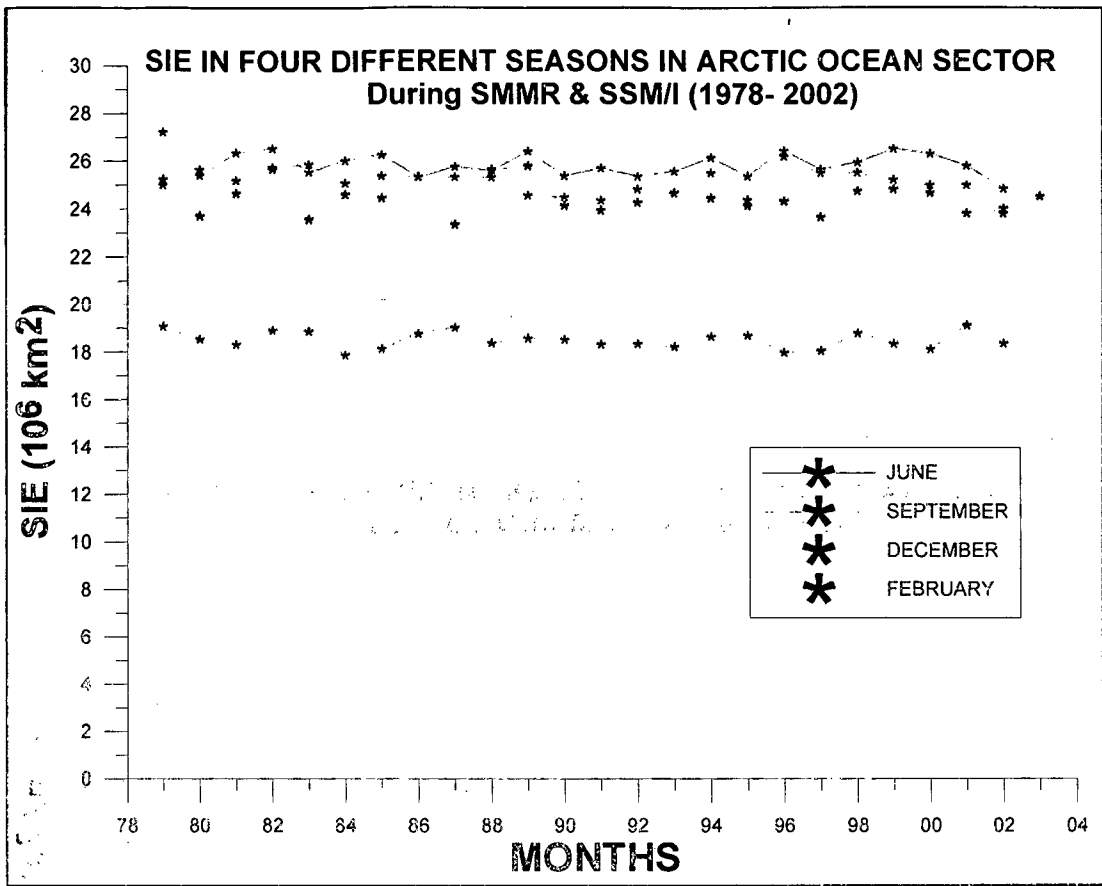


Fig 8.2: SIE in four different Seasons in the total NPR during SMMR and SSM/I Period

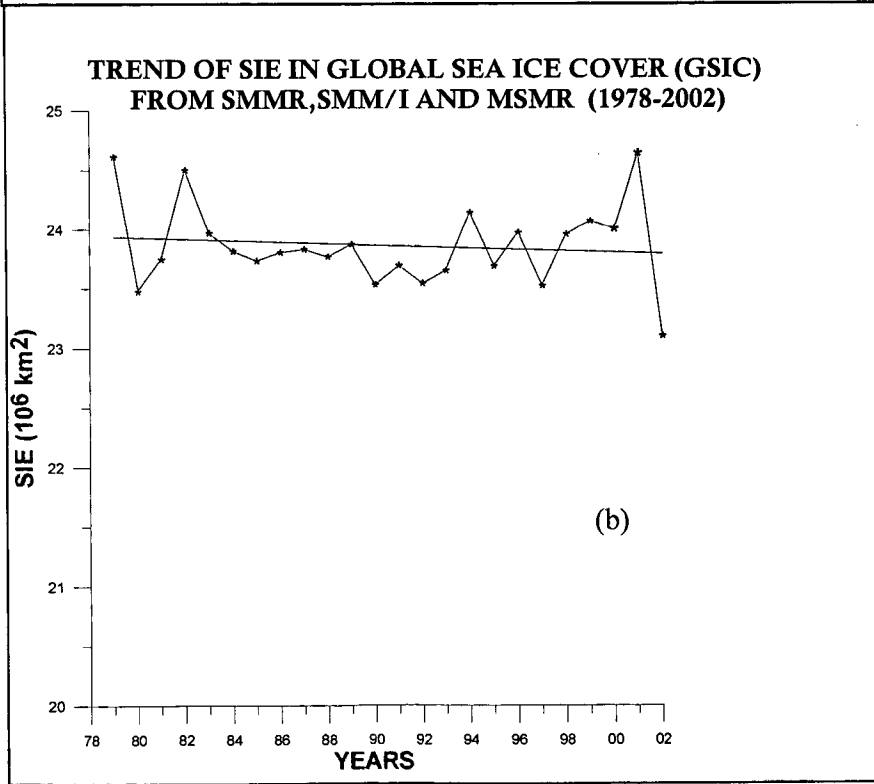
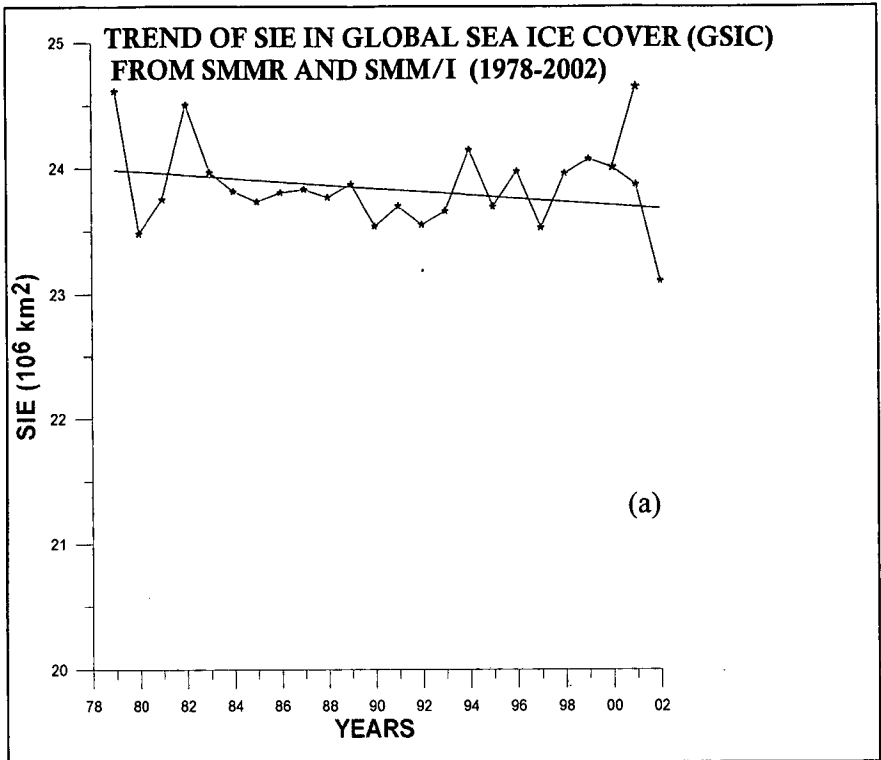


Fig 8.3: Yearly averaged SIE in the NPR with SMMR and SSM/I (a) and SMMR, SSM/I and MSMR (b)

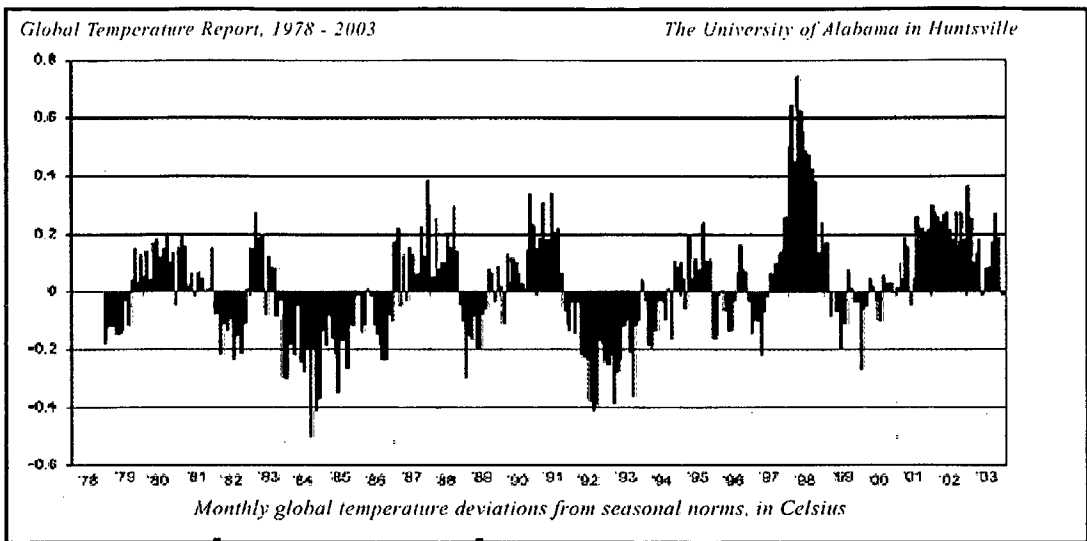


Fig: 8.4 The temperature trend from 1978-2003 (source: Global Temperature report 1978-2003, the Uni

CHAPTER -9

DISCUSSION, CONCLUSIONS AND SCOPE FOR FUTURE WORK

Chapter 9

In our study, we have mainly used the observations from three passive microwave sensors, the SMMR, the SSM/I and the MSMR. The SMMR provided information on the global ice cover from 1978 to 1987. SSM/I and SMMR flew for an overlapping period of 6 weeks during July and August 1987. This overlap period enabled the inter-comparison of the two sensors (Jezek et al., 1993), in spite of the fact that they differ in so many respects, like the local equatorial crossing time (by 6 hours), the altitude, the incidence angle, etc.

In our study, first we have inter-compared the MSMR and the SSM/I data at their brightness temperature product level as well as at the sea ice concentration and the sea ice extent level independently. The analysis shows that the T_B 's obtained from MSMR and SSM/I have a correlation of more than 95%. The sea ice concentrations derived through regression analysis using MSMR T_B 's in the first case and MSMR PR and GR values in the second case agree well with those obtained from SSM/I within an error margin of $\pm 10\%$. For the development of the algorithm from MSMR data, the sea ice concentrations derived using SSM/I data are taken as the reference. SSM/I has been taken as the reference, because it has been calibrated well with SMMR results during the 6 weeks' overlap period and since then, it has been working consistently and satisfactorily. This gives us the confidence on the use of MSMR data for the future cryospheric studies.

We have also studied the land ice features using the MSMR data. The emissivity of the land surface has been calculated using the ground observations carried out by the Indian Antarctic team stationed at Maitri during December 1999 and January 2000. The range of emissivity calculated, taking the surface to be covered with homogeneous ice cover, lies in the range 0.66 to 0.81, which matches well with that reported earlier by other investigators.

The trend of sea ice extent has been studied by various researchers since the launch of the ESMR onboard Nimbus – 5. But, more realistic and operational sea ice extent (SIE) and sea ice area (SIA) are available from SMMR and SSM/I only. The sea ice extent in different sectors of the Southern Polar Ocean behaves differently. For example: the SIE in the Weddell sea sector shows a decreasing trend whereas the sea ice extent in the Ross Sea sector shows an increasing trend (Gloersen et al, 1992; Vyas et al., 2003). During the SMMR period, an increasing trend of $0.0030 \times 10^6 \text{ km}^2/\text{year}$ is reported (Gloersen et al, 1992) for the Southern Polar Ocean as a whole. The analysis of SMMR and SSM/I data for the period 1978 – 1995 shows a decreasing trend of -0.008×10^6 (-0.003×10^6) km^2/year in SIE (SIA) (Bjorgo et al., 1997). But, Hanna and Bamber (2001) analyzed the SSM/I data from July 1987 to December 1997 and found an increasing trend in SIE and SIA by $3 \pm 0.3\%$ per decade and $3 \pm 1.5\%$ per decade respectively for the above period. More recently, Vyas et al. (2003) combined the SMMR and MSMR data and found further strengthening of the increasing trend in the SIE ($0.043 \times 10^6 \text{ km}^2/\text{year}$) in the Antarctic. A combined analysis of SMMR, SSM/I and MSMR data shows an increasing trend of $0.0314 \times 10^6 \text{ km}^2/\text{year}$. From this analysis, the behaviour of the polar sea ice extent during the past two and a half decades can be summarized as follows :

Initially, during 1979 to 1987, the SIE was more or less stable with random fluctuations but without any appreciable increasing or decreasing trend. From 1987 to 1997, it showed a small but definite increasing trend. Thereafter, it has been showing a strengthening of the increasing trend as judged from combined SMMR and MSMR observations. A very interesting scientific result was found in the sea ice trend analysis, which has been described in Chapter 8.

The maximum positive and the maximum negative deviation in sea ice extent and the sea ice area seem to occur generally at interval of 5 – 8 years. This is seen for all the individual sectors and for the Global Polar Ocean, taken as a whole (see table 8.1). This could be due to the effect of some external forcing which appears to be quasi-periodic in nature. The interval between the occurrence of maximum deviation and minimum

deviation could possibly be attributed to the Antarctic Circumpolar Wave (ACW) / Antarctic Circumpolar Current (ACC) (White and Peterson, 1996; White et al., 1998).

On the other hand, in the Arctic region, the sea ice extent is reducing at an alarming rate (Rothrock et al., 1999; Parkinson et al., 1999; Parkinson 1991; Johannssen et al., 1995; Cavalieri et al., 1999; Cavalieri et al., 1997; Gloersen et al., 1999). During the SMMR period, there has been a decrease in the sea ice extent by 2.4% per decade (Gloersen and Campbell, 1991). The trend analysis of the data showed a decrease of 4.5% in SIE and 5.7% in SIA over the period 1978 – 1995 of observations in the Arctic (Bjorgo, et al. 1997). Maslanik et al. (1996) reported that the perennial ice pack is reduced by 9% during 1990 – 1995 period compared with that during 1979-1989 period. This shows that the Arctic sea ice is gradually thinning and the ice cover area in the northern polar region is decreasing. Northern Polar region shows a clear signal of human induced green house warming over and above the variability caused by the natural processes. It is found that the global ice cover (North and South Polar Regions, combined together) is reducing at a rate of (-) $0.014 \times 10^6 \text{ km}^2/\text{year}$.

Still the reasons for the hemispheric asymmetry are not clearly understood. This has to be investigated in future as to why the southern polar region behaves in an opposite way in spite of the warming induced by the anthropogenic factors uniformly over the global scale.

9.1 SCOPE FOR FUTURE WORK

The above studies demonstrate the capability of Passive Microwave Radiometers (PMRs), in general, and that of MSMR onboard OCEANSAT –1 in particular, in capturing the sea ice distribution over the Northern Polar region

In view of the importance of Polar Regions as a key sensitive indicator of green house induced global warming, tremendous thrust is being given worldwide to space-based remote sensing of the polar ice covered regions. A number of innovative satellite missions are being planned to measure and monitor the changes in the extent, concentration and thickness of sea ice.

Polar remote sensing efforts in India will get a further boost when OCEANSAT -2, proposed to carry a Ku-band scatterometer, will go into orbit in 2007. This will enlarge the scope of our studies in the field of climate change, changes in ozone layer and ice processes. More and more availability of sophisticated active and passive instruments on satellite based platforms, in near future, will gear up the process of understanding our earth more precisely and correctly.

From the satellite derived sea ice and land ice studies it is clearly seen that the sea ice extent in the Arctic is decreasing, and on the other hand, the sea ice extent in the Antarctic is increasing. The Greenland ice sheet is thinning day by day, whereas the east Antarctic ice sheet is undergoing cooling and the Antarctic Peninsula is showing a warming trend. The warming of Antarctic Peninsula and the cooling in east Antarctica may be due to the Antarctic Oscillation (AAO) spending more and more time in its positive phase. Kerr (2002) and Thompson and Solomon (2002) associated the positive phase of AAO to the springtime loss of stratospheric ozone layer over the Antarctic. But, still the cause of the hemispheric asymmetry is not well understood. Further investigation and research is required to explain it.

Polynyas and leads play major role in the atmosphere-ice-ocean interaction in polar seas. They are the major regions where the energy, mass and momentum transfer occur between the atmosphere and the Ocean. The role of polynyas and leads in global climate models is poorly represented. For qualitative and quantitative prediction of future climate, a proper energy balance study of the polar Cryosphere is required.

Different types of sea ice have different emissivities and albedoes. Different types of sea ice and their spatial extent in a region, contribute greatly to the energy balance study of that region. For suitable representation of cryosphere in the regional and global atmospheric and oceanic circulation models, the types of sea ice (e.g. nenas, pancake ice, new ice etc.) are more important. The active sensor imagery is very relevant for classifying different types of sea ice. For studying the meso-scale processes in Polar Regions proper ice-type classification is very important.

Mass balance of the major global ice sheets, in the Antarctic and in Greenland, are very important from the point of view of global warming and sea level rise. The study of the

thinning and the mass balance of ice sheets over large spatial extent would give us an idea about the potential sea level rise and the hydrological changes in the region. This is one of the major thrust areas where more and more research is required.

Study of the effect of cryosphere on the monsoon winds and rainfall activity is another challenging area in earth science studies. We may be able to predict the monsoon better by adding the cryospheric parameters (e.g., the variations in the global energy balance due to the variations in the ice cover) to the physics of the monsoon forecasting models.

REFERENCE

- Abdalti, W. and k. Steffen (1998); Accumulation and hoar effects on microwave emission in the Greenland ice sheet dry snow zones; *J. Glaciol.*; *44*, pp 523 – 531
- Akitomo, K., T. Awaji and N. Imasato (1995); Open-ocean deep convection in the Weddell Sea : two-dimensional numerical experiments with a non-hydrostatic model; *Deep-Sea Res. Part I : Oceanogr. Res.*; *42*; pp. 53 – 73
- Ali, M. M. et al (2000); Validation of Multifrequency Scanning Microwave Radiometer Geophysical parameter data products, Proceedings of PORSEC-2000, Goa, India; Vol. I; pp. 182 – 191
- Andreas, E. L and B. A. Cash (1999); Convective heat transfer over winter time leads and polynyas; *J. Geophys. Res.*; *104*; pp. 25,721 – 25,734
- Andreas, E. L. and B. Murphy (1986); Bulk transfer coefficients for heat and momentum over leads and polynyas; *J. Phys. Oceanogr.*; *16*; pp. 1875 – 1883
- Barnett, T. P., D. W. Pierce and R. Schnur (2001); Detection of anthropogenic climate change in the world's oceans, *Science*; *292*; pp 270 – 274
- Bamber J. L., C. R. Bentley, J. G. Morley and C. G. Rapley (1994); Antarctic topography derived from ERS – 1 Altimetry; ESA SP – 361; pp. 113 – 117
- Barnett, T. P., L. Dumenil, U. Schlese; E. Roeckner, M. Latif (1989); The effect of Eurasian snow cover on regional and global climate variations; *J. Atmos. Sci.*; *46*, pp. 661 - 685
- Bhandari, S. M., M. K. Dash, N. K. Vyas, N. Khare and P. C. Pandey (2002); Microwave remote sensing of ice in the Antarctic region; *Advances in Marine and Antarctic science*; (Eds. D. Sahoo and P. C. Pandey); APH Pub. Corp.; New Delhi; pp. 423 – 441
- Bjorgo, E., Ola M. Johannessen and M. W. Miles (1997); Analysis of merged SMMR-SSM/I time series of Arctic and Antarctic sea ice parameters 1978 – 1995; *Geophys. Res. Letter*; *24*; pp. 413 – 416
- Brix, H. and R. Gerdes (2003); North Atlantic deep water and Antarctic bottom water: their interaction and influence on the variability of the global ocean circulation; *J. Geophys. Res.*; *108*; pp. 4-1 to 4 –17
- Brown, R. D. (1995), Spatial and temporal variability of North American Snow cover, 1971 – 1992, Proc. 52nd eastern snow conference, Toronto, Ontario, June 7-8, 1995, pp 69 – 78.
- Bryan, F. O. (1998); Climate drift in a multi-century integration of the NCAR climate system model; *J. Climate*; *11*, pp. 1455 – 1471
- Budd, W. F. (1975); Antarctic sea ice variations from satellite sensing in relation to climate, *J. Glaciol.*; *15*; pp. 417 – 426
- Campbell, W. J., P. Gloersen and H. J. Zwally (1984), Aspect of Arctic sea ice observable by sequential passive microwave observations from the Nimbus – 5 satellite, in *Arctic Technology and Policy*; Eds. I. Dyer and C. Chrysostomidis; Hemisphere Publishing; New York, pp. 197 – 222
- Carmark, E. C. (1977); Water characteristics of the Southern Ocean south of polar front; In: Azd, M. (Ed.); *A voyage of discovery; George Deacon 70th Anniversary Volume*, Pergamon Press; New York; pp. 15 – 37.
- Carsey, F. D. (1980); Microwave observation of the Weddell Polynya; *Monthly Weather Review*; *108*, pp. 2032 – 2044

- Cavaliere, D. J., C. L. Parkinson, P. Gloersen, J. C. Comiso and H. J. Zwally (1999); Deriving long term time series of sea ice cover from satellite passive microwave multi-sensor data sets; *J. Geophys. Res.*; *104*; pp. 15,803 – 15,814
- Cavaliere D. J., P. Gloersen, C. L. Parkinson, H. J. Zwally and J. C. Comiso (1997); Observed hemispheric asymmetry in global sea ice change; *Science*; *278*, pp. 1104 – 1106
- Cavaliere, D. J. and C. L. Parkinson (1987); On the relationship between atmospheric circulation and the fluctuations in the sea ice extents of the Bering and Okhotsk Seas; *J. Geophys. Res.*; *92*; pp. 7141 – 7162
- Cavaliere, D.J, W. J. Campbell, P. Gloersen (1984); Determination of sea ice parameters with the Nimbus 7 SMMR, *J. Geophys. Res.*, *89*, pp 5355 – 5369
- Chandrasekhar, S (1960); *Radiative Transfer*; Dover, New York; 393 pp
- Church, J. A., J. M. Gregory, Ph. Huybrechts, M. Kuhn, C. Lambeck, M. T. Nhuan, D. Qin and P. L. Woodworth (2001); Changes in sea level, Chapter 11, in : *IPCC Third Scientific Assessment of climate change*; Eds. J. Houghton and D. Yihui; Cambridge University Press; pp. 641 – 693
- Comiso, J. C. and K. Steffen (2001); studies of Antarctic sea ice concentrations from satellite data and their applications; *J. Geophys. Res.*; *106*; pp. 31,361 – 31, 385
- Comiso, J. C. (2000); Variability and trends in Antarctic surface temperatures from in situ and satellite infrared measurements; *Journal of Climate*; *13*, pp. 1674 – 1696
- Comiso, J. C. and A. L. Gordon (1998); Interannual variability in summer sea-ice minimum, coastal polynyas and bottom water formation in the Weddell Sea; in *Antarctic Sea Ice: Physical Processes, Interactions and Variability*; *Antarctic Res. Ser.*; Vol. *74*; Ed. M. O. Jeffries; AGU; Washington, D. C.; pp. 293 – 315
- Comiso, J. C., D. J. Cavaliere, C. L. Parkinson and P. Gloersen (1997); Passive microwave algorithms for sea ice concentration: a comparison of two techniques; *Remote Sen. Environ.*; *60*; pp. 357 – 384
- Comiso, J. C. and A. L. Gordon (1996); The Cosmonaut polynya in the Southern Ocean: Structure and variability, *J. Geophys. Res.*; *101*; pp. 18,297 – 18,313
- Comiso, J. C. (1994); Surface Temperature in polar regions using Nimbus – 7 THIR; *J. Geophys. Res.*; *99*; pp. 5181 – 5200
- Comiso, J. C. and A. L. Gordon (1987); Recurring polynyas over the Cosmonaut Sea and the Maud Rise; *J. Geophys. Res.*; *92*; pp. 2819 – 2833
- Comiso, J.C. (1986); Characteristics of Arctic winter sea ice from satellite multi-spectral microwave observations; *J. Geophys. Res.*; *91*; pp. 975 – 994
- Comiso, J. C. (1983); Sea ice effective microwave emissivities from satellite passive microwave and infrared observations; *J. Geophys. Res.*; *88*; pp. 7686 – 7704
- Curry, J. A., Julie L. Schramm and Elizabeth E. Ebert (1995); Sea ice-albedo climate feedback mechanism; *J. of climate*; *8*; pp. 240 – 247
- Dash M. K., S. M. Bhandari, N. K. Vyas, N. Khare, A. Mitra and P. C. Pandey (2001); Oceansat MSMR Imaging of the Antarctic and the Southern Polar Ocean; *International Journal of Remote Sensing*; *22*; pp. 3253 – 3259
- Desnos, Yves-Louis (2002); The working group on Calibration, CEOS News letter # *19*, pp. 5

- Drinkwater, M. R. and X. Liu (2000); Seasonal to interannual variability in Antarctic sea ice surface melt; *IEEE Trans. Geosci. Remote Sens.*; 38; pp 1827 – 1842
- Editorial (1989); The Arctic: a key to world climate; *Science*; 243; p. 873
- Elachi, C. (1982); Radar images of the earth from space, *Scientific American*; 247; pp. 54 – 61
- Enomoto, H. and A. Ohmura (1990); The influences of atmospheric half-yearly cycle on the sea ice extent in the Antarctic; *J. Geophys. Res.*; 95; pp 9497 – 9511
- Fahnestock, M., R. Bindshaler, R. Kowk and K. Jezek (1993), Greenland ice sheet surface properties and ice dynamics from ERS – 1 SAR imagery, *Science*, 262, pp 1530 – 1534
- Ferrick, M. G. and T. D. Prowse (2000); Two communities join forces to study ice covered rivers and lakes; *EOS* 81 (10); p. 108
- Fletcher, J. O. (1969); Ice extent in the Southern Ocean and its relation to world climate; Memorandum RM – 5729 – NSF, Rand Corporation; Santa Monica; California; 108 pp.
- Fu, L. L. and A. Cazenave (2001); Satellite Altimeter and Earth Sciences – A Handbook of Techniques and Applications; International Geophysical series; Vol. 69; Academic Press; 463 p.
- Gloersen P., C. L. Parkinson, D. J. Cavalieri, J. C. Comiso and H. J. Zwally (1999); Spatial distribution of trends and seasonality in the hemisphere sea ice covers: 1978 – 1996; *J. Geophys. Res.*; 104; pp. 20,827 – 20,835
- Gloersen, P. (1995); Modulation of hemispheric sea ice cover by ENSO events; *Nature*; 373; pp. 503 – 506
- Gloersen P., W. J. Campbell, D. J. Cavalieri, J. C. Comiso, C. L. Parkinson and H. J. Zwally (1992); Antarctic and Arctic sea ice, 1978 – 1987: Satellite passive-microwave observations and analysis; *NASA SP – 511*; Washington DC; 290 pp.
- Gloersen, P. and W. J. Campbell (1991 a) Variations of extent, area, and open water of the polar sea ice covers: 1978-1987, Proceedings of the International conference on the role of the polar regions in Global Change, Eds. G. Weller, C. L. Wilson and B. A. B. Severin; Geophysical Institute, University of Fairbanks, Alaska, 778pp.
- Gloersen, P. and W. J. Campbell (1991 b) Recent variations in Arctic and Antarctic sea ice covers, *Nature*, 352; pp. 33 – 36
- Gloersen, P. and W. J. Campbell (1988); Variations in Arctic, Antarctic and global sea ice covers during 1978 – 1987 as observed with the Nimbus 7 Scanning Multichannel Microwave Radiometer; *J. Geophys. Res.*; 93; pp. 10,666 – 10,674
- Gloersen, P. and D.J Cavalieri (1986), Reduction of weather effects in the calculation of sea ice concentration from microwave radiances, *J. Geophys. Res.*, 91, pp. 3913 – 3919
- Gloersen, P., T.T. Wilheit, T.C. Chang, W. Nordberg and W.J. Campbell (1974a), Microwave maps of the polar ice of the earth, *Bull. Am. Meteorological Soc.*, 55, pp. 1442 – 1448
- Gloersen, P, T.C. Chang., T.T. Wilheit, and W.J. Campbell (1974b); Polar sea ice observations by means of microwave radiometry, in *Advanced Concepts and Techniques in the Study of Snow and Ice*, eds. H. S. Santeford and J. L. Smith; National Academy of Science; pp. 541 – 550

- Gloersen, P, W. Nordberg, T. J. Schmugge, T.T. Wilheit, and W.J. Campbell (1973); Microwave Signatures of first – year and multi-year sea ice; *J. Geophys. Res.*; 78; pp. 3564 – 3572
- Gohil, B. S., A. K. Mathur and A. K. Verma (2000); Geophysical parameters retrieval over oceans from IRS – P4 /MSMR; Proceedings of PORSEC-2000, Goa, India; Vol. I; pp. 207 – 211
- Goldstein, M. R., H. Engelhardt, B. Kamb and R. M. Frolich (1993), Satellite radar interferometry for monitoring ice sheet motion : application to an Antarctic ice stream; *Science*; 262; pp. 1525 – 1530
- Gordon, C., C. Cooper, C. A. Senior, H. Banks, J. M. Gregory, T. C. Johns, J. F. B. Mitchell and R. A. Wood (2000); The simulation of SST, sea ice extents and ocean heat transports in a version of the Hadley Centre coupled model without flux adjustments; *Climate Dynamics*; 16; pp 147 – 168
- Gordon, A. L. (1998); Western Weddell Sea thermohaline stratification; *Ocean, Ice and Atmosphere :interactions at the Antarctic continental margin*; Eds. S. S. Jacobs and R. F. Weiss; *Antarctic Res. Ser.*, Vol. 75; AGU; Washington, D. C.; pp. 215 – 240
- Gordon , A. L. (1991); Two stable modes of Southern Ocean winter stratification, *Deep Convection and Water Mass Formation in the Ocean*, edited by J. Gascard and P. Chu; Elsevier Publisher; pp. 17 – 35
- Gordon, A. L. and B. A. Huber (1990); Southern Ocean Winter mixed layer; *J. Geophys. Res*; 95; pp. 11,655 – 11,672
- Gordon, A. L. and J. C. Comiso (1988); Polynyas in the Southern Ocean; *Scientific Americana*; 256; pp. 90 – 97
- Gordon, A. L. and E. M. Molineelli (1982); *Southern Ocean Atlas: Thermohaline Chemical Distributions and the Atlas Data Set*, 233 plates; Columbia University Press; N.Y.
- Gordon, A. L. (1978); Deep Antarctic Convection west of Maud Rise; *J. Phys. Oceanogr.*; 8; pp. 600 – 612
- Gordon, A.L. (1974); Varieties and Variability of Antarctic Bottom Water, *Processus de Formation des eaux oceaniques Profondes en particulier en Mediterranee Occidentale*, Colloques Internationaux du C.N.R.S. No. 215; Editions du Centre National de la Recherche Scientifique; pp. 33 – 47
- Grotzner, A., R. Sausen, and M. Claussen (1996); The impact of sub-grid scale sea ice inhomogeneities on the performance of the atmospheric general circulation model ECHAM; *Climate Dyn.*; 12; pp. 477 – 496
- Hanna, E. and J. Bamber (2001); Derivation and optimization of new Antarctic sea-ice record; 22; pp. 113 – 139
- Hofer, R. and E. G. Njoku (1981); Regression techniques for oceanographic parameter retrieval using space-borne microwave radiometry, *IEEE Trans. on Geosc. and Remote Sensing*; *GE – 19*, pp 178 – 189
- IPCC, (2001); *Climate Change 2001: The Scientific Bases*; Eds. J. T. Houghton, Y. Ding, D. J. Griggs, M. Noguer, P. J. van der Linden, X. Dai, K. Maskell and C. A. Johnson; Cambridge University Press; Cambridge; UK.

- ISRO (1999), IRS – P4 MSMR data products format, DOC.NO.ISRO-SAC-IRS-P4-DP/MSMR/FORMAT/VERSION2.0/2/99; 31 pp.
- Jacobs, S. S. and J. C. Comiso (1997); Climate variability in the Amundsen and Bellingshausen seas, *J. Climate*; *10*; pp. 697 – 709
- Jacobs, S. S. and J. C. Comiso (1993); A recent sea ice retreat west of Antarctic Peninsula, *Geophys. Res. Letter*; *20*; pp. 1171 – 1174
- Jacob, S. S. and J. C. Comiso (1989); Sea ice and oceanic processes on the Ross sea continental shelf; *J. Geophys. Res.*; *94*; pp. 18,195 – 18,211
- Jacobs, S. D., D. Georgi, and S. Patla (1980); Technical report, Conrad 17 hydrographic station in the southwest-Indian Antarctic Ocean; Tech. Rep. CU-1-80-TRI; Lamont – Doherty Geological Observation; Palisades; N.Y.
- Jezek K. C., C. J. Merry and D. J. Cavalieri (1993); Comparison of SMMR and SSM/I passive microwave data collected over Antarctica; *Annals of Glaciology*; *17*; pp. 131 – 136
- Jiang, L. and R. W. Garwood Jr. (1995); A numerical study of three dimensional dense bottom water plumes on a Southern Ocean continental slope, *J. Geophys. Res.*; *100*; pp. 18,471 – 18,488
- Johannessen O. M., E. V. Shalina and M. W. Miles (1999); Satellite evidence for an arctic sea ice cover transformation, *Science*, pp. 1973 – 1979
- Johannessen O. M., M. W. Miles and E. Bjorgo (1995), The Arctic's shrinking sea ice, *Nature*, *376*, pp. 126 – 127
- Johannessen, O. M., W. J. Campbell, R. Shuchman, S. Sandven, P. Gloersen, J. A. Johannessen, E. G. Josberger and P.M. Haugan (1992), Microwave study programs of air-sea-ice interactive process in the seasonal ice zone of the Greenland and Barents sea, in microwave remote sensing of sea ice, *Geophys. Monogr. Ser.*, 68, edited by F. Carsey, pp 261 – 289, AGU, Washington, D.C.
- Joughin, I. and S. Tulaczyk (2002); Positive mass balance of Ross ice streams, West Antarctica; *Science*; *295*; pp. 476 – 480
- Kerr A. R. (2002); A single climate mover for Antarctica; *Science*; *296*; pp. 825 – 826
- Khodri, M., Y. Leclainche, G. Ramstein, P. Braconnot, O. Marti and E. Cortijo (2001); Simulating the amplification of orbital forcing by ocean feedbacks in the last glaciation; *Nature*; *410*; pp 570 – 574
- Killworth, P. D. (1983); Deep convection in the world ocean; *Rev. Geophys. Space Phys.*; *21*; pp 1 – 26
- Kim, J. W., S. Hong, J.-S. Hwang, Ho-Il Yoon, Bang Yong and Y. Kim (2002); Distribution of Antarctic Sea ice from satellite Altimetry in the Weddell Sea : preliminary results; *Ocean and Polar research*; *24*; pp. 255 – 261
- Kim, S.-J. and A. Stossel (1998); On representation of the Southern Ocean water masses in an ocean climate model; *J. Geophys. Res.*; *103*; pp. 24,891 – 24,906
- King, J. C. and J. Turner (1997), *Antarctic Meteorology and Climatology*; Cambridge University Press; Cambridge, U. K.; 409 pp.
- King, J. C. (1994); Recent climate variability in the vicinity of the Antarctic Peninsula; *Int. J. Climatol.*; *14*; pp. 357 – 369
- Kondratyev K. Ya, O. M. Johannessen and V. V. Melentyev (1996); High latitude climate and remote sensing; John Wiley & sons Ltd.; 202 p

- Kowk, R. and J. C. Comiso (2002); Southern Ocean climate and sea ice anomalies associated with the Southern oscillation; *J. Climate*; *15*; pp. 487 – 501
- Kukla, G. and J. Gavin (1981); Summer ice and carbon dioxide; *Science*; *215*; pp. 497 – 503
- Kurtz, D. D. and D. H. Bromwich (1985); A recent, atmospherically forced polynya in Terra Nova Bay, in *Oceanology of the Antarctic Continental Shelf*; Ed. S. S. Jacobs; Antarctic research series vol. 43, American Geophysical Union; Washington, D. C.; pp. 177 - 201
- Kwok, R., G. F. Cunningham, S. Yueh (1999); Area balance of the Arctic Ocean perennial ice zone: October 1996 to April 1997; *J. Geophys. Res.*; *104*; pp 25,747 – 25,759
- Lee, B. Y., T.-Y. Kwon, J.-S. Lee, Y. -I. Won (2002); Surface Air Temperature Variations around the Antarctic Peninsula: comparison of the West and east sides of the Peninsula; *Ocean and Polar Research*; *24*; pp 267 – 278
- Liu, A. K., Y. Xhao and S. Y. Wu (1999); Arctic sea ice drift from wavelet analysis of NSCAT and special sensor microwave imager data; *J. Geophys. Res.*; *104*; pp 11,529 – 11,538
- Long, D. G. and M. R. Drinkwater (1994); Greenland ice-sheet properties observed by the Seasat – A scatterometer at enhanced resolution, *J. Glaciology*, *40*, pp. 213 – 230
- Long, D. G. and M. R. Drinkwater (1999); Cryosphere application on NSCAT data; *IEEE Trans. Geosci. Remote Sens.*; *37*; pp 1671 – 1684
- Markus, T., C. Kottmeier and E. Fahrbach (1998); Ice formation in coastal polynyas in the Weddell Sea and their impact on oceanic salinity; in *Antarctic Sea Ice: Physical Processes, Interactions and Variability*; Ed. M. O. Jeffries; Antarctic Res. Ser.; Vol. 74; AGU; Washington, D. C.; pp. 273 – 292
- Martinson, D. G. and R. A. Iannuzzi (1998); Antarctic ocean-ice interactions from ocean bulk property distributions in the Weddell Gyre; *AGU – Antarctic series*; *74*; pp. 243 – 271
- Martinson, D. G. (1990); Evolution of the Southern Antarctic mixed layer and sea ice, Open ocean deep water formation and Ventilation; *J. Geophys. Res.* ; *95*; pp. 11,641 – 11,654
- Maslanik, J. A., M. C. Serreze and R. G. Barry (1996); Recent decreases in Arctic summer ice cover and linkages to atmospheric circulation anomalies, *Geophys. Res. Letter*, *23*, pp 1977 – 1680
- Massom, R. (1991); *Satellite remote sensing of polar regions*; Lewish Publisher, FL, USA
- Matson, M., C.F. Ropelewski and M.S. Varnadore (1986), *An atlas of satellite derived Northern hemispheric snow cover frequency*, U.S. Dept. of Commerce, National Oceanic and Atmospheric Administration, Data and Information Service, Washington, D.C.
- Maul, G.A., (1985); *Introduction to Satellite Oceanography*; Martinus Nijhoff Publishers; Dordrecht/Bosto/Lancaster; 606 pp.
- Meeks, D. C.; R. O. Ramseier and W.J. Campbell (1974); A study of Microwave emission properties of sea ice AIDJEX 1972; *Proceedings of the Ninth International Symposium on Remote Sensing*; Willow Run Laboratories of the Institute of Science and Technology; The University of Michigan; Ann Arbor; Michigan, pp. 307 – 322

- Mishra, T., A. M. Jha, D. Putrevu, J. Rao, D. B. Dave and S. S. Rana (2002); Ground calibration of multifrequency scanning microwave radiometer (MSMR); *IEEE Trans. On Geosci. and Remote Sensing*, *40*; pp. 504 – 508
- Moore, G. W. K., K. Alverson and I. A. Renfrew (2002); A reconstruction of the Air – Sea interaction associated with the Weddell polynya; *J. of Phys. Oceanogr.*; *32*; pp. 1685 – 1698
- Nghiem, S. V. and W. –Y. Tsai (2001); Global snow cover monitoring with spaceborne Ku-band scatterometer; *IEEE Trans. Geosci. Remote Sens.*; *39*; pp 2118 – 2134
- Niebauer, H. J. (1988); Effect of El Nino-Southern Oscillation and North Pacific weather patterns on interannual variability in sub-arctic Bering Sea; *J. Geophys. Res.*; *93*; pp 5051 – 5068
- Orsi, A. H., G. C. Johnson, J. L. Bullister (1999), Circulation. Mixing and production of Antarctic bottom water; *Progresses in Oceanography*; *43*; pp 55 – 109
- Palsule, S., A. Garg, H. Pandya and A. Sharma (2002); Multifrequency scanning microwave radiometer (MSMR) sensor performance; *Proc. of ISPRS Comm. VII Symp. On “Resource and Environment Monitoring”*, Hyherabad, India; *1*; pp 220 – 225
- Pandey, P. C. and R. K. Kakar (1983); A two-step statistical technique for retrieval of geophysical parameters from microwave radiometer data; *IEEE Trans. Geosc. and Remote Sensing*, *GE – 21*; pp 208 – 214
- Park, Y. H., E. Charriaud and M. Fieux (1998); Thermohaline structure of the Antarctic Surface Water/Winter Water in the Indian sector of the Southern Ocean; *Journal of Marine Systems*, *17*, pp. 5 – 23
- Parkinson, C. L. (2002); Trends in the length of the Southern Ocean sea ice season 1979 – 1999; *Annals of Glaciology*; *34*; pp. 435 – 440
- Parkinson C. L., D. J. Cavalieri, P. Gloersen, H. J. Zwally and J. C. Comiso (1999); Arctic sea ice extents, areas and trends, 1978 – 1996; *J. Geophysical Research*; *104*; pp. 20,837 – 20,856
- Parkinson. C. L. (1991); Inter-annual variability of the spatial distribution of sea ice in the north polar region; *J. Geophysical Research*; *96*; pp. 4791 – 4801
- Parkinson, C. L. and D. J. Cavalieri (1989); Arctic sea ice, 1973 – 1987: seasonal, regional and interannual variability, *J. Geophys. Res.*; *94*, pp 14,499 – 14,523
- Parkinson, C. L., J. C. Comiso, H. J. Zwally, D. J. Cavalieri, P. Gloersen and W. J. Campbell (1987); Arctic sea ice, 1973 – 1976 : Satellite Passive Microwave Observations, NASA SP – 489; National Aeronautics and Space Administration; Washington, D. C.; 296 pp
- Petit, J. R., J. Jouzel, D. Raynaud, N. I. Barkov, J. –M. Barnola, I. Basile, M. Benders, J. Chappellaz, M. Davis, G. Delayque, M. Delmotte, V. M. Kotlyakov, M. Legrand, V. Y. Lipenkov, C. Lorius, L. Pepin, C. Ritz, E. Saltzman and M. Stievenard (1999); Climate and atmospheric history of the past 420, 000 years from the Vostok ice core, Antarctica; *Nature*; *399*; pp. 429 – 436
- Pickard, G. L. and W. J. Emery (1993); *Descriptive Physical Oceanography An Introduction*; Pergamon Press; New York; 320 pp.
- Remund, Q. P. and D. G. Long (1999); Sea ice extent mapping using Ku band scatterometer data; *J. Geophys. Res.*; *104*; pp 11,515 – 11,527

- Rind, D., R. Healy, C. Parkinson and D. Martinson (1995); The role of sea ice in $2\times\text{CO}_2$ climate model sensitivity. Part I: The Total influence of sea ice thickness and extent, *J. climate*; 8; pp. 449 – 463
- Robinson, D. A., K. F. Dewey and R. R. Heim (1993); Global snow cover monitoring: an update; *Bull. Am. Meteorol. Soc.*; 74; pp. 1689 – 1696
- Rothrock D. A., Y. Yu and G. A. Maykut (1999); Thinning of the Arctic sea-ice cover; *Geophysical Research Letters*; 26; pp. 3469 – 3472
- Sandven, E., O. M. Johannessen, M. W. Miles, L. H. Peterson and K. Kloster (1999); Barents Sea seasonal ice zone features and processes from ERS – 1 SAR : SIZE92; *J. Geophys. Res.*; 104; pp. 15,843 – 15,857
- Schanda, E. (1976); *Remote Sensing for Environmental Sciences* : Berlin; Springer Verlag; 367 pp.
- Schmidt, G. A. and J. E. Hansen (1999); Role of sea ice in global change pondered. *EOS; Trans. American Geophysical Union* 80, pp 317 – 339
- Sehra, P. S. (1976); *Atmospheric structure : exploration over Antarctica and Inter-hemispheric comparison*, Thesis submitted to Gujarat University, Ahmedabad, India, for Degree of Doctor of Philosophy; 285 pp.
- Sharma, R., K. N. Babu, A. K. Mathur and M. M. Ali (2002); Identification of large scale atmospheric and oceanic features from IRS – P4 Multifrequency Scanning Microwave Radiometer : preliminary Results; *Journal of Atmospheric and Ocean Technology*; 19; pp. 1127 – 1134
- Shuman, C. A., R. B. Alley, S. Anandakrishnan and C. R. Stearns (1994); An empirical technique for estimating near surface air temperatures in central Greenland from SSM/I brightness temperatures; *Remote Sens. Environ.*; 51; 245 – 252
- Sissala, J.F., R.R. Sabatini and H.J. Ackerman (1972), Nimbus Satellite Data for polar ice survey, *Polar Rec.*, 16, pp. 367 – 373
- Smith, D. A. and John Klinck (2002); Water properties on the west Antarctic Peninsula continental shelf: a model study of effects of surface fluxes and sea ice; *Deep-sea Research Part – II*; 49; pp. 4863 – 4886
- Seffen, K., W. Abdalti and I. Sherjal (1999); Faceted crystal formation in the northeast Greenland low accumulation region; *J. Glaciol.*; 45, pp. 63 – 68
- Steffen, K. and A. Schweiger (1991); DMSP – SSMI NASA team algorithm for sea ice concentration retrieval : Comparison with Land sat satellite imagery, *J. Geophys. Res.*; 96; pp. 21,971 – 21,987
- Stossel, A.; K. Yang and Seong-Joong Kim (2002); On the role of sea ice and convection in a global ocean model; *J. of Physical Oceanography*, 32, pp 1194 – 1208
- Svendsen, E., K. Kloster, B. Farrelly, O. M. Johannessen, J. A. Johannessen, W. J. Campbell, P. Gloersen, D.J. Cavalieri and C. Maatzler (1983), Norwegian Remote Sensing Experiment : Evaluation of the Nimbus 7 Scanning Multichannel Microwave Radiometer for sea ice research, *J. Geophys. Res.*, 88, pp 2781 – 2791
- Thompson David W. J. and Susan Solomon (2002); Interpretation of recent southern hemisphere climate change; 296, pp. 895 – 899
- Ulaby, F., R. Moore and A. Fung (1982); *Microwave remote sensing - vol. I - Fundamentals and Radiometry*, Addison – Wesley, MA, USA

Ulaby, F., R. Moore and A. Fung (1986), Microwave remote sensing active and passive - Vol. III – from theory to applications, Addison – Wesley

US-GCRP: “Our changing planet” (2001); The FY 2001 U. S. Global Change Research Program

Vaughan, D. G. and C. S. M. Doake (1996); Recent Atmospheric warming and retreat of ice shelves on Antarctic Peninsula; *Nature*; 379; pp 328 – 331

Venegas, S. A. and M. R. Drinkwater (2001); Sea ice, atmosphere and upper ocean variability in the Weddell Sea, Antarctica; *J. Geophys. Res.*; 106; pp. 16,747 – 16,765

Verma, A. K., R. M. Gairola, A. K. Mathur, B. S. Gohil and V. K. Agarwal (2000); Intercomparison of IRS – P4 MSMR derived geophysical products with DMSP-SSM/I, TRMM – TMI and NOAA – AVHRR finished products; PORSEC Proceedings; I; pp 192 – 196

Vyas, N. K., M. K. Dash, S. M. Bhandari, N Khare, A. Mitra and P. C. Pandey (2003); On the secular trend in sea ice extent over the Antarctic region based on OCEANSAT - ! MSMR Observations, *International Journal of Remote Sensing*; 24; pp. 2277-2287

Vyas N. K., M. K. Dash, S. M. Bhandari, N. Khare, A. Mitra and P. C. Pandey (2001), Large Scale Antarctic Features Captured by Multi - Frequency Scanning Microwave Radiometer Onboard Oceansat - 1, *Current Science*, 80, pp 1391 – 1322

Vyas, N. K. and M. K. Dash (2000), Oceansat - MSMR observes interesting features on the frozen continent and surrounding sea, *Journal of the Indian Society of Remote Sensing*, 28, 2&3, pp 67Dash et al. 2001

White W. B., Shyh-Chin Chen and Ray G. Peterson (1998); The Antarctic circumpolar wave: A beta effect in Ocean-Atmosphere coupling over the Southern Ocean, *J. of Physical Oceanography*; 28; pp. 2345 – 2361

White, J. W. C. and E. J. Steig (1998); Timing is everything in a game of two hemispheres; *Nature*; 394; pp. 717 – 718

White, W. B., Shyh-Chin Chen and Ray G. Peterson (1998); The Antarctic circumpolar wave: a beta effect in ocean-atmosphere coupling over the Southern ocean; *J. Geophys. Res.*; 28; pp. 2345 – 2362

White, W. B. and Ray G. Peterson (1996); An Antarctic circumpolar wave in surface pressure, wind, temperature and sea ice extent; *Nature*; 380; pp. 699 – 702

Whitworth, T., A. H. Orsi, S.-J. Kim, W. D. Nowlin and R. A. Locarnini (1998); Water masses and mixing near the Antarctic slope front, *Ocean, Ice and Atmosphere :interactions at the Antarctic continental margin*; Eds. S. S. Jacobs and R. F. Weiss; Antarctic Res. Ser., Vol. 75; AGU; Washington, D. C.; pp. 1 – 27

Wilheit, T. T., R. F. Adler, R. Burpee, R. Sheets, W. E. Shenk and P. W. Rosenkranz (1978); Monitoring of severe storms, Ch – 5 in High resolution Passive microwave Satellites, Eds. D. Staesin and P. Rosenkranz, Applications Review Panel Final Report, Res. Lab of Elec. ; Mass. Inst. Technol.; Cambridge; MA

Wilheit, T. T. (1972); A model for microwave emissivity for ocean surface as a function of Wind speed; *IEEE Trans. Geosc. Electron.*; GE – 17; pp 960 – 972

World Climate Research Program; Climate and Cryosphere (CliC) Project, Science and Co-ordination Plan, version 1(2001); Eds. Ian Allison, R. G. Barry and B. E. Goodison, WCRP – 114; WMO/TD No. 1053; 75 pp.

- Wu Xingren, W. F. Budd and Ian Allison (2003); Modeling the impacts of persistent Antarctic polynyas with an atmospheric – sea – ice general circulation model; Deep-Sea Research Part – II; 50; pp. 1357 – 1372
- Yuan, X. and D. G. Martinson (2001); The Antarctic dipole and its predictability; Geophys. Res. Lett.; 28; pp. 3609 – 3612
- Yuan, X. and D. G. Martinson (2000); Antarctic sea ice extent Variability and its Global Connectivity; J. Climate; 13; pp 1697 – 1717
- Yuan, X., D. J. Martinson and W. T. Liu (1999); The effect of air sea interaction on winter 1996 Southern Ocean sub polar storm distribution; J. Geophys. Res; 104; pp. 1991 – 2007
- Yueh, S. H., R. Kwok, S. Lou and W. Tsai (1997); Sea ice identification using dual-polarized Ku-band scatterometer data; IEEE Trans. Geosci. Remote Sens.; 35; pp 560 – 569
- Zavody, A. M., C. T. Mutlow and D. T. Llewellyn-Jones (1995); A radiative transfer model for sea surface temperature retrieval for the along – track scanning radiometer; J. Geophys. Res.; 100; pp 937 - 952
- Zwally, H. J., J. C. Comiso and A. L. Gordon (1985); Antarctic offshore leads and polynyas and oceanographic effects; Oceanology of the Antarctic Continental Shelf, Antarctic Research Series ; 43; edited by S. S. Jacobs; American Geophysical Union; Washington, D. C.; pp. 203 – 226
- Zwally, H. J., J. C. Comiso, C. L. Parkinson, W. J. Campbell, F. D. Carsey and P. Gloersen., P. (1983); Antarctic Sea Ice, 1973 – 1976: Satellite Passive Microwave Observations, NASA SP – 459; National Aeronautics and Space Administration, Washington DC, 206 pp.
- Zwally, H.J., (1984); Passive Microwave Remote Sensing for Sea Ice Research; NASA HQ Report*